Holographic Approaches to Strongly-Interacting Systems

Nikola Ivanov Gushterov Totev

Balliol College

University of Oxford

A thesis submitted for the degree of

Doctor of Philosophy

Trinity 2018

Holographic Approaches to Strongly-Interacting Systems

Nikola Ivanov Gushterov Totev

Balliol College
University of Oxford

A thesis submitted for the degree of Doctor of Philosophy

Trinity 2018

Abstract

In this thesis, we investigate some applications of the gauge/string duality to strongly-coupled quantum field theories. After a brief review of the duality and the main entries of the holographic dictionary, we explore the asymptotic nature of the gradient expansion for Bjorken flow using the fluid/gravity correspondence. We link the divergence of the series to the presence of non-perturbative quasi-normal modes and construct the hydrodynamic attractor, using Borel-Padé summation techniques. We find that different initial conditions hydrodynamise, at large values of the pressure anisotropy, before the plasma has had time to reach thermal equilibrium. We then explore the transport properties of zero sound modes in a family of holographic strange metals. We find sound modes with speed given by the conformal value and attenuation constant given by hydrodynamic form at arbitrarily low temperatures, even outside of the usual hydrodynamic regime. The sound attenuation constant as a function of temperature qualitatively resembles that of a Landau Fermi liquid zero sound, including a maximum between the collisionless and the hydrodynamic regimes. In order to get insight into these low temperature sound modes, we introduce a new quantity called "entanglement density", which we study holographically for a range of systems and relevant deformations. We conclude that its asymptotic nature is linked to the area theorem of entanglement, and that it can be used to classify states of quantum matter according to their long-range entanglement and the violation of the area theorem.

To the memory of my Grandfather

Acknowledgements

I would like to express my gratitude to my supervisors Andrew O'Bannon and Andrei Starinets for their continuous support, invaluable guidance and advice throughout my DPhil. I would also like to thank my collaborators, Jorge Casalderrey Solana, Ben Meiring and Ronnie Rodgers for numerous illuminating discussions and time spent working together. I further acknowledge important advice and support from T. Andrade, R. Davison, J. Erdmenger, A. Ficnar, S. Grozdanov, N. Kaplis, J. Probst and J. Tarrio. I am thankful to Balliol College, the Royal Society, and the European Research Council for the financial support of my doctoral work. Finally, I would like to thank my family, especially my parents, Galya and Ivan, for their endless support and care, and Patricia for her understanding, patience and love.

Statement of Originality

This thesis is based on research and contains no material that has already been accepted, or is concurrently being submitted, for any degree or diploma or certificate or other qualification in this university or elsewhere. To the best of my knowledge and belief this thesis contains no material previously published or written by another person, except where due reference is made in the text.

Chapter 4 is based on J. Casalderrey-Solana, N. I. Gushterov and B. Meiring, *Resurgence and Hydrodynamic Attractors in Gauss-Bonnet Holography*, *JHEP* **04** (2018) 042, [1712.02772]. Chapter 5 is based on N. I. Gushterov, A. O'Bannon and R. Rodgers, *Holographic Zero Sound from Spacetime-Filling Branes*, arXiv [1807.11327], and on N. I. Gushterov, *Quasinormal Modes and Correlators in the Shear Channel of Spacetime-Filling Branes*, arXiv [1807.11390]. Chapter 6 is based on N. I. Gushterov, A. O'Bannon and R. Rodgers, *On Holographic Entanglement Density*, *JHEP* **10** (2017) 137, [1708.09376].

Contents

Chapter 1

Introduction

In the late 90's, an unexpected connection emerged between two seemingly unrelated theories. On the one side, we have a theory of classical gravity, the force which governs nature on large scales and describes black holes. On the other side, we have quantum field theories, which describe interactions between fundamental particles at various scales. The key insight to connect these two branches of physics came from the study of non-perturbative objects in string theory, which can be described by quantum gauge theories or classical gravity, depending on their backreaction on the surrounding geometry. In the small backreaction limit, the low energy effective description is a weakly-coupled gauge theory with the coupling proportional to the backreaction. On the other side, in the large backreaction limit, the extended objects collapse into a black hole with low energy effective description given by gravity.

The *gauge/string duality*, also known as holography or the AdS/CFT correspondence [1–4], conjectures that these two descriptions are in fact equivalent for all values of the coupling (backreaction). In particular, the weakly-coupled string theory described by (classical) gravitational theory provides a dual description of the strongly-coupled gauge theory (this part of the correspondence is known as *gauge/gravity duality*). The best-understood realisation of the duality relates a d-dimensional conformal field theory (CFT_d) in flat Minkowski spacetime to gravity on $(d+1)$-dimensional anti-de Sitter (AdS_{d+1}) spacetime. The AdS/CFT duality was originally formulated between the conformal, maximally supersymmetric $\mathcal{N} = 4$ Yang-Mills theory with gauge group $SU(N_c)$ in $d = 4$ dimensions and type IIB string theory on $AdS_5 \times S^5$, which in the

strong coupling limit of the gauge theory reduces to classical (super)gravity on AdS_5 [1].

The most attractive feature of the correspondence is that it is a weak-strong duality, providing a tool to understand general properties of non-perturbative quantum field theories (QFTs) by using well-understood methods in classical general relativity and black hole physics. Conventional calculations in QFTs usually rely on perturbation theory and Feynman diagrams, which have been extremely useful in understanding the electroweak forces and the high energy limit of the asymptotically free theory of quantum chromodynamics (QCD). Apart from these fundamental forces, most of condensed matter theory is based on the existence of weakly-interacting quasi-particles, described by an effective QFT. However, there are well-known examples such as strange metals and high-temperature superconductors in condensed matter systems, or strongly-interacting systems such as QCD at low and intermediate energies describing e.g. the quark-gluon plasma (QGP), which defy a perturbative approach. A common alternative is lattice gauge theory, which allows for a non-perturbative numerical evaluation of the Euclidean quantum path integral. However, lattice gauge theory is known to suffer from the "sign problem" at finite chemical potential and is also ill-suited for computing real-time correlation functions and transport properties [5]. In many cases, there are simply no other tools available that would allow for necessary calculations in strongly-interacting systems. By contrast, holography drastically simplifies calculations at strong coupling, such as e.g. the calculations of real-time correlation functions, which essentially reduce to solving linear wave equations in the dual gravitational theory. Moreover, the dual gravitational perspective offers a geometric description for strongly-coupled processes which goes beyond the weakly-interacting quasi-particle picture [6].

These simplifications, however, come at a price: QFTs with dual gravity description are very particular and in fact rather different from realistic theories such as QCD. First, they are typically supersymmetric and conformal matrix gauge theories. Second, in order to suppress quantum effects on the gravity side, one has to take the large N_c limit [7] in the gauge theory, typically based on a gauge group such as $SU(N_c)$ or similar. Due to these restrictions, QFTs with gravity duals can at best serve as useful toy models for real strongly-coupled systems, if we concentrate on the *universal* features of these

models, i.e. properties that only depend on the IR physics and are thus common to different theories, regardless of their microscopic details. One of the intriguing examples of such a universality is the ratio of shear viscosity η to entropy density s which, in natural units, is given by $\eta/s = 1/4\pi$ in all rotationally-invariant holographic fluids dual to Einstein gravity [8–12], which is surprisingly close to the η/s estimated for strongly interacting cold atoms and the QGP [13]. AdS/CFT has also revealed universality in second-order transport [14–18] and anomalies in transport [19–21].

In this thesis, we use holographic approaches to investigate strongly-interacting quantum systems at finite temperature and density. Chapter 2 motivates the origin of gauge/gravity duality within string theory and Chapter 3 summarises the relevant entries in the holographic dictionary, which translates between the gauge theory and gravity sides. In Chapter 4, we explore the "unreasonable effectiveness" of hydrodynamics, i.e. its ability to describe the QGP even for extreme pressure gradients, questioning the traditional applicability criteria of this effective theory. We study the boost-invariant Bjorken flow at finite coupling using the fluid/gravity correspondence to show that the hydrodynamic expansion is an asymptotic series, which, employing the theory of Borel-Padé summation, can be used to construct an early time "hydrodynamic attractor" to justify the applicability at large gradients. In Chapter 5 we explore the sound modes in strongly-coupled strange metals at finite temperature and chemical potential. We find sound modes with attenuation constant given by hydrodynamic form at arbitrarily low temperatures, outside the usual hydrodynamic regime, and we comment on the universal presence of these "zero sound" modes in the case where the system is described by an effective $(0+1)$-dimensional CFT_1 at low energies. Finally, in Chapter 6, we explore the properties of the effective CFT_1, by studying the dependence of the entanglement entropy on the size of the entangled region in several holographic systems with low-dimensional effective IR descriptions. We find that at low temperatures and/or large enough dimension, the systems violate the "area theorem" [22, 23] and develop long-range entanglement, which could explain the presence of the "zero sound" modes at low temperatures. We conclude with a summary of our results in Chapter 7.

Chapter 2

The Gauge/Gravity Duality

In this chapter we introduce the gauge/gravity duality which is the main working instrument of this thesis. In Section 2.1, following the ideas summarised in ref. [24], we motivate the duality, first omitting technical details of string theory, and then returning to them in Section 2.2, where we explore the original motivation for the duality using non-perturbative objects in string theory called D-branes. Finally, in Section 2.3 we reconstruct the general argument for the canonical example of the duality between $\mathcal{N} = 4$ SYM and type IIB string theory on $AdS_5 \times S^5$.

2.1 Motivating the duality

Although the AdS/CFT correspondence was originally motivated in the context of D-branes and string theory, the existence of the duality could in principle be inferred by considering certain aspects of gauge theories and gravity or string theory.[1] In this section, we motivate the connection between gauge theories and string theory.

2.1.1 The geometrisation of the renormalisation group flow

Consider a QFT in d-dimensional Minkowski spacetime with coordinates $(t, \vec{x})$, defined with a short-distance cutoff ϵ. As shown in the work of Kadanoff and Wilson in the 60's, a good way to organise the degrees of freedom of the system is according to the energy or length scales. Whenever one is interested in the properties of the theory at

[1] Since string theory is a quantum theory of gravity whose low energy description is given by classical general relativity, we will use the terms string theory and gravity interchangeably.

large length scales $z \gg \epsilon$, it is more convenient to obtain an effective description of the theory by integrating out the microscopic details encoded in the short distance physics. If we are interested in even larger length scales $z' \gg z$, we could further integrate out the degrees of freedom present between those scales. This procedure defines a Renormalisation Group (RG) flow, and creates a continuous family of effective theories in a d-dimensional Minkowski spacetime labeled by the RG scale z. If we now consider z to be a physical coordinate, then what we have created is a $(d+1)$-dimensional theory, where a $(d+1)$-dimensional region defined by $z \geq z'$ is completely described by the d-dimensonal effective theory of the system defined on the z' slice.

In particular, if we take $z' \to 0$, we discover something remarkable, which is that this $(d+1)$-dimensional theory would be completely described by a theory in one lower dimension, living on the $z' = 0$ slice, assuming we know how to connect the slices together. These ideas were advocated by Polyakov long before the AdS/CFT correspondence was discovered [25].

However, *a priori* we do not know how exactly the degrees of freedom of a $(d+1)$-dimensional system can be encoded by the degrees of freedom of a theory in one lower dimension. The clue comes from the holographic principle [26, 27], which says that a theory of quantum gravity in a region of space can be described by a *non-gravitational* theory living on the boundary of that region. This suggests that the $(d+1)$-dimensional theory we are looking for might be a theory of quantum gravity/string theory, realising the holographic principle, where, in our case, the non-gravitational theory is a QFT living on the $z' = 0$ slice, at the boundary of the entire space.

The heuristic arguments presented above serve as a motivation rather than a precise recipe on how to contruct the correspondence, making the relation between the Wilsonian cut-off ϵ and the holographic coordinate z precise. Establishing such a relation remains an open problem in holography.[2]

At this point, we can try to establish some general properties that this $(d+1)$-dimensional spacetime should satisfy. The most general metric that we can construct

[2]See e.g. the recent work in [28], where some progress has been made in the context of dimensional renormalisation in AdS/CFT.

in $d+1$ dimensions consistent with the d-dimensional Poincare symmetry of the dual field theory can always be written in the form

$$ds^2 = \Omega(z)^2(-dt^2 + d\vec{x}^2 + dz^2), \tag{2.1}$$

where the metric components can depend only on z and we have used diffeomorphism invariance to factor out an overall scaling factor $\Omega(z)$. For a general field theory, not much can be said about $\Omega(z)$. However, if we consider theories with extra symmetries, such as CFTs, we can determine $\Omega(z)$ using the additional restrictions. The conformal symmetry would imply that our theory will be invariant under a constant rescaling of the coordinates $(t, \vec{x}, z) \to \lambda(t, \vec{x}, z)$, since z represents a length scale in our boundary theory. Under this additional symmetry, the only possible metric becomes

$$ds^2 = \frac{R^2}{z^2}(-dt^2 + d\vec{x}^2 + dz^2), \tag{2.2}$$

which is precisely the metric describing AdS_{d+1} spacetime with constant curvature radius R and negative cosmological constant $\propto 1/R^2$ [29]. In addition to Poincare and scaling symmetries, conformal field theories are also invariant under additional transformations, collectively forming a d-dimensional conformal group $SO(2,d)$. Remarkably, the isometry group of the metric in Eq. (2.2) precisely matches[3] the symmetry group of CFT_d!

An inmediate question then is what type of QFT could possibly look like a string theory? As we will see in the next section, the perfect candidate turns out to be a non-Abelian matrix gauge theory in the 't Hooft's large-N_c limit [7].

2.1.2 The 't Hooft large-N_c limit and stringy connections

A strong indication that a string theory description may exist for matrix non-Abelian gauge theories comes from the large-N_c expansion proposed by 't Hooft [7], where the basic idea is to treat the number of colours N_c of the gauge group as a large parameter, and expand physical quantities in powers of $1/N_c$. As an example, consider

[3]The isometry group $SO(2,d)$ of AdS_{d+1} is most easily understood by embedding AdS_{d+1} as a hyperboloid in a flat $\mathbb{R}^{2,d}$ space [3, 4, 30].

the Euclidean partition function of the theory with the gauge group $U(N_c)$ and coupling g_{YM},

$$Z = \int \mathcal{D}A_\mu \exp\left(-\frac{1}{4g_{YM}^2}\int d^4x \mathrm{Tr} F_{\mu\nu}F^{\mu\nu}\right) . \tag{2.3}$$

After introducing the 't Hooft coupling $\lambda \equiv g_{YM}^2 N_c$, the vacuum-to-vacuum amplitude, given by $\log Z$, is expanded as

$$\log Z = f_0(\lambda)N_c^2 + f_1(\lambda) + f_2(\lambda)\frac{1}{N_c^2} + ... = \sum_{h=0}^{\infty} f_h(\lambda) N_c^{2-2h}. \tag{2.4}$$

The power $\chi = 2-2h$ can be recognised as the Euler character, which is telling us that in this limit, the Feynman diagrams of the theory reorganise themselves according to the topology of 2-dimensional compact manifolds. In particular, any of the coefficients $f_h(\lambda)$ will only get contributions from the diagrams that can be consistently respresented as two-dimensional surfaces with h holes without crossing any lines.

Remarkably, such an expansion is reminiscent of a perturbative expansion in closed string theory, where the worldsheet of a string expanded perturbatively in the string coupling g_s is also organised by the topologies of two-dimensional surfaces. For example, the vacuum-to-vacuum amplitude in the string theory can be written as

$$\mathcal{A} = F_0(\alpha)\frac{1}{g_s^2} + F_1(\alpha) + F_2(\alpha)g_s^2 + ... = \sum_{h=0}^{\infty} F_h(\alpha) g_s^{2h-2}, \tag{2.5}$$

where

$$\alpha = 2\pi l_s^2 \tag{2.6}$$

is the inverse of the string tension given as function of the string length l_s. Comparing these two expressions, one is temped to identify

$$g_s \sim \frac{1}{N_c}, \tag{2.7}$$

which heuristically explains how a large-N_c field theory can be described by a string theory in the first place.

The large-N_c limit has another interesting property: it suppresses contributions from matter in the fundamental representation of the gauge group. One may ask, for example, how the equation (2.4) gets modified, if we include matter in the fundamental representation. In a theory with N_f flavours, the single quark loop planar diagram

contribution to the vacuum amplitude scales as $\log Z \sim N_f N_c$, and therefore the contribution from quark loops will be suppressed by powers of $N_f/N_c \ll 1$. Thus, to leading order in N_c, it is safe to ignore the quark contribution.[4] From this discussion, we conclude that in order to have a gravity/string dual description, we might need to consider matrix QFTs in the large-N_c limit.

2.2 Non-perturbative objects and Dp-branes

Perturbatively, string theory is a theory of strings, involving both open and closed strings. Non-perturbatively, the theory also contains a variety of higher-dimensional solitonic-like objects. Of particular interest to us will be the Dirichet p-branes (Dp-branes) of type II superstring theories in 10 spacetime dimensions, which are extended objects where closed strings can break and open strings can end.[5]

Consider one of these Dp-branes branes extending along the $x^\mu = (x^0, x^1, ..., x^p)$ directions, with $y^i = (y^{p+1}, ..., y^9)$ denoting transverse directions. After quantising the excitations along the brane, one can see that the low energy degrees of freedom consist of an Abelian $U(1)$ field $A_\mu(x)$ with the field strength $F_{\mu\nu} = \partial_\mu A_\nu - \partial_\nu A_\mu$ and $9-p$ scalar fields $\phi^i(x)$ parametrising the transverse directions of the brane y^i, with their respective fermionic superpartners.

The low energy effective action of a single D-brane can be described by the so-called Dirac-Born-Infeld (DBI) action [32, 33][6]

$$S_{DBI} = -T_D \int d^{p+1}x \sqrt{-\det\left(g_{\mu\nu} + \alpha F_{\mu\nu}\right)}, \qquad g_{\mu\nu} = \eta_{\mu\nu} + \alpha^2 \partial_\mu \phi^i \partial_\nu \phi^i. \tag{2.8}$$

Here T_D is the tension of the brane which, using $\alpha \sim l_s^2$, scales as

$$T_D = \frac{1}{(2\pi)^p g_s l_s^{p+1}} \sim \frac{1}{g_s l_s^{p+1}}, \tag{2.9}$$

[4] Here we assume that N_f is kept fixed in the large N_c limit, but one may consider other options, such as the Veneziano limit [31], where $N_c \sim N_f$.

[5] In superstring theory, Dp-branes carry conserved charges associated with Ramond-Ramond (RR) (p+1)-form fields which makes them stable objects.

[6] The bosonic part of the Dp-brane action consists of two terms. The DBI part, which couples to the closed-string sector, namely the metric, dilaton and Neveu-Schwarz-Neveu-Schwarz (NS-NS) 2-form, and the Wess-Zumino part which couples to the RR terms [34–36]. We will only consider the DBI part and we will consistently set the NS-NS 2-form to zero and the dilaton to a constant.

with $g_{\mu\nu}$ being the induced metric on the brane parametrised by the transverse scalars. To leading order in α, the DBI action reduces to the usual $U(1)$ Maxwell form plus scalars and a constant term $\propto T_D$

$$S_{DBI} \approx -T_D \int d^{p+1}x \sqrt{-\det\left(g_{\mu\nu}\right)} \left(1 + \frac{\alpha^2}{4} F_{\mu\nu}F^{\mu\nu} + \dots\right) \tag{2.10}$$

$$\approx -T_D \int d^{p+1}x \left(1 + \frac{\alpha^2}{4} F_{\mu\nu}F^{\mu\nu} + \frac{\alpha^2}{2} \partial_\mu \phi^i \partial_\nu \phi^i + \dots\right). \tag{2.11}$$

It is important to notice that the inverse dependence of the tension $T_D \propto 1/g_s$ on the coupling signals the non-perturbative nature of the Dp-branes: they decouple from the spectrum in the $g_s \to 0$ limit. Note that the dependence of the tension on the coupling is different from the one typically found for field theory solitons and instantons, which normally scale as $1/g^2_{YM}$. If a QFT were to be dual to a string/gravity theory, by looking at the non-perturbative sector, we see that this would suggest the relation $g^2_{YM} \sim g_s$ between the two couplings, which will be confirmed later in the specific realisation of the duality.

Since Dp-branes have finite tension, they gravitate and therefore modify the space-time around them. In particular, the gravitational effect around a stack of N_c Dp-branes will be controlled by the 10-dimensional analogue of Newton's constant,

$$\kappa^2_{10} = 16\pi l_p^8 \sim g_s^2 l_s^8. \tag{2.12}$$

The dependence on the Planck length l_p, or the string length l_s, is completely determined by the dimensional analysis, whereas the g_s^2 dependence emerges from the fact that the low energy effective gravitational coupling at tree level is determined by the exchange of closed strings $\propto g_s^2$ [34]. Combining these results, we find that the quantity

$$N_c T_D \kappa^2_{10} \sim g_s N_c l_s^{7-p} \tag{2.13}$$

controls the effects of the backreaction on the geometry, or the coupling to the closed string sector of the system.[7]

[7]Notice that if we want to have finite backreaction in the small l_s limit, we can only consider branes with $p \leq 7$. In particular, the presence of a D7-brane will modify the asymptotic geometry and introduce a deficit angle.

2.2.1 Open strings and probe D3-branes

From now on, we will be only concerned with the D3-branes of the type IIB superstring theory. In particular, consider a stack of N_c D3-branes in two different limits, according to their backreaction or coupling to the closed string sector.

In the probe limit, where $g_s N_c \ll 1$, their gravitational effects are negligible, and we find a description in terms of *only open strings* stretching between the D3-branes, in 10-dimensional flat spacetime. Something remarkable happens when we consider N_c of those branes stacked on top of each other. In addition to the degrees of freedom of each D3-brane, there are now N_c^2 ways to attach the endpoints of an open string between them. The gauge fields and scalars thus become $N_c \times N_c$ matrices and the $U(1)$ Maxwell action is extended to the $U(N_c)$ Yang-Mills action, with the gauge field and scalars in the adjoint representation. Supersymmetry extends the Yang-Mills action to the maximally supersymmetric Yang-Mills or $\mathcal{N} = 4$ SYM action in $(3+1)$ dimensions [37], with the bosonic part of the Lagrangian given by

$$\mathcal{L} = -\mathrm{Tr}\left(\frac{1}{2g_{YM}^2} F_{\mu\nu}F^{\mu\nu} + D_\mu \phi^i D^\mu \phi^i - \frac{g_{YM}^2}{2}[\phi^i, \phi^j]^2\right), \tag{2.14}$$

where the Yang-Mills coupling is related to the string coupling via[8]

$$g_{YM}^2 = 4\pi g_s. \tag{2.15}$$

Due to the large number of supersymmetries, this theory has many interesting properties, including the fact that the beta function $\beta(g_{YM}) = 0$ vanishes exactly [38, 39]. Consequently, the coupling constant is scale-independent and the theory is conformally invariant. The $U(1)$ part of the $U(N_c) = SU(N_c) \otimes U(1)$ group can be ignored, since it physically corresponds to a translation of the whole system, and therefore the dynamical theory we are considering has $SU(N_c)$ gauge group. From this section we conclude that the low energy effective description in the open string picture is given by $SU(N_c)$ $\mathcal{N} = 4$ SYM CFT_4 in $(3+1)$ dimensions.

[8] The exact factor of 4π can found in two different ways. First, by comparing the F^2 terms in the two actions, from Eqs. (2.14) and (2.10). The second way uses the $SL(2,\mathbb{Z})$ self-duality symmetry of both theories, which relate the axi-dilaton $\tau = \frac{i}{g_s} + \frac{\chi}{2\pi}$ on the gravity side, to the complexified coupling $\tau = \frac{4\pi i}{g_{YM}^2} + \frac{\theta}{2\pi}$ of the dual Yang-Mills theory [4]. Here we have included the relationship between the parity violating terms given by the θ angle, and the dual axion field χ.

2.2.2 Closed strings and extremal black 3-branes

On the other hand, as we start increasing the backreaction, ultimately to the limit $g_s N_c \gg 1$, the D3-branes will gravitate very strongly, eventually forming what is known as an extremal black 3-brane geometry [40], a planar analogue of an extremal black hole. In this regime, the solution is described by gravity, and therefore by *closed strings only*. The general black 3-brane metric at finite temperature reads

$$ds^2 = H(r)^{-\frac{1}{2}} \left(-f(r)dt^2 + d\vec{x}^2\right) + H(r)^{\frac{1}{2}} \left(\frac{dr^2}{f(r)} + r^2 d\Omega_5^2\right), \tag{2.16a}$$

$$H(r) = 1 + \frac{R^4}{r^4}, \qquad f(r) = 1 - \frac{r_H^4}{r^4}. \tag{2.16b}$$

Since we have D3-branes extending along 3 spatial directions, their gravitational effect is similar to that of a point particle in the 6 transverse directions, with mass $M \propto N_c T_D$. This is the reason why the metric (2.16a) only depends on the radial coordinate transverse to the brane. For $r/R \gg 1$, we have $H(r) \sim 1$ and the metric reduces to that of the flat space. The parameter R can thus be considered as the characteristic length scale of the gravitational effect of N_c D3-branes. The other parameter $r_H \propto T$ is the position of the horizon proportional to the Hawking temperature T of the system. In the extremal limit, $T = 0$, the black 3-brane solution can be identified with N_c coincident D3-branes, where R is given by [24]

$$R^4 = 4\pi g_s N_c l_s^4. \tag{2.17}$$

Notice that since we are considering the large backreaction limit $N g_s \gg 1$, this implies that $R \gg l_s$ holds, and classical geometry is not affected by stringy corrections.

In the limit we are concerned with here, $r/R \ll 1$, we can neglect the "1" in $H(r)$. This is commonly known as the *near horizon limit* of the extremal black 3-branes. The metric reduces to[9]

$$ds^2 = ds^2_{AdS_5} + R^2 d\Omega_5^2, \tag{2.18}$$

[9]The general black p-brane metric will have a Ricci scalar $\sim r^{-(p-3)^2/8}$ in the near horizon limit. If we want to avoid curvature singularities and have a classical solution in this limit, we are forced to consider D3-branes.

where

$$ds^2_{AdS_5} = \frac{r^2}{R^2}\left(-dt^2 + d\vec{x}^2\right) + \frac{R^2}{r^2}dr^2\,. \tag{2.19}$$

Changing variables via $r = R^2/z$, one finds that the metric (2.19) is the same as (2.2). We thus see that the near-horizon metric *factorises* into $AdS_5 \times S^5$, and a "throat" geometry develops, with the size of the throat and the 5-sphere set by the same parameter R known as the AdS radius. A natural question arises, namely, what is the low-energy effective description in this case?

A far away observer will see two type of low-energy excitations. At infinity, we have closed strings with proper energy $E_\infty \sim 1$, small compared to the string length scale $E_\infty\, l_s \ll 1$. We also have open strings inside the throat, which are strongly gravitationally redshifted and have arbitrary proper energy compared to the string length scale $E(r)l_s \sim 1$. These two type of excitations decouple in the low energy limit. To see this consider the probability of an open string falling into the throat, which is given by the cross-section of a graviton scattering $\sigma \sim \kappa_{10}^2 \sim l_s^8$. By dimensional analysis, we expect that $[\sigma] = L^5$ and therefore, combining both expression leaves us with $\sigma \sim E_\infty^3 l_s^8$ for a string at infinity, which vanishes in the low energy limit. In a similar way, we see that the energy needed to escape from the potential well of the throat become infinite in the near horizon limit $E(r) = H(r)^{1/4}E_\infty \sim R/r \gg 1$.

From this discussion we conclude that in the limit $Ng_s \gg 1$, the low energy effective description of the system is given by *all the excitations of type IIB closed string theory on the (near-horizon)* $AdS_5 \times S^5$ in an otherwise flat Minkowski space. This can be seen as an alternative low-energy description of the stack of N_c D3-branes.

2.3 The AdS/CFT correspondence

In the last two sections we have seen two equivalent descriptions of a stack of N_c D3-branes. In the open string description, using Eq. (2.15) we have

$$4\pi g_s N_c = \lambda \ll 1, \tag{2.20}$$

and the D3-branes are hyperplanes in an otherwise flat spacetime. In this description, excitations are only open strings stretching between the branes, whose effective low

energy description is given by $SU(N_c)$ CFT in $(3+1)$ dimensions. In contrast, in the closed string description we need

$$4\pi g_s N_c = \lambda \gg 1, \tag{2.21}$$

and D3-branes form a non-trivial spacetime geometry in the near-horizon region. In this description, excitations are only closed strings, whose low energy limit consists of all the excitations of type IIB closed string theory inside the $AdS_5 \times S^5$ throat. Assuming that the variation in Ng_s and the low-energy limit commute [39], Maldacena conjectured [1] that

$$\{\ \mathcal{N} = \mathbf{4}\ \textbf{SYM in (3+1) Minkowski}\ \} = \{\ \textbf{IIB string theory on}\ \mathbf{AdS_5 \times S^5}\ \}$$

for *all values of* $g_s N_c$. This is the canonical realisation of the *AdS/CFT correspondence* or *gauge/string duality*. In particular, we can relate the AdS radius R to the two fundamental scales in string theory, the string length l_s and the Planck length l_p via [41]

$$\frac{R^4}{l_p^4} = 4\pi N_c, \qquad\qquad \frac{R^4}{l_s^4} = \lambda. \tag{2.22}$$

Let us now examine the limits in which either side of the correspondence becomes tractable. In order to suppress quantum gravity effects, keeping $g_s N_c$ fixed, we need to demand $R/l_p \gg 1$. At this stage, we are still left with strings propagating in a classical spacetime. Unfortunately, we don't know how to fully treat this "classical" string theory either, so we also need to take the classical low energy limit of the strings by requiring $R/l_s \gg 1$, which approximates type IIB superstring theory by type IIB supergravity [42, 43]. According to Eq. (2.22), this is equivalent to taking the following limits, respectively, on the field theory side:

$$N_c \gg 1, \qquad\qquad \lambda \gg 1 \tag{2.23}$$

For Maldacena's original realisation of the duality [41], the isometries of AdS_5 and S^5 in the gravity dual correspond to the conformal symmetry $SO(2,4)$ and the R-symmetry $SU(\mathcal{N}=4) \sim SO(6)$ of $\mathcal{N}=4$ SYM, respectively. There is thus a correspondence between global symmetries in the gauge theory and gauge symmetries in the bulk

$$\{\ \textbf{Boundary Global symmetries}\ \} \longleftrightarrow \{\ \textbf{Bulk Gauge symmetries}\ \}.$$

This is an important general feature of all known gauge/gravity dualities, and it is also consistent with the general belief that no global symmetries can exist in a theory of quantum gravity due to the presence of black holes [44].

Given that the S^5 part factorises, it can be considered as an"internal space" and it is often convenient to truncate the 10-dimensional fields on AdS_5 by expanding them in terms of spherical harmonics along the S^5 directions. Indeed, the Kaluza-Klein (KK) compactification of type IIB supergravity preserves the AdS_5 metric, and contains an $SU(4)$ gauge field, dual to the R-current. Together with the other lowest KK modes they form $\mathcal{N} = 8$ supergravity on AdS_5 [45, 46], which is believed to be a consistent truncation [4] of the theory. This compactification manifestly shows that the duality can be viewed as an explicit realisation of the holographic principle, with the bulk spacetime being AdS_5 and the boundary being 4-dimensional Minkowski spacetime. This is yet another important feature of the duality which can be formulated as

$$\{\ \textbf{Large } \mathbf{N_c} \textbf{ boundary } \mathbf{CFT_d}\ \} \longleftrightarrow \{\ \textbf{Asymptotically } \mathbf{AdS_{d+1}} \textbf{ spacetime}\ \}.$$

Other brane constructions in string theory or M-theory also lead to explicit realisations of the gauge/string duality (see e.g. [4, 47]). These models are considered to be *top-down* constructions, since the exact field theory contents and relations between the parameters on both sides of the duality are explicitly known. In this thesis, however, we will be exploring various *bottom-up* models, in which we propose a sensible classical gravity construction that retains only the minimum bulk matter content required to describe the relevant features of a dual strongly coupled matrix gauge theory in the 't Hooft large-N_c limit (see e.g. [48–51]). This last approach has some clear advantages because it allows us to focus only on the relevant features of the strongly coupled field theory.

Chapter 3

The Holographic Dictionary

In Section 3.1 of this chapter, we introduce the field/operator correspondence, which can be used to compute n-point functions of gauge-invariant QFT opeartors from dual gravity. In sections 3.2 and 3.3 we explore the way in which holography geometrises the thermodynamics and the entanglement entropy of the dual field theory.

3.1 Field-operator correspondence and GKPW formula

We now describe how we can put the AdS/CFT correspondence to work and extract properties of the strongly coupled CFT from its AdS dual. Shortly after Maldacena's conjecture, Gubser, Klebanov, Polyakov [2] and, independently, Witten [3] realised that boundary values of fields in AdS bulk can be viewed as sources of gauge-invariant operators in the boundary CFT. Specifically, the GKPW formula states that

$$\left\langle e^{\int d^d x\, \mathcal{O}(x)\phi_0(x)} \right\rangle \equiv Z_{\text{CFT}}\left[\phi_0(x)\right] = Z_{\text{string}}\left[\phi(x,z)|_{\partial AdS}\right] \approx e^{S[\phi_0(x)]}\,. \tag{3.1}$$

Here, Z_{string} denotes the Euclidean partition function of the string theory on AdS, subject to the bulk fields $\phi(x,z)$ assuming the value $\phi_0(x)$ at the AdS boundary. Z_{CFT} is the Euclidean generating functional for an operator $\mathcal{O}(x)$ in the CFT, coupled to the source $\phi_0(x)$. The last approximation is the classical supergravity limit, where the GKPW formula states that the classical gravity on-shell action S is the generating functional for connected correlators in the strongly coupled large-N_c CFT.

3.1.1 Expectation values of operators and scaling dimension

The best way to illustrate this field-operator correspondence, is through the simplest example of a minimally coupled scalar field $\phi(x,z)$ with mass m in AdS. The metric is given by Eq. (2.2). The boundary value of the scalar field $\phi(x,z)$ acts as a source for the scalar operator $\mathcal{O}(x)$ in the field theory. The AdS boundary $z=0$ is a regular singular point of the bulk equation of motion

$$\Box\phi(x,z) = m^2\phi(x,z)\,, \tag{3.2}$$

and therefore the solution takes the form of a Frobenius series [52]

$$\phi(x,z) = A(x)z^{\Delta_-} + \ldots + B(x)z^{\Delta_+} + \ldots\,, \tag{3.3}$$

where $\Delta_\pm$ are the roots of the equation $\Delta\,(\Delta-d) = m^2R^2$, given by

$$\Delta_\pm = \frac{d}{2} \pm \nu, \qquad \nu = \sqrt{\frac{d^2}{4} + m^2R^2}, \qquad \Delta_+ + \Delta_- = d\,. \tag{3.4}$$

Note that the roots are only real if

$$m^2R^2 \geq -\frac{d^2}{4}\,. \tag{3.5}$$

This is the Breitenlohner-Freedman (BF) bound, below which scalar fields in AdS have negative energies and become unstable [47, 53, 54]. Since we expect $A(x)$ to act as a source for $\mathcal{O}(x)$, we can use this information to compute the mass dimension of the dual operator $\mathcal{O}(x)$. For this purpose let us see how $A(x)$ transforms under a scale transformation $x \to \widetilde{x} = \lambda x$. This scaling is implemented by the bulk diffeomorphism $(x,z) \to (\lambda x, \lambda z)$, which leaves the AdS metric invariant:

$$\phi(x,z) = \widetilde{\phi}(\lambda x, \lambda z) = \widetilde{A}(\lambda x)\ (\lambda z)^{d-\Delta_+} + \ldots + \widetilde{B}(\lambda x)\ (\lambda z)^{\Delta_+}\ldots \tag{3.6}$$

This confirms that

$$[A(x)] = [\phi_0(x)] = d - \Delta_+, \qquad [B(x)] = [\mathcal{O}(x)] = \Delta_+\,, \tag{3.7}$$

and implies that $\phi_0(x) \propto A(x)$ couples to an operator $\mathcal{O}(x)$ with dimension given by $d-(d-\Delta_+) = \Delta_+$. This is yet another entry in the holographic dictionary, namely

$$\{\,\textbf{Scaling dimension } \boldsymbol{\Delta_+} \textbf{ of } \mathcal{O}(\mathbf{x})\,\} \longleftrightarrow \{\,\textbf{Mass of the dual field } \phi(\mathbf{x},\mathbf{z})\,\}.$$

Moreover, an application of the GKPW formula (3.1) shows that the expectation value $\langle \mathcal{O}(x) \rangle$ corresponds to the sub-leading mode $B(x) \propto \langle \mathcal{O}(x) \rangle$, as suggested by their mass dimensions [55–57].[1]

$$\{ \textbf{Source } \phi_{\mathbf{0}}(\mathbf{x}) \textbf{ for operator } \mathcal{O}(\mathbf{x}) \} \longleftrightarrow \{ \phi(\mathbf{x}, \mathbf{z}) \propto \phi_{\mathbf{0}}(\mathbf{x})\, \mathbf{z}^{\mathbf{\Delta}_-} + \langle \mathcal{O}(\mathbf{x}) \rangle\, \mathbf{z}^{\mathbf{\Delta}_+} + \dots \}.$$

However, there is a catch. Formally speaking, the on-shell action is infinite and requires regularisation and then the "holographic renormalisation" to obtain a finite result. In order to do so, recall that the extra holographic dimension z can be interpreted as a length scale in the dual field theory. In particular, the UV divergences in the field theory appear on the gravity side as divergences near the AdS boundary [3,25,59,60]. In order to obtain finite results, we have to renormalise the gravity action, which is known as holographic renormalisation. We start by introducing a near-boundary cutoff $z = \epsilon$, and then remove all divergences in the on-shell action S^{ϵ} by adding local counterterms S^{ϵ}_{ct} defined on the cutoff surface, and finally remove the cutoff which leaves us with the *finite* renormalised action $S^{(ren)}$ [56, 57, 61–64]. In order to do so, it is convenient to recall the Hamilton-Jacobi theory, with z playing the role of time. In particular, the derivative of the on-shell action with respect to a field on a constant slice $z = \epsilon$ is equal to the field's canonical momentum with respect to $z = \epsilon$ [65–68],

$$\langle \mathcal{O}(x) \rangle = \frac{\delta S^{(ren)}[\phi]}{\delta \phi_0(x)} = \lim_{z \to 0} z^{\Delta_-} \frac{\delta S^{(ren)}[\phi]}{\delta \phi(x,z)} \equiv - \lim_{z \to 0} z^{\Delta_-} \frac{\partial \mathcal{L}^{(ren)}[\phi]}{\partial \left(\partial_z \phi \right)} = 2\nu B(x)\,, \tag{3.8}$$

where $\mathcal{L}^{(ren)}$ is the renormalised Lagrangian density. Repeating the same process for a gauge field $A_\mu(x)$ coupled to a conserved current $J^\mu(x)$, or the metric $g_{\mu\nu}(x)$ coupled to the conserved stress-energy tensor $T^{\mu\nu}(x)$, we have, respectively

$$\langle J^\mu(x) \rangle = \lim_{z \to 0} \frac{\delta S^{(ren)}[A]}{\delta A_\mu(x,z)}, \qquad \langle T^{\mu\nu}(x) \rangle = \lim_{z \to 0} \frac{2}{\sqrt{-g(x,z)}} \frac{\delta S^{(ren)}[g]}{\delta g_{\mu\nu}(x,z)}. \tag{3.9}$$

In order to compute the field theory stress-energy tensor, we need to take functional derivatives of the renormalised action with respect to the boundary metric $g_{\mu\nu}$. To correctly renormalize the action, we need the the Gibbons-Hawking-York boundary term

[1] This is valid as long as we are in the regime $m^2 R^2 \geq -d^2/4+1$. In the special range of $-d^2/4+1 \geq m^2 R^2 \geq -d^2/4$, the fall of both terms is small enough so that one can consider either of them to be sources [58].

S_{GH} [69], as well as additional counterterms S_{ct} [63], which depend on the dimension you are considering. In particular for $d \leq 4$, we have

$$S_{GH} = \frac{1}{\kappa^2}\int_{\partial M} d^d x\sqrt{-g}K, \qquad S_{ct} = \frac{1}{\kappa^2}\int_{\partial M} d^d x\sqrt{-g}\left[\frac{d-1}{R} + \frac{R}{2(d-2)}\mathcal{R}\right], \quad (3.10)$$

where K in the trace of the extrinsic curvature $K_{\mu\nu} = -\left(\nabla_\mu \hat{n}_\nu + \nabla_\nu \hat{n}_\mu\right)/2$, $\hat{n}_\mu$ is the outward-pointing unit normal vector to the regularised boundary, ∇_μ is the covariant derivative with respect to the induced metric $g_{\mu\nu}$ and $\mathcal{R}$ is the Ricci scalar associated to the induced metric. Using this expressions, the stress-energy tensor can be written in a compact form

$$\langle T_{\mu\nu}\rangle = \lim_{z\to 0}\frac{1}{8\pi G_N}\frac{R^{d+2}}{z^{d+2}}\left[K_{\mu\nu} - g_{\mu\nu}K - \frac{d-1}{R}g_{\mu\nu} - \frac{R}{(d-2)}\mathcal{G}_{\mu\nu}\right], \quad (3.11)$$

where $\mathcal{G}_{\mu\nu} = \mathcal{R}_{\mu\nu} - \frac{1}{2}\mathcal{R}g_{\mu\nu}$ is the boundary Einstein tensor. The first two terms in the bracket of Eq. (3.11) came from the Gibbons-Hawking-York boundary term [69], while the last part comes from the counterterms and is required to make the result finite.[2]

3.1.2 Retarded two-point functions

We can extend the result to n-point Euclidean correlation functions by taking functional derivatives of the action, since $\log\left(Z_{CFT}[\phi_0]\right) = S^{(ren)}[\phi_0]$ is effectively the generating functional for connected graphs, namely

$$\langle \mathcal{O}(x_1)\ldots\mathcal{O}(x_n)\rangle \equiv \left.\frac{\delta^n S^{(ren)}[\phi]}{\delta\phi_0(x_1)\ldots\delta\phi_0(x_n)}\right|_{\phi_0=0}. \quad (3.12)$$

In particular, in momentum space with $k_E = (\omega_E, \vec{k})$ we have

$$\langle \mathcal{O}(k_E)\rangle = (2\Delta_+ - d)B(k_E), \qquad G^E_{\mathcal{O}\mathcal{O}}(k_E) \equiv \frac{\langle \mathcal{O}(k_E)\rangle}{\phi_0(k_E)} \propto \frac{B(k_E)}{A(k_E)}, \quad (3.13)$$

where $G^E_{\mathcal{O}\mathcal{O}}(k_E)$ is the Euclidean correlation function. To compute $G^E_{\mathcal{O}\mathcal{O}}(k_E)$, it will be enough to solve the linearised equations of motion for the perturbations of the bulk fields, in order to find the relation $B(A(k_E))$. A solution to a linear second-order differential equation is completely specified by two boundary conditions. The first one is fixed by the source $A(x)$ in the CFT, whereas $B(A(k_E))$ is determined by

[2] For general d, we expect counterterms of up to $\mathcal{O}\left(\mathcal{R}^{d/2}\right)$, which will modify the expression for the stress-energy tensor. For example, in $d = 5, 6$, we find counterterms of the form $\mathcal{R}^2$ and $\mathcal{R}_{\mu\nu}\mathcal{R}^{\mu\nu}$.

requiring regularity in the bulk in the Euclidean case. If $G^E_{\mathcal{O}\mathcal{O}}(k_E)$ is known exactly, there is a unique way of obtaining the retarded Green's function $G^R(\omega, \vec{k})$ in Minkowski momentum space by using the analytic continuation

$$G^R_{\mathcal{O}\mathcal{O}}(\omega, \vec{k}) = G^E_{\mathcal{O}\mathcal{O}}(-i(\omega + i\epsilon), \vec{k})\,. \tag{3.14}$$

In most cases of interest, however, $G^E_{\mathcal{O}\mathcal{O}}$ is only known numerically. Thus it is important to develop ways to compute real-time correlation functions directly.

In Lorentzian signature, we do not find irregular and regular solutions at the horizon but a combination of incoming and outgoing waves. In order to obtain the causal (retarded) response of the system to the source $\phi_0(x)$, we have to impose incoming-wave boundary condition at the horizon [70, 71]. Intuitively, the energy that is dissipated into the system by the external source $\phi_0(x)$ is related to the energy absorbed by the black brane. Imposing this condition, in AdS, we can determine the subleading mode $B(x)$ in terms of the leading mode $A(x)$, and then determine the one-point function of the dual operator in the presence of the source $\phi_0(x) = A(x)$. We can compute the two-point function by taking derivatives of $B(x)$ with respect to $\phi_0(x)$

$$G^R_{\mathcal{O}\mathcal{O}}(k) \equiv \frac{\langle \mathcal{O}(k) \rangle}{\phi_0(k)} \propto \frac{B(k)}{A(k)}\,. \tag{3.15}$$

This implies that the *quasi-normal modes* of the black brane background, i.e. the complex eigenmodes of the linearised equations of motion which satisfy the incoming-wave boundary condition at the horizon and Dirichlet boundary condition $\phi_0(x) = A(x) = 0$ at the boundary, correspond to poles of $G^R_{\mathcal{O}\mathcal{O}}$ in momentum-space [70, 72].

The computation of correlators was central in the early checks of the correspondence between $\mathcal{N} = 4$ SYM and supergravity on $AdS_5 \times S^5$. Many of these checks were based on comparing anomalies, which are fully determined at one-loop and are thus the same at weak and at strong coupling [4]. Both the conformal symmetry and the R-symmetry of $\mathcal{N} = 4$ SYM are anomalous when the theory is coupled to external sources. The holographic results for the conformal anomaly [61–64], which shows up in the one-point function of the stress-energy tensor's trace, and for the R-symmetry anomaly, which shows up in the non-conservation of the R-symmetry current J^μ [3] and in three-point functions of J^μ [73, 74], agree perfectly with the field theory results in the planar limit.

3.2 Finite temperature and thermodynamics

Until now, we have been concentrating on the vacuum solution only, which for the CFT_d corresponds to a pure AdS_{d+1} spacetime. To generalise to finite temperature, it is convenient to work in Euclidean time compactified on a circle of radius β. For this case, the GKPW formula (3.1) tells us that the gravity renormalised on-shell action equals β times the free energy of the field theory [75]. Finite temperature states of the field theory are thus described by finite temperature solutions in gravity where temperature and entropy are the same on both sides. In particular, field theories in flat space are dual to AdS black brane geometries with a planar horizon [1]. This can be easily deduced by considering the near-horizon limit $r_H < r \ll R$ of the general black p-brane solution, which in the z coordinate and after rotating back to real time becomes

$$ds^2 = \frac{R^2}{z^2}\left(-f(z)dt^2 + d\vec{x}^2 + \frac{dz^2}{f(z)}\right), \tag{3.16}$$

where $f(z) = 1 - z^d/z_H^d$. The position of the horizon $z_H \propto 1/T$ controls the temperature of the solution, once we require the periodicity of the boundary and bulk Euclidean theories to be the same. In general, any thermodynamic quantity or relation will be encoded in the black brane thermodynamics of the dual bulk theory. In particular, the entropy density s will be given by the entropy density of the black-branes[3]

$$s = \frac{R^{d-1}}{4G_N}\frac{1}{z_H^{d-1}} \propto N_c^2 T^{d-1}. \tag{3.17}$$

This solution will also have finite energy density $\epsilon = \langle T^{tt}\rangle$ and will source the energy-momentum tensor $\langle T^{\mu\nu}\rangle$, which is encoded in the subleading term of the metric $g_{\mu\nu}$,

$$g_{tt}(x,z) \sim \frac{R^2}{z^2}\left(-1 + \frac{z^d}{z_H^d} + \dots\right). \tag{3.18}$$

For the simple case of the black brane, using Eq. (3.11) we obtain

$$\langle T_{\mu\nu}\rangle = \frac{R^{d-1}}{16\pi G_N}\frac{1}{z_H^d}\left[\eta_{\mu\nu} + d\,\delta_{\mu t}\delta_{\nu t}\right] \propto N_c^2 T^d\left[\eta_{\mu\nu} + d\,\delta_{\mu t}\delta_{\nu t}\right] \tag{3.19}$$

[3]From the discussion in the previous section, we expect that $R^{d-1}/G_N \sim R^{d-1}/l_p^{d-1} \sim N_c^2$ in order to suppress quantum gravity effects on the geometry.

If we are interested in studying a $U(1)$ global symmetry, we can do this by turning on a chemical potential μ for the corresponding $U(1)$ charge density $\langle J^t \rangle$. This requires that the bulk gauge field A_μ, which is dual to the conserved current J^μ, behaves schematically as

$$A_t(x, z) \sim \mu + \left\langle J^t \right\rangle z^{d-2} + \dots \,. \tag{3.20}$$

The above condition along with requiring A_μ to be regular at the horizon, implies that the black brane is now charged and there would be a homogeneous radial electric field in the bulk. In this thesis, we will encounter several examples of charged black brane solutions which we will explore in detail in relevant chapters.

3.3 Holographic entanglement entropy

The entanglement entropy (EE) is an important concept of relevance for condensed matter and other areas of physics. Due to its non-local nature, it has important properties that can be used to characterise phases of matter, when the usual Ginzburg-Landau classification, based on classical order parameters and spontaneous symmetry breaking is not applicable. Usually, computing EE in field theory is very challenging. In contrast, computing EE in dual gravity turns out to be very simple.

Consider a quantum mechanical system characterised by a density matrix ρ. If the system is in a normalised pure state $|\Psi\rangle$, then the density matrix is given by $\rho = |\Psi\rangle \langle\Psi|$, and satisfies the equation $\rho^2 = \rho$. Another important property of pure states is that their von Neumann entropy, defined as

$$S_{\text{vN}} \equiv -\text{Tr}\left(\rho \log(\rho)\right) \,, \tag{3.21}$$

vanishes exactly. In the case of a mixed state, we can use S_{vN} as a definition of EE. As an example, consider dividing our system into two subsystems, $\mathcal{A}$ and $\mathcal{B}$. For system $\mathcal{A}$, we define the reduced density matrix by tracing out the $\mathcal{B}$ states in the Hilbert space $\mathcal{H} = \mathcal{H}_\mathcal{A} \otimes \mathcal{H}_\mathcal{B}$:

$$\rho_\mathcal{A} \equiv \text{Tr}_\mathcal{B}(\rho). \tag{3.22}$$

The EE for the system $\mathcal{A}$ is then defined in analogy with S_{vN} by

$$S_{\text{ent}} \equiv -\text{Tr}_\mathcal{A}\left(\rho_\mathcal{A} \log(\rho_\mathcal{A})\right) = -\left.\frac{\partial}{\partial n} \log\left(\text{Tr}_\mathcal{A}\left(\rho_\mathcal{A}^n\right)\right)\right|_{n=1} \tag{3.23}$$

and measures the amount of quantum correlation between the two subsystems. The second part of Eq. (3.23) is called the *replica trick*, and allows us to compute EE by computing $\mathrm{Tr}_{\mathcal{A}}\left(\rho_{\mathcal{A}}^{n}\right)$.[4]

In the context of quantum field theory the EE is formally UV divergent, so we need a cutoff ϵ to regulate it. For any QFT_d, we expect the EE to obey the *Area law* [76–79]

$$S_{\text{ent}} \propto \frac{\text{Area}(\mathcal{A})}{\epsilon^{d-2}} + \dots \tag{3.24}$$

due to the short range correlations across the area of the entangled region. This Area law is logarithmically violated in some special cases, including CFT_2, where instead of a constant, S_{ent} is given (at finite temperature T) by

$$S_{\text{ent}} = \frac{c}{3}\log\left(\frac{\sinh\left(\pi LT\right)}{\pi\epsilon T}\right) . \tag{3.25}$$

In the expression (3.25), c is the central charge of CFT_2 and L is the size of the entangled region [80,81]. There are two important limits controlled by the relative size of the entangled region. First, at very small $LT \ll 1$, we expect to find the vacuum CFT_2 result S_{CFT_2}, which is the "area law" and is formally divergent. In the opposite limit, for very large subsystems $LT \gg 1$, when $\rho_{\mathcal{A}} \to \rho$, we expect the EE to become the *extensive* thermodynamic entropy S_{th}, which is exactly what we find in the case of (3.25), namely

$$S_{CFT_2} = \frac{c}{3}\log\left(\frac{L}{\epsilon}\right) + \dots , \qquad S_{th} = \frac{c}{3}\pi LT + \dots . \tag{3.26}$$

One of the important properties of holographic systems is that their entanglement entropies are related to purely geometric quantities. In the simplest case, where the bulk is described by Einstein gravity coupled to matter, the Ryu-Takayanagi prescription [82, 83] states that the entanglement entropy of a region $\mathcal{A}$ for a QFT with a holographic dual is given by

$$S_{\text{ent}} \equiv \frac{\Sigma_{\text{min}}^{\mathcal{A}}}{4G_N} , \tag{3.27}$$

where $\Sigma_{\text{min}}^{\mathcal{A}}$ is the area of the minimal surface extended to the bulk from the entangled region $\mathcal{A}$ of the boundary (for a schematic representation see Fig. 6.2).

[4] Remember that the reduced density matrix ρ_A is normalised so that $\mathrm{Tr}_{\mathcal{A}}(\rho_{\mathcal{A}}) = 1$.

To illustrate the formula, let us compute the vacuum CFT_2 result, which in our case will be dual to an empty AdS_3 spacetime with the metric

$$ds^2 = \frac{R^2}{z^2}(-dt^2 + dx^2 + dz^2)\,. \tag{3.28}$$

The area $\Sigma^{\mathcal{A}}$ of a general static surface parametrised by $z(x)$ is given by the integral over the induced metric,

$$\Sigma^{\mathcal{A}} = \int_{-L/2}^{L/2} \frac{\sqrt{1+z'(x)^2}}{z} dx\,, \tag{3.29}$$

where we are considering the sub-region $\mathcal{A}$ to be $-L/2 \leq x \leq L/2$. To find the minimal area, we need to find the extrema of the integral. If we consider x to play the role of a time variable, we observe that there is a "Hamiltonian" independent of x which can be used to find

$$\frac{dz}{dx} = \frac{\sqrt{z_*^2 - z^2}}{z}\,, \tag{3.30}$$

where z_* is an integration constant that corresponds to the turning point of the surface we are considering, which by symmetry is located at $x = 0$. This expression can be used to parametrise both the size L and the minimal area $\Sigma^{\mathcal{A}}_{\text{min}}$ as functions of z_* as

$$L = 2\int_0^{z_*} dz\, \frac{z}{\sqrt{z_*^2 - z^2}} = 2z_*, \tag{3.31a}$$

$$\Sigma^{\mathcal{A}}_{\text{min}} = 2R\int_\epsilon^{z_*} \frac{dz}{z}\frac{z_*}{\sqrt{z_*^2 - z^2}} = 2R\log\left(\frac{2z_*}{\epsilon}\right), \tag{3.31b}$$

where in the last integral we had to introduce a small cutoff ϵ in the bulk, in order to regularise the infinite area. Inverting the two relations and using Eq. (3.27), we find that the holographic entanglement entropy (HEE) reads

$$S_{\text{ent}} = \frac{R}{2G_N^{(3)}}\log\left(\frac{L}{\epsilon}\right) = \frac{c}{3}\log\left(\frac{L}{\epsilon}\right)\,. \tag{3.32}$$

We recover the result in Eq. (3.25), if in the last expression we use the fact that the central charge c of the dual CFT_2, which counts the effective degrees of freedom, is given by [84]

$$c = \frac{3R}{2G_N^{(3)}} \propto \frac{R}{l_p} \propto N_c^2 \gg 1\,. \tag{3.33}$$

This can be viewed as an alternative derivation of the well-known result, or as a check of the Ryu-Takayanagi prescription. The result is also consistent with the fact that

holographic theories can be viewed as theories with many degrees of freedom "per lattice site". Considering a CFT at finite temperature by using a dual BTZ geometry, we recover the result given by Eq. (3.25) [85]. Now we can understand the motivation behind the proposal (3.27). Indeed, for a thermal state, we expect the HEE to reduce to the extensive thermodynamic entropy S_{th} of the theory, which in holographic systems is given by the quarter of the black brane horizon area measured in Planck units,

$$S_{th} = \frac{A_{\text{hor}}}{4G_N}. \tag{3.34}$$

This gives a geometric intuition on how the HEE interpolates between the *under-extensive* area law and the *extensive* thermodynamic entropy. For small surfaces, $z_* \ll z_H$, and the main contribution to $\Sigma^{\mathcal{A}}_{\text{min}}$ comes from the divergent term near the boundary of AdS_{d+1}, proportional to the area of the entangled region $\mathcal{A}$ of the QFT_d. On the contrary, when $z_* \lesssim z_H$, the minimal area starts probing the horizon, and eventually becomes the dominant contribution when $\Sigma^{\mathcal{A}}_{\text{min}} \to A_{\text{hor}}$. In Chapter 6, we will explore this crossover from under- to over-extensive regime in detail, and discover that it encodes non-trivial information about the long-range entanglement in the systems we study.

Chapter 4

Hydrodynamic Attractor in Gauss-Bonnet Holography

In this chapter, we will study the convergence of the hydrodynamic gradient expansion in the holographic dual of Gauss-Bonnet gravity. In Section 4.2, we introduce the boost invariant Bjorken flow and show how to compute its gradient expansion using the fluid/gravity correspondence, including finite coupling corrections. The gradient expansion is an asymptotic series which can be understood in the light of resurgence and Borel summation, as in the example shown in Section 4.3. Finally, in Section. 4.4 we construct the "hydrodynamic attractor" by summing the divergent series, which provides an analytic continuation of hydrodynamics at early times and for large pressure anisotropies.

4.1 Introduction and motivation

In recent years there has been increasing interest in understanding the emergence of hydrodynamic behaviour in relativistic theories. In addition to many new theoretical advances, the strong multi-particle correlations observed in heavy ion collisions both at RHIC [86–88] and the LHC [89–91] and its successful description via hydrodynamical modelling [92–97] has provided a testing ground to explore how this collective behaviour arises from a microscopic theory. One of the most surprising empirical insights that this type of modelling of subnuclear dynamics has revealed is the fact that hydrodynamics can describe the bulk properties of the system even for extreme pressure

gradients, which at face value, question the applicability of this long distance effective theory to those collisions. The recent observation of collective phenomena also in even smaller systems, such as p-p collisions [98–100] together with the success of the same hydrodynamic modelling in describing them [101–103] poses new challenges to our understanding of the applicability of this theory.

In conjunction with the above phenomenological observations, in recent years several numerical experiments have been performed to test the validity of hydrodynamics in different ultra-relativistic scenarios. Both in the infinitely strongly-coupled limit of $\mathcal{N} = 4$ SYM, described via holography, [104–107] and in the weakly-coupled (perturbative) limit of gauge theories, described via kinetic theory [108], the direct comparison of the full stress-energy tensor in different out of equilibrium processes with the hydrodynamic expectation showed that hydrodynamics can provide an accurate description of the evolution of the system even when the gradient terms are as large as the leading order terms. These experiments demonstrate that hydrodynamics can be applied even if the system under consideration is very far away from local thermal equilibrium and with strong deviations from the equation of state, as explicitly demonstrated in the analysis of non-conformal theories [109].

Complementary to these numerical studies, the convergence of the hydrodynamic series has been recently analysed. In a seminal paper [110], the late time behaviour of boost invariant expansion of $\mathcal{N} = 4$ SYM was analysed in a power series of the inverse proper time up to very high order. The analysis of these large order perturbations showed that the hydrodynamic expansion is an asymptotic series, exhibiting a factorial growth of the series coefficients. Similar behaviour was found in different ultraviolet completions of second order hydrodynamics [111–113] and kinetic theory in the relaxation time approximation (RTA) [114] (see also [115] for a complementary analysis of the convergence of the hydrodynamic series). Interestingly, the analysis of these series via Borel-Padé techniques showed that these large order gradient expansions are sensitive to non-hydrodynamic modes, which play an equivalent role to non-perturbative corrections in perturbation theory.

Numerical analyses of these same boost invariant flows led Heller and Spaliński

to suggest the existence of a hydrodynamic attractor [111] which may be thought as an extension of hydrodynamics beyond local thermal equilibrium [116]. These are special time dependent configurations to which all other boost invariant evolutions of the system converge at different times. These solutions have been found in different theories, such as Israel-Stewart (IS) [117] and Baier-Romatschke-Son-Starinets-Stephanov (BRSSS) [118] hydrodynamics [111, 119], $\mathcal{N} = 4$ SYM, kinetic theory [116] or anisotropic hydrodynamics [120]. It has been further argued that these special solutions may be found, or at least well approximated, via a trans-series solution of the system evolution [111, 121], that non-perturbatively completes the gradient expansion. These types of solutions have also been recently analysed in less symmetric situations, including non-conformal theories and less symmetric flows [122, 123]. Quite remarkably in all those cases the hydrodynamic attractor is very well approximated up to unexpectedly large values of the gradient by first order hydrodynamics, providing a dynamical understanding to the unexpected success of this theory.

The emergence of these solutions has only been studied in the two extreme cases of infinitely strong and perturbatively weak coupling. However, to better connect these theoretical advances with phenomenological applications it is important to understand how these special types of solutions behave at intermediate coupling. Starting from the infinite coupling limit, finite coupling corrections are studied via the gauge/gravity duality by introducing higher curvature terms in the dual gravitational theory [42, 43]. For the gravity dual of $\mathcal{N} = 4$ SYM, the relevant correction that affects the dynamics of the field theory stress-energy tensor are expressed in terms of the Weyl tensor and are quartic in the curvature. These types of corrections have been vigorously studied in the past, exploring the correction of many different quantities (see [124] for a recent compilation of results). Recently, the relaxation of small stress-energy tensor fluctuations in the thermal ensemble of $\mathcal{N} = 4$ SYM has been studied in detail [18, 125], (see also [126, 127] for previous studies). In these studies, a new set of purely dissipative modes have been found, which are an intrinsic consequence of finite coupling.

Another higher-derivative theory which has also received significant attention in the holographic context is Gauss-Bonnet gravity. The action of this theory includes both

quadratic and quartic curvature terms, governed by a single parameter λ_{GB}; nevertheless, as a Lovelock theory, its classical equations of motion contain only up to quadratic derivatives of the metric, which in principle allows the non-perturbative treatment of the high-derivative terms. Unfortunately, the dual field theory to Gauss-Bonnet gravity is unknown. Nevertheless, in this holographic construction it is possible to extract static (thermodynamic) and transport properties of the putative dual field theory, as well as the relaxation of small non-thermal perturbations [18, 125], its off-equilibrium dynamics [128, 129] and corrections to its hydrodynamic expansion [130]. The comparison of those analysis and the results obtained from finite coupling corrections of $\mathcal{N} = 4$ SYM show that for negative λ_{GB} these two theories share many common qualitative aspects, which makes Gauss-Bonnet holography a toy model to study finite coupling effects in holographic theories. Note however that causality, positivity of energy and hyperbolicity considerations constrain the range of values of λ_{GB} [131–138] (see [18] for a detailed discussion on these limitations).

As a first step towards intermediate coupling, in this chapter we analyse the convergence of the hydrodynamic series in the gradient expansion of matter dual to Gauss-Bonnet holography. As in the previously mentioned examples, we find that the series is asymptotic as a consequence of non-perturbative (in gradient strength) contributions, given by the quasi-normal modes of the dual black brane. Remarkably, these characteristic modes dictate that the structure of singularities of the Borel transform associated to the hydrodynamic expansion interpolate between the known examples of infinitely strongly and weakly-coupled theories. After characterising the analytic properties of the Borel transform, we sum the hydrodynamic series and constrain the dynamics of the hydrodynamic attractor. For all values of λ_{GB} considered, the summation approaches first order hydrodynamics even when gradient corrections to the stress-energy tensor are large and at comparable values of the pressure anisotropy. Therefore, even though as the viscosity increases the approach to hydrodynamics occurs at a decreasing value of the gradient, these hydrodynamisation processes take place at comparable values of a viscosity-rescaled gradient, as suggested in [139]. Analysing the leading contributions in the trans-series, we estimate how close the summation is to the attractor solution.

By varying the amplitude of those non-perturbative corrections we observe that the convergence of different initial configurations towards the attractor occurs at values of the viscosity-rescaled gradient for which the summation has hydrodynamised. We also perform an identical analysis of the hydrodynamic series of RTA kinetic theory [114] and find that both hydrodynamisation and convergence to the attractor solution occurs at smaller viscosity-rescaled gradients than in the strong coupling computations.

4.2 Fluid/gravity correspondence

If we start with a continuous, homogeneous and isotropic many-body system at finite temperature and we study its low energy long wavelength physics, we will discover that the effective description of its excitations is governed by hydrodynamics [140]. In particular, hydrodynamics is also the description for the low energy excitations of globally conserved quantities, such as energy, momentum and charge. Its universality comes form the fact that it relies on symmetries and the second law of thermodynamics to restrict the possible structures and hydrodynamic parameters, and therefore has no assumptions about the underlying system.

In order to assign values to the hydrodynamic parameters, such as the equations of state and various transport coefficients, one needs a microscopic description. In the case of weakly-interacting systems, the way to establish these coefficients is through Boltzmann's kinetic theory, where we assume that the transport of macroscopic quantities is the consequence of microscopic collision processes between nearly free particles. This procedure breaks down completely in the strongly-interacting case. Nevertheless, since we still have conservation equations, a fluid description should emerge at low energies. As we have already seen, the stress-energy tensor in the boundary QFT is equivalent to the propagation of gravitons in the bulk. One of the iconic achievements of the holographic duality is the explicit derivation of Navier-Stokes equations in the boundary, from the gravity in the bulk [141].

The non-relativistic Navier-Stokes equations are essentially a consequence of the conservation of energy and momentum. In the case of relativistic systems, this can be

expressed in a very compact form

$$\nabla_\mu \langle T^{\mu\nu} \rangle = 0. \tag{4.1}$$

The structure of relativistic hydrodynamics is then obtained by assuming that we have a fluid with a local four-velocity U^μ correctly normalised to $U^\mu U_\mu = -1$. Assuming local equilibrium, one can assume a gradient expansion around the equilibrium and then express the local energy density ϵ and pressure P in terms of the local temperature $T(x)$, and the fluid velocities [118]. To zeroth order in gradients, the "perfect fluid" non-dissipative hydrodynamics reduces to [142]

$$\langle T^{\mu\nu} \rangle = (\epsilon + P) U^\mu U^\nu + \eta^{\mu\nu} P, \tag{4.2}$$

where in addition, the thermodynamic relation $\epsilon + P = Ts$ is satisfied. Away from this ideal hydrodynamics, we can to expand the previous result to include dissipative effects

$$\langle T^{\mu\nu} \rangle = (\epsilon + P(\epsilon))\, U^\mu U^\nu + \eta^{\mu\nu} P(\epsilon) + \Pi^{\mu\nu}\,, \tag{4.3}$$

encoded in the the transverse traceless tensor given by

$$\Pi^{\mu\nu} = -\eta \sigma^{\mu\nu} - \zeta \nabla^\mu U_\mu + \dots\,, \qquad \Pi^\mu_\mu = \Pi^{\mu\nu} U_\nu = 0 \tag{4.4}$$

where η and ζ are the first order transport coefficients, known as shear and bulk viscosity respectively, and $\sigma^{\mu\nu}$ is the shear tensor, constructed from the symmetrised and traceless space gradient of the velocity field.[1] In this expression the ellipses indicates additional gradient corrections. These transport coefficients can be extracted from two-point functions using Kubo relations [143] by looking at the linear response of the system to infinitesimal perturbations around equilibrium. A further simplification occurs in the case of conformal systems where $\zeta = 0$ because of

$$\left\langle T^\mu_\mu \right\rangle = 0, \tag{4.5}$$

and the pressure is given by the conformal value $P(\epsilon) = \epsilon/(d-1)$.

[1] Space gradients are defined as the projection of the space-time gradient into the space components in the fluid rest fame, $\nabla^\mu = \Delta^{\mu\nu}\partial_\nu$ with the projector $\Delta^{\mu\nu} = \eta^{\mu\nu} + U^\mu U^\nu$. With this notation, we can express the shear tensor as $\sigma^{\mu\nu} = \Delta^{\mu\alpha}\Delta^{\nu\beta}(\nabla_\alpha U_\beta + \nabla_\beta U_\alpha) - \frac{2}{d-1}\Delta^{\mu\nu}\nabla^\alpha U_\alpha$.

4.2.1 Boost invariant Bjorken flow

As an example, consider a boost invariant or Bjorken flow [144] in 3+1 dimensions, which is obtained by assuming boost invariance in one of the special directions $x_\parallel$. This is a particular solution to the conformal relativistic Navier-Stokes equations. If we now want to go to the local rest frame of the fluid, then it is useful to switch to proper time and rapidity coordinates $(t, x_\parallel) = (\tau\cosh(y), \tau\sinh(y))$, which transform the flat Minkowski metric into

$$ds^2 = -d\tau^2 + \tau^2 dy^2 + dx_\perp^2. \tag{4.6}$$

We assume that the fluid is homogeneous and isotropic in the perpendicular directions and that because of the boost invariance the physical observables would be independent of the rapidity y. In particular, we can show that the late time description of the Bjorken flow ($\Pi^{\mu\nu} = 0$) consists of an expanding conformal plasma with temperature $T \sim \tau^{-1/3}$ and therefore at infinite τ should reduce to the vacuum solution. To see this, it is important to notice that once the functional form of the energy density is determined, energy-momentum conservation and conformal symmetry completely fix the components of the stress-energy tensor. Indeed, these two conditions reduce to the following set of equations for the components of $\langle T_{\mu\nu}\rangle$[2] in the local rest frame

$$\left\langle T^\mu_\mu \right\rangle = -T_{\tau\tau} + \tau^{-2}T_{yy} + 2T_{xx} = 0, \qquad \nabla_\mu \left\langle T^{\mu\nu}\right\rangle = \tau\dot{T}_{\tau\tau} + T_{\tau\tau} + \tau^{-2}T_{yy} = 0. \tag{4.7}$$

We define the longitudinal ($P_L(\tau) \equiv T^y_y$) and transverse ($P_T(\tau) \equiv T^x_x$) pressures as the diagonal components of the stress-energy tensor in the fluid rest frame in the direction of expansion and perpendicular to it respectively. Using Eq. (4.7), the pressures are completely determined by the energy density ($\epsilon(\tau) \equiv T_{\tau\tau}$)

$$P_L(\tau) = -\epsilon(\tau) - \tau\dot{\epsilon}(\tau)\,, \quad P_T(\tau) = \epsilon(\tau) + \frac{1}{2}\tau\dot{\epsilon}(\tau)\,. \tag{4.8}$$

Note that these expressions are valid even when the system is not in local thermal equilibrium. From this, and knowing that in thermal equilibrium both pressures must be the same, we can extract an equation for $\epsilon(\tau)$ at equilibrium

$$4\epsilon(\tau) + 3\tau\dot{\epsilon}(\tau) = 0. \tag{4.9}$$

[2]We will omit the expectation value in the components of the $\langle T_{\mu\nu}\rangle$ to simplify the notation.

This equation has a well known "equilibrium Bjorken solution" with $\epsilon_{\rm eq}(\tau) \sim \tau^{-4/3}$. In particular, there is a scaling symmetry in τ which allows us to express the energy density and temperature as[3]

$$\epsilon_{\rm eq}(\tau) \equiv \epsilon_* T_{\rm eq}(\tau)^4 = \epsilon_* \frac{\Lambda^4}{(\Lambda\tau)^{4/3}}, \qquad T_{\rm eq}(\tau) \equiv \frac{\Lambda}{(\Lambda\tau)^{1/3}} \tag{4.10}$$

where Λ is a characteristic scale of mass dimension one, which in the hydrodynamic limit encodes all the information on the initial conditions of the flow and is set such that at $\Lambda\tau = 1$, then $T_{\rm eq}(\tau) = \Lambda = 1/\tau$. In particular, this fixes the dimensionless normalisation constant ϵ_*. Away from equilibrium ($\Pi^{\mu\nu} \neq 0$), we expect corrections to these expressions in inverse powers of the proper time $u \equiv (\tau\Lambda)^{-2/3} = (\tau T_{\rm eq})^{-1}$ of the form

$$\epsilon(\tau) \equiv \epsilon_* T(\tau)^4 = \epsilon_{\rm eq}(u) \left(1 + \epsilon_1 u + \epsilon_2 u^2 + ...\right) , \tag{4.11}$$

where we have now defined an out-of equilibrium temperature $T(\tau)$, which will reduce to the equilibrium value at large τ, and the coefficients ϵ_n are dimensionless constants which are solely dependent on the degrees of freedom and transport coefficients. The leading gradient correction from the equilibrium energy density $\epsilon_{\rm eq}(\tau)$ is controlled by the shear viscosity and similarly all additional coefficients are a combination of the transport coefficients up to the corresponding order.[4]

Using Eq. (4.8), we observe that $P_L(\tau) \neq P_T(\tau)$ and therefore, we may quantify how far the system is from local thermal equilibrium by monitoring how anisotropic the system is. We can define the dimensionless anisotropy parameter

$$R(\tau) \equiv \frac{P_T(\tau) - P_L(\tau)}{\epsilon(\tau)/3} = 6\left(1 + \frac{3}{4}\tau\,\partial_\tau \log \epsilon(\tau)\right), \tag{4.12}$$

where the equilibrium value of the pressure $\epsilon(\tau)/3$ has been used to normalise the pressure anisotropy. The anisotropy parameter $R(\tau)$ can be used to monitor the approach of a system to hydrodynamics [104]. Following the hydrodynamic expansion in

[3]Notice that equilibrium corresponds to late time dynamics, where the energy density and temperature scale as $\epsilon(\tau) \sim \tau^{-4/3}$ and $T(\tau) \sim \tau^{-1/3}$ and are not constants.

[4]The complete set of second order coefficients and their operators can be found in [118,141] and [145] for conformal and non-conformal theories respectively.

Eq. (4.11), for a conformal theory the anisotropy parameter $R(\tau)$ becomes a function of the dimensionless gradient,[5]

$$w = \tau T(\tau)\,, \tag{4.13}$$

where out of equilibrium temperature $T(\tau)$ is defined through Eq. (4.11). In the hydrodynamic limit, $R(w)$ admits an expansion in inverse powers of w as

$$R(w) = \sum_{n=1} \frac{r_n}{w^n}\,, \tag{4.14}$$

where, to first order in hydrodynamics, the anisotropy function is given by

$$R^{\text{1st}}_{\text{hyd}}(w) = 8\frac{\eta}{s}\frac{1}{w}\,. \tag{4.15}$$

4.2.2 Holographic dual of Bjorken flow

The idea that there is a deep connection between the dynamics of a black hole horizon and the hydrodynamic equations dates back to the 80's, where people realised that the fluctuations of black holes can be understood with the dynamics of a fictitious fluid living just outside the horizon, with dynamics governed by Einstein's equations, the so called "membrane paradigm" [68, 146]. The crucial new addition coming from the gauge/gravity duality, is that in the fluid/gravity correspondence the fluid lives on the boundary of AdS. We know that hydrodynamics is the description of long-lived, low energy excitations near thermal equilibrium. Using the GKPW formula, the low energy fluctuations near the horizon can be "uplifted" and converted to hydrodynamics of the boundary system.[6]

Since we want to find the holographic dual of this fluid, we start by considering the solution corresponding to the finite temperature black brane in AdS_5

$$\begin{aligned} ds^2 &= -r^2 f(r) dt^2 + \frac{dr^2}{r^2 f(r)} + r^2 d\vec{x}^2 \\ &= -r^2 f(r) dt_+^2 + 2dt_+ dr + r^2(dx_\parallel^2 + dx_\perp^2), \end{aligned} \tag{4.16}$$

[5] Other dimensionless quantities have been used in the literature for identifying attractor solutions such as $f(w) \equiv \tau\,\partial_\tau \log w = 1 + \frac{1}{4}\tau\,\partial_\tau \log \epsilon$ which are related to the anisotropy parameter via $R(w) = -12 + 18 f(w)$.

[6] This statement can be made precise by showing that Einstein's equations admit a gradient expansion in terms of $T(x)$ and velocity gradients, which give the desired constitutive relations using Eq. (3.11).

where $f(r) = 1 - r_H^4/r^4$ with the horizon position related to the temperature $T \sim r_H$, and we have used the infalling Eddington-Finkelstein (EF) time coordinate given by $dt_+ = dt + dr/r^2 f(r)$ to make the metric regular at the horizon. Because we are looking for an expanding plasma with temperature, $T(\tau) \sim r_H \sim \tau^{-1/3}$, and boundary metric given by Eq. (4.6) at $r \to \infty$, we would naturally consider a metric of the form

$$ds^2 = -r^2 f(\tau, r) d\tau^2 + 2dr d\tau + r^2 \left(\tau^2 dy^2 + dx_\perp^2\right). \tag{4.17}$$

However, in the case of $T \propto r_H = 0$, the metric should reduce to the AdS_5 vacuum solution, which Eq. (4.17) does not. The easy way to fix this discrepancy is to realise that after a shift of the form $\tau \to 1/r + \tau_+$ the vacuum solution can be rewritten as

$$\begin{aligned} ds^2 &= \frac{dr^2}{r^2} + r^2(-d\tau^2 + \tau^2 dy^2 + dx_\perp^2) \\ &= -r^2 d\tau_+^2 + 2d\tau_+ dr + (1 + r\tau_+)^2 dy^2 + r^2 dx_\perp^2. \end{aligned} \tag{4.18}$$

The most general boost invariant metric that implicitly incorporates the structures from Eq. (4.17) and Eq. (4.18) can be written in the following form:

$$ds^2 = -r^2 A(\tau, r) d\tau^2 + 2dr d\tau + (1 + r\tau)^2 e^{b(\tau,r)} dy^2 + r^2 e^{c(\tau,r)} dx_\perp^2 \tag{4.19}$$

This parametrisation of the metric components is convenient for calculations, since it reduces to vacuum AdS_5 for the empty fluid case ($A = 1, b = c = 0$). In order to compute the field theory stress-energy tensor, we can use Eq. (3.11) with $d = 4$, and the fact that the near boundary expansion of the metric components is given by

$$A(\tau, r) = 1 + \frac{A^{(4)}(\tau)}{r^4} + ..., \quad b(\tau, r) \quad = \frac{b^{(4)}(\tau)}{r^4} + ..., \quad c(\tau, r) = \frac{c^{(4)}(\tau)}{r^4} + ... \tag{4.20}$$

With the conventions $\langle T_{\mu\nu} \rangle = \text{diag}\,(\epsilon;\, \tau^2 P_L;\, P_T;\, P_T)$, the final result in the case of Bjorken flow is given by [7] [8]

$$\langle T_{\mu\nu} \rangle = \frac{N_c^2}{2\pi^2} \text{diag}\left(-\frac{3A^{(4)}}{4};\ \tau^2\left(-2c^{(4)} - \frac{A^{(4)}}{4}\right);\ \ c^{(4)} - \frac{A^{(4)}}{4};\ \ c^{(4)} - \frac{A^{(4)}}{4}\right). \tag{4.21}$$

[7] The functions $A^{(4)}(\tau)$, $b^{(4)}(\tau)$ and $c^{(4)}(\tau)$ cannot be determined from the near boundary expansion. However, these are not all independent, since the power series expansion imposes $b^{(4)}(\tau) = -2c^{(4)}(\tau)$.

[8] We have used the relation between the 5d Newtons constant $G_N^{(5)}$ and N_c which in units of the AdS radius reads $(8\pi G_N^{(5)})^{-1} = N_c^2/(4\pi^2)$.

Motivated by the expansion of the energy densities in inverse powers of τ, we expect that different metric functions can also be expanded in a power series in $u = \tau^{-2/3}$. Before doing that, it is convenient to introduce a new holographic coordinate $s = 1/(r\tau^{1/3})$, which we will consider independent of u. With this rescaled variable, a series solution of the Einstein equation can be found by expanding

$$A(\tau, r) = \sum_{i=0} u^i A_i(s), \qquad b(\tau, r) = \sum_{i=0} u^i b_i(s), \qquad c(\tau, r) = \sum_{i=0} u^i c_i(s). \tag{4.22}$$

With this assumption, the solutions of Einstein's equations become a set of ordinary differential equations (ODE's) in s (instead of PDE's in r and τ) that can be solved order by order in u.[9] Imposing the AdS asymptotics at $s = 0$ and regularity of the metric near the horizon at $s = 1$, the leading order solution is then given by

$$A_0(s) = 1 - s^4, \qquad b_0(s) = c_0(s) = 0, \tag{4.23}$$

which coincides with the black-brane metric.[10] From this set of differential equations, the energy density can be computed by analysing the $s \to 0$ limit of the functions A_i. Comparing the expression of the holographic stress-energy tensor, Eq. (4.21) with the gradient expansion from Eq. (4.11), the energy density of the dual field theory is given by

$$\epsilon(\tau) = -\frac{N_c^2}{2\pi^2}\frac{3}{4}u^2 \sum_{n=0} u^n \frac{1}{4!}\frac{d^4}{ds^4}A_n(s)\bigg|_{s=0}. \tag{4.24}$$

which we can now use to compute the anisotropic function $R(w)$ to arbitrary order. The first three coefficients are given by [147]

$$R(w) = \frac{2}{\pi}\frac{1}{w} + \frac{2 - 2\log 2}{3\pi^2}\frac{1}{w^2} + \frac{15 - 2\pi^2 - 45\log 2 + 24\log^2 2}{54\pi^3}\frac{1}{w^3} + \ldots, \tag{4.25}$$

which is consistent with the normalisation in Eq. (4.15), since $\eta/s = r_1/8 = 1/4\pi$ in the infinite coupling limit of the dual $\mathcal{N} = 4$ SYM fluid.

[9] Using a similar Ansatz, the first three coefficients were explicitly obtained in [130].

[10] The expansion of the non-trivial prefactor of the g_{yy} component in Eq. (4.19) to leading order in u must also be performed to obtain the black-brane metric.

4.2.3 Hydrodynamics in Gauss-Bonnet holography

The Gauss-Bonnet gravity action is given by

$$S = \frac{1}{2\kappa_5^2}\int d^5x\,\sqrt{-g}\left(R + \frac{12}{L^2} + \frac{\lambda_{GB}L^2}{2}\left(R_{MNOP}R^{MNOP} - 4R_{MN}R^{MN} + R^2\right)\right), \tag{4.26}$$

where κ_5^2 is proportional to the five dimensional Newton constant, L is the AdS radius of the $\lambda_{GB} = 0$ theory, and λ_{GB} is a dimensionless coupling which controls the magnitude of the higher derivative corrections. Without loss of generality, in the rest of this work we will set $L = 1$. An important feature of this theory is that in spite of incorporating higher derivative terms, black-brane solutions can be found for non-perturbative values of the Gauss-Bonnet parameter. From these the equation of state of the dual field theory can be extracted [42, 43, 129]

$$\epsilon = \frac{3}{8}\frac{\pi^2 N_c^2}{L_c^3}T^4\,, \quad L_c^2 = \frac{1+\sqrt{1-4\lambda_{GB}}}{2}\,. \tag{4.27}$$

As expected the $\lambda_{GB} \to 0$ limit of Eq. (4.27) agrees with the equation of state of $\mathcal{N} = 4$ SYM. This expression indicates that not all values of λ_{GB} are physical, since only $\lambda_{GB} \in (-\infty, 1/4]$ yield real energy densities. As already mentioned in the introduction, for arbitrary values of λ_{GB} this theory possesses causality problems associated with the superluminal propagation of high-momentum modes as well as negativity of the energy flux. [134, 148]. These considerations impose further constraints on the allowed values[11] of $-7/36 < \lambda_{GB} \leq 9/100$. Nevertheless, since these constraints concern the ultraviolet behaviour of the theory, we may still consider values of λ_{GB} beyond this region to explore its infrared dynamics, such as the approach towards hydrodynamics of the theory, as already done in [18, 125].

In addition to the equation of state, the transport coefficients of the Gauss-Bonnet system have also been analysed. In particular, the ratio of shear viscosity to entropy density is given by [148]

$$\frac{\eta}{s} = \frac{1-4\lambda_{GB}}{4\pi}\,. \tag{4.28}$$

[11] The analysis of three point functions of gravitons in high-derivative theories has led the authors of [135] to suggest that these theories are pathological for any strength of the higher derivative couplings unless a complete tower of stringy states is also considered. See however [136].

Second order transport coefficients of this theory have also been analysed in [18]. From this expression we can observe that positive values of λ_{GB} yield smaller values of $\frac{\eta}{s}$ than $\mathcal{N}=4$ SYM [131]. However, negative values of λ_{GB} yield larger viscosity to entropy density ratios, as expected from finite 't Hooft coupling corrections of the infinite coupling limit in $\mathcal{N}=4$ SYM [149]. The analysis of the relaxation of small fluctuations of the thermal state via the computations of the quasi-normal mode spectrum of the dual black-branes indicates that many qualitative features of finite coupling corrections to $\mathcal{N}=4$ SYM are captured by Gauss-Bonnet holography with negative λ_{GB} [125]. For this reason, we will only consider negative values of this parameter.

Numerical solutions of Einstein's equations (with $\lambda_{GB}=0$) with boost invariant symmetry from initial data at $\tau=0$ have been found in [104]. These solutions first showed the success of viscous hydrodynamics to describe the evolution of strongly-coupled $\mathcal{N}=4$ SYM even when gradient corrections are large, later confirmed in less symmetric solutions. Using the same Ansatz for the metric as in Eq. (4.19), we can find boost invariant solutions of the Gauss-Bonnet equations of motion. Imposing AdS asymptotics (with effective radius L_c) leads to the following near boundary ($r\to\infty$) expansion of the different metric functions

$$A(\tau,r)=\frac{1}{L_c^2}+\frac{A^{(4)}(\tau)}{r^4}+\ldots \tag{4.29}$$

$$b(\tau,r)=-2\log\left(L_c\right)-\frac{2\left(1-L_c^2\right)}{r\tau}+\frac{1-L_c^4}{r^2\tau^2}-\frac{2\left(1-L_c^6\right)}{3r^3\tau^3}+\frac{b^{(4)}(\tau)}{r^4}+\ldots \tag{4.30}$$

$$c(\tau,r)=-2\log\left(L_c\right)+\frac{c^{(4)}(\tau)}{r^4}+\ldots \tag{4.31}$$

where we observe that in the $L_c=1$ limit, we recover the results from Section 4.2.2. The functions $A^{(4)}(\tau)$, $b^{(4)}(\tau)$ $c^{(4)}(\tau)$ cannot be determined from the near boundary expansion and additional infrared conditions, such as regularity, must be imposed. However, these are not all independent, since the power series expansion imposes

$$b^{(4)}(\tau)=\frac{1-L_c^8}{2\tau^4}-2c^{(4)}(\tau)\,. \tag{4.32}$$

Energy-momentum conservation, which emerges from the boundary expansion as well, relates these functions to $A^{(4)}(\tau)$ which must be extracted from the numerical computation.

From these solutions the dual field theory stress-energy tensor can be extracted after holographic renormalisation, which has been performed for Gauss-Bonnet gravity in [129, 150, 151]. In terms of those functions, the stress-energy tensor is diagonal and with the same conventions $\langle T_{\mu\nu}\rangle = \text{diag}\,(\epsilon;\, \tau^2 P_L;\, P_T;\, P_T)$ is given by

$$\langle T_{\mu\nu}\rangle = \frac{N_c^2}{2\pi^2}\frac{(2L_c^2-1)}{L_c^3}\text{diag}\left(-\frac{3A^{(4)}}{4};\ \tau^2\left(-\frac{2c^{(4)}}{L_c^2}-\frac{A^{(4)}}{4}\right);\ \ \frac{c^{(4)}}{L_c^2}-\frac{A^{(4)}}{4};\ \ \frac{c^{(4)}}{L_c^2}-\frac{A^{(4)}}{4}\right). \tag{4.33}$$

Imposing the AdS asymptotics at $s=0$ and regularity of the metric near the horizon $s=1$, the leading order solution is now given by

$$A_0(s) = \frac{1}{2\lambda_{GB}}\left(1-\sqrt{1-4\lambda_{GB}(1-s^4)}\right), \tag{4.34}$$

$$b_0(s) = -2\log\left(L_c\right), \tag{4.35}$$

$$c_0(s) = -2\log\left(L_c\right). \tag{4.36}$$

In this case the asymptotic behaviour changes to, $A_0(s=0) = 1/L_c^2$, but we still need to require that all metric coefficients A_i for $i \geq 1$ must vanish at $s=0$. The presence of λ_{GB} modifies the energy density formula, which is now given by

$$\epsilon(\tau) = -\frac{N_c^2}{2\pi^2}\frac{(2L_c^2-1)}{L_c^3}\frac{3}{4}u^2\sum_{n=0}u^n\frac{1}{4!}\frac{d^4}{ds^4}A_n(s)\Big|_{s=0}. \tag{4.37}$$

which we can use to determine the coefficients of anisotropy function $R(w)$ as defined in r_i, as defined in Eq. (4.14).

Following the procedure outlined above, 240 coefficients in the gradient expansion of the energy density in Eq. (4.11) for strongly-coupled $\mathcal{N}=4$ SYM, were determined in [110]. We have extended this computation up to 380 coefficients and explored the effects that different values of $\lambda_{GB} < 0$ have on the coefficients and asymptotics. Because of the presence of more terms in the Gauss-Bonnet equations of motion as well as the presence of square root singularities in s, the computation of higher order expansion coefficients becomes much more numerically demanding than for $\mathcal{N}=4$ SYM case. For this reason, we have obtained a different number of coefficients for each coupling N_{coef} =(380, 94, 86, 80, 66), for $\lambda_{GB} = (0, 0.1, -0.2, -0.5, -1)$ respectively.

4.3 Resurgence and non-perturbative effects

In quantum mechanics and in QFT, weak coupling perturbative expansions and semi-classical expansions are often the only available computational techniques. Yet perturbative expansions almost always yield asymptotic series, with a zero radius of convergence. While these asymptotic expansions are often very useful when the coupling is small, $g \ll 1$, we also often want to understand what happens when $g \gg 1$ or $g \sim 1$. Even if we are content to focus on the small coupling regime $g \ll 1$, we may want to understand non-perturbative effects which are schematically of the form $e^{-A/g}$ with A a positive real number.

In many examples, resurgence theory [152–155] has been intensively used to gain intuition about the structure of divergences in perturbative expansions, and has revealed surprising new connections between perturbative and non-pertubative effects in both quantum mechanics and QFT. The easiest way of understanding the subject is with a specific example in the context of ordinary exponential integrals, which can be considered as a zero-dimensional prototype for Euclidean path integrals and partition functions. In general, the usual perturbative expansion around the perturbative saddle point, can fail to be a good approximation in two different ways

- The perturbative result for $g \ll 1$, fails to accurately approximate the strong coupling limit $g \gg 1$.
- For complex coupling $g = |g|e^{i\theta}$, even when the magnitude is arbitrarily small $|g| \ll 1$, perturbation theory fails to approximate the exact result at generic θ.

The surprising fact which resurgence teaches us is that these two issues are deeply connected and have a common origin related to the existence of non-perturbative saddles that have been neglected. When we consistently incorporate all the saddle points by constructing a *resurgent trans-series*, we can construct an Ansatz which respects the analytic continuation in the small coupling for any θ. By doing so, we fix the second issue, and as a by-product, we obtain a solution that is valid for both weak and strong coupling i.e, providing an analytic continuation at large coupling from perturbative data! To see why this could be the case, consider one of the exponentially suppressed

effects $e^{-A/g} \ll 1$ that we were neglecting in the weak coupling limit $|g| \ll 1$. Because we have constructed a solution valid for every θ, we can in particular choose $g = -|g|$, which would then turn an exponentially small effect in to the dominant contribution of the form $e^{A/|g|} \gg 1$. On the other hand, if we choose $\theta = 0$ and study very strong coupling $g \gg 1$, the non-perturbative effect can not be neglected any more $e^{-A/g} \sim 1$.

The reason that the weak coupling resurgent expansion is capable of reproducing the exact result at arbitrary coupling is that resurgent trans-series have the same monodromy properties under global analytic continuation as exact solutions, by construction. This is to be contrasted with naive perturbation theory, which manifestly does not have the correct monodromy properties.

4.3.1 A toy model for resurgence

To illustrate these concepts, consider the following exponential integral

$$Z(g) = \frac{1}{\sqrt{g}} \int_{-\pi/2}^{\pi/2} dx\, e^{-\frac{1}{2g}\sin^2(x)} = \frac{\pi}{\sqrt{g}} e^{-\frac{1}{4g}} I_0\left(\frac{1}{4g}\right) \tag{4.38}$$

which can be solved in terms of known Bessel functions. The action $S \equiv \frac{1}{2g}\sin^2(x)$ has two saddle points: a perturbative saddle point $x = 0$ with action $S_0 = 0$, and a non-perturbative saddle point at $x = \pi/2$ with action $S_1 = 1/(2g)$. When $Z(g)$ is evaluated perturbatively around each saddle point, the contributions can be expressed as power series weighed by exponentials of the saddle-point action or trans-series as

$$Z(g) = C_0 e^{-S_0} \Phi_0(g) + C_1 e^{-S_1} \Phi_1(g) \tag{4.39}$$

where $C_{0,1}$ are called Stokes parameters and the asymptotic series have the form

$$\Phi_0(g) = \sqrt{2\pi} \sum_{n=0}^{\infty} \frac{\Gamma(n+1/2)^2 2^n}{\Gamma(n+1)\Gamma(1/2)^2} g^n = \sqrt{2\pi} \sum_{n=0}^{\infty} p_{n,0} g^n \tag{4.40a}$$

$$\Phi_1(g) = \sqrt{2\pi} \sum_{n=0}^{\infty} \frac{\Gamma(n+1/2)^2 2^n (-1)^n}{\Gamma(n+1)\Gamma(1/2)^2} g^n = \sqrt{2\pi} \sum_{n=0}^{\infty} p_{n,1} g^n \tag{4.40b}$$

It is easy to see that these are Gevrey order-1 series since $p_n \sim n!/A^n \sim (n/Ae)^n$ at large n. In particular we can identify asymptotic series by looking at the large n behaviour of the coefficients

$$|p_n|^{1/n} \sim n/Ae. \tag{4.41}$$

The parameter ($A = 1/2$ in our case), is directly related to the action of the non-perturbative saddle $S_1 = -1/2g = -A/g$. This is not a coincidence, and in fact it becomes obvious once we perform a Borel transform of the series, to make them finite by taking away the factorial behaviour by hand. The Borel transforms of our series are thus given by

$$B\Phi_0(t) \equiv \sqrt{2\pi}\sum_{n=0}^{\infty}\frac{p_{n,0}}{n!}t^n, \qquad B\Phi_1(t) \equiv \sqrt{2\pi}\sum_{n=0}^{\infty}\frac{p_{n,1}}{n!}t^n. \tag{4.42}$$

Notice that these series are functions of another complex variable t, which is commonly referred to as the Borel plane. This Borel transform has a finite radius of convergence in the Borel plane given by $|t| \leq A$ by construction. In the case in which we can analytically continue the Borel transform from $t = 0$ to $t = \infty$, then we can relate them to the original series via an inverse Borel transform, or a Laplace transform:

$$S\Phi(g) = \frac{1}{g}\int_0^{+\infty} dt e^{-t/g} B\Phi(t). \tag{4.43}$$

Where $S\Phi(g)$ is often called the Borel sum of $\Phi(g)$, and provides an analytic continuation of the original divergent series. The tricky part, however, is to find a suitable analytic continuation for $B\Phi(t)$. There are two main ways of doing this, depending on your knowledge of the coefficients p_n. If you happen to know all the p_n, then your best guess is to use hypergeometric functions, by comparing the Borel transform to

$${}_2F_1\left[a, b; c; z\right] = \frac{\Gamma(c)}{\Gamma(a)\Gamma(b)}\sum_{n=0}^{\infty}\frac{\Gamma(a+n)\Gamma(b+n)}{\Gamma(c+n)\Gamma(n+1)}z^n, \tag{4.44}$$

which then provides us with

$$B\Phi_0(t) = \sqrt{2\pi}{}_2F_1\left[\frac{1}{2}, \frac{1}{2}; 1; 2t\right], \tag{4.45a}$$

$$B\Phi_1(t) = \sqrt{2\pi}{}_2F_1\left[\frac{1}{2}, \frac{1}{2}; 1; -2t\right]. \tag{4.45b}$$

Having the exact result is a rare luxury, and is not necessary for the machinery to work. Normally, you have a finite amount of coefficients up to $n = N_{\text{coef}}$. A standard method is then to use a Padé approximant (see e.g. [52])

$$B\Phi(t) \approx \mathcal{P}_{N,M}(t) = \frac{\sum_{j=0}^{N} n_i t^j}{1 + \sum_{i=1}^{M} d_i t^i} \tag{4.46}$$

where all $N+M+1$ coefficients are fixed by demanding that the power series of the Padé agrees with $B\Phi(t)$. The choice of N and M are arbitrary, with the constraint that $N+M=N_{\text{coef}}$. This type of approach is commonly known as Borel-Padé summation and it becomes more accurate as we increase N_{coef}, so in general requires a large number of coefficients to be known.

Independent of the origin of our analytic continuation, once we have it we need to find its Laplace transform, in order to relate to the original series. The only complication that may arise is in the special case when we have a singularity (pole or branch cut) along the positive real axis in the Borel plane and therefore the integral would have to be done along a ray in the complex t plane. This is indeed the case for $B\Phi_0(t)$, which has a branch point at $t=+1/2$, whereas $B\Phi_1(t)$ has a branch point at $t=-1/2$, and therefore the integral can be performed for real t. In the first case, we can define a generalised Borel sum for an arbitrary ray in the complex t plane

$$S_\theta\Phi(g)=\frac{1}{g}\int_0^{+\infty e^{i\theta}}dt\,e^{-t/g}B\Phi(t). \tag{4.47}$$

Even if the Borel sum for $\Phi_0(g)$ does not exist for $\theta=0$, it does exist for $\theta=0^{\pm}$. The difference between the two integration contours is a purely imaginary ambiguity coming from the residue of the pole or the discontinuity along the branch cut. To see this let us compute the difference between the two contours

$$\begin{aligned}
(S_{\theta^+}-S_{\theta^-})\,\Phi_0(g) &= \lim_{\epsilon\to 0}\frac{\sqrt{2\pi}}{g}\int_{1/2}^{\infty}dt\,e^{-t/g}\left({}_2F_1\left[\frac{1}{2},\frac{1}{2};1;2t+i\epsilon\right]-{}_2F_1\left[\frac{1}{2},\frac{1}{2};1;2t-i\epsilon\right]\right)\\
&= \frac{2i\sqrt{2\pi}}{g}\int_{1/2}^{\infty}dt\,e^{-t/g}{}_2F_1\left[\frac{1}{2},\frac{1}{2};1;1-2t\right]\\
&= \frac{2i\sqrt{2\pi}}{g}\,e^{-1/2g}\int_0^{\infty}dt e^{-t/g}{}_2F_1\left[\frac{1}{2},\frac{1}{2};1;-2t\right]\\
&= 2i\,e^{-1/2g}S_0\Phi_1(g)
\end{aligned} \tag{4.48}$$

Here we have used the known discontinuity property of hypergeometric functions. We observe that the ambiguity is proportional to the action of the leading singularity in the complex plane! However this puts us in a compromise: we started with a real result, but because of the summation, we obtained a purely imaginary part. Namely depending of which contour we chose, the sign of the imaginary ambiguity will change!

The only way of making the Borel sum of $Z(g)$ real and free of ambiguity, is to realise that the Stokes parameters must be *piece-wise constants*, that jump discontinuously every time the integration contour crosses a singularity. In our case, for $C_0 = 1$, we then require for an arbitrary contour that

$$S_\theta Z(g) = \begin{cases} S_\theta \Phi_0(g) - ie^{-1/2g} S_\theta \Phi_1(g) & \theta \in (0, \pi) \\ S_\theta \Phi_0(g) + ie^{-1/2g} S_\theta \Phi_1(g) & \theta \in (-\pi, 0) \end{cases}$$

The places where the Stokes parameters jump discontinuously are known as Stokes lines. We see that the only role of the non-perturbative saddle in this case is to cancel the imaginary ambiguity coming from $S_0\Phi(g)$. In order to make the result real and independent of the contour of integration

$$S_0 Z(g) = S_{0^\pm} \Phi_0(g) \mp ie^{-1/2g} S_{0^\pm} \Phi_1(g) = \mathrm{Re}\left[S_{0^\pm} \Phi_0(g)\right] \tag{4.49}$$

This expression exactly agrees with the analytic result from Eq. (4.38). In this case, we can think of the imaginary part as an error term, which is exponentially suppressed for $g \ll 1$, but might become relevant for $g \gg 1$ and then the error becomes significant.

In more general situations, the logic of the argument can be reversed to find new non-perturbative contributions. For instance, suppose we originally knew nothing about the existence of the non-perturbative saddle point, but we did know the perturbative contribution to $Z(g)$. Requiring $Z(g)$ to be free of ambiguity across the $\theta = 0$ Stokes line would tell us that we are missing non-perturbative effects which are completely determined by the discontinuity structure of the Borel sum of $S\Phi_0(g)$.

4.4 Resurgence in hydrodynamics

One of the main conclusions of the analysis of boost invariant flows is that the hydrodynamic expansion does not converge and behaves instead as an asymptotic series [110]. This conclusion is based on the factorial growth of the coefficients in the large order hydrodynamic series. As a consequence, the hydrodynamics gradient expansion has formally zero radius of convergence. This behaviour has been observed in $\mathcal{N} = 4$ SYM [110] as well as RTA kinetic theory [114] and phenomenological completions of

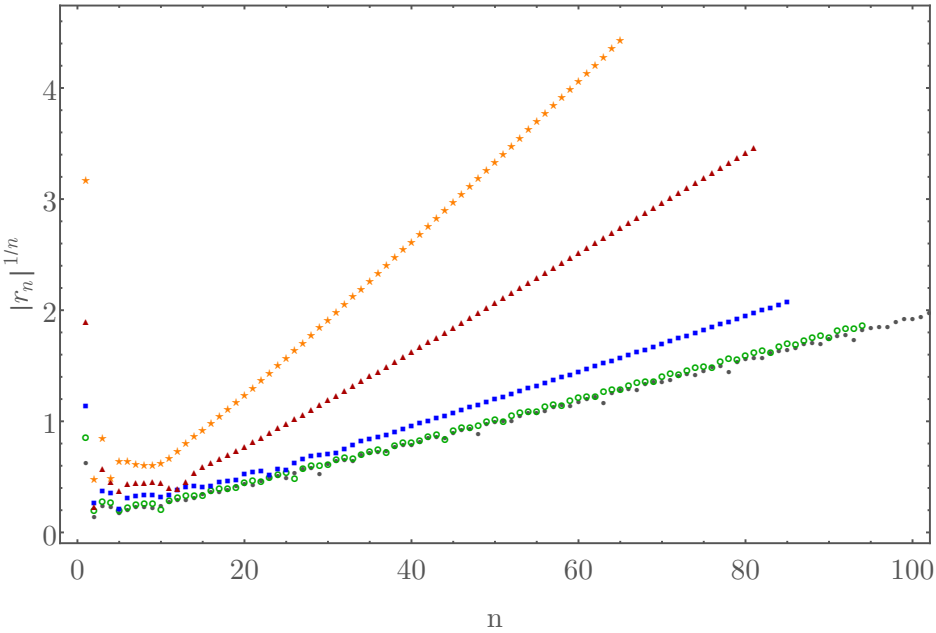

Figure 4.1: Behaviour of the series coefficients for the anisotropy function Eq. (4.12) as a function of the expansion order n for $\lambda_{GB} = 0$ (grey solid circles), $\lambda_{GB} = -0.1$ (green open circles), $\lambda_{GB} = -0.2$ (blue squares), $\lambda_{GB} = -0.5$ (red triangles) and $\lambda_{GB} = -1$ (orange stars). The large n behaviour is given by $|r_n|^{1/n} \sim (n/Ae)|\cos(\theta n)|^{1/n}$ with A and θ determined by the position of the nearest singularity to the origin $\xi_0 = Ae^{i\theta}$ in the Borel plane.

hydrodynamics [111]. This behaviour is expected for any type of gradient expansion where there are non-perturbative quasi-normal modes present.

The factorial growth of the series coefficients indicates that the hydrodynamic series may be Borel summable. As is standard (see Section 4.3), we may define the series expansion of the Borel transform of the anisotropy function R, as

$$R_B(\xi) = \sum_{n=1}^{N_{\text{coef}}} \frac{r_n}{n!}\xi^n \,. \tag{4.50}$$

Unlike the hydrodynamic series, since the leading $n!$ growth has been removed, the Borel transform defined above has a finite radius of convergence A, which controls the asymptotic large n slope of the coefficient as shown in Fig. 4.1. The slopes of these curves grow as λ_{GB} becomes more negative, which in turns means that the radius of convergence of each series decreases with decreasing λ_{GB}. It is also worth noticing that for $\lambda_{GB} = 0$ and $\lambda_{GB} = -0.1$ the leading behaviour of the coefficients at large n follows the form of an oscillating factorial function ($r_n \sim n!\cos(\theta n)$) where θ is related to the

argument of the position of the leading complex singlularity $\xi_0 = Ae^{i\theta}$, in a similar fashion to scenarios noted in [113, 121]. As we vary λ_{GB}, we find that the oscillating behaviour becomes suppressed and the coefficients tend to follow $r_n \sim n!$ as in [114]. This is consistent with the dominant contribution to the large n coefficients for the hydrodynamic series transitioning from two propagating non-hydrodynamic modes, to a single dissipative non-hydrodynamic mode.

The Borel transform and the original series are related via a Laplace transform. In order to be able to perform this integral, we will need to first analytically continue the Borel transform beyond its radius of convergence. Since we have a finite number of coefficients N_{coef}, we will approximate the Borel transform via a Padé approximant of the form

$$R_B(\xi) \approx \mathcal{P}_{N,M}(\xi) = \frac{\sum_{j=0}^{N} n_i \xi^j}{1 + \sum_{i=1}^{M} d_i \xi^i}\,, \tag{4.51}$$

where all $N + M + 1$ coefficients are now fixed by demanding that the power series around $\xi = 0$ of the Padé approximant agrees with Eq. (4.50). In this chapter, we will only consider symmetric Padé approximants, with $N = M \leq N_{\text{coef}}/2$, and we will compare the results for different N and M to check the stability of our results.

One of the advantages of the Padé approximant is the fact that, by construction, it allows for the emergence of poles in the complex ξ plane, which can be related to the finite radius of convergence of the Borel transform. In Fig. 4.2 we show the positions of the poles of the Padé approximant for different values of λ_{GB}. In the upper left panel we show the pole structure for $\mathcal{N} = 4$ SYM as previously computed in [110, 147], but including an additional 140 coefficients of the gradient series. The rest of the panels show our results for different negative values of $\lambda_{GB} = (-0.1, -0.2, -0.5, -1)$. For comparison, in the lower right panel we show the Borel plane for the same analysis[12] in kinetic theory within the RTA, using the coefficients tabulated in [114]. For all these cases additional poles exist for very large values of $|\xi|$; however these have a strong dependence on the Padé order, which indicates that they are numerical artefacts.

The singularity structure of the Borel plane is particularly interesting. As a first observation, the locations of the poles control the convergence of the Borel transform,

[12]Note that in [114] the definition of the Borel transform was slightly different to ours, which implies that our results are not identical

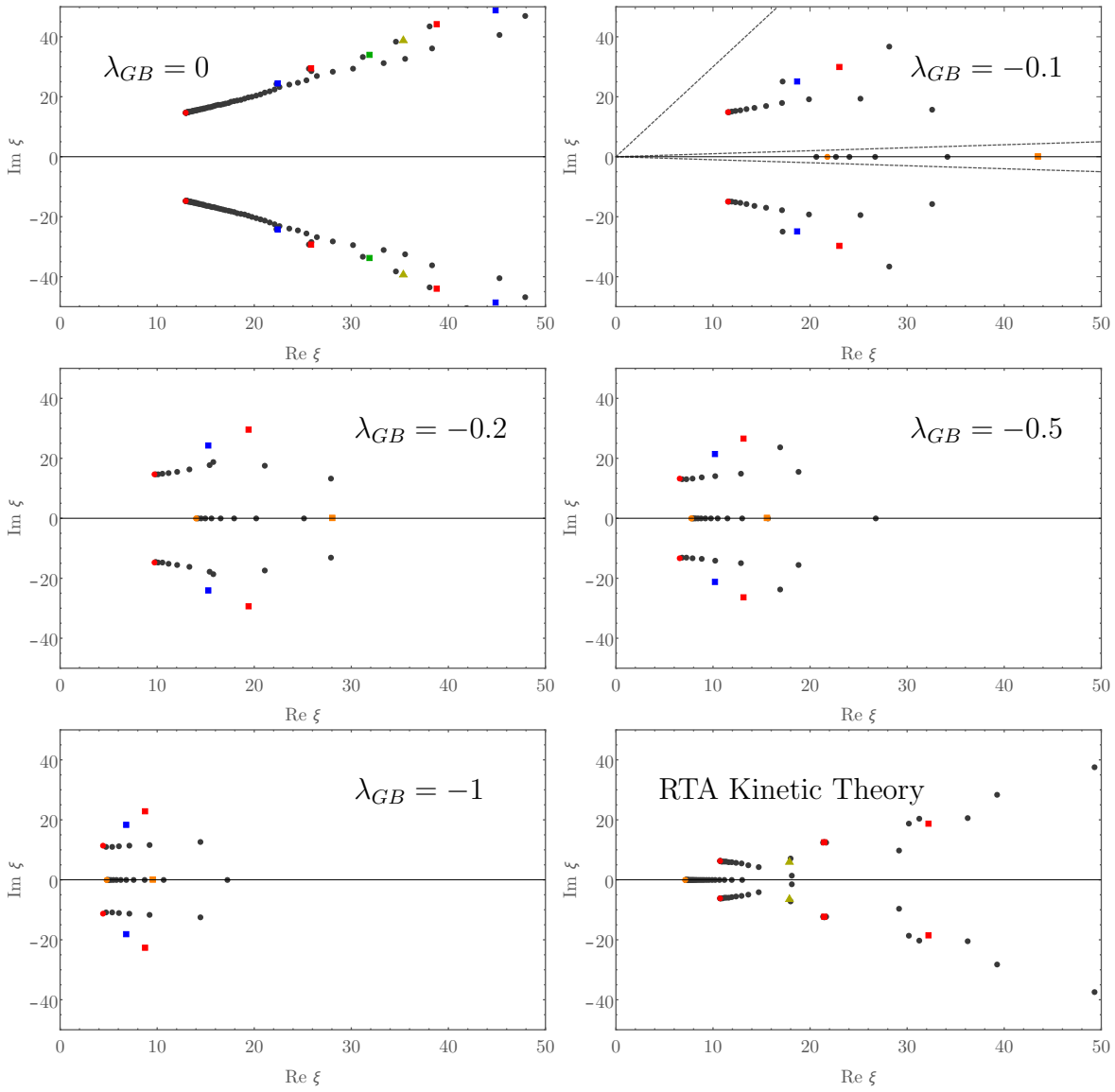

Figure 4.2: The solid grey circles indicate poles of the Padé approximant of $R_B(\xi)$. The expected positions of singularities predicted from the quasi-normal mode frequencies closest to the origin, both for complex (red) and purely dissipative modes (orange), are marked by solid circles. All integer multiples of these frequencies are given by squares of the same colour. The subsequent 2^{nd} and 3^{rd} QNM frequencies are marked by blue and green squares. The modes that correspond to the sum of the 1^{st} and 2^{nd} QNM frequencies (in the $\mathcal{N} = 4$ case) or the sum of the first two leading modes (in the RTA case) are given by a yellow triangle. The lower right panel is the Borel plane of kinetic theory in the RTA approximation using the coefficients computed in [114]. For this plot we have chosen the product of the relaxation time times temperature, $\gamma \equiv \tau_R T = \pi/15$, so that shear viscosity of the RTA coincides with the $\lambda_{GB} = -1$ value. The dashed lines in the upper right panel shows the contours of integration used in the generalised Borel sum ($\mathcal{C}_c$, $\mathcal{C}_+$ and $\mathcal{C}_-$) in order to avoid the real singularities at finite coupling.

since the distance of the closest pole to the origin is proportional to the inverse of the slope of coefficients shown in Fig. 4.1. Furthermore, in all cases, the Padé approximant exhibits an accumulation of alternating poles and zeroes, starting at a well defined point in the Borel plane. This concentrated sum of simple poles indicates the emergence of a branch cut [156]. The structure of poles at finite λ_{GB} is qualitatively different to that of $\mathcal{N} = 4$ SYM at infinite coupling. While in the latter case all poles are complex, for all finite λ_{GB} new branch cuts emerge along the real axis. For small negative λ_{GB} these new branch cuts are far from the origin, but as λ_{GB} becomes more negative these poles move closer to $\xi = 0$, and eventually dominate the radius of convergence for the Borel transform. This behaviour qualitatively interpolates the structure of the infinitely coupled limit of $\mathcal{N} = 4$ SYM with the expectation from perturbation theory as obtained via kinetic theory in the RTA approximation.

Having analytically continued the Borel transform beyond the power expansion, we can determine the anisotropy function by performing a generalised Borel sum for an arbitrary ray in the complex ξ plane (see Section 4.3)

$$R(w) = w \int_{\mathcal{C}} d\xi \, e^{-w\xi} R_B(\xi) \,, \tag{4.52}$$

where $\mathcal{C}$ is a contour in the complex plane which connects $\xi = 0$ and $\xi = \infty$. The presence of singularities in R_B shows that different choices of contour $\mathcal{C}$ yield different answers. The theory of resurgence therefore suggest that the correct Ansatz for $R(w)$ is not a power series, but rather a trans-series that incorporate non-perturbative contributions in the gradient strength. Denoting by $\xi_0^{(\alpha)}$ the position of each branching point in R_B this trans-series is given to leading order by [110, 113, 147],

$$R(\omega) = \Phi_0(w) + \sum_{\alpha=1}^{\infty} \Omega_\alpha(w) \Phi_\alpha(w) + \mathcal{O}(\Omega^2) \tag{4.53}$$

where $\Phi_\alpha(w)$ are series in inverse powers of w and to first order we can neglect higher powers and mixing between the modes. The non-perturbative behaviour of each mode is encoded in the non-perturbative coefficient Ω_α, given by

$$\Omega_\alpha(w) = C_\alpha w^{\gamma^{(\alpha)}} e^{-\xi_0^{(\alpha)} w} \,, \tag{4.54}$$

where $\gamma^{(\alpha)}$ is constant characterising each branch cut and C_α are Stokes parameters, which must be chosen such that the non-perturbative ambiguity obtained in the Borel sum of $\Phi_0(w)$, is exactly cancelled by the next terms in the trans-series, yielding a real result [113, 153]. In order to do so, these parameters must jump discontinuously every time the contour $\mathcal{C}$ crosses a singularity in the Borel plane. However, this reality condition only fixes the imginary contribution of the Stokes parameters [113], leaving the real contribution undetermined. This non-perturbative real contribution is encoding the information about the initial conditions of the system, and will be subsequently exponentially suppressed and "forgotten" at late times when $\Omega(w) \ll 1$.

At strong coupling these non-hydrodynamic excitations are characterised by a set of characteristic complex frequencies, which in the dual theory coincide with the quasi-normal modes of the associated black brane. In the adiabatic approximation, we expect each of these excitations to relax according to the local relaxation given by

$$\delta R^{(\alpha)} \sim e^{-i\int \omega^{(\alpha)}(\tau)d\tau} \sim e^{-i\int\left(\omega^{(\alpha)}_{\rm QNM}\tau^{-1/3}+i\frac{2}{3}\gamma^{(\alpha)}\tau^{-1}+\ldots\right)d\tau} \sim \tau^{\frac{2}{3}\gamma^{(\alpha)}} e^{-i\frac{3}{2}\omega^{(\alpha)}_{\rm QNM}\tau^{2/3}}, \tag{4.55}$$

where $\omega^{(\alpha)}(\tau)$ is the characteristic frequency of each mode. Since the system under consideration is conformal, the τ-dependence of those frequencies is controlled by the effective local temperature. From the late time $T(\tau) \sim \tau^{-1/3}$ dependence, the position of the branch cut can be related to the frequencies of the static quasi-normal modes $\omega^{(\alpha)}_{\rm QNM}$ (normalised by the temperature) as

$$\xi_0^{(\alpha)} = i\frac{3}{2}\omega^{(\alpha)}_{\rm QNM} \tag{4.56}$$

The emergence of these characteristic frequencies in the expanding case can be found explicitly by searching for power series solutions of the form

$$\delta A^{(\alpha)}(\tau, r) = \Omega_\alpha \sum_{i=0} u^i \delta A_i^{(\alpha)}(s), \tag{4.57}$$

for each metric coefficient. New solutions emerge when we consider Gauss-Bonnet gravity since as noted in [125], this higher-derivative theory possesses a new set of dissipative (imaginary) quasi-normal modes in addition to the characteristic discrete complex modes of $\mathcal{N} = 4$ SYM. These purely imaginary poles are a common feature of

several higher-derivative theories, including the higher-derivative term responsible for finite coupling corrections to $\mathcal{N}=4$ SYM. In fact, the 't Hooft coupling dependence of these poles is qualitatively similar to the Gauss-Bonnet theory with negative λ_{GB} and we can therefore expect that the structure of the Borel plane singularities for $\mathcal{N}=4$ SYM at finite coupling will also be qualitatively similar to the one observed in our analysis.

To explicitly show the relation between the quasi-normal mode spectrum and the Borel plane singularities we show the positions of these characteristic frequencies, after an appropriate rescaling, in Fig. 4.2. In this figure the positions of the singularities associated with the first purely imaginary and complex QNM's (with smallest imaginary part, i.e. the smallest damping rate) are shown by the orange and red solid circles respectively. Contrary to the simple toy model from Section 4.3 where the number of non-perturbative contributions were fixed, now we have an *infinite* set of quasi-normal modes and therefore the hydrodynamic expansion now encodes information about *all* the quasi-normal modes!

In all panels in Fig. 4.2, such poles coincide with the start of an accumulation of singularities in the Padé approximant, which may be interpreted as the origin of a branch cut. In addition, because of the presence of non-linearities in the system, we also expect interactions between these modes, which would create new branching points at multiples of the QNM's positions or linear combinations of them, which are also shown in the Borel plane of $\mathcal{N}=4$ SYM and are expected to be further suppressed at order $\Omega(w)^2$. In Fig. 4.2 we have shown the positions of all these singularities associated with non-hydrodynamic excitations and their interactions or "resonances". Because of the numerical limitations, we can not observe any poles coinciding with higher order modes in the finite coupling cases.

4.4.1 Hydrodynamic attractor and Borel summation

We will now construct the hydrodynamic attractor for Gauss-Bonnet hydrodynamics by analytic continuation of the anisotropy function $R(w)$, by performing the generalised Borel sum as in Eq. (4.52). As we stressed in the previous section the presence of poles

in the Padé approximant, $R_B(\xi)$, will lead to imaginary ambiguities of the Borel sum depending on the choice of contour of integration. This ambiguity can be fixed by allowing the Stokes parameters C_α to be discontinuous across each singularity (Stokes lines), in order to render the final result real. As already mentioned, in principle this procedure can only fix the imaginary contributions of these parameters. The remaining real contribution can only be determined from additional knowledge of the early time dynamics and initial conditions. In fact, specifying different values of these parameters is equivalent to selecting different choices of initial configurations for the evolution.

Once the information about the initial conditions is lost, all configurations converge exponentially to the same curve. This is known as the *hydrodynamic attractor* [111]. While currently there is not a precise definition of the attractor[13], summation techniques and numerical analysis of different theories have been able to identify well defined attractors to which all initial configurations converge to. The main goal of this section will be to construct and constrain the properties of the attractor solution in the case of holographic Gauss-Bonnet by summing the hydrodynamic series.

In the case where we don't have any singularities on the real axis, the Borel sum of the gradient expansion coincides with the numerically computed attractor using the full non-linear equations as was illustrated in a hydrodynamic theory with a similar singularity structure to that of $\mathcal{N} = 4$ SYM [113]. For finite λ_{GB}, because of the presence of poles in the real axis, we need to perform a generalised Borel summation, which will inevitably lead to a complex $R(w)$ and a trans-series. However, in practice we found that computing these non-perturbative corrections and their series is numerically very challenging and therefore in order to obtain a sensible answer, we will be forced to naively take the real part of the complex Borel sum of $\Phi_0(w)$. In essence, by this prescription we are effectively incorporating part of the first trans-series corrections and setting all their real contributions to zero. Roughly speaking, we can expect that the error we are introducing will be exponentially suppressed at large w, and it would be of the order of the imaginary part that we are neglecting (assuming that $\mathrm{Im}[\mathrm{C}_\alpha] \sim \mathrm{Re}[\mathrm{C}_\alpha] \sim 1$, which is normally the case).

[13] See [123] for a recent attempt to provide such a definition based on the theory of non-autonomous dynamical systems.

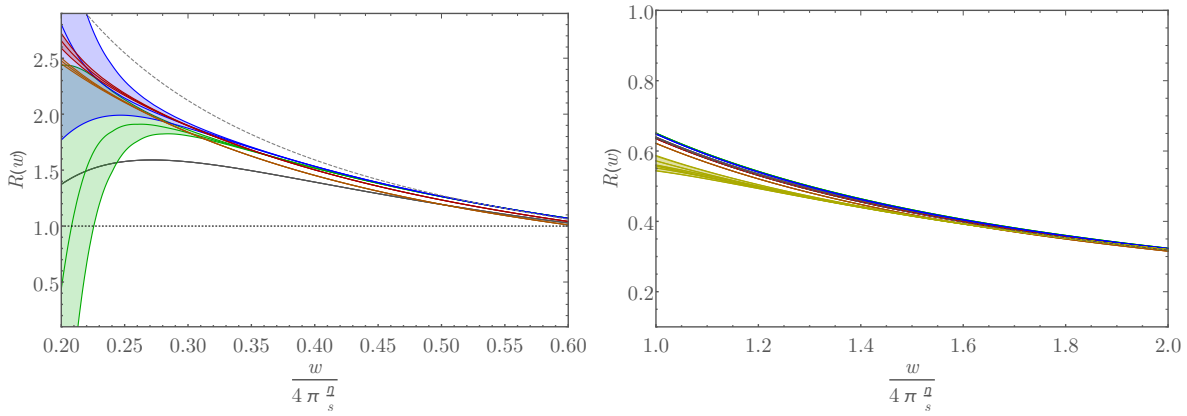

Figure 4.3: Anisotropy function for different values of λ_{GB} (left) and RTA (right) as a function of rescaled gradient $ws/4\pi\eta$. The grey, green, blue, red and orange curves correspond to the real parts of the inverse Borel transform of the leading order in the trans-series while the yellow curve in the right panel corresponds to RTA (for different choices of the Padé order N). The bands are determined by adding and subtracting the imaginary part of the inverse Borel transform, as a gauge of the importance of additional trans-series contributions. In both panels, the dashed line corresponds to the first order hydrodynamic prediction $R^{\rm 1st}_{\rm hyd}$. The grey, red and orange curves show no noticeable deviation for the entire range plotted above. The green and blue curves are stable with respect to the choice of N for $\frac{w}{4\pi\frac{\eta}{s}} > 0.25$, with deviations remaining within the same order of magnitude as the curves plotted above. The sensitivity of the RTA bands to different choices of N is no greater than 6% for $\frac{w}{4\pi\frac{\eta}{s}} > 1$.

We will consider contours of integration given by a straight line in the complex plane $\xi = |\xi|e^{i\theta}$, with $\theta = (0^+, 0^-, \theta_c)$ corresponding to $(\mathcal{C}_+, \mathcal{C}_-, \mathcal{C}_c)$ respectively, as shown in the upper right panel of Fig. 4.2. In analogy with Section 4.3, we see that the discontinuity across the real axis is purely imaginary. The results of this integration along the $\mathcal{C}_\pm$ contour for the different values of the coupling $\lambda_{GB} = (0, -0.1. -0.2, -0.5, -1)$ are given by the grey, green, blue, red and orange curves displayed in the left panel of Fig. 4.3. For all non-zero values of λ_{GB} we have supplemented each curve with a band generated by adding and subtracting to the real part the imaginary part of the integral as an error estimate, which we expect to be exponentially suppressed by $\Omega(w)$ at late times. Following [139], to better compare the different theories we have rescaled the values of w by the viscosity to entropy density ratio, such that the first order hydrodynamic prediction $R^{\rm 1st}_{\rm hyd}$, shown by the dashed line, agrees in all theories by construction. As the width of the band increases at early times, the sensitivity to the Padé order

and the number of coefficients drastically increases. This is because at this point, all the contributions from the trans-series become order one and can not be neglected. We find this special value of the gradient to be at $ws/4\pi\eta \approx 0.25$, which means that the results for the hydrodynamic attractors are reliable only in the range $w \gtrsim \pi\eta/s$, away from the validity of usual hydrodynamics, which is expected to fail when the first gradient corrections become of order one and $w \approx 4\pi\eta/s$.

In the right panel of Fig. 4.3 we compare the results from our holographic computation to the summation of the RTA kinetic theory coefficients from [114]. Even though the RTA computation is performed with 200 coefficients of the hydrodynamics series, we find that the inverse Borel transform is much more sensitive to the Padé order, which prevents us from studying the very small ws/η regime. In fact, in the case of RTA, the hydrodynamic attractor is reliable only in the range $w \gtrsim 4\pi\eta/s$, which is what you would expect to be the scale at which the hydrodynamic series is valid.

When the width of the bands is small, we can use the summation to explore the process of hydrodynamisation of the system. As already observed in [121] for $\mathcal{N} = 4$, the result of these summations quickly approaches the first order hydrodynamic predictions for all the values of λ_{GB}. To better quantify this process, we will assume that the system has hydrodynamised at w_{hyd} if for any value of w the anisotropy function satisfies

$$0.1 = \left| \frac{R - R_{\text{hyd}}}{R_{\text{hyd}}} \right|_{w=w_{\text{hyd}}} , \tag{4.58}$$

where R_{hyd} is the first order hydrodynamic expression Eq. (4.14). The values of w_{hyd} and the corresponding anisotropy for the different theories are tabulated in Table 4.1. As λ_{GB} becomes more negative, the value of the temperature-normalised gradient w at which hydrodynamisation occurs increases, as expected by the fact that the dual fluid is more viscous. Nevertheless, as in other theories where the summation has been performed [111, 121], R_{hyd} approximates the summed result even when the value of this normalised gradient is comparable to the microscopic scale. At these small values of the inverse gradient, the anisotropy function is larger than 1, which means that the viscous contribution to the pressures is as large as the equilibrium pressure, demonstrating that the contribution of higher order terms is potentially large. This is a manifestation of hydrodynamisation without isotropisation as discussed in [104, 157].

λ_{GB}	0	-0.1	-0.2	-0.5	-1	RTA
$w_{\rm hyd}$	0.43	0.46	0.56	0.93	1.85	2.5 - 2.8
$\frac{w_{\rm hyd}s}{4\pi\eta}$	0.43	0.33	0.31	0.31	0.37	1.0 - 1.1
$R\vert_{w_{\rm hyd}}$	1.33	1.74	1.87	1.85	1.57	0.55 - 0.57

Table 4.1: Inverse gradient size and anisotropy function at hydrodynamisation for different theories. Note that for RTA the quoted range reflects the sensitivity of the summation to Padé order and does not include the uncertainty associated with the imaginary part of the inverse Borel transform.

In this table we have also quoted the values obtained for RTA. As already mentioned, these results are much more sensitive to the Padé order and the extracted values reflect this sensitivity. This sensitivity hints towards a larger contribution of the non-perturbative corrections, which we will explore below in detail, making the hydrodynamisation interpretation harder. Nevertheless, it is worth noting that all the computations performed via the gauge/gravity duality hydrodynamise at comparable values of the viscosity rescaled gradient ws/η, and significantly earlier than in RTA kinetic theory. Since both RTA and λ_{GB} may be viewed as oversimplified treatments of finite coupling effects in gauge theories, it would be interesting to investigate more realistic higher derivative corrections and collision kernels to explore whether the size of the rescaled gradient at hydrodynamisation shows consistent trends in these complementary approaches towards gauge theories at intermediate coupling.

As we have stressed, in performing our summations we have implicitly selected some particular values of the initial conditions, which is tantamount to a specific selection of the constants C_α in Eq. (4.53). It is therefore unclear whether this choice leads to the hydrodynamic attractor. In the simpler example of [111], where the trans-series program has been performed, non-trivial values for this constant, beyond the cancellation of imaginary parts, must be introduced (fitted) to describe the numerically computed attractor. This can be done by studying numerically the early time evolution of a set of initial conditions like in the case of [116]. In our case, this would require using the fluid/gravity correspondence and computing the full non-linear numerical solution for several initial conditions. The effect of these different initial conditions would be eventually encoded in the trans-series Stokes constants. Therefore when we are scanning

through the space of initial conditions, we are effectively considering different values for the undetermined Stokes parameters, so we can avoid solving non-linear PDE's if we just consider the the dynamics of the leading non-perturbative corrections that we have been neglecting.

We can determine the late time behaviour of these contributions by examining the discontinuities of the inverse Borel transform for different choices of the contour integration. By inspection of the Borel planes at finite λ_{GB}, Fig. 4.2, we identify three representative contours of integration, which yield different answers for the inverse Borel transform. We have already used one of those contours, $\mathcal{C}_+$, to define the inverse Borel transform above. The second contour $\mathcal{C}_-$, is the reflection of the previous to the lower half plane. Finally, the third contour is a straight line in the upper half plane at angle above the argument of the start of the complex branch cut, $\mathcal{C}_c$. All these contours are shown in Fig. 4.2. Denoting by R_+, R_- and R_c the results of integrating Eq. (4.52) over each of these contours, we define the discontinuities by

$$iD_\pm(w) = R_+ - R_-, \quad D_c(w) = R_c - R_+. \tag{4.59}$$

$D_\pm$ is real and coincides with the imaginary part of R_+ while D_c is complex.[14] Within the above approximation, the late time behaviour of the different initial conditions is given by

$$R_{IC}(w) = R + a_1 D_\pm + a_2 \mathrm{Re}\left[D_c\right] + a_3 \mathrm{Im}\left[D_c\right] , \tag{4.60}$$

where $R(w)$ is the result of the summation described above and the coefficients a_i contain information from the early proper time evolution of the system beyond the hydrodynamic approximation.

Note that the edges of the band displayed in Fig. 4.3 corresponds to setting $a_2 = a_3 = 0$ and $a_1 = \pm 1$. Varying the values of this constant, we can estimate how different initial configurations deviate from our summed result.

In Fig. 4.4 we explore the effect of different initial conditions on the time evolution of boost invariant expansion of different theories. We will vary the coefficients $a_i \in (-1, 1)$

[14]Note that we could have defined an equivalent discontinuity by reflecting both $\mathcal{C}_c$ and $\mathcal{C}_+$ to the lower half; however, this discontinuity is simply the complex conjugate of $D_c(w)$.

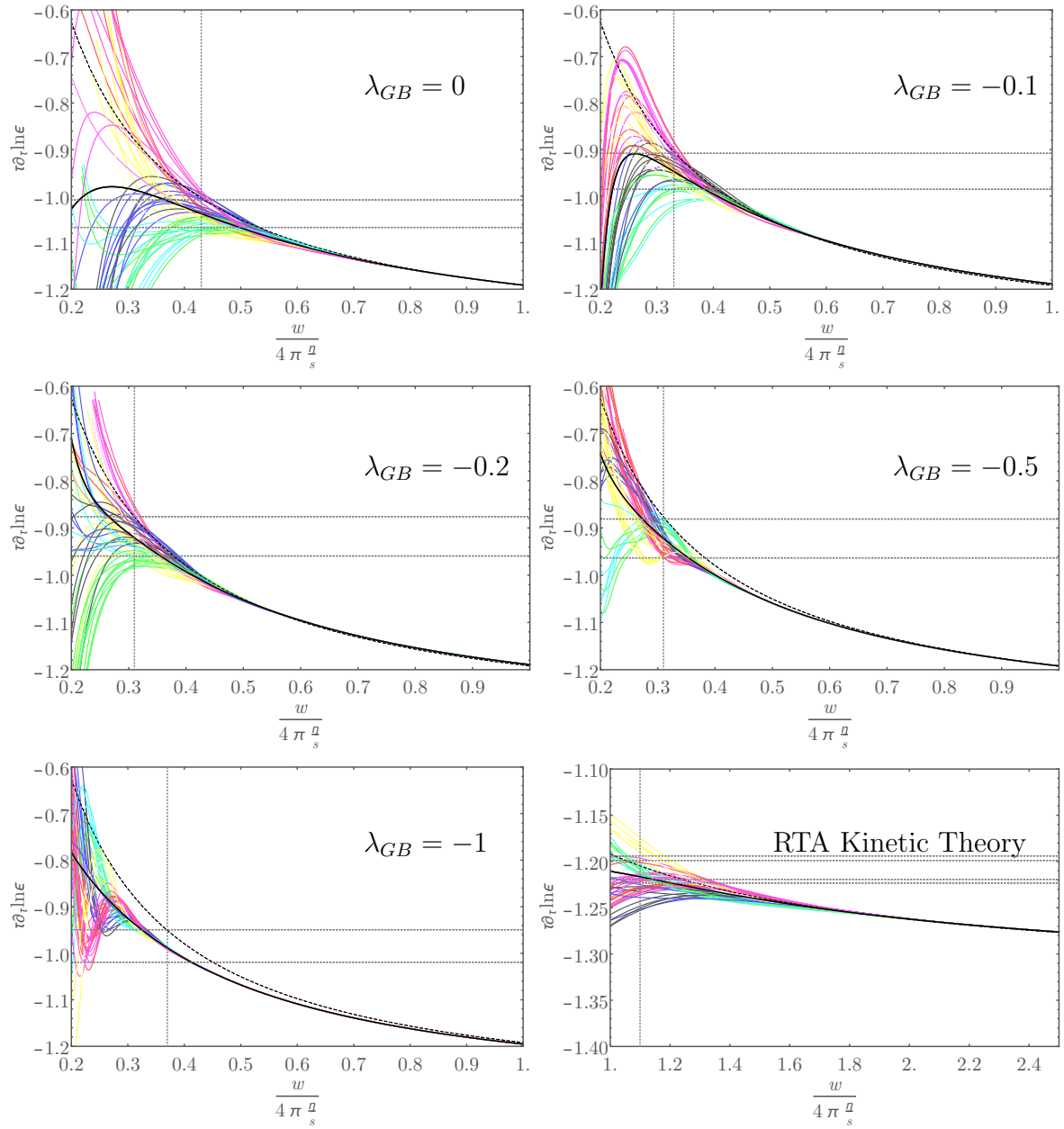

Figure 4.4: Logarithmic derivative of the energy density as a function of the viscosity-rescaled gradient for different values of λ_{GB}. In all panels, the thick solid line is the result of the summation of the hydrodynamic series, while the dashed line corresponds to the first order hydrodynamic prediction. The thin coloured lines correspond to adding to the sum the discontinuities defined in Eq. (4.59) for a range of coefficients. The vertical dotted line indicates the rescaled hydrodynamisation time $\frac{w_{\rm hyd}s}{4\pi\eta}$, the horizontal lines give the corresponding $R = (1 \pm 0.1)\, R|_{w_{\rm hyd}}$ as displayed in Table 4.1 (including its uncertainties for RTA).

to gauge the spread of typical initial conditions of such time evolution.[15] Following different extractions of attractor solutions in the literature, [111,116,122], the attractor may be identified by the so called "slow roll" condition, which demands that the time derivative $\tau\partial_\tau \log\epsilon$, is small all along the evolution of the system. For this reason, in Fig. 4.4 we show the logarithmic derivative of the energy density, $\tau\partial_\tau \log\epsilon$, from which such a derivative may be inferred. In these plots, the solid thick line corresponds to the summation, while the colourful thin lines correspond to different time evolutions obtained by varying a_i. In all panels, the dashed line corresponds to the first order hydrodynamic prediction for this quantity. Finally, the vertical dotted line marks the hydrodynamisation $w_{\rm hyd}$ time extracted in Table 4.1 and the horizontal dotted lines indicate the values of $\tau\partial_\tau \log\epsilon$ which correspond to varying R by 10% around the summation.

The inspection of this figure shows that in all holographic calculations the result of the summation provides a good proxy to the attractor at hydrodyanamisation time. For all values of λ_{GB}, the variation within typical initial conditions of the evolution of the energy density is consistent within the hydrodynamisation criterion used to determine the $w_{\rm hyd}$. This shows that our extraction of $w_{\rm hyd}$ is reliable. Furthermore, the spread of the different initial conditions also show that, while specific initial conditions may converge faster, for typical configurations, we only expect convergence towards the attractor when the attractor is well approximated by first order hydrodynamics.

We close this section by noticing that the RTA computation exhibits a much stronger dependence on initial conditions than the holographic computations.[16] For RTA our estimated hydrodynamisation time $w_{\rm hyd}$ occurs much later than for the holographic computations, and we observe that many of the individual initial conditions are not well approximated by the attractor or first order hydrodynamics.

[15] We have checked that this procedure leads to a spread in anisotropy paramater comparable to that induced by the different initial conditions in $\mathcal{N}=4$ SYM reported in [121].

[16] We thank M. Heller, M. Spaliński and V. Svensson for private communication on recent analysis of RTA kinetic theory with a non-conformal relaxation time [158] which exhibits a trans-series structure with multiple independent contributions with identical exponential suppressions. This indicates that for conformal RTA the trans-series may be more complicated than what we have assumed in this work.

4.5 Discussion

Understanding the unexpected success of hydrodynamics to describe the off-equilibrium dynamics of interacting systems is an important challenge, not only theoretically but also with important practical applications to heavy ion physics and beyond. To address the success of this low energy effective theory much beyond its expected regime of validity, the emergence of special time-dependent configurations of the interacting theory, which act as attractors for all possible system evolutions and which generalise the hydrodynamic expansion beyond the limit of small gradients, has been suggested as a possible explanation. Motivated by this suggestion, in this work we have applied the extension of hydrodynamics beyond the gradient expansion to the boost invariant flow of the field theory dual of Gauss-Bonnet gravity in 5D, which may be viewed as a laboratory to study finite coupling corrections to infinitely strongly-coupled theories.

As we have already stressed, we have chosen to analyse Gauss-Bonnet holography since, at least in principle, it allows us to explore non-perturbative values of λ_{GB}, the parameter that controls higher-derivative corrections to Einstein gravity. The relaxation dynamics of non-hydrodynamic modes at finite (and negative) λ_{GB} exhibits qualitative similarities to the effect of finite 't Hooft coupling corrections for those dynamics in $\mathcal{N} = 4$ SYM. In particular, both theories exhibit purely dissipative relaxation channels which, from the point of view of holography, are due to higher curvature terms.[17]

One of our main results is the analysis of singularities of the Borel transform of the hydrodynamic series in this theory. In accordance with the general theory of resurgence, and as already observed in $\mathcal{N} = 4$ SYM, these singularities reflect the characteristic QNM frequencies that control the relaxation of small non-hydrodynamical excitations in the dual black-brane geometry. A direct consequence of the new purely dissipative modes is the presence of singularities on the real axis in the complex Borel plane. These, together with the complex singularities associated to other QNM's of the dual theory make the analytical structure of the fixed coupling calculation richer than in the infinite coupling limit. But even more importantly, the structure of singularities

[17] Note also that our analysis has been performed for values of λ_{GB} beyond the causality bounds of [134, 148]. For this reason, we are not able to explore the boost invariant expansion in the $\tau \to 0$ limit.

qualitatively interpolates between the infinite coupling limit obtained via holography and the weakly-coupled limit, obtained by kinetic theory in the RTA. This may be viewed as an additional motivation to study the large order gradient expansion in this higher-derivative theory.

To explore the effect of this analytic structure on the early time dynamics of the system, we have summed the hydrodynamic series via Borel-Padé techniques. This allows us to extend the information in the large order gradient expansion to the large gradient region at early times. Remarkably, as in all other examples studied in the literature, the summation of the gradient expansion of the field theory dual to this high-derivative gravity is approximated by first order hydrodynamics at an unexpectedly early time, in a region where viscous effects are large. At this hydrodynamisation time, the pressure anisotropy in the expansion is large and comparable in all strongly-coupled computations, independent of λ_{GB}, which implies that the hydrodynamisation occurs at comparable viscosity-scaled gradients, ws/η. By comparison, our analysis of the RTA kinetic theory gradient expansion computed in [114] indicates that hydrodynamisation occurs later, at smaller values of the anisotropy parameter. Our results are consistent with the numerical solutions of RTA described in [114].

This summation allows us to explore the dynamics of the hydrodynamic attractor in this holographic model. Certainly, summation techniques cannot solely determine the behaviour of the attractor. To fully determine this configuration, analysis able to explore the $w \to 0$ limit must be performed. However, at sufficiently late times, when all non-perturbative contributions have relaxed, the summation must coincide with the attractor. To gauge how close the summation is from the attractor, we have estimated the relaxation of transient behaviour by studying the discontinuities of the inverse Borel transform over different contours of integration. Since those discontinuities must be cancelled by non-perturbative contributions, they provide a natural scale for the magnitude of these corrections. By varying the magnitude of these modes we can quantify the deviation from the summation of generic initial conditions. From this analysis we conclude that in all holographic computations, the expected deviation of generic initial conditions from the summation, is comparable to the difference be-

tween the summation and first order hydrodynamics at hydrodynamisation time. As a consequence, our summation will be a good approximation to the attractor at hydrodynamisation time. From this analysis, we conclude that while individual configurations may converge to the attractor earlier, in all the strongly-coupled computations the relaxation of generic initial conditions occurs whenever the system has hydrodynamised. Our analysis also suggests that the sensitivity of kinetic theory to initial conditions persists up to significantly smaller viscosity-rescaled gradients.

Chapter 5

Holographic Zero Sound from Spacetime-Filling Branes

After a brief introduction to Fermi liquid "zero sound", we review the charged black brane solution of the fully backreacted DBI action in Section 5.2 of this chapter. In Section 5.3 we present our numerical results for the poles of the Green's functions, spectral functions, and sound attenuation. We conclude with discussion of our results and outlook in Section 5.4. The appendix contains the technical details for the numerical computation of retarded Green's functions and QNMs in holography.

5.1 Introduction and motivation

Many systems involve strongly-interacting degrees of freedom with non-zero chemical potential, $\mu \neq 0$. Examples include neutron stars, cold atoms at unitarity, graphene, and more. Such systems can exhibit remarkable properties, such as cold atom's extremely low ratio of shear viscosity, η, to entropy density, s [13]. However, few reliable techniques exist to derive these properties from first principles. Perturbation theory is manifestly unreliable, and when $\mu \neq 0$ the "sign problem" renders numerical techniques, such as quantum Monte Carlo, practically useless. As a result, the origins of such remarkable properties remain mysterious.

The AdS/CFT correspondence offers an alternative approach allowing us to study strongly-interacting CFTs with non-zero temperature T and μ by studying charged black branes in AdS. The CFT stress-energy tensor, $T^{\mu\nu}$ (with $\mu, \nu = 0, 1, \ldots, d-1$), is dual to the metric, g_{MN} (with $M, N = 0, 1, \ldots, d$), and a $U(1)$ current J^{μ} is dual

to a $U(1)$ gauge field A_M. AdS/CFT cannot yet describe any real system. Nevertheless, AdS/CFT has the potential to reveal universal principles applicable to real systems. Indeed, AdS/CFT already has several success stories. For example, all rotationally-invariant holographic fluids dual to Einstein gravity, have the *same* value of η/s, namely $\eta/s = 1/(4\pi) \approx 0.08$ [8–12], which is surprisingly close to the η/s estimated for cold atoms and the quark-gluon plasma [13]. In other words, AdS/CFT revealed that strongly-interacting fluids have characteristically small $\eta/s \sim 0.1$. AdS/CFT has also revealed universality in second-order transport [14–18]and anomalies in transport [19–21].

In particular, evidence has accumulated for the possible universality of *sound modes* in holographic compressible quantum matter [6, 159–187]. "Compressible" means the charge density $\langle J^t \rangle \neq 0$ is a smooth function of $\mu \neq 0$ with $d\langle J^t \rangle / d\mu \neq 0$, and "quantum" means $T = 0$, so that quantum, rather than thermal, effects determine the ground state [188]. "Sound modes" means poles in the longitudinal channel of $T^{\mu\nu}$ and/or J^μ's retarded two-point functions with dispersion relation $\omega(k) = \pm v k + \ldots$, with frequency ω, momentum k, speed v, and $\ldots$ stands for terms with higher powers of k, and where $\mathrm{Im}\,(\omega)$ determines the mode's attenuation.

To be more specific, $T = 0$ sound modes have been found in two classes of holographic models. In both classes the bulk action includes an Einstein-Hilbert term,

$$S_{\rm EH} = \frac{1}{16\pi G_N} \int d^{d+1}x \sqrt{-g} \left(R + \frac{d(d-1)}{L_0^2} \right), \tag{5.1}$$

with Newton's constant G_N, $g = \det(g_{MN})$, Ricci scalar R of g_{MN}, and AdS_{d+1} radius L_0. The two classes of models differ in A_M's dynamics. The first class is "probe brane" models [6, 159–164, 166–171, 173–180, 182–187], in which A_M has a Dirac-Born-Infeld (DBI) action,

$$S_{\rm DBI} = -T_D \int d^{d+1}x \sqrt{-\det\left(g_{MN} + \alpha\, F_{MN}\right)}, \tag{5.2}$$

with tension T_D, constant α of dimension $(\text{length})^2$, and $F_{MN} = \partial_M A_N - \partial_N A_M$. These models employ the probe limit: expand solutions for g_{MN} and A_M in $G_N T_D \ll 1$ to leading non-trivial order. In the probe limit, A_M's stress-energy tensor is neglected in Einstein's equation, and A_M's equation of motion reduces to that in the "unperturbed"

background g_{MN}. We will consider only spacetime-filling branes [189], *i.e.* the integral in Eq. (5.2) is over all $(d+1)$ bulk dimensions, although defect branes, of non-zero co-dimension, can also give rise to $T=0$ sound modes [159, 163].

In field theory terms, the probe limit is justified when the charged fields comprise a negligibly small fraction of the total degrees of freedom. For example, in string theory a D-brane action includes a DBI term [35]. In holography, a D-brane that reaches the AdS_{d+1} boundary is typically dual to "flavor fields," meaning fields in the gauge group's fundamental representation, just like quarks in QCD [190]. The $U(1)$ is then a flavor symmetry, analogous to QCD's quark number symmetry. In such cases, typically $T_D \propto N_f N_c$ whereas $G_N \propto 1/N_c^2$, so that $G_N T_D \propto N_f/N_c \ll 1$. In other words, the order N_c^2 adjoint fields (gluons) vastly outnumber the order $N_f N_c$ flavor fields (quarks), which are thus negligible.

The second class of models is Einstein-Maxwell theory [165,172] with no probe limit, *i.e.* A_M's stress-energy tensor is not neglected in Einstein's equation. The gauge field thus backreacts on the metric, hence we will also call these models "backreacted." In field theory terms, in backreacted models the charged fields comprise a non-negligible fraction of the total number of degrees of freedom. Moreover, a DBI action truncated at second order in αF_{MN} is a Maxwell action. From that perspective, using a Maxwell action means discarding certain all-orders corrections in α.

In both classes of models, sound modes appear in extremal solutions where A_M's only non-zero component is A_t, and both g_{MN} and A_t depend only on the holographic radial coordinate. For example, in Einstein-Maxwell theory sound modes appear in the extremal AdS_{d+1}-Reissner-Nordström (AdS-RN) charged black brane solution [165, 172].

The physical origin of these sound modes in holographic compressible quantum matter is mysterious. To see why, consider the three most familiar forms of compressible quantum matter, each characterised by symmetry breaking, and each supporting a sound mode [188, 191–196]. In solids, translational symmetry breaking produces a phonon. In Bose-Einstein condensates, spontaneous breaking of the particle number $U(1)$ produces a superfluid phonon. In a Landau Fermi liquid (LFL), no symmetries

are necessarily broken, but fluctuations of the Fermi surface's shape produce Landau's "zero sound" excitation [191–196], a longitudinal excitation with a dispersion relation of the form of a hydrodynamic sound mode, $\omega = \pm vk - i\Gamma k^2 + \ldots$(with real-valued k and complex-valued ω), where Γ is the attenuation constant.

In holographic compressible quantum matter the sound modes appear in states that preserve the translational and $U(1)$ symmetries, hence they cannot be (superfluid) phonons. Moreover, they almost certainly cannot be zero sound either, because the effective theories describing holographic quantum compressible matter differ dramatically from LFL theory.

In LFL theory, the ground state is a degenerate system of interacting fermionic quasi-particles, producing a Fermi surface, and fluctuations about the ground state are either quasi-particles/holes or collective excitations, such as zero sound. In contrast, probe brane models show no sign of a Fermi surface [6, 159–164, 166–171, 173–180, 182–187], although they do exhibit spectral weight at $\omega = 0$ for k up to some finite value, similar to a smeared Fermi-Dirac distribution [197]. The equations of their effective description have the same form as hydrodynamics with weak momentum relaxation, but with momentum replaced by $\langle J^t \rangle$ [187, 198].

Einstein-Maxwell models can have a Fermi surface [50, 51, 199], but violate Luttinger's theorem: the Fermi surface volume is smaller than $\langle J^t \rangle$ by powers of N_c [6, 165, 172, 181]. In these models, the effective description remains mysterious, primarily because extremal AdS-RN has a near-horizon AdS_2, indicating some $(0+1)$-dimensional CFT among the light modes [51]. Indeed, correlators of $T^{\mu\nu}$ and J^μ exhibit branch cuts due to these light modes, in addition to the sound modes [165, 200]. The effective description is thus neither LFL theory nor hydrodynamics, but rather some kind of "semi-local quantum liquid" [201] wherein space divides into "patches" of size $\ell \propto 1/\mu$, such that correlators at separations $< \ell$ exhibit $(0+1)$-dimensional scale invariance, and at separations $> \ell$ exhibit exponential decay.

Although the sound modes in holographic compressible quantum matter are almost certainly not LFL zero sound, following convention we will call them "holographic zero sound" (HZS) [159, 163], where "zero sound" is chosen mainly because they are not

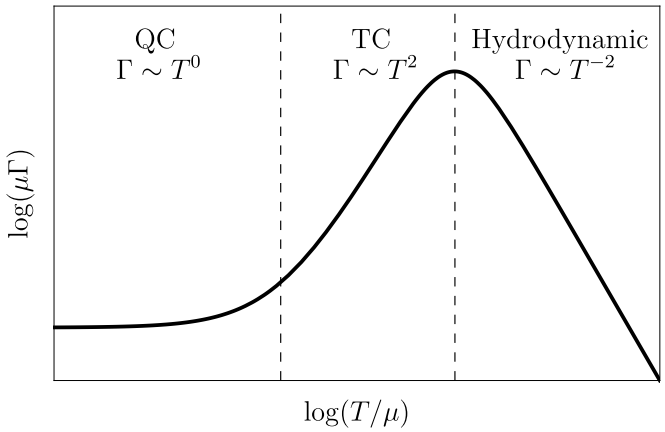

Figure 5.1: Schematic depiction of the LFL theory form of $\ln(\mu\Gamma)$, with sound attenuation constant Γ, as a function of $\ln(T/\mu)$ at fixed frequency ω and momentum k. The two vertical dashed black lines represent $\pi T/\mu = \omega/\mu$ (left) and $\sqrt{\omega/\mu}$ (right). In the quantum collisionless (QC) regime $\Gamma \propto T^0$, in the thermal collisionless (TC) regime $\Gamma \propto T^2$, and in the hydrodynamic regime $\Gamma \propto T^{-2}$. A maximum appears between the thermal collisionless and hydrodynamic regimes, signaling the collisionless-to-hydrodynamic crossover.

phonons, while "holographic" emphasises that they are probably not LFL zero sound.

Remarkably, however, in probe models the fate of HZS when $T > 0$ is strikingly similar to that of LFL zero sound [171,172]. LFL theory is an expansion in ω about the Fermi energy [191–196], so the LFL zero sound dispersion relation is typically expressed as $k(\omega) = \pm\omega/v + i\Gamma\omega^2/v^2 + \ldots$(with real-valued ω and complex-valued k). When $T/\mu = 0$, $|\mathrm{Im}(k)| \propto \omega^2/\mu$ at leading order in ω. As T/μ increases with μ and ω fixed, LFL theory predicts a three-stage "collisionless-to-hydrodynamic" crossover, characterised by changes to $\mathrm{Im}(k)$ due to collisions with thermally-excited quasi-particles. Fig. 5.1 is a schematic depiction of the crossover. The LFL prediction for the crossover has been confirmed experimentally in liquid Helium 3 [192].

First, in the "quantum collisionless" regime, $0 \leq \pi T/\mu < \omega/\mu$, the collisions are too weak and infrequent to change zero sound's dispersion from the $T/\mu = 0$ form, that is, $|\mathrm{Im}(k)| \propto \omega^2/\mu$ persists. Second, in the "thermal collisionless" regime, $\omega/\mu < \pi T/\mu < \sqrt{\omega/\mu}$, the collisions become sufficiently strong and frequent that $|\mathrm{Im}(k)|$ increases at a rate $\propto (\pi T)^2/\mu$. Third, in the "hydrodynamic" regime, the collisions are so strong and frequent as to destroy zero sound, however the thermal

excitations now support the usual hydrodynamic ("first") sound mode, whose attenuation decreases at a rate $\propto \mu\omega^2/T^2$. The transition from thermal collisionless scaling, $|\mathrm{Im}(k)| \propto T^2$, to hydrodynamic scaling, $|\mathrm{Im}(k)| \propto T^{-2}$, is thus marked by a maximum of $\mathrm{Im}(k)$, which provides a definition for a precise moment (value of T/μ) of crossover from collisionless to hydrodynamic regimes. For more details on the collisionless-to-hydrodynamic crossover in LFLs, see for example refs. [171, 172, 193, 196].

In probe brane models the HZS attenuation behaves identically to LFL zero sound in the quantum and thermal collisionless regimes [171]. However, in the probe limit the HZS pole appears only in correlators of J^μ, and not those of $T^{\mu\nu}$, so when $T/\mu > \sqrt{\omega/\mu}$, HZS crosses over to charge diffusion, not hydrodynamic sound: returning to complex-valued ω and real-valued k, the dispersion becomes $\omega = -iDk^2 + \ldots$, with charge diffusion constant D. As a result, the sound attenuation exhibits no maximum. Nevertheless, a precise moment of crossover can be defined from the pole movement in the complex ω/μ plane as T/μ increases with fixed k and μ [171], as depicted schematically in Fig. 5.2a. This pole movement is in fact identical to that of a harmonic oscillator evolving from under- to over-damped [187]. First, the two HZS poles move down, approximately along semi-circles, and eventually meet on the imaginary axis, subsequently splitting into two purely imaginary poles, one that descends down the imaginary axis and one that rises to become the charge diffusion pole. The meeting point provides a precise definition for the exact moment of crossover [171].

However, in Einstein-Maxwell models the crossover is qualitatively different from both LFL and probe brane models [172]. At low T/μ the sound attenuation scales as $|\mathrm{Im}(k)| \propto T^0$, similar to the LFL quantum collisionless regime, but at intermediate T/μ it scales as a power of T less than the T^2 of the LFL thermal collisionless regime. At higher T/μ a hydrodynamic regime emerges where $|\mathrm{Im}(k)| \propto T^{-1}$, unlike the T^{-2} of a LFL, but as expected for a CFT: for T/μ high enough that all scales besides T are negligible, dimensional analysis requires $|\mathrm{Im}\,(\omega)\,| \propto T^{-1}$, the AdS-Schwarzschild (AdS-SCH) result [72, 202]. Nevertheless, for sufficiently small k the sound attenuation exhibits a maximum before the hydrodynamic regime, so the LFL definition of the crossover remains viable.

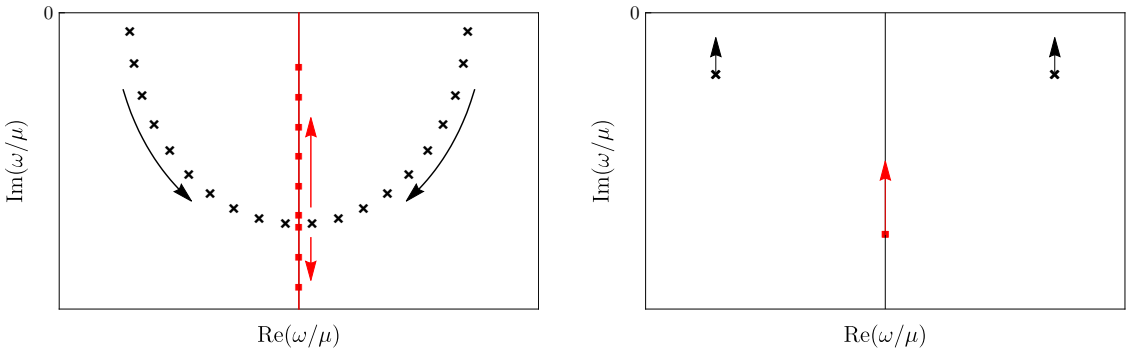

(a) Probe brane models (b) Einstein-Maxwell models

Figure 5.2: Schematic depictions of the movement of poles in the complex ω/μ plane in sound-channel J^μ and/or $T^{\mu\nu}$ correlators in HZS models. The arrows indicate the motion of poles as T/μ increases. The black crosses represent sound poles, while the (upper) red square represents the charge diffusion pole. (a) In spacetime-filling probe brane models, the two HZS poles move down, approximately tracing semi-circles, collide on the imaginary axis, and split into two purely imaginary poles, one moving up and one moving down, where the former is the charge diffusion pole. (b) In Einstein-Maxwell models, all three poles simply move up towards the real axis, with the sound poles' real parts constant.

Moreover, in Einstein-Maxwell models the pole movement differs dramatically from probe brane models. In the complex ω/μ plane, the sound-channel correlators of J^μ and $T^{\mu\nu}$ exhibit both sound and charge diffusion poles for all T/μ, which simply move up, closer to the real axis, as T/μ increases, as depicted schematically in Fig. 5.2b. Indeed, a crossover is apparent only in the charge density's spectral function, which we denote ρ_J, where as T/μ increases, a peak produced by the sound poles is suppressed, and a peak produced by the charge diffusion pole rises. A second definition of the crossover is then possible, as the T/μ where the charge diffusion peak first becomes taller than the sound peak [172]. No crossover is apparent in the energy density spectral function, which we denote ρ_{tt}, where only a single peak produced by the sound poles is apparent for all T/μ. Equivalently, this crossover occurs as a transfer of dominance in the *residues* of the poles in the charge density's retarded Green's function, which partly determine the corresponding spectral weights in ρ_J.

In short, the LFL and holographic results present us with three possible definitions for a precise T/μ of crossover. The LFL definition is the sound attenuation maximum.

The probe limit definition is the collision of poles on the imaginary axis in Fig. 5.2a. The AdS-RN definition is the transfer of dominance in ρ_J from the sound peak to the charge diffusion peak. A natural question is how common each of these behaviors is, and whether a "universal" definition exists, applicable to all cases above, and more generally to all quantum compressible matter.

5.1.1 The model

As a small step towards answering these questions, and to provide some larger context for the existing holographic results, in this paper we consider a simple model which reduces in different limits to the two classes of models described above. Specifically, we consider a backreacted DBI model, with bulk action

$$S = S_{\text{EH}} + S_{\text{DBI}}, \tag{5.3}$$

and study the collisionless-to-hydrodynamic crossover as a function of the "effective tension" or "backreaction" parameter,

$$\tau \equiv (8\pi G_N)\, T_D L^2 \tag{5.4}$$

which appears in Einstein's equation, controlling S_{DBI}'s backreaction (the backreacted AdS radius L depends on T_D: see Eq. (5.7)). In particular, the probe limit is an expansion in $G_N T_D \propto \tau \ll 1$ to leading non-trivial order. As suggested above, τ measures the ratio of the number of charged degrees of freedom to total degrees of freedom, and $\tau \ll 1$ simply means the number of charged degrees of freedom is $\ll N_c^2$.

In order to obtain a Maxwell action, it is convenient to define a dimensionless coupling

$$\tilde{\alpha} \equiv \alpha / L^2, \tag{5.5}$$

which controls the strength of higher-order terms in F_{MN}. We can recover a Maxwell action from S_{DBI} by sending $\tilde{\alpha} \to 0$ with $\tau\tilde{\alpha}^2$ and F_{MN} fixed. In probe D-brane models, $\tilde{\alpha}$ is proportional to the string length squared, and is holographically dual to an *inverse* power of the 't Hooft coupling, so that S_{DBI} includes an infinite sum of finite-coupling corrections. For the theory with action in Eq. (5.3), an exact, closed-form charged

black brane solution is known for all values of τ and $\tilde{\alpha}$ [189, 203–206]. The solution is analogous to AdS-RN, and indeed shares many qualitative features with AdS-RN. For example, for any $\tau \neq 0$, the extremal solutions have near-horizon AdS_2, so the effective theory is a semi-local quantum liquid.

To be concrete, we restrict to $d = 3$ and $T/\mu > 0$ (never $T/\mu = 0$), and numerically compute the the positions of sound-channel poles in J^μ and $T^{\mu\nu}$ correlators in the complex ω/μ plane, as a function of either T/μ or, to determine dispersion relations, k/μ. In holography, the poles in retarded Green's functions are dual to normalisable ingoing solutions of the linearised fluctuation equations, *i.e.* quasi-normal modes (QNMs) of the charged black brane solution [70, 72, 207–209]. For any $\tau > 0$ these poles are shared by all sound-channel correlators of J^μ and $T^{\mu\nu}$, because the dual linearised metric fluctuations are coupled. We also numerically compute ρ_J and ρ_{tt} holographically, from the on-shell action of the bulk fluctuations [70, 207, 209].

In our model, the coupling $\tilde{\alpha}$ appears in the action only as a coefficient of the gauge field strength, and hence $\tilde{\alpha}$ may be rescaled by an appropriate redefinition of the gauge field.[1]

5.1.2 Summary of results

We explore the effect of the backreaction on the spectrum of excitations, starting with the probe limit, $\tau = 0$, and then increasing τ through several values at fixed $\tilde{\alpha} = 1$ and small k/μ. In each case we calculate the spectrum of poles closest to the origin of the complex ω/μ plane, the spectral functions ρ_{tt} and ρ_J, and the sound dispersion. Our results are summarised as follows.

Pole Movement: At low T/μ we always find two HZS poles and a few other poles, which depending on the value of τ, may be propagating (non-zero real part) or purely dissipative (zero real part). As we increase T/μ the motion of these poles is more complicated than either case in Fig. 5.2, and indeed depends sensitively on the value

[1] To be more precise, the gravity theory's action is invariant under the re-scaling $\alpha \to \lambda\alpha$ and $F_{MN} \to \lambda^{-1} F_{MN}$ with constant $\lambda \in \mathbb{R}^+$. We could use this re-scaling symmetry to absorb α into F_{MN},, however we will retain α to facilitate comparison to the existing literature, to keep track of powers of the 't Hooft coupling and to facilitate the Maxwell limit of $S_{\rm DBI}$.

of τ. We leave the details to Section 5.3.1, and here just provide a sketch of some key general features.

When we increase τ, purely imaginary poles begin moving up the imaginary axis and "interfering" with the poles closer to the origin, producing various complicated pole collisions and splittings as T/μ increases. However, for τ below a critical value, two poles eventually emerge at high enough T/μ that move similarly to the probe limit of Fig. 5.2a, i.e. they collide on the imaginary axis and produce the charge diffusion pole. On the other hand, for τ above the critical value the three poles closest to the origin move similarly to the AdS-RN case in Fig. 5.2b, unaffected by the complicated collisions and splittings occurring lower in the complex ω/μ plane. The probe limit definition of the crossover thus remains viable only for τ below a critical value.

For all $\tau \neq 0$ we find sound poles for all T/μ, representing HZS at low T/μ which evolves into hydrodynamic sound as temperature is increased. This is in contrast to the probe limit, where the HZS poles collide on the imaginary axis for some critical temperature, forming the hydrodynamic diffusion pole, and another pole that moves deeper into the complex plane with increasing temperature.

Spectral Functions: For all τ that we consider, the energy density spectral function ρ_{tt} as a function of ω/μ exhibits only a single peak for all T/μ, arising from the sound pole, whether HZS or hydrodynamic.

The charge density spectral function ρ_J at low T/μ exhibits a peak from the HZS pole. As T/μ increases a second peak rises closer to $\omega/\mu = 0$, due to the charge diffusion pole. The charge diffusion peak eventually grows taller than the sound peak, so the AdS-RN definition of crossover thus remains viable in these cases. However, we suspect that for τ non-zero but smaller than we could access numerically the AdS-RN definition will eventually fail, because in the probe limit, $\tau = 0$, ρ_J always exhibits only a single peak, from either HZS (before the HZS poles collide) or charge diffusion (after the HZS poles collide). In that case no transfer of dominance is possible. Instead, the single peak simply moves towards $\omega/\mu = 0$ and broadens as T/μ increases. We compare our numerical results for ρ_{tt} and ρ_J to a simple approximation that treats each underlying Green's function as a sum of just a few poles close to the origin of the complex ω/μ

plane. This approximation turns out to work extremely well for many, but not all, values of τ and T/μ that we consider.

In short, when the DBI action backreacts the AdS-RN definition of the crossover can become viable, but only for sufficiently large τ.

Sound Dispersion: For all τ that we consider, the sound speed always takes the conformal value, $v = 1/\sqrt{2}$ (within our numerical accuracy), as in other backreacted models [172, 181]. If we increase τ, then the sound pole's $|\mathrm{Im}\,(\omega)\,|$ (shown in Fig. 5.12) at low T/μ always scales as T^0, similar to a LFL's quantum collisionless regime, and at high T/μ scales as T^{-1}, as expected for a CFT. However, at intermediate T/μ the power of T decreases as τ increases, from the T^2 of the probe limit down to, but never quite exactly to, T^0. An immediate consequence is that a maximum always appears in $|\mathrm{Im}\,(\omega)\,|$ at the transition from the intermediate T/μ scaling to the high T/μ hydrodynamic scaling.

Furthermore, as τ increases the maximum's position drifts to higher T/μ. The maximum's height also shrinks, which is perhaps surprising if we recall that τ effectively measures the number of charged degrees of freedom. In particular, if we increase the number of charged degrees of freedom, and hence increase τ, then naïvely we expect a larger number of "decay channels" for practically any mode, including sound. The naïve expectation is thus for $|\mathrm{Im}\,(\omega)\,|$ to *increase*, that is for sound to be *dampened*, as τ increases. Instead we find the opposite: in our holographic model, sound becomes *less* damped as we increase τ.

In short, for all τ that we consider the sound pole's $|\mathrm{Im}\,(\omega)\,|$ as a function of T/μ is qualitatively similar to that of a LFL in Fig. 5.1, though quantitatively distinct at intermediate and high T/μ. Most prominently, a maximum always appears in $|\mathrm{Im}\,(\omega)\,|$, so that the LFL definition of the crossover remains viable.

Finally, for all τ that we consider, we find numerically that the sound attenuation constant takes the hydrodynamic form, $\Gamma = \frac{1}{2}\eta/(\varepsilon + P)$, with shear viscosity η, energy density ε, and pressure P, for all T/μ. In particular, we find this form even at low T/μ, or equivalently for energies $\gg T/\mu$, *outside* the usual hydrodynamic regime. The fact that our model, like all (rotationally-invariant) holographic models, has $\eta =$

$s/(4\pi)$ with entropy density s [8, 10, 11], thus implies that $\Gamma \propto s/(\varepsilon + P)$ is in fact completely determined by thermodynamics. Plugging the Einstein-DBI charged black brane's values of s, ε, and P into $\Gamma = \frac{1}{2}s/(\varepsilon+P)$ then enables us to obtain an extremely good approximate expression for the position of the maximum in $|\mathrm{Im}\,(\omega)\,|$.[2]

These same phenomena occur in other backreacted models [181, 211, 212], and suggest that in these models the hydrodynamic derivative expansion may be valid even for energies $\gg T/\mu$, outside the normal hydrodynamic regime, so long as $k \ll \mu$ or T. More generally, hydrodynamics may be reliable for all T/μ, on length scales larger than a mean free path defined by $\eta/\left(\varepsilon + P\right)$ [211], giving a mean free path $\propto 1/T$ at high T/μ but $\propto 1/\mu$ at low T/μ.

Surveying of all the results above makes clear that no definition of the crossover is "universal". The probe limit definition is viable only for sufficiently small τ, the AdS-RN definition is viable only for sufficiently large τ and the LFL definition is viable for all τ except the probe limit.

5.2 Charged black brane solutions

The equations of motion arising from the action in Eq. (5.3) with $d = 3$ admit the charged black brane solution [189, 203–206],

$$ds^2 = g_{MN}\,dx^M dx^N = \frac{L^2}{z^2}\left(\frac{dz^2}{f(z)} - f(z)\,dt^2 + dx^2 + dy^2\right), \tag{5.6a}$$

$$f(z) = 1 - \frac{z^3}{z_H^3} + \frac{\tau}{3}\left[1 - \frac{z^3}{z_H^3} + {}_2F_1\left(-\frac{1}{2}, -\frac{3}{4}; \frac{1}{4}; -\tilde{\alpha}^2 Q^2\right)\frac{z^3}{z_H^3} - {}_2F_1\left(-\frac{1}{2}, -\frac{3}{4}; \frac{1}{4}; -\tilde{\alpha}^2 Q^2 \frac{z^4}{z_H^4}\right)\right],$$

$$F_{tz} = -F_{zt} = \frac{Q/z_H^2}{\sqrt{1 + \tilde{\alpha}^2 Q^2 z^4/z_H^4}}, \tag{5.6b}$$

with CFT time coordinate t and spatial coordinates x and y, and holographic coordinate z. The horizon z_H is the smallest real solution of $f(z_H) = 0$, and the asymptotic AdS_4 boundary is at $z \to 0$, with AdS_4 radius L given by

$$L^2 = \frac{L_0^2}{1 - (8\pi G_N)\,T_D L_0^2/3} \tag{5.7}$$

[2] In particular, we obseve the same result in the shear channel of the system studied in ref. [210]. A key numerical result of ref. [210] is that the shear diffusion constant $\propto \Gamma$ computed numerically from the Einstein-DBI charged black brane also retains the hydrodynamic form down to arbitrarily low T/μ.

The brane changes the AdS_4 radius from L_0 to L because when $F_{MN} = 0$, the DBI action is simply the brane's volume, which makes a positive contribution to the cosmological constant. Roughly speaking, L is a measure of the total degrees of freedom in the CFT, for example when $d = 4$ the central charges are L^3/G_N [47]. Clearly $L^2 \geq 0$ if and only if $(8\pi G_N)\, T_D \leq 3L_0^{-2}$. As suggested in Section 5.1, T_D is a measure of the number of charged degrees of freedom in the CFT. The bound $(8\pi G_N)\, T_D \leq 3L_0^{-2}$ suggests that the model in Eq. (5.3) describes a CFT in which the number of charged degrees of freedom can increase while preserving conformal symmetry, *i.e.* zero beta function(s), only up to a limit determined by the number of uncharged degrees of freedom. Indeed, appealing to our intuition from probe branes, generically flavor fields make a positive contribution to the gauge coupling's beta function, hence we expect the flavor fields to preserve conformal symmetry only within some "conformal window."

In subsequent sections we use units with $L \equiv 1$. In that case, if we change $(8\pi G_N)\, T_D$ then implicitly we also change L_0 to maintain $L \equiv 1$, or more precisely, to maintain all quantities in units of L. As a result, $(8\pi G_N)\, T_D$, and hence τ, will effectively have no upper limit

$$L_0^2 = \frac{L^2}{1 + \tau/3}. \tag{5.8}$$

For a given τ and $\tilde{\alpha}$, the dimensionless integration constant Q completely determines the solution in Eq. (5.6). Correspondingly, the CFT's state is determined by the single dimensionless parameter T/μ, hence Q must determine T/μ. For the solution in Eq. (5.6),

$$T = \frac{|f'(z_H)|}{4\pi} = \frac{3 + \tau\left(1 - \sqrt{1 + \tilde{\alpha}^2 Q^2}\right)}{4\pi z_H}, \tag{5.9a}$$

$$\mu = \int_0^{z_H} dz\, F_{tz} = \frac{Q}{z_H}\, {}_2F_1\left(\frac{1}{2}, \frac{1}{4}; \frac{5}{4}; -\tilde{\alpha}^2 Q^2\right), \tag{5.9b}$$

where $f'(z) \equiv \partial f(z)/\partial z$. The mapping from Q to T/μ is thus given by

$$\frac{T}{\mu} = \frac{3 + \tau\left(1 - \sqrt{1 + \tilde{\alpha}^2 Q^2}\right)}{4\pi Q\, {}_2F_1\left(\frac{1}{2}, \frac{1}{4}; \frac{5}{4}; -\tilde{\alpha}^2 Q^2\right)}. \tag{5.10}$$

All thermodynamic quantities can be written as a function of T/μ only, or equivalently of Q only, times an overall factor of either T or μ to a power determined by dimensional

analysis. For example, using Eq. (5.9a) the solution's Bekenstein-Hawking entropy density s, namely $1/(4G_N)$ times the horizon area density, can be written as

$$s = \frac{L^2}{4G_N}\frac{1}{z_H^2} = \frac{L^2}{4G_N}\left(\frac{4\pi T}{3}\right)^2\left[1+\frac{\tau}{3}\left(1-\sqrt{1+\tilde{\alpha}^2Q^2}\right)\right]^{-2}. \tag{5.11}$$

The on-shell Euclidean gravity action density equals the CFT's free energy density times $1/T$ [75]. To compute the energy density, $\varepsilon \equiv \langle T^{tt}\rangle$, and pressure, $P \equiv \langle T^{xx}\rangle = \langle T^{yy}\rangle$, we must therefore evaluate the Euclidean version of the action, Eq. (5.3), on the Euclidean version of the solution, Eq. (5.6). The result diverges, and requires holographic renormalisation [57, 213], which proceeds similarly to the AdS-RN case.[3] We thus find

$$\varepsilon = \frac{L^2}{8\pi G_N}\left(\frac{4\pi T}{3}\right)^3 \frac{1+\frac{\tau}{3}\left[1-{}_2F_1\left(-\frac{1}{2},-\frac{3}{4};\frac{1}{4};-\tilde{\alpha}^2Q^2\right)\right]}{\left[1+\frac{\tau}{3}\left(1-\sqrt{1+\tilde{\alpha}^2Q^2}\right)\right]^3}, \tag{5.12}$$

and $P = \varepsilon/2$, as required by scale invariance [215]. In the hydrodynamic regime, $v^2 = \frac{\partial P}{\partial \varepsilon} = 1/(d-1)$ [215], which in our case is $v^2 = 1/2$. Remarkably, for both AdS-RN and probe branes, HZS also has $v^2 = 1/(d-1)$ [159, 165, 171, 172], as we will see in Section 5.3. In a LFL the speeds of hydrodynamic and zero sound coincide only in the limit of infinite quasi-particle interaction strength [193]. The charge density $\langle J^t\rangle$ of the solution in Eq. (5.6) is

$$\langle J^t\rangle = \frac{L^2}{8\pi G_N}\left(\frac{4\pi T}{3}\right)^2 \frac{\tau\tilde{\alpha}^2\, Q}{\left[1+\frac{\tau}{3}\left(1-\sqrt{1+\tilde{\alpha}^2Q^2}\right)\right]^2}, \tag{5.13}$$

which obeys $\varepsilon + P = s\,T + \mu\langle J^t\rangle$, as expected. Moreover, we can write $\langle J^t\rangle$ in terms of s as $\langle J^t\rangle = \tau\tilde{\alpha}^2 Q\, s/(2\pi)$, which we will use in Section 5.3.3.

The solution in Eq. (5.6) admits an extremal limit, $T = 0$, with Q's corresponding extremal value, Q_{ext}, given by

$$Q_{\text{ext}}^2 = \frac{1}{\tau\tilde{\alpha}^2}\left(6+\frac{9}{\tau}\right). \tag{5.14}$$

[3] To compute correlators via holographic renormalisation, we introduce a cutoff surface near the asymptotic AdS_4 boundary, $z = \epsilon$, introduce covariant counterterms at $z = \epsilon$, take variational derivatives of the on-shell bulk action plus counterterms, and then send $\epsilon \to 0$. The Einstein-DBI counterterms are identical to those of Einstein-Maxwell, namely the Gibbons-Hawking term, a counterterm proportional to the cutoff surface's volume, a counterterm proportional to the cutoff surface's intrinsic curvature, and a counterterm proportional to a Maxwell term for F_{MN}. The latter is actually unnecessary for the solution in Eq. (5.6), consistent with the field theory statement that the vacuum counterterms suffice for renormalisation at non-zero T and μ [214]. The Einstein-Maxwell counterterms appear explicitly for example in ref. [165].

We can show that the extremal limit of the solution in Eq. (5.6) has near-horizon geometry $AdS_2 \times \mathbb{R}^2$ in the usual way. We expand $f(z)$ near the horizon, *i.e.* in powers of $(z_H - z)$, where of course $f(z_H) = 0$, and if $Q = Q_{\text{ext}}$ then also $f'(z_H) = 0$. In that case, truncating the expansion at order $(z_H - z)^2$ and defining a new radial coordinate

$$\xi \equiv \frac{1}{(z_H - z)\,\frac{1}{2}\,f''(z_H)|_{Q_{\text{ext}}}}, \tag{5.15}$$

produces the near-horizon metric

$$ds^2 = \frac{L_{AdS_2}^2}{\xi^2}\left(d\xi^2 - dt^2\right) + \frac{L^2}{z_H^2}\left(dx^2 + dy^2\right), \tag{5.16}$$

which is $AdS_2 \times \mathbb{R}^2$, with AdS_2 radius L_{AdS_2} given by

$$L_{AdS_2}^2 = \frac{L^2}{z_H^2\,\frac{1}{2}\,f''(z_H)|_{Q_{\text{ext}}}}, \tag{5.17}$$

where for the solution in Eq. (5.6)

$$z_H^2\,\frac{1}{2}f''(z_H)\bigg|_{Q_{\text{ext}}} = \frac{9+6\tau}{3+\tau}. \tag{5.18}$$

As in AdS-RN, the near-horizon $AdS_2 \times \mathbb{R}^2$ indicates that the dual CFT state is a semi-local quantum liquid [201]. In $T^{\mu\nu}$ and J^μ's Green's functions we then expect branch cuts along the imaginary axis [165,200]. However, in subsequent sections we will always have $T/\mu > 0$, so instead of branch cuts we expect poles along the imaginary axis that grow more and more dense as T/μ decreases, presumably coalescing into a branch cut when $T/\mu = 0$ [165, 200]. In Section 5.3 we will not explore T/μ small enough to see any such dense collection of poles.

5.2.1 The probe limit

As mentioned below Eq. (5.4), the probe limit is an expansion in $G_N T_D \propto \tau \ll 1$, with $\tilde{\alpha}$ fixed. More specifically, we expand in τ, and in all field theory quantities retain all terms up to the first non-trivial order in τ. In the holographically dual gravity theory, those leading non-trivial contributions come from the probe DBI action evaluated in the uncorrected background metric. For the g_{MN} in Eq. (5.6) we thus set $\tau = 0$, in which case $L^2 = L_0^2$ and $f(z) = 1 - z^3/z_H^3$, that is, g_{MN} becomes that of AdS-SCH in

$d = 3$ with radius L_0. Consequently, the probe limit expressions for T, μ, and T/μ are simply those in Eqs. (5.9a), (5.9b), and (5.10), respectively, but with $\tau = 0$. Moreover, in Eq. (5.14) taking $\tau \to 0$ sends $Q_{\text{ext}} \to \infty$. In that limit, g_{MN} is that of AdS_4, with no horizon and hence no near-horizon $AdS_2 \times \mathbb{R}^2$.

However, in these conformal cases the probe limit breaks down when $T/\mu = 0$ [216, 217]. To see why, consider for example the probe limit of s, or any other quantity obtained from the on-shell action/free energy.[4] Expanding Eq. (5.11) to first order in $G_N T_D$ gives

$$s = \frac{L_0^2}{4G_N}\left(\frac{4\pi T}{3}\right)^2\left[1 - \frac{1}{3}\tau + \frac{2}{3}\tau\sqrt{1+\tilde{\alpha}^2 Q^2} + \mathcal{O}\left(\tau^2\right)\right], \tag{5.19}$$

where now $\tau = (8\pi G_N)\, T_D L_0^2$ and $\tilde{\alpha} = \alpha/L_0^2$. Following refs. [159, 163], we next replace Q with T/μ, or equivalently $T^2/\langle J^t\rangle$, using the probe limit of Eq. (5.13)

$$\langle J^t\rangle = \frac{L_0^2}{8\pi G_N}\left(\frac{4\pi T}{3}\right)^2 \tau\tilde{\alpha}^2\, Q, \tag{5.20}$$

where, as in Eq. (5.19), τ and $\tilde{\alpha}$ now involve L_0 rather than L. Inserting Eq. (5.20) into Eq. (5.19) and expanding in $T^2/\langle J^t\rangle \ll 1$ gives

$$s = \frac{L_0^2}{4G_N}\left(\frac{4\pi T}{3}\right)^2\left[1 - \frac{1}{3}\tau\right] + \frac{4\pi}{3}\frac{\langle J^t\rangle}{\tilde{\alpha}} + \frac{1}{2}\left(\frac{4\pi}{3}\right)^5 \frac{\tau^2\tilde{\alpha}L_0^4}{(8\pi G_N)^2}\frac{T^4}{\langle J^t\rangle} + \mathcal{O}\left(\frac{\tau^4 T^8}{\langle J^t\rangle^3}\right) + \mathcal{O}\left(\tau^2\right). \tag{5.21}$$

On the right-hand-side of Eq. (5.21), the first term is s of $d = 3$ AdS-SCH minus the probe's $\langle J^t\rangle$-independent order τ correction. The second term is T-independent, leading to a residual entropy: if $T/\mu = 0$ then $s \propto \langle J^t\rangle/\tilde{\alpha} + \mathcal{O}\left(\tau^2\right)$. In that case the probe limit clearly breaks down because the order $\langle J^t\rangle \propto \tau$ term is larger than the order τ^0 term [216, 217]. As mentioned above, in subsequent sections we will always have $T/\mu > 0$, avoiding such probe limit breakdown. The third term on the right-hand-side of Eq. (5.21) gives the leading $\langle J^t\rangle$-dependent contribution to the heat capacity, $T\partial s/\partial T$, which is $\propto T^4$. For general d that term is $\propto T^{2(d-1)}$, in stark contrast to T of free fermions or T^{d-1} of free bosons [159, 163].

[4] The entropy density s can be calculated either from the horizon area or from $-\frac{\partial}{\partial T}$ of the free energy density. In the first case, calculating the order $G_N T_D$ contribution to s requires calculating S_{DBI}'s linearised backreaction and the corresponding change in z_H. The second case requires only calculating the on-shell S_{DBI} with the un-corrected g_{MN} and then taking $-\frac{\partial}{\partial T}$. In particular, the second calculation requires no backreaction. The two calculations agree, as required by thermodynamic consistency: see for example refs. [218–220].

5.2.2 The AdS-RN limit

As mentioned below Eq. (5.5), to recover Einstein-Maxwell from Einstein-DBI we take $\tilde{\alpha} \to 0$ keeping $\tau\tilde{\alpha}^2$ fixed, so that τ diverges as $\tilde{\alpha}^{-2}$. Moreover we adjust L_0 to keep L fixed. In that limit, $f(z)$, and hence T/μ, takes the AdS-RN form,

$$f(z) = 1 - \frac{z^3}{z_H^3} - \frac{1}{2}\tau\tilde{\alpha}^2 Q^2 \frac{z^3}{z_H^3} + \frac{1}{2}\tau\tilde{\alpha}^2 Q^2 \frac{z^4}{z_H^4}, \tag{5.22}$$

$$\frac{T}{\mu} = \frac{3 - \frac{1}{2}\tau\tilde{\alpha}^2 Q^2}{4\pi Q}. \tag{5.23}$$

In particular, now $Q_{\text{ext}}^2 = 6/(\tau\tilde{\alpha}^2)$, which is also obvious from taking $\tau \propto \tilde{\alpha}^{-2} \to \infty$ in Eq. (5.14). That same limit of Eq. (5.17) gives $L_{AdS_2}^2 = L^2/6$, as expected. In the AdS-RN limit, we also find the expected form of the entropy density,

$$s = \frac{L^2}{4G_N}\left(\frac{4\pi T}{3}\right)^2 \left[1 - \frac{1}{6}\,\tau\tilde{\alpha}^2\, Q^2\right]^{-2}. \tag{5.24}$$

In contrast to the probe limit, for AdS-RN at small T/μ the heat capacity's leading $\langle J^t\rangle$-dependent term is $\propto T$, similar to free fermions—though other observables differ dramatically from those of free fermions, as discussed in Section 5.1. The AdS-RN limit of Eq. (5.13) is

$$\langle J^t\rangle = \frac{L^2}{8\pi G_N}\left(\frac{4\pi T}{3}\right)^2 \tau\tilde{\alpha}^2\, Q \left[1 - \frac{1}{6}\tau\tilde{\alpha}^2 Q^2\right]^{-2}. \tag{5.25}$$

In the limit $T^2/\langle J^t\rangle \ll 1$, we thus find

$$s = \frac{2\pi}{\sqrt{6}}\frac{\langle J^t\rangle}{\sqrt{\tau\tilde{\alpha}^2}} + \frac{8\pi^2}{6^{5/4}}\frac{L}{\sqrt{8\pi G_N}}\frac{T\sqrt{\langle J^t\rangle}}{(\tau\tilde{\alpha}^2)^{1/4}} + \mathcal{O}\left(T^2\right), \tag{5.26}$$

where the first term is T-independent, leading to a residual entropy $\propto \langle J^t\rangle/\sqrt{\tau\tilde{\alpha}^2}$, while the second term gives a leading contribution to the heat capacity $\propto T$, as advertised.

5.3 Numerical results

For given values of τ, we want to know whether a sound pole exists at low T/μ, and how its dispersion changes in the crossover to hydrodynamics as T/μ increases. More generally we want to know the spectrum of poles in the sound channel of the charge and

energy retarded Green's functions, G_J and G_{tt} respectively, at low T/μ and small k/μ, and how they move as T/μ increases (the crossover) or as k/μ increases (the dispersion relations). We also want to know how the poles affect the charge and energy spectral functions, ρ_J and ρ_{tt}, respectively.

In the appendix we explain in detail how we compute G_J and G_{tt}, their poles, and ρ_J and ρ_{tt} holographically, by solving for the linearised fluctuations of the gravity fields dual to J^μ and $T^{\mu\nu}$, using the techniques of ref. [164]. Crucially, in the gravity theory in general the fluctuations couple, implying that G_J and G_{tt} share poles. However, in the probe limit the fluctuations decouple, in which we can distinguish which poles appear in G_J versus G_{tt}

As mentioned in Section 5.1.2, we will sample various values of τ, starting from the probe limit, $\tau = 0$, and then going through $\tau = 10^{-5}, 10^{-4}, 10^{-3}$, and 10^{-2}. We will set $\tilde{\alpha} = 1$ throughout for all of the numerical results we present in this section, as discussed in Section 5.1.1. We present our numerical result for the poles in G_J and G_{tt} in Section 5.3.1, for the spectral functions ρ_J and ρ_{tt} in Section 5.3.2, and for the sound attenuation in Section 5.3.3.

5.3.1 Poles and dispersion relations

In the probe limit with $T/\mu = 0$ the metric g_{MN} is that of AdS_4, in which case conformal invariance fixes G_{tt} (up to an overall constant) [221], whose only non-analyticities are branch points at $\omega = \pm k$ and $\omega = \infty$, connected by an arbitrary contour. However, G_J has no branch points, but rather two highest poles identified as HZS [159, 163], with dispersion

$$\omega = \pm v\, k - i\, \Gamma\, k^2 + \mathcal{O}\left(k^3\right), \tag{5.27}$$

with $v = 1/\sqrt{d-1}$ and attenuation constant

$$\Gamma = \frac{v^2}{2\mu} = \frac{\Gamma\left(\frac{1}{2}\right)}{\Gamma\left(\frac{1}{2(d-1)}\right)\Gamma\left(\frac{d-2}{2(d-1)}\right)} \langle J^t \rangle^{-\frac{1}{d-1}}, \tag{5.28}$$

both with $d = 3$. When $T/\mu > 0$, but still in the probe limit, the metric g_{MN} is that of AdS-SCH, so G_{tt} will have the usual hydrodynamic sound poles, with dispersion of

the same form as in Eq. (5.27), where scale invariance requires $v = 1/\sqrt{d-1}$ and now

$$\Gamma = \frac{d-2}{d-1}\frac{\eta}{\varepsilon + P}, \tag{5.29}$$

with $d = 3$. In (rotationally-invariant) holographic QFTs the shear viscosity $\eta = s/(4\pi)$ [8, 10, 11]. The s and ε of AdS-SCH in $d = 3$ are simply the probe limits of Eqs. (5.11) and (5.12), respectively, where also $P = \varepsilon/2$. These values give $v = 1/\sqrt{2}$ and $\Gamma = 1/(8\pi T)$ [72, 202].

As reviewed in Section 5.1, in the probe limit with $T/\mu > 0$, the HZS survives for $0 < \pi T/\mu < \omega/\mu$, with dispersion unchanged from the $T/\mu = 0$ form [171, 187], just like the LFL quantum collisionless regime. The HZS also survives for $\omega/\mu < \pi T/\mu < \sqrt{\omega/\mu}$, still with $v = 1/\sqrt{2}$, but now with $\Gamma \propto T^2$, just like the LFL thermal collisionless regime [171, 187]. However, in the hydrodynamic regime, $\pi T/\mu > \sqrt{\omega/\mu}$, J^μ's conservation equation dictates that the highest pole in G_J is not that of sound, but rather hydrodynamic charge diffusion, with dispersion

$$\omega = -i\, D\, k^2 + \mathcal{O}\left(k^3\right), \tag{5.30}$$

where a probe DBI action in $d = 3$ AdS-SCH gives a charge diffusion constant [162, 222]

$$D = \frac{3}{4\pi T}\sqrt{1+\tilde{\alpha}^2 Q^2}\,{}_2F_1\left(\frac{3}{2}, \frac{1}{4}; \frac{5}{4}; -\tilde{\alpha}^2 Q^2\right). \tag{5.31}$$

Fig. 5.3a shows our numerical results for the positions of poles in the complex ω/μ plane for $\tau = 0$, i.e. the probe limit. The arrows indicate the motion of the poles as T/μ increases from $T/\mu = 5 \times 10^{-4}$ to 0.1.

Our results are similar to those of refs. [72, 209] for G_{tt} and refs. [171, 187] for G_J, the main difference being that our spacetime is asymptotically AdS_4 rather than AdS_5. At low temperature, $T/\mu = 5 \times 10^{-4}$, we find four poles, two in G_{tt}, denoted by blue dots in Fig. 5.3a, with relativistic dispersion $\omega = \pm k + \ldots$ [72], and two in G_J, denoted by black crosses in Fig. 5.3a, with dispersion well-approximated by the $T/\mu = 0$ HZS form in Eqs. (5.27) and (5.28) [171, 187].

As T/μ increases the blue dots first descend into the complex ω/μ plane before turning around and moving back up, always with decreasing real part. By the time $T/\mu = 0.1$ they have become the hydrodynamic sound poles. Similar crossover behavior

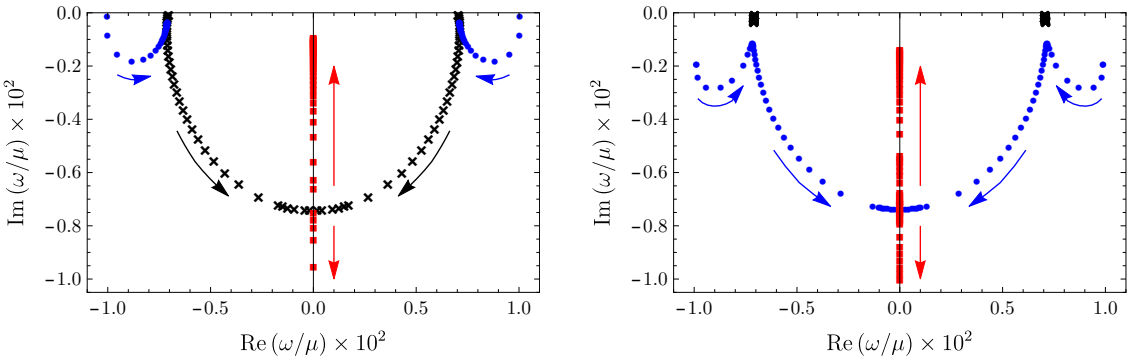

Figure 5.3: Positions of poles of G_J and G_{tt} in the complex ω/μ plane for increasing T/μ, with $\tilde{\alpha} = 1$ and $k/\mu = 10^{-2}$. We have enhanced $\mathrm{Re}\,(\omega/\mu)$ and $\mathrm{Im}\,(\omega/\mu)$ by 10^2 for clarity. The arrows indicate the movement of poles as T/μ increases. (a) $\tau = 0$ and $5 \times 10^{-4} \leq T/\mu \leq 0.1$. At $T/\mu = 5 \times 10^{-4}$ we find four of poles, two only in G_{tt}, with relativistic dispersion (blue dots), and two only in G_J, with dispersion well-approximated by the HZS dispersion in Eqs. (5.27) and (5.28) (black crosses). As T/μ increases the blue dots move down and then back up, eventually becoming hydrodynamic sound poles. The black crosses move down and eventually collide and split on the imaginary axis, producing two purely imaginary poles (red squares), one of which moves up and becomes the charge diffusion pole (see also Fig. 5.2a). (b) $\tau = 10^{-4}$ and $10^{-4} \leq T/\mu \leq 0.05$. At $T/\mu = 10^{-4}$ we again find four poles, similar to $\tau = 0$, however now all poles are shared by G_J and G_{tt}, and the black crosses denote sound poles which persist mostly unchanged as T/μ increases, while the poles with relativistic dispersion collide and split on the imaginary axis, producing the charge diffusion pole. (An animated version of this figure is available on the arXiv page of [223].)

in G_{tt}'s poles from relativistic to sound dispersion was observed in ref. [72]. Meanwhile the black crosses move down and towards the imaginary axis, approximately tracing semi-circles [171, 187], and ultimately collide on the imaginary axis at $T/\mu = 0.033$, and then split into two purely imaginary poles, one moving up the axis and the other moving down. The one moving up eventually becomes the charge diffusion pole, with dispersion given by Eqs. (5.30) and (5.31). Such crossover behavior in G_J in the probe limit was observed in refs. [171, 187]. As mentioned in Section 5.1, in ref. [171] the collision of poles on the imaginary axis was used as a definition of the precise moment of crossover (value of T/μ) to the hydrodynamic regime.

We next introduce small backreaction, $\tau \neq 0$ but $\ll 1$. We found that the pole movement for $\tau = 10^{-5}$ is qualitatively similar to that for $\tau = 10^{-4}$, so we will only

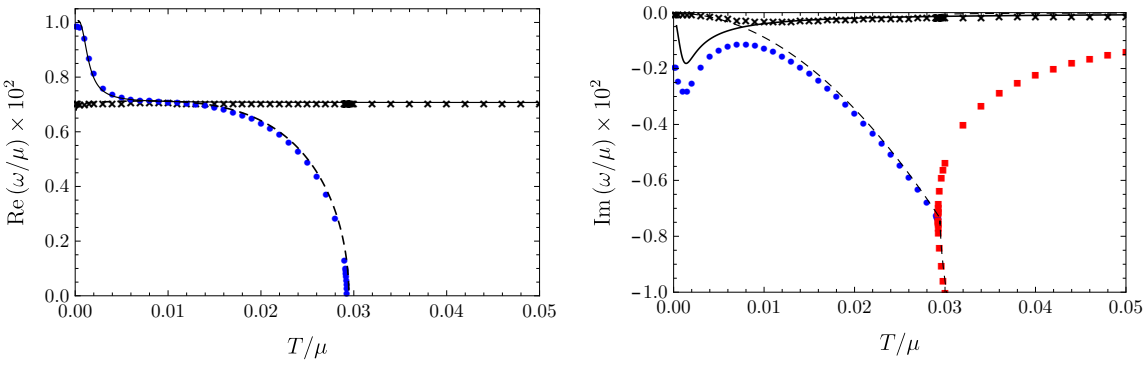

(a) (b)

Figure 5.4: The same data as Fig. 5.3b but with separate plots for (a) $\mathrm{Re}\,(\omega/\mu)$ and (b) $\mathrm{Im}\,(\omega/\mu)$, each enhanced by 10^2 for clarity, as functions of T/μ. The color and shape coding are the same as Fig. 5.3b. The dashed black lines denotes the probe limit HZS dispersion in Eqs. (5.27) and (5.28) while the solid black line denotes the hydrodynamic sound dispersion. At low T/μ the black crosses follow the black dashed line, identifying those poles as HZS, and as T/μ increases they crossover to the solid black line, indicating they have become hydrodynamic sound. The upper branch of red squares eventually approaches the probe limit charge diffusion dispersion in Eqs. (5.30) and (5.31) (not shown), identifying that as the diffusion pole.

present results for the latter. Fig. 5.3b shows our numerical results for the pole positions for $\tau = 10^{-4}$, for $10^{-4} \leq T/\mu \leq 0.05$. For clarity, Fig. 5.4 shows the same data as Fig. 5.3b, but with $\mathrm{Re}\,(\omega/\mu)$ and $\mathrm{Im}\,(\omega/\mu)$ plotted separately versus T/μ in Figs. 5.4a and 5.4b, respectively.

In Fig. 5.3b and Fig. 5.4, at the low temperature $T/\mu = 10^{-4}$, similar to Fig. 5.3a we again find four poles, two with relativistic dispersion, again denoted by blue dots, and two with HZS dispersion, again denoted by black crosses. However as T/μ increases the pole movement has some dramatic qualitative differences from the probe limit. The blue dots again first move down and up while their real part decreases, but then they move down again, still with decreasing real part. Meanwhile the black crosses barely move: Fig. 5.4a shows the real part is constant, with $v = 1/\sqrt{2}$, while Fig. 5.4b shows the imaginary part changes by at most 10%, with the largest deviation at the point of closest approach to the blue dots. However, after that point of closest approach the remaining evolution is similar to the probe limit. The blue dots approximately trace semi-circles and ultimately collide on the imaginary axis at $T/\mu = 0.029$, where they

then split into two purely imaginary poles, one moving up the axis and one moving down, where the one moving up eventually becomes the charge diffusion pole. The black crosses eventually become the hydrodynamic sound poles, with $\Gamma = 1/(8\pi T)$.

Fig. 5.5 shows dispersion relations for $\tau = 10^{-4}$, $T/\mu = 10^{-2}$, and $10^{-4} \leq k/\mu \leq 0.1$. The two poles with least negative imaginary part (the black crosses) follow the probe HZS dispersion in Eqs. (5.27) and (5.28) to excellent approximation everywhere in this regime of k/μ. The next two highest poles (the blue dots) have relativistic dispersion $\mathrm{Re}\,(\omega) = k$ for large k/μ, but upon decreasing to $k/\mu \approx 0.02$ they have $\mathrm{Re}\,(\omega) \approx k/\sqrt{2}$, suggesting they have become an *additional* two sound poles. However, as k/μ continues decreasing to $k/\mu \lesssim 0.02$, these two poles meet on the imaginary axis and split into two purely imaginary poles (the red squares), one of which moves up the imaginary axis and becomes the hydrodynamic diffusion pole, with the probe limit dispersion in Eqs. (5.30) and (5.31).[5]

Fig. 5.5 will be the only plot of dispersion relations that we present. However, in subsequent cases we have calculated dispersion relations, which we use to identify poles as HZS, relativistic, hydrodynamic sound, or hydrodynamic charge diffusion. Crucially, for all τ and T/μ, we have found that the speed of sound, whether HZS or hydrodynamic, always takes the conformal value, $v = 1/\sqrt{2}$, as in other backreacted models [172, 181].

The main effect of small backreaction $\tau = 10^{-4}$, compared to the probe limit $\tau = 0$, is clearly a "pole switch" in the crossover. In the probe limit, the two relativistic poles crossover to the hydrodynamic sound poles, while the two HZS poles trace semicircles and collide on the imaginary axis, producing two purely imaginary poles, one of which becomes the charge diffusion pole. However, with a small amount of backreaction the two relativistic poles at first move similarly to the probe limit case, but then change direction and become the two poles tracing semicircles and eventually giving rise to the charge diffusion pole. Meanwhile the HZS crosses over directly to the hydrodynamic sound poles, with no change in $\mathrm{Re}\,(\omega)$ and only slight change in $\mathrm{Im}\,(\omega)$. Such sound

[5] To clarify terminology: in Section 5.3.3 we will show that in fact Γ takes the hydrodynamic form, $\Gamma = \frac{1}{2}\frac{\eta}{\varepsilon+P}$, for all T/μ, and thus could be called "hydrodynamic" for all T/μ. In this section, if Γ approaches the probe value in Eq. (5.28) as $T/\mu \to 0$ then we call the poles HZS, whereas if $\Gamma \to 1/(8\pi T)$ as $T/\mu \to \infty$ then we call the poles hydrodynamic sound.

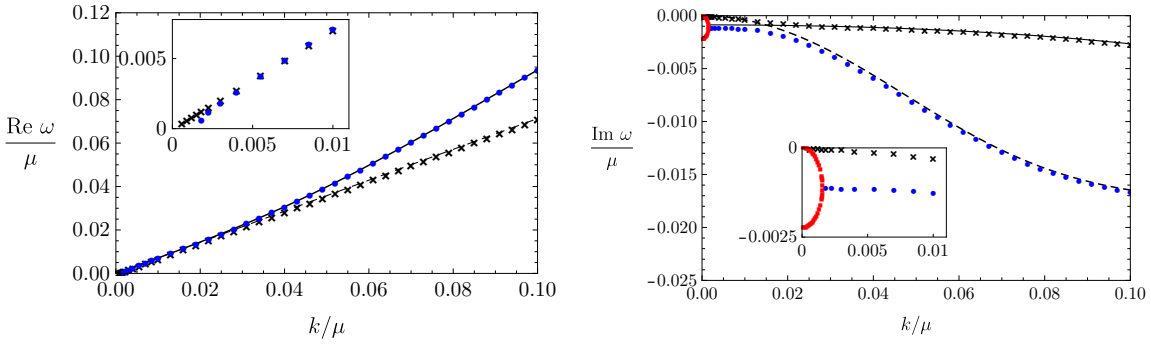

(a) (b)

Figure 5.5: Dispersion relations of the four highest poles for $\tau = 10^{-4}$, $\tilde{\alpha} = 1$, $T/\mu = 10^{-2}$, and $10^{-4} \leq k/\mu \leq 0.1$. (a) $\mathrm{Re}\,(\omega)/\mu$ and (b) $\mathrm{Im}\,(\omega)/\mu$, each versus k/μ. The solid and dashed black lines show the poles in G_{tt} and G_J in the probe limit, respectively. The black crosses follow the probe HZS dispersion for large k/μ, with Γ from Eq. (5.28), and the hydrodynamic sound dispersion for small k/μ, with Γ in Eq. (5.29). At large k/μ the blue dots have the dispersion of the poles in G_{tt}, with $\mathrm{Re}\,(\omega) = \pm k$, but at $k/\mu \approx 0.02$ have $\mathrm{Re}\,(\omega) = \pm k/\sqrt{2}$, and for $k/\mu \lesssim 0.02$ they drop to $\mathrm{Re}\,(\omega) = 0$ around $k/\mu \approx 0.002$, as shown in the inset of (a). They then split into two purely imaginary poles, the red squares, as shown in the inset of (b). One of these moves up the imaginary axis and becomes the charge diffusion pole, with the probe limit dispersion in Eqs. (5.30) and (5.31).

pole behavior is similar to the crossover in AdS-RN [172]. Nevertheless, despite the pole switch we could still define a precise moment the crossover occurs in the same way as the probe limit [171], when the two poles collide on the imaginary axis and produce the charge diffusion pole.

Fig. 5.6 shows our numerical results for the poles with larger backreaction, $\tau = 10^{-3}$, still with $k/\mu = 10^{-2}$, and now for $1.25 \times 10^{-3} \leq T/\mu \leq 0.05$. The arrows again indicate the pole movement as T/μ increases.

The crossover with $\tau = 10^{-3}$ is more complicated than with $\tau = 10^{-5}$ or 10^{-4}, so we divide the evolution into three regimes of T/μ. First, Fig. 5.6a shows the six highest poles for $1.25 \times 10^{-3} \leq T/\mu \leq 2.23 \times 10^{-3}$. At the smallest T/μ we find two poles with HZS dispersion (black crosses), and then lower in the complex ω/μ plane we find two purely imaginary poles (green squares and gray triangles) and two poles with non-zero real parts (blue dots). As we increase T/μ, the black crosses barely move, while the green squares and gray triangles move down the imaginary axis, and the two blue

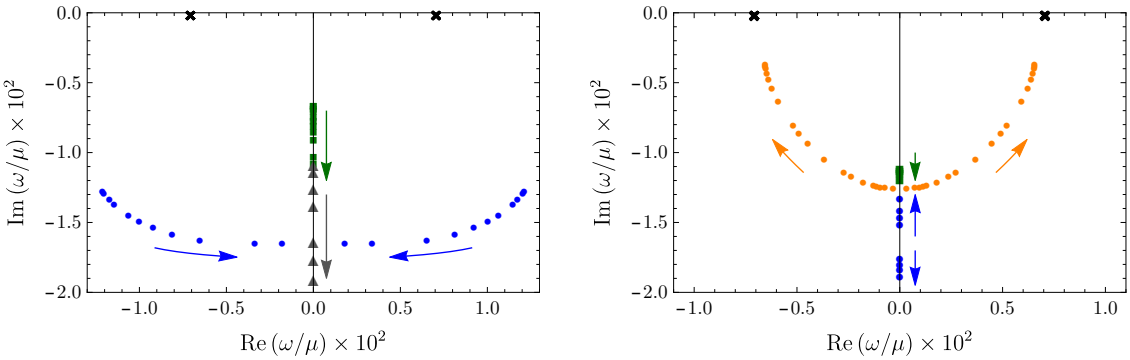

(a) $T/\mu = 1.25 \times 10^{-3}$ to 2.23×10^{-3}.

(b) $T/\mu = 2.23 \times 10^{-3}$ to 10^{-2}.

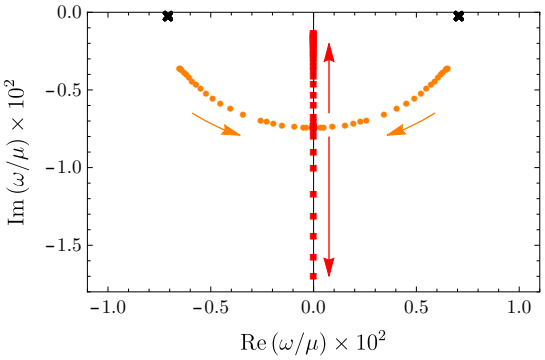

(c) $T/\mu = 0.011$ to 0.05.

Figure 5.6: Positions of poles of G_J and G_{tt} in the complex ω/μ plane, with $\tau = 10^{-3}$, $\tilde{\alpha} = 1$ $k/\mu = 10^{-2}$, and (a) $1.25 \times 10^{-3} \leq T/\mu \leq 2.23 \times 10^{-3}$, (b) $2.23 \times 10^{-3} \leq T/\mu \leq 10^{-2}$, and (c) $0.011 \leq T/\mu \leq 0.05$. We have enhanced $\mathrm{Re}\,(\omega/\mu)$ and $\mathrm{Im}\,(\omega/\mu)$ by 10^2 for clarity. The arrows indicate the movement of poles as T/μ increases. The pole motion is considerably more complicated than the previous smaller τ cases, so for detailed descriptions of the poles and their movement, including the color and shape coding, see the accompanying text. (An animated version of this figure is available on the arXiv page of [223].)

dots move down and towards the imaginary axis, meeting there at $T/\mu = 2.23 \times 10^{-3}$. Crucially, they meet below the green square but above the gray triangle. That is a key difference from $\tau = 10^{-4}$, where two poles met on the imaginary axis but with no purely imaginary poles above them.

Fig. 5.6b then shows the four highest poles for $2.23 \times 10^{-3} \leq T/\mu \leq 10^{-2}$. The two poles that met on the imaginary axis split into two purely imaginary poles (still blue dots), one of which moves up while the other moves down. The one moving up collides with the green square at $T/\mu = 2.24 \times 10^{-3}$ and splits into two poles with non-zero real

parts (orange dots), which move away from the imaginary axis and up towards the real axis as T/μ increases (the U-shape in Fig. 5.6b). However at $T/\mu \approx 10^{-2}$ the orange dots stop, reaching their maximum distance from the imaginary axis and highest point in the complex ω/μ plane.

Fig. 5.6c shows the subsequent evolution for $0.011 \leq T/\mu \leq 0.05$ which is in fact similar to the previous cases. The orange dots reverse direction, moving closer to the imaginary axis and back down into the complex ω/μ plane, tracing semicircles before colliding on the imaginary axis at $T/\mu \approx 0.027$ and then splitting into two purely imaginary poles (red squares), one of which moves down the imaginary axis while the other moves up and eventually becomes the hydrodynamic charge diffusion pole.

In short, the key difference with $\tau = 10^{-3}$, compared to $\tau = 10^{-4}$, is that when the two propagating poles (blue dots) hit the imaginary axis a purely imaginary pole is already present on the axis above them. As a result, when they split into two purely imaginary poles, one moving up the axis and one moving down, the one moving up must collide with this "extra" imaginary pole. Those two poles then "pop off" the imaginary axis and become increasingly long-lived propagating poles (orange dots), until at $T/\mu \approx 10^{-2}$ they stop and reverse course. The subsequent evolution is then similar to the previous cases: they trace semicircles until they hit the imaginary axis, producing the charge diffusion pole. As a result, despite the more complicated pole movement at low T/μ, the probe limit definition of the crossover actually remains viable at $\tau = 10^{-3}$, and gives a crossover temperature of $T/\mu \approx 0.027$, i.e. the temperature of the *second* pole collision on the imaginary axis.

More generally, we have learned that as τ increases, purely imaginary poles rise up the imaginary ω/μ axis and begin to "interfere" with the relativistic poles that collide on the axis. Clearly a critical value of τ exists, somewhere between $\tau = 10^{-4}$ and 10^{-3}, where as τ increases the highest of these purely imaginary poles first has imaginary part equal to that of the colliding poles. We have found this critical value to be $\tau \approx 9 \times 10^{-4}$.

Fig. 5.7a shows our numerical results for the pole positions for higher backreaction, $\tau = 10^{-2}$, still with $k/\mu = 10^{-2}$, and now for $0.005 \leq T/\mu \leq 0.0083$. At the smallest T/μ we again find two poles with HZS dispersion (black crosses) but now also a purely

imaginary pole high in the complex ω/μ plane (red square). Lower in the complex ω/μ plane we find four poles, two purely imaginary (orange and gray triangles) and two with non-zero real parts (blue dots). As T/μ increases, the black crosses and red square barely move, while the orange and gray triangles move down the imaginary axis and the blue dots move down and towards the imaginary axis, colliding there at $T/\mu \approx 0.0083$, above the orange and gray triangles. Fig. 5.7b shows the subsequent movement for $0.0083 \leq T/\mu \leq 10^{-2}$, where the poles that collided split into two purely imaginary poles (purple triangles), one of which moves up the axis while the other moves down. However, *both* remain below the red square.

Indeed, as T/μ continues increasing, to $10^{-2} \leq T/\mu \leq 0.05$, Fig. 5.7c shows $\mathrm{Im}\,(\omega/\mu)$ for the black crosses, red square, and purple triangle. The purple triangle reaches a highest point around $T/\mu \approx 0.024$, well below the red square, before turning around and descending back down the imaginary axis. Fig. 5.7d shows a close-up of $\mathrm{Im}\,(\omega/\mu)$ for the black crosses and red square for $0 \leq T/\mu \leq 0.05$. In that T/μ range, the black crosses decrease from $\mathrm{Im}\,(\omega/\mu) \approx -0.05$ only to ≈ -0.1 while the red square decreases from $\mathrm{Im}\,(\omega/\mu) \approx -1.6$ down to a minimum of ≈ -2 at $T/\mu \approx 0.02$ before rising again to $\mathrm{Im}\,(\omega/\mu) \approx -1.1$. As T/μ increases, the black crosses and red square eventually become the hydrodynamic sound and charge diffusion poles, respectively.

In short, the evolution with $\tau = 10^{-2}$ is qualitatively different from that with smaller τ. With $\tau = 10^{-2}$ we find two propagating poles and a single purely imaginary pole relatively high in the complex ω/μ plane, and then lower in the complex ω/μ plane two poles that collide on the imaginary axis and split into two purely imaginary poles, one moving up the axis and one moving down, where the one moving up eventually stops, turns around, and moves back down, never becoming the highest purely imaginary pole. The two highest propagating poles cross over from HZS to hydrodynamic sound, and the highest purely imaginary pole becomes the hydrodynamic charge diffusion pole at sufficiently high T/μ.

Recalling that as τ increases purely imaginary poles move farther up the imaginary axis, clearly a second critical value of τ exists, somewhere between $\tau = 10^{-3}$ and 10^{-2}, where the highest purely imaginary pole no longer moves down and "interferes"

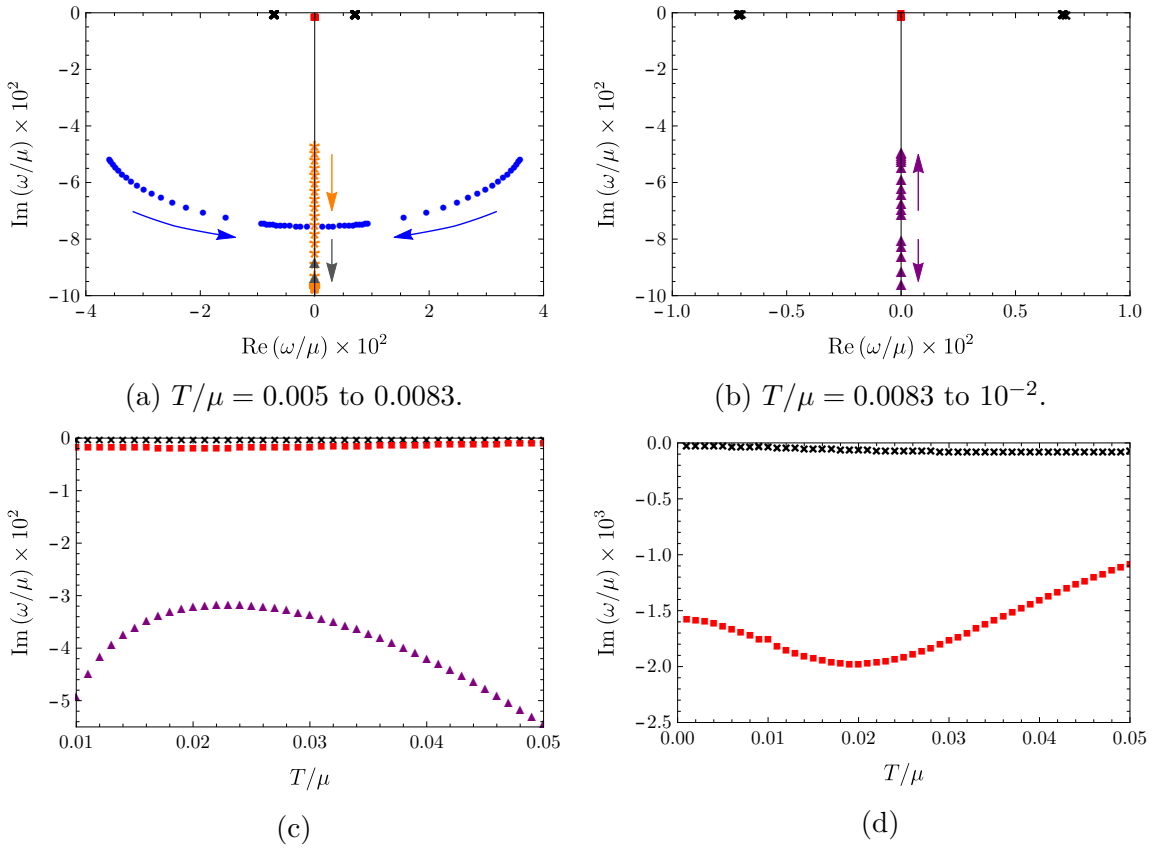

(a) $T/\mu = 0.005$ to 0.0083.

(b) $T/\mu = 0.0083$ to 10^{-2}.

(c)

(d)

Figure 5.7: Positions of poles of G_J and G_{tt} in the complex ω/μ plane with $\tau = 10^{-2}$, $\tilde{\alpha} = 1$, $k/\mu = 10^{-2}$, and (a) $0.005 \leq T/\mu \leq 0.0083$ and (b) $0.0083 \leq T/\mu \leq 10^{-2}$. For clarity we have enhanced the axes by 10^2. Arrows indicate the movement of poles as T/μ increases. At $T/\mu = 0.005$ we find seven highest poles, the three highest being two HZS poles (black crosses) and a purely imaginary pole (red square), and four lower poles, two purely imaginary (orange and gray triangles), and two with non-zero real parts (blue dots). As T/μ increases the three highest poles barely move, while the orange and gray triangles move down. The blue dots move down and collide on the imaginary axis, above the orange and gray triangles, and then split into two purely imaginary poles (purple triangles), one moving up the axis and one moving down. However, unlike the previous smaller τ cases, the one moving up does not become the charge diffusion pole, instead stopping, reversing direction, and moving back down the axis. The three highest poles eventually become the hydrodynamic sound and charge diffusion poles, respectively. (c) $\mathrm{Im}\,(\omega/\mu) \times 10^2$ versus T/μ for the four highest poles, showing the upper purple triangle's highest point at $T/\mu \approx 0.024$. (d) Close-up of (c) for the three highest poles, showing how little these move compared to the others. (An animated version of this figure is available on the arXiv page of [223].)

with the colliding poles, and instead crosses over directly to the hydrodynamic charge diffusion pole. We have found this critical value to be $\tau \approx 3.2 \times 10^{-3}$. Moreover, we

have sampled various $\tau \gtrsim 3.2 \times 10^{-3}$, including values $\tau > 10^{-2}$, and found behavior qualitatively similar to $\tau = 10^{-2}$.

Clearly for $\tau > 3.2 \times 10^{-3}$ we cannot use the probe limit definition of the crossover, since at no point do poles collide on the imaginary axis and produce the hydrodynamic charge diffusion pole. Instead, the three highest poles behave similarly to the AdS-RN case, namely they move very little as T/μ increases. In Section 5.3.2 we will show that the AdS-RN definition of the crossover, via a transfer of dominance in peaks of ρ_J, is viable for $\tau \gtrsim 3.2 \times 10^{-3}$.

5.3.2 Spectral functions

In this section we present our numerical results for the charge and energy spectral functions, ρ_J and ρ_{tt}, respectively, obtained via Eqs. (A.1) and (A.16). We will compare our numerical results to an approximation in which the Green's function matrix is simply a sum of poles,

$$G_{ij}(\omega, k) \approx \sum_n \frac{\mathcal{R}_{ij}^{(n)}(k)}{\omega - \omega_*^{(n)}(k)}, \tag{5.32}$$

where $\omega_*^{(n)}(k)$ are our numerical results for the highest poles, specifically the sound poles and the next highest pole or pair of poles, and $\mathcal{R}_{ij}^{(n)}(k)$ is a matrix of pole residues, which are generically complex-valued. In the appendix we explain how we compute the matrix of residues, using the techniques of ref. [164].

To our knowledge, in principle nothing requires $G_{ij}(\omega, k)$ to be simply a sum of poles, i.e. nothing forbids either additional terms analytic in ω or terms more singular in ω, such as branch cuts.[6] However, this sum of poles will lead to approximations for ρ_J and ρ_{tt} that agree very well with our numerical results for many, but not all, values of τ, and T/μ, indicating that the great majority of spectral weight comes only from the few highest poles—and indeed primarily from the sound and charge diffusion poles, as we will see.

Fig. 5.8 shows our numerical results for ρ_J and ρ_{tt} for $\tau = 10^{-5}$, $k/\mu = 10^{-2}$ and $T/\mu = 10^{-2}$, 2×10^{-2}, and 3×10^{-2}. In Fig. 5.8 the blue dots are our numerical data while

[6] Indeed, via the Mittag-Leffler theorem, a partial fraction expansion would provide a more accurate approximation, by including additional terms that, among other things, would capture the large-ω asymptotics. For a recent example of such an expansion in holography, see ref. [224].

the solid black line comes from the sum-of-poles approximation to the Green's functions in Eq. (5.32). This approximation is excellent over most of the regime shown, except for one curious outlier, namely ρ_J at $T/\mu = 2 \times 10^{-2}$, where the sum of poles roughly captures some key features of the shape, but otherwise is clearly a poor approximation.[7]

In both ρ_J and ρ_{tt} at $T/\mu = 10^{-2}$ we find a peak from the sound pole at $\omega \approx k/\sqrt{2}$. As T/μ increases through the values shown, in ρ_J the sound peak's height decreases by a factor of ≈ 20, while in ρ_{tt} the height increases by a factor of ≈ 25, indicating that as T/μ increases the sound pole's residue decreases in G_J but increases in G_{tt}. In both cases the sound peak's width decreases as T/μ increases. These features are consistent with our results for the pole positions, which are similar to those at $\tau = 10^{-4}$ in Figs. 5.3b, 5.4, and 5.5. In particular, as T/μ increased the HZS poles (black crosses) cross over to the hydrodynamic sound poles, with constant real part $\approx k/\sqrt{2}$ and decreasing imaginary part.

Crucially, aside from the sound peak no other significant features are visible in ρ_{tt}. Our numerical results from Eq. (A.17) indicate that in G_{tt} the charge diffusion pole does generically have non-zero residue, however at the T/μ shown in Fig. 5.9 the sound pole's residue is ≈ 10 times larger, explaining why no charge diffusion peak is visible in ρ_{tt} in Fig. 5.9.

However, in ρ_J a dramatic new feature appears as T/μ increases, namely a charge diffusion peak rises closer to $\omega/\mu = 0$. Indeed, while the sound peak shrinks the charge diffusion peak grows and eventually dominates the spectral weight. Such behavior is qualitatively similar to that of AdS-RN [172], despite the more complicated motion of poles, which is similar to that in Fig. 5.3b. Indeed, following ref. [172], in principle we could define a precise moment of crossover as the T/μ where the charge diffusion and sound peaks have equal height, which occurs between $T/\mu = 2 \times 10^{-2}$ and 3×10^{-2}. In practice, however, given how small the sound peak was and how broad the charge diffusion peak was, we struggled to extract a more precise crossover value of T/μ from our numerics.

[7] We have not found any other poles that provide a significant contribution to the spectral functions in the plotted regimes, suggesting that this is a genuine breakdown of the approximation.

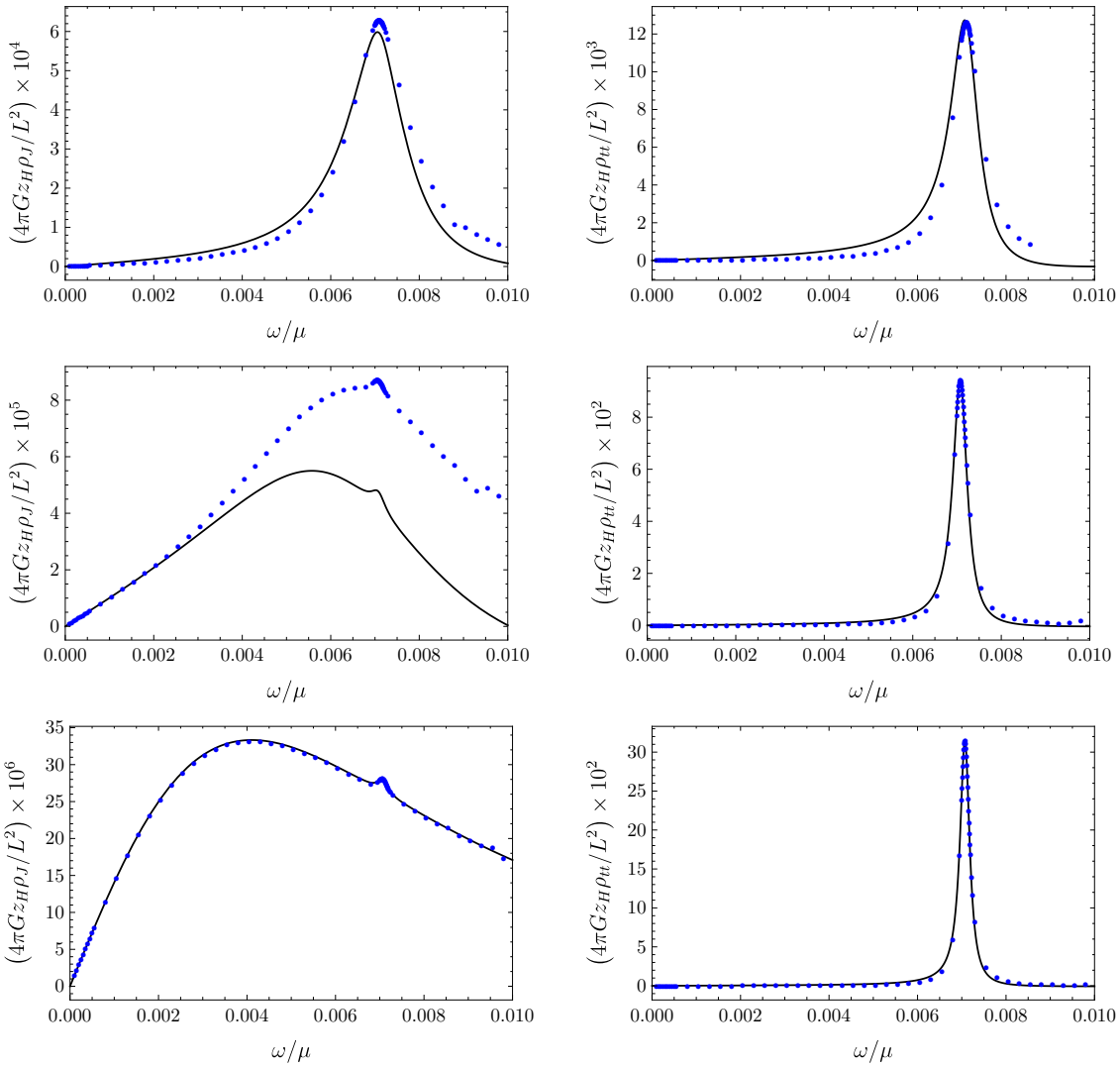

Figure 5.8: Our numerical results (blue dots) for the charge spectral function, ρ_J (left column) and energy spectral function, ρ_{tt} (right column), each made dimensionless by a factor of $4\pi G_N z_H/L^2$ and enhanced by 10^2 to 10^6 for clarity, as functions of ω/μ for $\tau = 10^{-5}$, $\tilde{\alpha} = 1$, $k/\mu = 10^{-2}$ and $T/\mu = 10^{-2}$ (top row), 2×10^{-2} (middle row), and 3×10^{-2} (bottom row). The solid black lines come from the sum-of-poles approximation to the Green's functions in Eq. (5.32). Both ρ_J and ρ_{tt} exhibit a peak from the sound pole (HZS or hydrodynamic) at $\omega/\mu \approx v\,k/\mu \approx 7.1\times 10^{-3}$. As T/μ increases the sound peak's height decreases in ρ_J but increases in ρ_{tt}. Simultaneously, in ρ_J a second peak rises closer to $\omega/\mu = 0$, from the charge diffusion pole, while ρ_{tt} exhibits no other significant features. The crossover can be defined as the value of T/μ where the two peaks in ρ_J have equal height [172].

Fig. 5.9 shows our numerical results for ρ_J and ρ_{tt} for $\tau = 10^{-4}$, $k/\mu = 10^{-2}$ and $T/\mu = 10^{-2}$, 0.03, and 0.05, with the same color coding as in Fig. 5.8. Unlike the

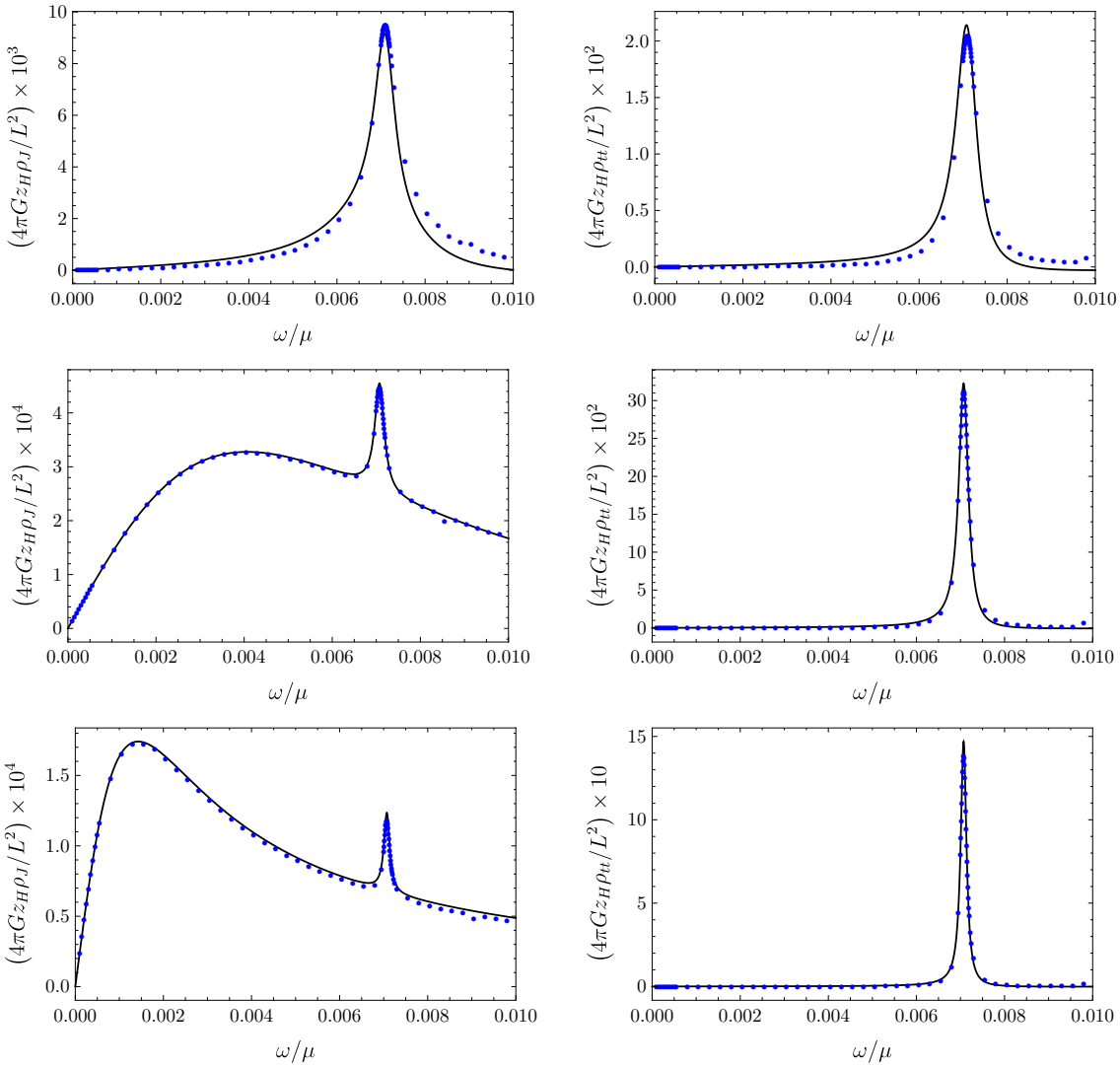

Figure 5.9: Our numerical results (blue dots) for the charge spectral function, ρ_J (left column) and energy spectral function, ρ_{tt} (right column), each made dimensionless by a factor of $4\pi G_N z_H/L^2$ and enhanced by 10 to 10^4 for clarity, as functions of ω/μ for $\tau = 10^{-4}$, $\tilde{\alpha} = 1$, $k/\mu = 10^{-2}$ and $T/\mu = 10^{-2}$ (top row), 0.03 (middle row), and 0.05 (bottom row). The solid black lines come from the sum-of-poles approximation to the Green's functions in Eq. (5.32). Both ρ_J and ρ_{tt} exhibit a peak from the sound pole (HZS or hydrodynamic) at $\omega \approx k/\sqrt{2}$. As T/μ increases the sound peak's height decreases in ρ_J but increases in ρ_{tt}. Simultaneously, in ρ_J a second peak rises near $\omega/\mu = 0$, from the charge diffusion pole, while ρ_{tt} exhibits no other significant features. The crossover can be defined as the value of T/μ where the two peaks in ρ_J have equal height [172], which gives $T/\mu = 0.039$. (An animated version of this figure is available on the arXiv page of [223].)

previous $\tau = 10^{-5}$ case, now the sum-of-poles approximation in Eq. (5.32) is clearly excellent over most of the regime shown. In general, the results are similar to the

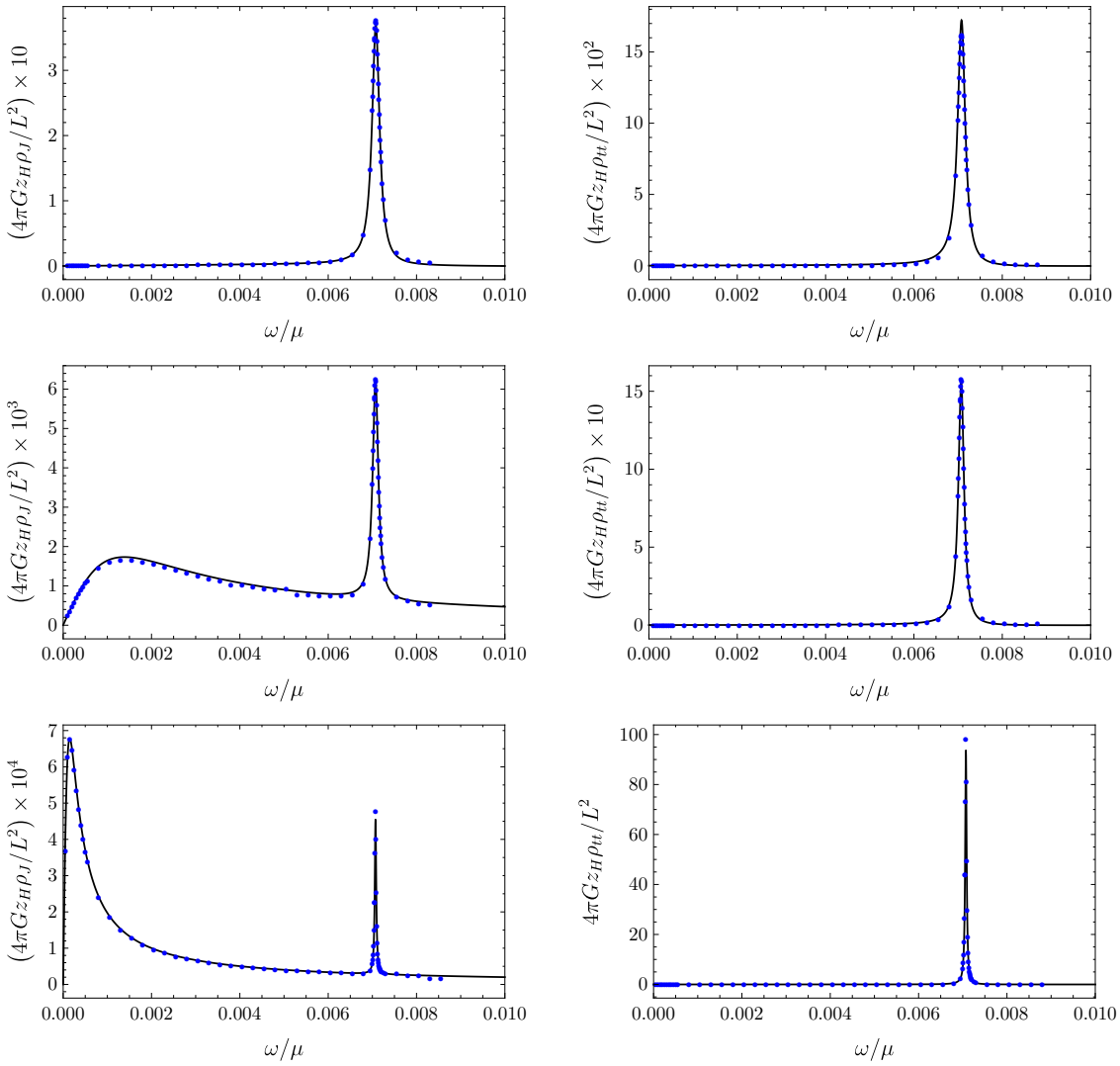

Figure 5.10: Our numerical results (blue dots) for the charge spectral function, ρ_J (left column) and energy spectral function, ρ_{tt} (right column), each made dimensionless by a factor of $4\pi G_N z_H/L^2$ and in some cases enhanced by 10 to 10^4 for clarity, as functions of ω/μ for $\tau = 10^{-3}$, $\tilde{\alpha} = 1$, $k/\mu = 0.01$ and $T/\mu = 0.01$ (top row), 0.05 (middle row), and 0.2 (bottom row). The solid black lines come from the sum-of-poles approximation to the Green's functions in Eq. (5.32). As T/μ increases, the behaviors of both ρ_J and ρ_{tt} are similar to the $\tau = 10^{-4}$ case in Fig. 5.9: in ρ_J the sound peak shrinks while the charge diffusion peak grows, and in ρ_{tt} the only significant feature is a sound peak that grows. The crossover can be defined as the value of T/μ where the two peaks in ρ_J have equal height [172], which gives $T/\mu = 0.136$

previous case. In both ρ_J and ρ_{tt} at $T/\mu = 10^{-2}$ we find a peak from the sound pole at $\omega \approx k/\sqrt{2}$. As T/μ increases through the values shown, in ρ_J the sound peak's height decreases by a factor of $\approx 10^2$, while increasing in ρ_{tt} by a factor of ≈ 75. In both cases

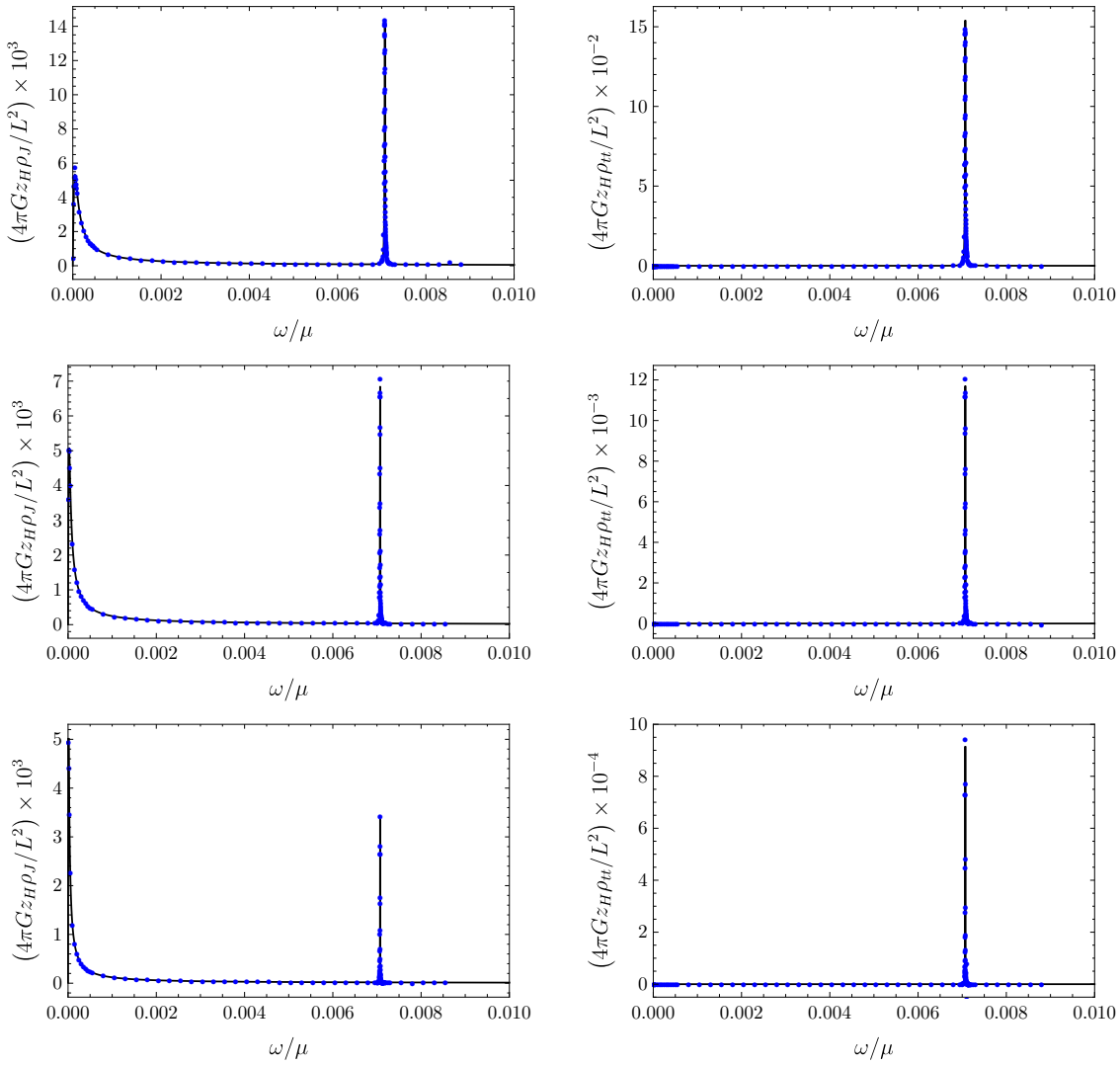

Figure 5.11: Our numerical results (blue dots) for the charge spectral function, ρ_J (left column) and energy spectral function, ρ_{tt} (right column), each made dimensionless by a factor of $4\pi G_N z_H/L^2$ and re-scaled by 10^{-4} to 10^4 for clarity, as functions of ω/μ for $\tau = 10^{-2}$, $\tilde{\alpha} = 1$, $k/\mu = 10^{-2}$ and $T/\mu = 0.5$ (top row), 1 (middle row), and 2 (bottom row). The solid black lines come from the sum-of-poles approximation to the Green's functions in Eq. (5.32). As T/μ increases, the behaviors of both ρ_J and ρ_{tt} are similar to the $\tau = 10^{-4}$ and 10^{-3} cases in Figs. 5.9 and 5.10: in ρ_J the sound peak shrinks while the charge diffusion peak grows, and in ρ_{tt} the only significant feature is a sound peak that grows. The crossover can be defined as the value of T/μ where the two peaks in ρ_J have equal height [172], which gives $T/\mu = 1.45$

the sound peak's width decreases, though only slightly, as T/μ increases. These features are consistent with our results for the pole positions at $\tau = 10^{-4}$ in Figs. 5.3b, 5.4, and 5.5. Aside from the sound peak no other significant features are visible in ρ_{tt}.

Our numerical results from Eq. (A.17) indicate that in G_{tt} the charge diffusion pole does generically have non-zero residue, however at the T/μ shown in Fig. 5.9 the sound pole's residue is ≈ 20 times larger. Again in ρ_J as T/μ increases a charge diffusion peak rises near $\omega/\mu = 0$. Defining the precise moment of crossover as the T/μ where the charge diffusion and sound peaks have equal height gives $T/\mu = 0.039$. In contrast, the definition based on the collision of poles in Fig. 5.3b gave the smaller value $T/\mu \approx 0.029$.

Fig. 5.10 shows our numerical results for ρ_J and ρ_{tt} for $\tau = 10^{-3}$, $k/\mu = 10^{-2}$ and $T/\mu = 0.01$, 0.05, and 0.2. These results are qualitatively similar to the $\tau = 10^{-5}$ and 10^{-4} cases in Figs. 5.8 and 5.9. As T/μ increases, in ρ_J the sound peak shrinks by a factor of $\approx 10^3$ for the T/μ shown, while a charge diffusion peak rises at $\omega/\mu = 0$ and eventually dominates the spectral weight. In ρ_{tt} the only significant feature is the sound peak, which grows by a factor of $\approx 10^3$ for the T/μ shown. All peaks are narrower than in the $\tau = 10^{-4}$ case. Again, these features are consistent with our results for the pole positions in Fig. 5.6. In fact, the complicated motion of poles lower in the complex ω/μ plane has little or no apparent effect on ρ_J and ρ_{tt}, which are extremely well-approximated by our sum of highest poles in Eq. (5.32), i.e. the solid black lines in Fig. 5.10. Defining the crossover when the two peaks in ρ_J have equal height gives $T/\mu \approx 0.136$. In contrast, defining the crossover by the collision of poles that produces the charge diffusion pole in Fig. 5.6 gave $T/\mu \approx 0.027$.

Fig. 5.11 shows our numerical results for ρ_J and ρ_{tt} for $\tau = 10^{-2}$, $k/\mu = 10^{-2}$, and $T/\mu = 0.5$, 1, and 2. Again the results are similar to the previous cases. As T/μ increases, in ρ_J the sound peak shrinks by a factor of ≈ 5 for the T/μ shown, while the charge diffusion peak rises at $\omega/\mu = 0$ and eventually dominates the spectral weight. In ρ_{tt} the only significant visible feature is a sound peak which grows by a factor of ≈ 1.5 for the T/μ shown. All peaks are narrower than the previous cases, and moreover the sound peak is now taller in ρ_{tt} than in ρ_J by a relative factor of $\approx 10^6$, unlike the previous cases where the sound peak was roughly the same height in both spectral functions. Again, these features are consistent with our results for the positions of poles in Fig. 5.7, and again, the spectral functions are well approximated by the sum of highest poles in Eq. (5.32). In particular, the complicated pole motion in

Fig. 5.7 occurs at much smaller T/μ than those shown in Fig. 5.11. The changes shown in Fig. 5.11 come only from the three highest poles, and in fact must come primarily from their residues, since those highest poles move very little for the T/μ shown. Most importantly, unlike $\tau = 10^{-5}$, 10^{-4}, and 10^{-3}, when $\tau = 10^{-2}$ no collisions of poles producing a charge diffusion pole occurs, so the only definition for a precise moment of crossover is via the exchange of dominance of poles in ρ_J, which gives $T/\mu \approx 1.45$.

In short, for fixed k/μ and all τ we considered, the definition of crossover via a transfer of dominance in ρ_J, from the sound peak to the charge diffusion peak, remains viable. However, as $\tau \to 0$, we eventually expect to recover the probe limit result for ρ_J, where no transfer of dominance occurs [171]. Instead, in the strict probe limit ρ_J exhibits only a single peak at all T/μ, which at low T/μ comes from HZS and at high T/μ comes from the charge diffusion pole. More specifically, as shown in Fig. 5.3a, as T/μ increases the HZS poles collide on the imaginary axis and split, producing the charge diffusion pole, and correspondingly in ρ_J, the single peak simply moves towards $\omega/\mu = 0$ and shrinks in height [171]. Apparently $\tau = 10^{-5}$ is not small enough to reproduce the probe result. Additionally, we have shown that the retarded Green's functions are often, but not always, well-approximated simply by the sum of their few highest poles, Eq. (5.32).

5.3.3 Sound attenuation

In this section we present our results for the sound attenuation, meaning $\mathrm{Im}\,(\omega)$ of the sound pole, whether HZS or hydrodynamic sound, as a function of τ, $\tilde{\alpha}$, and T/μ.

As reviewed in Section 5.1, in a LFL, sound dispersion is typically expressed as complex-valued $k(\omega)$ with real-valued ω. As T/μ increases, sound exhibits three regimes: quantum collisionless, $0 \leq \pi T/\mu < \omega/\mu$, where $|\mathrm{Im}\,(k)\,| \propto \omega^2/\mu$, thermal collisionless, $\omega/\mu < \pi T/\mu < \sqrt{\omega/\mu}$, where $|\mathrm{Im}\,(k)\,| \propto (\pi T)^2/\mu$, and hydrodynamic, $\pi T/\mu > \sqrt{\omega/\mu}$, where $|\mathrm{Im}\,(k)\,| \propto \mu\omega^2/T^2$. In other words, in terms of powers of T, in a LFL $|\mathrm{Im}\,(k)\,|$ scales as T^0 in the quantum collisionless regime, T^2 in the thermal collisionless regime, and T^{-2} in the hydrodynamic regime. The collisionless-to-hydrodynamic crossover is

thus characterised by a maximum in the sound attenuation where the T^2 scaling transitions to T^{-2}.

In our holographic system, we express the sound dispersion as complex-valued $\omega(k)$ with real-valued k. Translating the LFL regimes to that form is easy: simply use the leading small-ω behavior, $|\omega| = v\,k$, to replace ω with k. For example, the quantum collisionless regime is $0 \leq \pi T/\mu < v\,k/\mu$, where $|\mathrm{Im}\,(\omega)\,| \propto (v\,k)^2/\mu$.

In probe brane models, as T/μ increases $|\mathrm{Im}\,(\omega)\,|$ exhibits T^0 scaling followed by T^2 scaling, similar to the quantum and thermal collisionless regimes of a LFL, but in the hydrodynamic regime crosses over to charge diffusion, rather than hydrodynamic sound [171]. In contrast, in AdS-RN $|\mathrm{Im}\,(\omega)\,|$ exhibits T^0 scaling at low T/μ, like a LFL, followed by a power of T smaller than T^2, unlike a LFL, and then T^{-1} scaling in the hydrodynamic regime, unlike a LFL's T^{-2}, but expected for a CFT. In AdS-RN, for sufficiently small k/μ the sound attenuation exhibits a (very small) maximum at $\pi T/\mu \approx \sqrt{v\,k/\mu}$, signaling the onset of the hydrodynamic regime, as in a LFL. In terms of the pole movement in Fig. 5.2b, as T/μ increases the poles are practically stationary at low T/μ and then start moving up at approximately the T/μ where $|\mathrm{Im}\,(\omega)\,|$ has a small maximum.

We start by fixing $k/\mu = 10^{-2}$ and $\tilde{\alpha} = 1$ and increasing τ. Fig. 5.12 shows our numerical results for $\ln|\mathrm{Im}\,(\omega/\mu)|$ versus $\ln(T/\mu)$ for $\tilde{\alpha} = 1$, $k/\mu = 10^{-2}$, and increasing values of τ from $\tau = 10^{-5}$ (pink diamonds) to $\tau = 2$ (green triangles), and also the AdS-RN result (purple stars). The solid gray line is the numerical result for $\ln|\mathrm{Im}\,(\omega/\mu)\,|$ in the probe limit, while the dashed gray line comes from $\mathrm{Im}\,(\omega) = -\Gamma k^2$ with the AdS-SCH result $\Gamma = 1/(8\pi T)$ [72, 202]. The vertical dotted black lines represent the LFL boundaries between quantum and thermal collisionless regimes, $\pi T/\mu = v\,k/\mu$, which for $v = 1/\sqrt{2}$ and $k/\mu = 10^{-2}$ gives $\ln(T/\mu) \approx -6.09$, and between thermal collisionless and hydrodynamic regimes, $\pi T/\mu = \sqrt{v\,k/\mu}$, which gives $\ln(T/\mu) \approx -3.62$. LFL sound attenuation exhibits a maximum at the latter boundary.

In Fig. 5.12, when $\tau = 10^{-5}$ (pink diamonds) and T/μ is small, the sound attenuation closely follows the probe limit (solid black line), exhibiting T^0 scaling when $\ln(T/\mu) \lesssim -6.09$ and T^2 scaling when $\ln(T/\mu) \gtrsim -6.09$. Such behavior is practi-

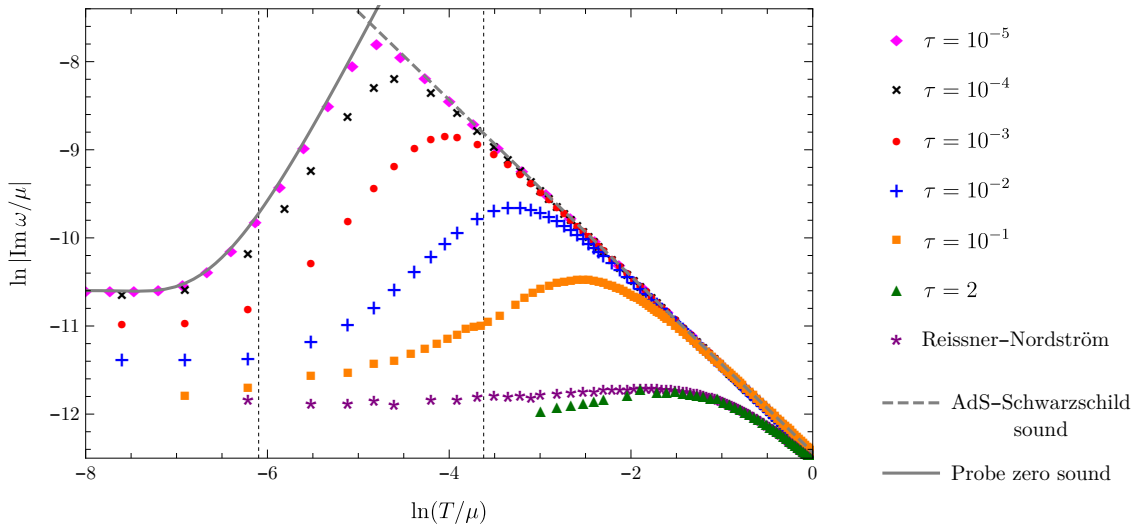

Figure 5.12: Our numerical results for $\ln|\mathrm{Im}\,(\omega/\mu)|$ versus $\ln(T/\mu)$ for $k/\mu = 10^{-2}$, $\tilde{\alpha} = 1$, and $\tau = 10^{-5}$ (pink diamonds), 10^{-4} (black crosses), 10^{-3} (red dots), 10^{-2} (blue plus signs), 10^{-1} (orange squares), and 2 (green triangles), as well as the AdS-RN result (purple stars). The solid gray line is the numerical result in the probe limit, while the dashed gray line comes from $\mathrm{Im}\,(\omega) = -\Gamma k^2$ with the $d = 3$ AdS-SCH value $\Gamma = 1/(8\pi T)$ (dashed gray). The vertical dashed black lines indicate the LFL definitions of the boundaries between quantum and thermal collisionless regimes, $\ln(T/\mu) \approx -6.09$, and between thermal collisionless and hydrodynamic regimes, $\ln(T/\mu) \approx -3.62$. For $\ln(T/\mu) \lesssim -6.09$, all cases exhibit $|\mathrm{Im}\,(\omega)| \propto T^0$, similar to the LFL quantum collisionless regime. For $\ln(T/\mu) \gtrsim -6.09$, $|\mathrm{Im}\,(\omega)|$ exhibits scaling with a power of T that decreases as τ increases, from T^2 down to, but not exactly to, T^0. As $\ln(T/\mu)$ increases, in all cases such scaling eventually ends in a maximum, followed by $|\mathrm{Im}\,(\omega)| \propto T^{-1}$, as expected for a CFT in the hydrodynamic regime. As τ increases the maximum's position moves beyond the LFL value, $\ln(T/\mu) \approx -3.62$, and its height decreases. Nevertheless, all cases have a maximum, so the LFL definition of the crossover is viable.

cally identical to a LFL. However, as T/μ increases the sound attenuation exhibits a maximum and transitions to the T^{-1} scaling of a CFT in the hydrodynamic regime. Such behavior is not possible in the probe limit. Moreover, the maximum occurs at $\ln(T/\mu) \approx -4.75 < -3.62$, in contrast to a LFL.

Fig. 5.12 also shows that the quantum collisionless type scaling T^0 for $\ln(T/\mu) \lesssim -6.09$ persists to higher τ. In contrast, for $\ln(T/\mu) \gtrsim -6.09$, the power of T clearly decreases as τ increases, from T^2 down to, but not exactly to, T^0. At sufficiently high T/μ the CFT hydrodynamic scaling T^{-1} always emerges, hence a maximum appears

in all cases, including AdS-RN. However, as τ increases the maximum's position drifts to higher and higher $\ln(T/\mu)$, blithely moving past the LFL value $\ln(T/\mu) \approx -3.62$.

Additionally, as τ increases the maximum's height decreases. As discussed in Section 5.1.2, such a result is perhaps surprising, if we recall that τ effectively counts the number of charged fields (such as quark flavors), so that naïvely we would expect that increasing τ would cause $\ln|\mathrm{Im}(\omega/\mu)|$ to increase, i.e. that increasing τ would *dampen* sound. Instead we find the opposite: in our holographic model, sound becomes *less* damped as we increase τ.

In any case, our results suggest that with $k/\mu = 10^{-2}$ and $\tilde{\alpha} = 1$, for all τ a maximum always appears in $|\mathrm{Im}(\omega)|$, and hence the LFL definition of crossover is viable. *Indeed, the shape of all our sound attenuation curves is qualitatively similar to that of a LFL in Fig. 5.1.*

We now consider a key numerical result of refs. [181, 212]: in AdS-RN, for ω and k sufficiently small compared to μ, the hydrodynamic form of the sound attenuation constant (Eq. (5.29) with $d = 3$), $\Gamma = \frac{1}{2}\frac{\eta}{\varepsilon+P}$, is valid not just in the hydrodynamic regime, but for all T/μ, down to and including $T/\mu = 0$. To check whether the same is true in our model, we fit our numerical results for the sound pole's $|\mathrm{Im}(\omega)|$ to a form $\Gamma k^2 + \delta k^4$ over a range of small k/μ, with fit parameters Γ and δ. Fig. 5.13 shows the resulting $\ln(\mu\Gamma)$ versus $\ln(T/\mu)$, for $k/\mu = 10^{-2}$ and increasing τ from $\tau = 10^{-5}$ (pink diamonds) to $\tau = 2$ (green triangles). Fig. 5.13 also shows the corresponding value of Γ's hydrodynamic form for each τ (dotted lines). The hydrodynamic form indeed agrees precisely with our numerical results for all τ and T/μ. In short, our results agree with and extend those of refs. [181, 212]: for charged black branes in Einstein-DBI theory, as for AdS-RN, the hydrodynamic form $\Gamma = \frac{1}{2}\frac{\eta}{\varepsilon+P}$ is in fact valid for all T/μ.

In hydrodynamics the shear diffusion constant is also $\propto \eta/(\varepsilon + P)$. A key result of ref. [210] for the Einstein-DBI charged black brane is that the numerical results for the shear diffusion constant also agree with the hydrodynamic form for all τ and T/μ.

Our model, like all rotationally-invariant holographic models dual to Einstein gravity, has $\eta = s/(4\pi)$ [8, 10, 11], so the hydrodynamic form $\Gamma = \frac{1}{2}\frac{\eta}{\varepsilon+P}$ is in fact completely determined by thermodynamics. We can eliminate s from Γ using $\eta = s/(4\pi)$,

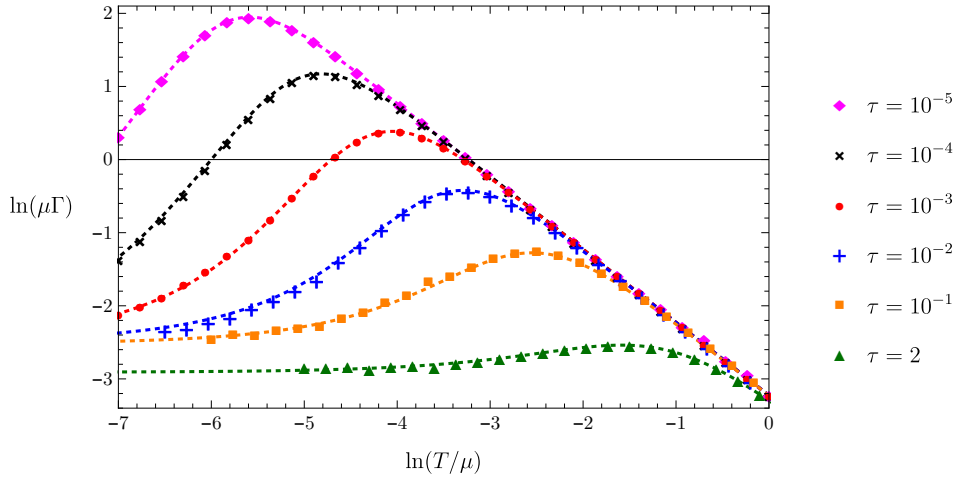

Figure 5.13: Our numerical results for $\ln(\mu\Gamma)$ versus $\ln(T/\mu)$ for $k/\mu = 10^{-2}$, $\tilde{\alpha} = 1$, and $\tau = 10^{-5}$ (pink diamonds), 10^{-4} (black crosses), 10^{-3} (red dots), 10^{-2} (blue plus signs), 10^{-1} (orange squares), and 2 (green triangles). We obtain Γ by numerically fitting $-\Gamma k^2 + \delta k^4$ to the sound pole's $\mathrm{Im}(\omega)$ over a range of small k/μ. The dashed lines show the corresponding results using the hydrodynamic form of Eq. (5.29) with $d = 3$, namely $\Gamma = \frac{1}{2}\frac{\eta}{\varepsilon+P}$. Clearly our numerical results for Γ agree with the hydrodynamic form for all τ and T/μ.

$\varepsilon + P = sT + \mu\langle J^t\rangle$, and as mentioned below Eq. (5.13), $\langle J^t\rangle = \tau\tilde{\alpha}^2 Q\, s/(2\pi)$, giving[8]

$$\Gamma = \frac{1}{2}\frac{\eta}{\varepsilon + P} = \frac{1}{8\pi T + 4\mu\,\tau\tilde{\alpha}^2\, Q}. \tag{5.33}$$

This form of Γ makes clear that the probe limit, $\tau \to 0$ with $\tilde{\alpha}$ and T/μ fixed, gives the AdS-SCH result $\Gamma = 1/(8\pi T)$, and that the extremal limit, $T/\mu \to 0$ with τ and $\tilde{\alpha}$ fixed, gives $\Gamma \to (4\mu\tau\tilde{\alpha}^2 Q_{\text{ext}})^{-1} \neq 0$.

From Eq. (5.33) we can deduce that the quantity $\tilde{\alpha}\,\mu\,\Gamma$ is scaling-invariant. In particular, fixing τ and changing $\tilde{\alpha}$ does not change the form of Γ as a function of T/μ, but rather just acts as a re-scaling. To see this, we normalise Γ by the scaling-invariant product $\tilde{\alpha}\mu$ and observe from Eq. (5.10) that $T/\tilde{\alpha}\mu$ is a function only of the scaling-invariant quantities τ and $\tilde{\alpha}\,Q$,

$$\tilde{\alpha}\,\mu\,\Gamma = \left(8\pi\frac{1}{\tilde{\alpha}}\frac{T}{\mu} + 4\tau\,\tilde{\alpha}Q\right)^{-1}, \qquad \frac{1}{\tilde{\alpha}}\frac{T}{\mu} = \frac{3 + \tau\left(1 - \sqrt{1+\tilde{\alpha}^2Q^2}\right)}{4\pi\,\tilde{\alpha}Q\;{}_2F_1\left(\frac{1}{2},\frac{1}{4};\frac{5}{4};-\tilde{\alpha}^2Q^2\right)}, \tag{5.34}$$

[8]For the remainder of the section we restore factors of $\tilde{\alpha}$ in all of our expressions.

which makes clear that $\tilde{\alpha}\,\mu\,\Gamma$ is scaling-invariant itself. Ideally we would invert Eq. (5.34) to find $\tilde{\alpha}\,Q$ as a function of τ and $T/\tilde{\alpha}\mu$, but that is impossible to do in full generality, due to the hypergeometric function in the denominator on the right-hand side. However, we can invert Eq. (5.34) in certain limits. For example, suppose τ is small, such that we can take $\tau = 0$ on the right-hand side of Eq. (5.34). Suppose we then take $T/\mu \ll 1$, which in $T/\tilde{\alpha}\mu$ with $\tau = 0$ means $Q \to \infty$. Expanding the hypergeometric function at large argument and solving for Q then gives

$$Q = \tilde{\alpha}\left(\frac{3}{\sqrt{\pi}\,\Gamma\left(\frac{1}{4}\right)^2}\right)^2\left(\frac{\mu}{T}\right)^2 + \mathcal{O}\left(\frac{\mu}{T}\right). \tag{5.35}$$

Dropping all sub-leading terms from Eq. (5.35) and inserting the result into Eq. (5.34) gives

$$\mu\Gamma = \left(\frac{8\pi T}{\mu} + \frac{36\,\tau\,\tilde{\alpha}^3}{\pi\,\Gamma\left(\frac{1}{4}\right)^4}\left(\frac{\mu}{T}\right)^2\right)^{-1}. \tag{5.36}$$

The approximations leading to Eq. (5.36) are brutal. For example, when $T/\mu \ll 1$ the $\mathcal{O}\left(\frac{\mu}{T}\right)$ term in Eq. (5.35) is *larger* than the T/μ term in Eq. (5.34) and hence should not be dropped. Indeed, Eq. (5.36) fails to capture key features of the actual result, for instance, when $T/\mu \to 0$ Eq. (5.36) gives $\mu\Gamma \to 0$, while the actual limit is non-zero. Eq. (5.36) nevertheless provides a surprisingly good approximation to certain features. In particular, Eq. (5.36) manifestly describes a transition in $\mu\Gamma$'s scaling from T^2 to T^{-1}, as expected at small τ, and has a maximum whose position $(T/\mu)_{\text{max}}$ is given by

$$(T/\mu)^3_{\text{max}} = \frac{9\,\tilde{\alpha}^3\tau}{\pi^2\Gamma\left(\frac{1}{4}\right)^4} \qquad \mu\Gamma_{\text{max}} = \frac{1}{12\pi}\frac{1}{(T/\mu)_{\text{max}}}. \tag{5.37}$$

Remarkably, Eq. (5.37) describes the actual $(T/\mu)_{\text{max}}$ extremely well—even *away* from small τ. In fact, Eq. (5.37) agrees with our numerical results for $(T/\mu)_{\text{max}}$ for all values of τ and $\tilde{\alpha}$ that we have checked! However, Eqs. (5.36) and (5.37) do not provide a good approximation to the *height* of the maximum, i.e. the *value* of $\mu\Gamma_{\text{max}}$ at $(T/\mu)_{\text{max}}$, and indeed the approximation to the height grows worse as τ increases. For example, when $\tilde{\alpha} = 1$ and $\tau = 10^{-5}$, Eqs. (5.36) and (5.37) suggest a maximum value $\ln(\mu\Gamma_{\text{max}}) \approx 1.96$, very close to the actual value in Fig. 5.13 (pink diamonds),

but when $\tau = 2$ they suggest a maximum value $\ln(\mu\Gamma_{\rm max}) \approx -2.11$, while the actual value in Fig. 5.13 (green triangles) is close to -3.[9]

In summary, we have three main results for sound attenuation. First is that fixing $\tilde{\alpha}$ and increasing τ preserves the T^0 and T^{-1} scalings at low and high T/μ, respectively, but suppresses the T^2 scaling at intermediate T/μ to a lower (but non-zero) power. Second is that both the full $\mathrm{Im}(\omega)$ and Γ are similar in form to that of a LFL for all τ and $\tilde{\alpha}$ we accessed, including in particular a maximum that can provide a definition for the crossover. Third is that Γ assumes the hydrodynamic form, $\Gamma = \frac{1}{2}\frac{\eta}{\varepsilon+P}$, for all τ, $\tilde{\alpha}$, and T/μ we accessed, which provided us with an excellent approximation for the location of the maximum, Eq. (5.37).

This third result is similar to phenomena observed in other backreacted models, including AdS-RN [181, 211, 212]. The proposal of refs. [181, 211, 212] was therefore that hydrodynamics remains reliable even for energies $\gg T/\mu$, outside the usual hydrodynamic regime, as long as $k \ll \mu$ or T. In other words, in several holographic models hydrodynamics appears to remain reliable at distances shorter than a mean free path $\propto 1/T$ at high T/μ but $\propto 1/\mu$ at low T/μ.

However, our model appears to provide counter-examples, because hydrodynamics predicts a charge diffusion pole, but in some cases we find no such pole at low T/μ. Specifically as en example, see the case in Figs. 5.3 and 5.6, where at low T/μ we find HZS and two relativistic poles, rather than a charge diffusion pole.

5.4 Discussion and outlook

For the large-N_c, strongly-coupled CFT states with non-zero T and μ holographically dual to the Einstein-DBI charged black brane we studied how the poles of G_{tt} and G_J, the associated spectral functions, and the sound dispersion evolved with increasing T/μ, and how that evolution depended on the backreaction parameter τ. We found that the probe limit definition of crossover, as a collision of HZS poles on the imaginary ω/μ axis,

[9] As a side comment, Einstein-DBI charged black brane solutions are known for any value of the CFT spacetime dimension d [189, 204–206]. The fact that Γ takes the hydrodynamic form at all T/μ persists to all d, then using the results for the thermodynamics for arbitrary d, and repeating the approximations leading to Eq. (5.36), gives a transition from T^{d-1} to T^{-1}. Apparently in Einstein-DBI models the T^2 scaling similar to the LFL thermal collisionless regime may be unique to $d = 3$.

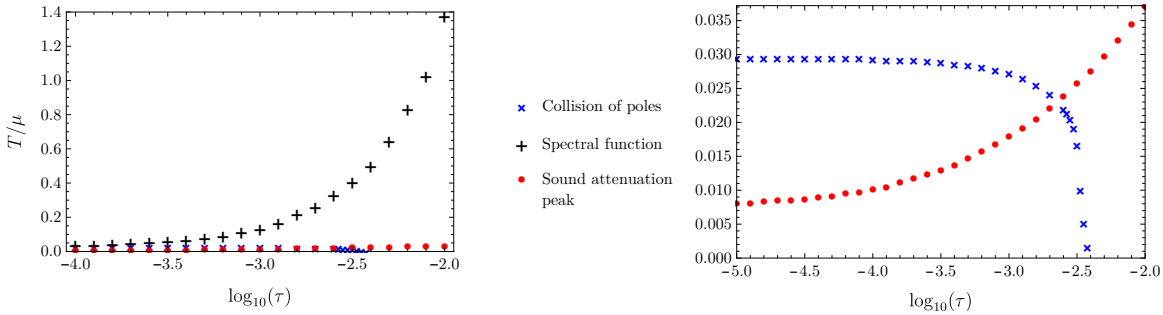

(a) Comparison of crossover definitions.

(b) Close-up of (a)

Figure 5.14: Our numerical results for the crossover value of T/μ as a function of $\log_{10}(\tau)$, for fixed $\tilde{\alpha} = 1$, using the three different definitions: the probe limit definition, via a collision of poles that produces the charge diffusion pole (black plus signs), the AdS-RN definition, via a transfer of dominance from sound to charge diffusion peak in ρ_J (blue crosses), and the LFL definition, via the sound attenuation maximum (red dots).

producing the charge diffusion pole, was viable only for sufficiently small τ. The AdS-RN definition of crossover, as a transfer in dominance from sound to charge diffusion peaks in ρ_J, was viable only for sufficiently larges τ. However, outside of the probe limit, the LFL definition of the crossover, as a maximum in the sound attenuation, was always viable. Moreover, the sound attenuation constant, Γ, took the hydrodynamic form, even outside the usual hydrodynamic regime, and hence in these holographic models was completely determined by thermodynamics.

Fig. 5.14 summarises our numerical results for the crossover value of T/μ as a function of $\log_{10}(\tau)$, for fixed $\tilde{\alpha} = 1$, using the three different definitions: the probe limit definition (black plus signs), the AdS-RN definition (blue crosses), and the LFL definition (red dots). The AdS-RN definition gives crossover T/μ larger than the others by about an order of magnitude. The AdS-RN and LFL definitions both appear to increase without bound as τ increases, while the probe limit definition instead decreases, eventually dropping to zero at the critical τ value when $\tau \approx 3.2 \times 10^{-3}$ or equivalently $\log_{10}(\tau) \approx -2.49$.

Low-temperature sound modes have been relatively under-explored in holography, especially outside of the probe limit. However, our results, combined with the accumulated body of evidence about low-temperature sound modes in holography, raise many

questions relevant to many strongly-coupled systems, and worthy of future research. In our model, one immediate task would be to attempt analytic, rather than numerical, calculations of the leading powers of k in the imaginary parts of correlators at exactly $T/\mu = 0$. We expect that, as in the backreacted models of refs. [165,212], these will be fixed by dimensions of operators in the $(0+1)$-dimensional CFT dual to the near-horizon AdS_2.

The primary task at hand is simply to continue searching for low-temperature sound modes in holographic quantum compressible matter. In what cases does HZS appear? Is it universal? If not, then what distinguishes systems with HZS from those without? To date, HZS has appeared in systems with and without extensive entropy at $T/\mu = 0$, with heat capacity scaling as various powers of T, etc. Indeed, so far only two patterns have emerged. First, HZS appears in systems with some form of non-linearity. In particular, a probe Maxwell action does not produce HZS. To obtain HZS we must introduce non-linearities, either by replacing the probe Maxwell action with the probe DBI action, or by allowing the Maxwell action to backreact, so that we must solve the Einstein equation, which is non-linear. Second, HZS appears in systems with non-zero spectral weight at $\omega = 0$ over a finite range of k, up to a characteristic value of k, in a fashion reminiscent of a Fermi-Dirac distribution [6]. Are these patterns universal? Moreover, when HZS does appear, how does it evolve in the crossover to hydrodynamics? Of course, the over-arching question is what lessons HZS may teach us about real strongly-coupled systems. Do real quantum compressible systems and non-Fermi liquids, such as graphene, the cuprates, the heavy fermion compounds, etc., support sound modes? Recent evidence suggests that in LFLs in two spatial dimensions described by kinetic theory, both zero sound and hydrodynamic sound are replaced by plasmons [225, 226]. However, the most important question remains: what types of effective theories give rise to low-temperature sound modes, and what do those sound modes, and their crossover to hydrodynamic sound, tell us about the underlying degrees of freedom?

Chapter 6

Holographic Entanglement Density

In this chapter we introduce a new quantity which we call "entanglement density" (ED), defined as the change in EE with respect to the vacuum EE, divided by the sub-region's volume. After reviewing its most important properties, we study the ED in several holographic systems, which can all be described by a general metric, as shown in Section 6.3. We study the ED in CFTs in the presence of RG flows (Section 6.3.1), temperature T (Section 6.3.2) and chemical potential μ (Section 6.3.3). We link the asymptotic behaviour of the ED to the violation of the "area theorem" and the emergence of long-range entanglement.

6.1 Introduction and motivation

A central goal of physics is to characterise and classify states of matter. At temperatures T low enough that quantum effects determine the properties of matter, the goal is to characterise and classify patterns of quantum entanglement. A growing body of evidence suggests that EE between a sub-region and the rest of the system, and specifically EE's dependence on the sub-region's size L (the radius of a sphere, for example), can play a central role in reaching that goal. For example, in d spacetime dimensions, EE receives characteristic contributions $\propto \ln L^{d-2}$ from a Goldstone boson [227], $\propto L^{d-2} \ln L$ from a Fermi surface [228–231], or independent of L from topologically-ordered degrees of freedom [232–235]. We define an "entanglement density" (ED)[1], and explore the extent to which it characterises the deformed CFTs mentioned above. Specifically, given

[1] Our ED should not be confused with the entanglement density of refs. [236, 237], defined as a second variation of EE under infinitesimal changes to the sub-region's boundary.

the EE of the deformed CFT, S_{ent}, the EE of the undeformed CFT's vacuum state, S_{CFT}, and the volume of the entangling region, V, we defined the entanglement density as

$$\sigma \equiv \frac{S_{\text{ent}} - S_{\text{CFT}}}{V}. \tag{6.1}$$

In continuum QFTs, S_{ent} generically has short-distance divergences from large correlations across the entangling surface (the sub-region's boundary). We regulate these with an UV cutoff, ε. For our deformed CFTs, these divergences are identical to those of the parent CFT, hence the subtraction $S_{\text{ent}} - S_{\text{CFT}}$ renders σ finite and cutoff-independent, and therefore physically meaningful.

Of course, we could remove the divergences in other ways, for instance by adding counterterms [238–240], and we could divide by other quantities intrinsic to the entangling surface besides V, such as surface area, A. However, our definition of ED is motivated by the so-called "entanglement temperature", T_{ent} [241, 242], defined as the ratio between a small change in the energy $\Delta E = V\langle T_{tt}\rangle$ inside the entangling region and the associate change in EE ΔS_{ent} that it generates, namely

$$\Delta E/\Delta S_{\text{ent}} \equiv T_{\text{ent}} \propto \frac{1}{L}. \tag{6.2}$$

This is known as the First Law of EE (FLEE) in analogy with the first law of thermodynamics $\Delta E = \Delta S_{\text{th}}\, T$. For states with constant $\langle T_{tt}\rangle$, and for sufficiently small L this implies that

$$\lim_{L\to 0} \sigma = \langle T_{tt}\rangle\, T_{\text{ent}}^{-1} \propto \langle T_{tt}\rangle L. \tag{6.3}$$

However, our σ generalises T_{ent}^{-1} for any L, not just for small L and for any change of energy, including zero change. This will be specifically important in the case of RG flows, where $\langle T_{tt}\rangle = 0$ and T_{ent}^{-1} is ill defined. In that case, since FLEE does not apply, we have that σ's small-L behavior is determined by the dimension Δ of the perturbing operator. Our goal is to use σ's dependence on L to characterise the deformed CFTs and extract some general properties about them.

As $L \to \infty$ relative to any other scale, the leading behavior of the EE is

$$S_{\text{ent}} = s\, V + \alpha\, A + \dots, \tag{6.4}$$

where s is the thermodynamic entropy density ($s = 0$ in some of our examples), α is a dimensionfull constant that makes the, and ... represents terms sub-leading in $1/L$ relative to those shown.

The leading "volume law" term $\propto V$ in Eq. (6.4) is expected for excited states, such as thermal states. In such cases, intuitively when $L \to \infty$ the sub-region becomes the entire system, and the sub-region's reduced density matrix becomes the total density matrix, which for a thermal state implies $S_{\rm ent} \to S_{\rm th} = sV$.

The sub-leading contribution $\propto A$ in Eq. (6.4) is the well-known "area law" term [76–79]. For a sphere of radius L, $A = \Omega_{d-2} L^{d-2}$, and in the vacuum of a CFT, the only other scale is the UV cutoff, ε, so that $\alpha \propto 1/\varepsilon^{d-2}$ by dimensional analysis. For a strip of width L, $A = 2L_\perp^{d-2}$, and in the vacuum of a CFT, two other scales are available, ε and L. Indeed, in that case α is a sum of two terms, one $\propto 1/\varepsilon^{d-2}$ and the other $\propto 1/L^{d-2}$ [82, 83]. If the CFT is deformed, then new terms appear related to any new scales, such as T and μ. Some deformations can also produce in $S_{\rm ent}$ a term $\propto A \ln A$, such as μ in a free fermion CFT, producing a Fermi surface [228–231], as mentioned above. For discussions about the conditions under which such "area law violation" can occur, see for example ref. [243].

Crucially, for Lorentz-invariant RG flows to a d-dimensional CFT in the IR, α obeys a kind of (weak) c-theorem, called the "area theorem" [22, 23]: the value of α in the UV CFT, $\alpha_{\rm UV}$, must be greater than or equal to that of the IR CFT, $\alpha_{\rm IR}$.

$$\alpha_{\rm UV} \geq \alpha_{\rm IR} \tag{6.5}$$

Of course, as mentioned above both $\alpha_{\rm UV}$ and $\alpha_{\rm IR}$ include a term $\propto 1/\varepsilon^{d-2}$, and hence diverge as $\varepsilon \to 0$. However, these terms $\propto 1/\varepsilon^{d-2}$ cancel in the difference $\Delta\alpha \equiv \alpha_{\rm UV} - \alpha_{\rm IR}$, so the meaningful statement of the area theorem is $\Delta\alpha \geq 0$. To be precise, the area theorem has been proven for a sphere in $d = 3$ using strong sub-additivity [22] and for a sphere in $d \geq 3$ using positivity of relative entropy [23].[2] Roughly speaking, strong sub-additivity is holographically dual to the Null Energy Condition (NEC) [245, 246]. All of our holographic examples will obey the NEC.

[2]For the strip, a similar, but distinct, theorem for the coefficient of an area term appears in refs. [83, 244].

Whenever a quantity is proven to decrease monotonically along an RG flow, a number of questions naturally arise. For example, does the quantity count degrees of freedom in any precise sense? Does the monotonicity extend to other types of deformations, such as T, μ, operators or sources that break Lorentz invariance, etc. [247]? We will answer some of these questions for $\Delta\alpha$, in holographic systems, using our σ. In particular, Eq. (6.4) implies that when $L \to \infty$ relative to all other scales, σ's leading behavior is

$$\lim_{L\to\infty} \sigma = s - \Delta\alpha \, \frac{A}{V} + \dots , \tag{6.6}$$

where the difference $\Delta\alpha = \alpha_{\rm UV} - \alpha_{\rm IR}$ appears because in Eq. (6.1) we subtract the UV CFT vacuum contribution, $S_{\rm ent} - S_{\rm CFT}$.

Eq. (6.6) shows how we can easily extract the sign of $\Delta\alpha$ from σ's large-L behavior: as $L \to \infty$, if σ approaches s from below ($\sigma \to s^-$) then $\Delta\alpha > 0$, while if σ approaches s from above ($\sigma \to s^+$) then $\Delta\alpha < 0$. The sign of $\Delta\alpha$ will therefore be immediately obvious to the naked eye, as our examples will illustrate. Dividing by V in Eq. (6.1) is thus technically trivial but practically useful: otherwise, to obtain $\Delta\alpha$'s sign we would have to extract (typically by numerical fitting) a subtle correction in $1/L$ from the EE itself.

Currently, holographic techniques are our only way to get insight into the entanglement structure of CFTs in higher dimensions and for excited states. As we reviewed in Section 3.3, in the dual geometry, $S_{\rm ent}$ is given by the area of the minimal surface in the bulk, that shares the boundary with the entangling region of the field theory, located at the asymptotic AdS_{d+1} boundary. This turns the calculation of EE into a well defined variational problem of finding the area of a static "soap bubble" in the dual geometry. However, all the discussion in this section applies in general for any QFT, not only holographic ones, and therefore we expect σ to be a well-defined quantity that can be used to characterise general states of matter in which the dependence of $S_{\rm ent}$ with the size of the entangling region L, could be computed by other means.

6.2 Summary of results

Table 6.1 summarises our main results and will be a useful reference throughout the discussion in this section.

Section	System	Deformation(s)	FLEE?	Area Theorem Violation?
6.3.1	$(d=4)$ RG Flows	$\mathcal{O}$	No	No
6.3.2	$(d+1)$ AdS-SCH	T	Yes	Yes, for $d > d_{\text{crit}}$
6.3.3	$(d+1)$ AdS-RN	T, μ	Yes	Yes, for low T or $d > d_{\text{crit}}$

Table 6.1: Summary of our main results.

In Section 6.3.1 we consider Lorentz-invariant RG flows, described holographically by gravity coupled to a single real scalar field with self-interaction potential designed to produce an RG flow or "domain wall" solution interpolating between an AdS_{d+1} near the boundary and another AdS_{d+1} deep in the bulk [248]. Lorentz invariance implies $\langle T_{\mu\nu}\rangle = 0$ and $s = 0$. We mostly focus on $d = 4$, and consider flows driven either by a source for the relevant scalar operator $\mathcal{O}$ dual to the bulk scalar field, or driven by $\langle\mathcal{O}\rangle \neq 0$ with zero source. As mentioned above, the FLEE does not apply in these cases, and $\mathcal{O}$'s dimension Δ controls the leading power of L in σ at small L. We find that $\sigma < 0$ for all L, and in particular $\sigma \to 0^-$ as $L \to \infty$, as required by the area theorem. To connect the small- and large-L limits, σ must have one or more minima as a function of L. We show how various scalar potentials, all consistent with the NEC, can produce various behaviors in σ at intermediate L, such as multiple minima or a discontinuous first derivative. We thus learn that, although universal principles such as the area theorem may govern σ's asymptotics, no universality is immediately obvious at intermediate L. We expect similar results for other d.

In Section 6.3.2 we consider the AdS-SCH black brane, dual to a translationally and rotationally invariant state of a holographic CFT deformed by T. In this case, the FLEE requires $\sigma \propto \langle T_{tt}\rangle L$ at small L. Section 6.3.2's main result is the existence of a critical dimension, $d_{\text{crit}} \approx 6.7$, such that if $d < d_{\text{crit}}$ then as L increases σ rises monotonically, and $\sigma \to s^-$ as $L \to \infty$, so that $\Delta\alpha > 0$, consistent with the area theorem. However, if $d > d_{\text{crit}}$ then σ increases to a single global maximum, which by dimensional analysis is at an $L \propto 1/T$, and then $\sigma \to s^+$ as $L \to \infty$, so that $\Delta\alpha < 0$,

violating the area theorem. Fig. 6.1 depicts these two behaviors schematically. (These results have also been obtained using the *exact* results for EE of a strip in AdS-SCH, *i.e.* without numerics, in ref. [249].) More generally, for any CFT excited state in which the FLEE applies and $s \neq 0$, these are the two simplest ways to connect $\sigma \propto \langle T_{tt} \rangle L$ at small L to $\sigma \to s^{\pm}$ at large L.

In Section 6.3.3 we consider an AdS-RN charged black brane, dual to a translationally and rotationally invariant state of a holographic CFT deformed by T and μ [250]. When $T/\mu \to \infty$, so that μ is negligible, AdS-RN approaches AdS-SCH, and we recover the results of Section 6.3.2, including in particular the existence of d_{crit}. However, when $T/\mu \to 0$, so that T is negligible, AdS-RN is dual to a "semi-local quantum liquid" state [201], which at $T/\mu = 0$ has a mysterious extensive ground state entropy $s \neq 0$. If $d > d_{\text{crit}}$ then for all T/μ, σ resembles the upper curve in Fig. 6.1, with a single maximum, whose position changes as T/μ decreases, and $\sigma \to s^{+}$ as $L \to \infty$. In particular, when $d > d_{\text{crit}}$ the area theorem is always violated. On the other hand, if $d < d_{\text{crit}}$, then at high T/μ we recover the result of Section 6.3.2, where σ resembles the lower curve in Fig. 6.1. However, as we lower T/μ, a transition occurs at a critical value of T/μ from the lower curve in Fig. 6.1 to the upper curve, *i.e.* a peak appears. In particular, at the critical T/μ, $\Delta\alpha$ changes sign and the area theorem is violated. In short, for any d, at sufficiently low T/μ, σ resembles the upper curve in Fig. 6.1, with a single maximum, $\sigma \to s^{+}$ as $L \to \infty$, and area theorem violation. This can also be linked to the emergence of *long-range entanglement* with a characteristic scale given by the position of the global maxima in

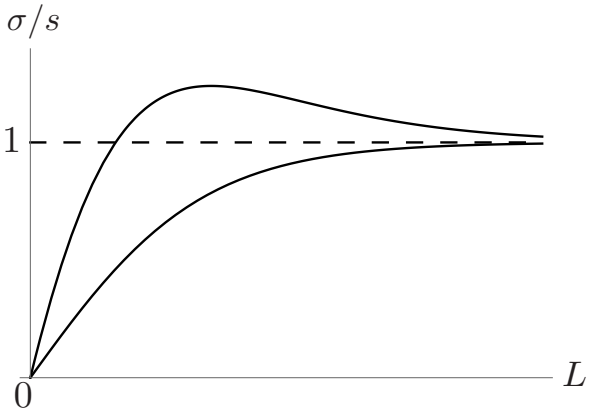

Figure 6.1: For a CFT excited state in which the FLEE applies and $s \neq 0$, we schematically depict the two simplest possibile behaviors of σ, in units of s, versus L, in arbitrary units. The FLEE implies $\sigma \propto L$ at small L. As $L \to \infty$, either $\sigma \to s^{-}$ (lower curve), consistent with the area theorem, or $\sigma \to s^{+}$ (upper curve), violating the area theorem. The latter case necessarily has at least one maximum, as shown.

σ where the EE per unit volume is maximal. This scale also provides us with a clear distinction between the UV and the IR, both in field theory and in the dual geometry.

In summary, we find area theorem violation in AdS-SCH at large d and AdS-RN at low T/μ. What do these all have in common? One obvious answer is: an IR fixed point that is not a d-dimensional CFT like the UV fixed point. In particular, the solutions describe $(0+1)$-dimensional IR fixed points, meaning invariance under rescaling of t but not $\vec{x}$ [201,251–253]. More precisely, in AdS-SCH when $d \to \infty$, in the near-horizon region t and the holographic radial coordinate, z, form the $SL(2,\mathbb{R})/U(1)$ group manifold, while $\vec{x}$ forms $\mathbb{R}^{d-1}$ [253]. In AdS-RN at $T/\mu = 0$, in the near-horizon region t and z form AdS_2 while the $\vec{x}$ form $\mathbb{R}^{d-1}$. As a result, in each near-horizon region, linearised fluctuations of fields transform covariantly under rescalings that act on t but not $\vec{x}$ [252,253]. Strictly speaking, such non-relativistic scale invariance occurs only for $d = \infty$ and $T/\mu = 0$. However, in our examples area theorem violation occurs at *intermediate values* of these parameters, as we dial them towards the limits while the non-relativistic scale invariance is not yet exact, and hence signals the emergence of non-relativistic massless degrees of freedom.

6.3 General analysis

In our examples we can use the symmetries of translations in t and translations and rotations in $\vec{x}$ to write the bulk metric in the form

$$ds^2 = \frac{R^2}{z^2}\left(-f(z)dt^2 + d\vec{x}^2 + \frac{dz^2}{g(z)}\right), \tag{6.7}$$

with the following near boundary expansion,

$$f(z) = 1 - mz^d + \ldots, \qquad g(z) = 1 - mz^d + \ldots, \tag{6.8}$$

which using Eq. (3.11) determines the dual theory's energy density to be

$$\langle T_{tt}\rangle = \frac{(d-1)R^{d-1}}{16\pi G_N}\, m. \tag{6.9}$$

The AdS_{d+1} metric has $f(z) = 1$ and $g(z) = 1$, so in particular $m = 0$ and hence $\langle T_{tt}\rangle = 0$, as expected for a CFT vacuum state. As z increases, *i.e.* as we move away

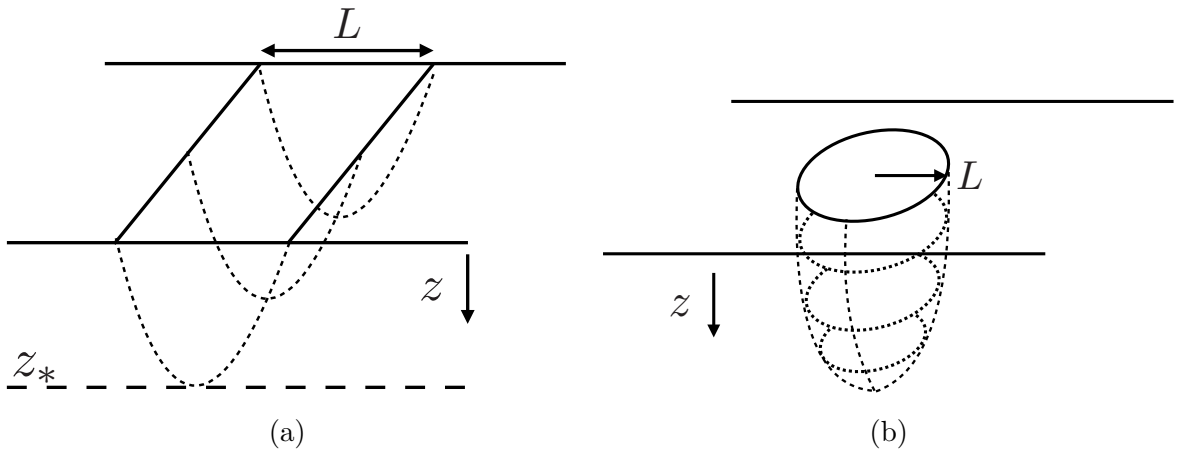

(a) (b)

Figure 6.2: (a) Schematic depiction of the minimal surface for a strip sub-region of width L. The asymptotically AdS_{d+1} boundary is at $z \to 0$. The minimal surface, depicted by the dashed lines, "hangs down" from the strip at the boundary to a maximal z value, z_*. (b) Similar schematic depiction of the minimal surface for a sphere sub-region of radius L.

from the boundary and into the bulk, the metric may approach that of another AdS_{d+1}, generically with different R (Section 6.3.1) or a horizon, where $f(z_H) = 0$. In the case of a non-extremal horizon, the dual field theory's temperature and entropy density for the metric in Eq. (6.7) are determined by

$$T = \frac{\sqrt{f'(z_H)g'(z_H)}}{4\pi}, \qquad s = \frac{R^{d-1}}{4G_N}\frac{1}{z_H^{d-1}}, \tag{6.10}$$

All our examples conform to the above, with the following exceptions. In the Lorents-invariant RG flows of Section 6.3.1, in $f(z) = 0$ and $g(z)$'s expansions the leading power of z depends on Δ, and in some cases can be smaller than z^d.

The strip's entangling surface consists of two infinite parallel planes of spatial co-dimension one, *i.e.* two copies of $\mathbb{R}^{d-2}$, separated by a distance L in the remaining spatial direction, x. As is well-known [82, 83], using the translational and rotational symmetry of $\mathbb{R}^{d-2}$ we can parametrise the minimal surface as $x(z)$, and for metrics of the form in Eq. (6.7), the area of the minimal surface Σ^{strip} depends only on $x'(z)^2$, leading to a first integral of motion. We can then solve for $x'(z)$ in terms of the first integral. The minimal surfaces "hang down" into the bulk to a largest z value, z_*, the turn-around point where $x'(z)$ diverges, as depicted in Fig. 6.2a. We then obtain L by

integrating $x'(z)$ from z_* to the boundary,

$$L = 2\int_0^{z_*} dz\, \frac{z^{d-1}}{z_*^{d-1}} \frac{1}{\sqrt{1-(z/z_*)^{2(d-1)}}} \frac{1}{\sqrt{g(z)}}, \tag{6.11}$$

where the overall factor of 2 appears because the solutions are invariant under the reflection $x(z) \to -x(z)$. The corresponding minimal area is

$$\Sigma_{\rm min}^{\rm strip} = R^{d-1}\, 2L_\perp^{d-2} \int_\varepsilon^{z_*} \frac{dz}{z^{d-1}} \frac{1}{\sqrt{1-(z/z_*)^{2(d-1)}}} \frac{1}{\sqrt{g(z)}}, \tag{6.12}$$

where the lower endpoint is a cutoff, $z = \varepsilon$, holographically dual to a UV cutoff. For AdS_{d+1}, where $g(z) = 1$, we can perform the integrals in Eqs. (6.11) and (6.12) exactly, leading to

$$L = 2\sqrt{\pi}\frac{\Gamma\left[\frac{d}{2(d-1)}\right]}{\Gamma\left[\frac{1}{2(d-1)}\right]} z_* \equiv \vartheta_{(0)} z_*. \tag{6.13a}$$

$$S_{\rm CFT}^{\rm strip} = \frac{R^{d-1}}{4G_N}\left[\frac{1}{(d-2)}\frac{A}{\varepsilon^{d-2}} - \frac{\vartheta_{(0)}^{d-1}}{2(d-2)}\frac{A}{L^{d-2}}\right]. \tag{6.13b}$$

which will greatly simplify the notation. In Eq. (6.13b) we see the form described below Eq. (6.4): an area law with $A = 2L_\perp^{d-2}$, where α is a sum of two terms, one $\propto 1/\varepsilon^{d-2}$ and the other $\propto 1/L^{d-2}$. At this stage we find useful to define the following parameter

$$\vartheta_{(F)} \equiv 2\sqrt{\pi}\frac{\Gamma\left[\frac{d+F}{2(d-1)}\right]}{\Gamma\left[\frac{1+F}{2(d-1)}\right]}, \tag{6.14}$$

which will greatly simplify the notation.

For the sphere sub-region we first write $d\vec{x}^2 = dr^2 + r^2 d\Omega_{d-2}^2$, where r is the radial coordinate and $d\Omega_{d-2}^2$ is the metric of a unit-sphere S^{d-2}, and then parametrise the minimal surface as $r(z)$. The resulting area functional is

$$\Sigma^{\rm sphere} = R^{d-1}\Omega_{d-2}\int_\varepsilon^{z_*} dz\, \frac{r(z)^{d-2}}{z^{d-1}}\sqrt{r'(z)^2 + \frac{1}{g(z)}}, \tag{6.15}$$

where Ω_{d-2} is the area of the unite S^{d-2} sphere. Extremising $\Sigma^{\rm sphere}$ leads to a non-linear second order ordinary differential equation for $r(z)$. For AdS_{d+1}, where $g(z) = 1$,

the exact solution is $r(z) = \sqrt{L^2 - z^2}$, and by using Eq. (6.15) we obtain

$$S_{\rm CFT}^{\rm sphere} = \begin{cases} \dfrac{R^{d-1}\Omega_{d-2}}{4G_N}\left[\displaystyle\sum_{j=1}^{(d-2)/2} c_j \left(\frac{L}{\varepsilon}\right)^{d-2j} + c_L \log\left(\frac{L}{\varepsilon}\right) + \tilde{c}_0 + \mathcal{O}\left(\frac{\varepsilon^2}{L^2}\right)\right], & (d \text{ even}) \\ \dfrac{R^{d-1}\Omega_{d-2}}{4G_N}\left[\displaystyle\sum_{j=1}^{(d-1)/2} c_j \left(\frac{L}{\varepsilon}\right)^{d-2j} + c_0 + \mathcal{O}\left(\frac{\varepsilon}{L}\right)\right], & (d \text{ odd}) \end{cases}$$

$$c_j = \frac{(-1)^{j-1}\Gamma\left[\frac{d-1}{2}\right]}{(d-2j)\Gamma\left[\frac{d-2j+1}{2}\right]\Gamma[j]}, \qquad c_L = \frac{(-1)^{\frac{d-2}{2}}\Gamma\left[\frac{d-1}{2}\right]}{\sqrt{\pi}\,\Gamma\left[\frac{d}{2}\right]}, \tag{6.16}$$

$$\tilde{c}_0 = \frac{(-1)^{\frac{d-1}{2}}\sqrt{\pi}\Gamma\left[\frac{d-1}{2}\right]}{2\,\Gamma\left[\frac{d}{2}\right]}, \qquad c_0 = \frac{(-1)^{\frac{d-2}{2}}\Gamma\left[\frac{d-1}{2}\right]}{2\sqrt{\pi}\,\Gamma\left[\frac{d}{2}\right]}\left(\psi\left[\frac{d}{2}\right] + \gamma_E + 2\log[2]\right),$$

where $\psi[d/2]$ is a Digamma function and $\gamma_E \approx 0.577$ is the Euler-Mascheroni constant.[3]

More generally, for a given $g(z)$ in one of our examples we compute σ as follows. First, we compute $S_{\rm ent}$ numerically, meaning for the strip we choose z_* and then integrate Eqs. (6.11) and (6.12) numerically, while for the sphere we solve for $r(z)$ numerically and then plug the solution into Eq. (6.15) and integrate numerically. Next, we subtract the corresponding $S_{\rm CFT}$ from Eq. (6.13b) or Eq. (6.16). Finally, we divide by

$$V = \begin{cases} L_\perp^{d-2} L = \frac{A}{2} L, & (\text{strip}) \\ \frac{\pi^{\frac{d-1}{2}}}{\Gamma\left(\frac{d+1}{2}\right)} L^{d-1} = \frac{A}{d-1} L. & (\text{sphere}) \end{cases} \tag{6.17}$$

We can determine σ's small-L behavior following ref. [241]. If L is small compared to all other length scales except ε, and in particular if $mL^d \ll 1$, then we can solve for the minimal surface order-by-order in a small-(mL^d) expansion, and expand the integrands in Eqs. (6.11), (6.12), and (6.15) in mL^d and integrate order-by-order, ultimately leading to an expansion of $S_{\rm ent}$ in powers of mL^d. Via Eq. (6.1) we then find

$$\sigma = \langle T_{tt}\rangle\, T_{\rm ent}^{-1} + \mathcal{O}\left(\langle T_{tt}\rangle^2 L^{d+1}\right), \tag{6.18}$$

where for the strip and for the sphere we find respectively

$$T_{\rm ent}^{\rm strip} = \frac{(d^2-1)\vartheta_{(0)}^2\vartheta_{(1)}}{4\pi^2}\,\frac{1}{L}, \qquad T_{\rm ent}^{\rm sphere} = \frac{d+1}{2\pi}\,\frac{1}{L}. \tag{6.19}$$

[3] Crucially, the coefficients c_L and $\tilde{c}_0$ were proven to be universal and can be shown to obey a holographic c-theorem. This means that for any deformation of the UV CFT to a new fixed point in the IR $c_L^{UV} > c_L^{IR}$ and $c_0^{UV} > c_0^{IR}$ using holographic techniques [254]. In a sense, we can say that those coefficients count degrees of freedom that get coarse-grained along an RG flow.

In short, $\sigma \propto \langle T_{tt} \rangle L$ at small L.

For bulk spacetimes with a horizon, we can determine σ's large-L behavior following refs. [255–257]. In Eq. (6.12) for $\Sigma_{\rm min}^{\rm strip}$, in order to extract the terms that diverge as $\varepsilon \to 0$, we add and subtract $1/z^{d-1}$ to the integrand, and integate over $1/z^{d-1}$. We next change the integration variable from z to $u = z/z_*$ to obtain

$$\frac{\Sigma_{\rm min}^{\rm strip}}{AR^{d-1}} = \frac{1}{d-2}\left(\frac{1}{\varepsilon^{d-2}} - \frac{1}{z_*^{d-2}}\right) + \frac{1}{z_*^{d-2}}\int_0^1 \frac{du}{u^{d-1}}\left(\frac{1}{\sqrt{1-u^{2(d-1)}}}\frac{1}{\sqrt{g(z_* u)}} - 1\right). \tag{6.20}$$

Our immediate goal is now to re-write the integral, as much as possible, in terms of that for L from Eq. (6.11), written with the coordinate u,

$$L = 2z_* \int_0^1 du \frac{u^{d-1}}{\sqrt{1-u^{2(d-1)}}}\frac{1}{\sqrt{g(z_* u)}}. \tag{6.21}$$

To do so, in the integrand of Eq. (6.20) we take

$$\begin{aligned} \frac{u^{-(d-1)}}{\sqrt{1-u^{2(d-1)}}} &= \frac{u^{-(d-1)} - u^{d-1} + u^{d-1}}{\sqrt{1-u^{2(d-1)}}} = \frac{u^{-(d-1)}(1-u^{2(d-1)}) + u^{d-1}}{\sqrt{1-u^{2(d-1)}}} \\ &= u^{-(d-1)}\sqrt{1-u^{2(d-1)}} + \frac{u^{d-1}}{\sqrt{1-u^{2(d-1)}}}, \end{aligned} \tag{6.22}$$

which allows us to re-write Eq. (6.20) as

$$\frac{\Sigma_{\rm min}^{\rm strip}}{AR^{d-1}} = \frac{1}{d-2}\left(\frac{1}{\varepsilon^{d-2}} - \frac{1}{z_*^{d-2}}\right) + \frac{1}{2}\frac{L}{z_*^{d-1}} + \frac{1}{z_*^{d-2}}\int_0^1 \frac{du}{u^{d-1}}\left(\sqrt{\frac{1-u^{2(d-1)}}{g(z_* u)}} - 1\right). \tag{6.23}$$

Collecting the $1/z_*^{d-2}$ terms, we find

$$\frac{\Sigma_{\rm min}^{\rm strip}}{AR^{d-1}} = \frac{1}{d-2}\frac{1}{\varepsilon^{d-2}} + \frac{1}{2}\frac{L}{z_*^{d-1}} + \frac{C(z_*)}{z_*^{d-2}},$$

with the dimensionless coefficient

$$C(z_*) \equiv -\frac{1}{d-2} + \int_0^1 \frac{du}{u^{d-1}}\left(\sqrt{\frac{1-u^{2(d-1)}}{g(z_* u)}} - 1\right). \tag{6.24}$$

Dividing by $4G_N$ to obtain $S_{\rm ent}^{\rm strip}$, subtracting $S_{\rm CFT}^{\rm strip}$ in Eq. (6.13b), and dividing by $V = AL/2 = L_\perp^{d-2} L$, we obtain the ED,

$$\sigma^{\rm strip} = \frac{R^{d-1}}{4G_N}\left[\frac{1}{z_*^{d-1}} + \frac{C(z_*)}{z_*^{d-2}}\frac{2}{L} + \frac{\vartheta_{(0)}^{d-1}}{(d-2)}\frac{1}{L^{d-1}}\right]. \tag{6.25}$$

So far we took no limits of L, *i.e.* Eq. (6.25) is valid for any L. As $L \to \infty$, we expect the minimal surface to probe deep into the bulk, and eventually to lie flat along the horizon,[4] so that in particular $\lim_{L\to\infty} z_* = z_H$. In that case Eq. (6.25) gives, using Eq. (6.10),

$$\lim_{L\to\infty} \sigma^{\text{strip}} = \frac{R^{d-1}}{4G_N}\frac{1}{z_H^{d-1}} = s. \tag{6.26}$$

We thus find that the leading term in σ's large-L expansion is the entropy density s, as expected. The leading $1/L$ correction is also straightforward to obtain: our examples have $d \geq 3$, so the final term in Eq. (6.25) is sub-leading, and thus

$$\sigma^{\text{strip}} = s + s\, z_H\, C(z_H)\, \frac{2}{L} + \mathcal{O}\left(\frac{1}{L^2}\right). \tag{6.27}$$

For the strip, $A/V = 2/L$, hence Eq. (6.27) is of the form in Eq. (6.6),

$$\sigma = s - \Delta\alpha\, \frac{A}{V} + \ldots, \tag{6.28}$$

where we identify

$$\Delta\alpha = -s\, z_H\, C(z_H). \tag{6.29}$$

Although the details are different, we find that σ's leading large-L correction for the sphere is also given exactly by Eq. (6.29). Such agreement between the strip and sphere at $L \to \infty$ is intuitive, since we expect the $L \to \infty$ limit to suppress any effects from the entangling surface's curvature. In short, $C(z_H)$ determines whether $\sigma \to s^{\pm}$ as $L \to \infty$, for *both the strip and sphere*.

Eq. (6.29) is the main novel result of this section, and allows us to test for area theorem violation simply by computing $C(z_H)$'s sign: if $C(z_H) < 0$ then $\Delta\alpha > 0$ and the area theorem is obeyed, while if $C(z_H) > 0$ then $\Delta\alpha < 0$ and the area theorem is violated.

[4] In fact, for sufficiently large L two solutions for $x(z)$ may exist. The first is our solution, described above. The second consists of two segments with constant $x(z)$, stretching from the boundary to the horizon, which must be connected by a third segment along the horizon, since minimal surfaces cannot cross a horizon [258]. The third segment contributes zero to the area. However, in all our examples with horizons we have checked explicitly that the latter solution always has larger area than our solution, *i.e.* is not the global minimum of the area functional, and hence may be safely ignored.

6.3.1 Lorentz-invariant RG flows

Starting from a CFT in the UV, we can induce an RG flow by sourcing a relevant operator. In the gravity picture, this means that we turn on the boundary value for the corresponding bulk field. Close to the boundary, the geometry remains asymptotically AdS, dual to the UV fixed point. Away from the boundary, however, the field's backreaction on the metric will deform the bulk geometry and break scale invariance. In this section we consider a bulk action

$$S_{\text{bulk}} = \frac{1}{16\pi G_N}\int d^{d+1}x\sqrt{-\det g_{MN}}\left[\mathcal{R} - \frac{1}{2}\partial_M\phi\partial^M\phi - V(\phi)\right], \tag{6.30}$$

where $\mathcal{R}$ is the Ricci scalar and ϕ is a real scalar field with potential $V(\phi)$. We want solutions to the equations of motion derived from S_{bulk} that describe Lorentz-invariant RG flows between CFTs, driven by the scalar operator $\mathcal{O}$ holographically dual to ϕ. We thus assume $V(\phi)$ has (at least) two stationary points, at which the equations of motion reduce to those of pure AdS_{d+1} with radius of curvature R given by

$$8\pi G_N\, V(\phi)|_{\text{stationary}} = -\frac{d(d-1)}{2R^2}. \tag{6.31}$$

All these solutions that interpolate between an asymptotic AdS_{d+1}, dual to the UV CFT, and another AdS_{d+1} deep in the bulk, dual to the IR CFT, have the form

$$ds^2 = \frac{R^2}{z^2}\left(-dt^2 + d\vec{x}^2 + \frac{dz^2}{g(z)}\right), \qquad \phi = \phi(z), \tag{6.32}$$

with $0 \leq z < \infty$. Following refs. [47, 248], if we introduce a "fake superpotential" W via

$$V(\phi) = \frac{1}{16\pi G_N}(\partial_\phi W)^2 - \frac{1}{2}\frac{d}{d-1}W^2, \tag{6.33}$$

then any solution to the equations of motion derived from S_{bulk} is also a solution to [248]

$$\phi' = \frac{d-1}{8\pi G_N}\frac{1}{zW}\,\partial_\phi W, \qquad g(z) = \frac{8\pi G_N}{(d-1)^2}\,R^2\,W^2. \tag{6.34}$$

We therefore only need to solve the first-order Eq. (6.34). In fact, for our purposes, we can *choose* $g(z)$, which then determines W and hence $\phi(z)$ via Eq. (6.34), which in turn is guaranteed to solve the equations of motion for the corresponding potential

$V(\phi)$ in Eq. (6.33). Crucially, $g(z)$ obeys several constraints. For instance, Eq. (6.34) implies

$$\phi'(z)^2 = \frac{d-1}{16\pi G_N}\frac{g'(z)}{z g(z)}, \tag{6.35}$$

so that $g'(z) \geq 0$, since by assumption $g(z) > 0$. The NEC also requires $g'(z) \geq 0$, so any solution of Eq. (6.34) is guaranteed to obey the NEC. We also want $\mathcal{O}$ to be relevant, $\Delta < d$, and unitary, $\Delta \geq \frac{d-2}{2}$, and moreover we want to avoid poorly-understood UV divergences in the EE that the subtraction $S_{\text{ent}} - S_{\text{CFT}}$ do not cancel, hence we restrict to $\Delta < (d+2)/2$ [23, 256]. We demand that asymptotically $\phi(z) = \phi_0 z^{\Delta_-} + \ldots$, where $\Delta_- = \text{Min}(d-\Delta, \Delta)$, ϕ_0 is proportional either to $\mathcal{O}$'s source ($\Delta_- = d - \Delta$) or to $\langle\mathcal{O}\rangle$ ($\Delta_- = \Delta$), and $\ldots$ represents terms with higher powers of z. Via Eq. (6.35), $g(z)$'s asymptotic expansion is then

$$g(z) = 1 + \frac{8\pi G_N \Delta_-}{d-1}\,\phi_0^2\, z^{2\Delta_-} + \ldots, \tag{6.36}$$

where again the $\ldots$ represents terms with higher powers of z.

The FLEE does not apply because Lorentz invariance requires $\langle T_{tt}\rangle = 0$ for these solutions. However, with the assumptions above, for the strip we can determine σ's small-L behavior by expanding Eq. (6.12) for $\Sigma_{\text{min}}^{\text{strip}}$ in small z_*, that is, for a minimal surface close to the asymptotic AdS_{d+1} boundary. Expanding also Eq. (6.13a) for L in small z_*, inverting order-by-order, and plugging the result into the expansion for $\Sigma_{\text{min}}^{\text{strip}}$ gives the leading small-L behavior

$$\sigma = -\frac{\pi\Delta_-\vartheta_{(2\Delta_-)}\vartheta_{(0)}^{d-2-2\Delta_-}}{(2\Delta_-+1)(2\Delta_-+2-d)}\phi_0^2\, R^{d-1}\, L^{2\Delta_-+1-d} + \ldots, \tag{6.37}$$

where $\ldots$ represents terms with higher powers of L. In the opposite limit, the area theorem requires $\sigma \to 0^-$ as $L \to \infty$, for both the strip and sphere, since ($s = 0$) and we only have the area term contribution $\propto -\Delta\alpha/L$. Our examples will conform to these limits.

EE in holographic RG flows has been studied in detail before, for example in refs. [244, 255, 256, 259], so we focus only on a few cases that illustrate some of σ's

possible behaviors in L. In particular, we restrict to $d = 4$ and choose

$$g(z) = \begin{cases} 1 + \tanh^4(\beta z), & \text{(6.38a)} \\ 1 + \tanh^4(\beta z) + \dfrac{3}{2}\tanh(\beta z - 2)\tanh^5(\beta z), & \text{(6.38b)} \\ 1 + \tanh^3(\beta z), & \text{(6.38c)} \\ 1 + \tanh^{7/2}(\beta z), & \text{(6.38d)} \end{cases}$$

where in each case β is a constant of mass dimension one, which may be related to ϕ_0 via Eq. (6.36). Table 6.2 summarises some properties of our choices of $g(z)$. In Table 6.2, the second column is R_{IR}, the value of the AdS_5 radius at $z \to \infty$, determined by the value of $\lim_{z\to\infty} g(z)$. The holographic c-theorem [248] requires $R_{\text{IR}} \leq R$. The third column shows $g(z)$'s leading asymptotic powers of z, which via Eq. (6.36) determines Δ_-, listed in the fourth column, with the corresponding Δ in the fifth column. The sixth column indicates whether ϕ_0 is proportional to $\mathcal{O}$'s source or to $\langle\mathcal{O}\rangle$. For $g(z)$ in Eqs. (6.38a) to (6.38b), $\phi(z)$ saturates the Breitenlohner-Freedman bound, hence $\phi(z)$'s leading asymptotic terms are z^{Δ_-} and $z^{\Delta_-}\log(z)$, however, we demand that the coefficient of the $\log(z)$ term vanish, so that in standard quantisation $\phi_0 \propto \langle\mathcal{O}\rangle$. In these cases, the RG flow is driven by $\langle\mathcal{O}\rangle \neq 0$ alone, with zero source.

Fig. 6.3 shows our numerical results for σ as a function of L. More specifically, we plot σ in units of $\beta^3 R^3/G_N$, where R^3/G_N is the UV CFT's central charge [47], versus L in units of β. In all cases, $\sigma < 0$ for all $L\beta$, with $\sigma \to 0^-$ as $L\beta \to \infty$, as required by the area theorem.

Fig. 6.3a shows the simplest behavior, for the $g(z)$ in Eq. (6.38a), in which $\sigma \propto -L$ at small L, and then a single minimum appears before $\sigma \to 0^-$ as $L\beta \to \infty$, for both the strip and sphere. Fig. 6.3b, for the $g(z)$ in Eq. (6.38b), is similar, but with a

$g(z)$	R_{IR}	Asymptotics	Δ_-	Δ	ϕ_0
(6.38a)	$R/\sqrt{2}$	$1 + (\beta z)^4 + \ldots$	2	2	$\propto \langle\mathcal{O}\rangle$
(6.38b)	$R/\sqrt{7/2}$	$1 + (\beta z)^4 + \ldots$	2	2	$\propto \langle\mathcal{O}\rangle$
(6.38c)	$R/\sqrt{2}$	$1 + (\beta z)^3 + \ldots$	3/2	5/2	source
(6.38d)	$R/\sqrt{2}$	$1 + (\beta z)^{7/2} + \ldots$	7/4	9/4	source

Table 6.2: Summary of properties of our choices of $g(z)$ in Eq. (6.38).

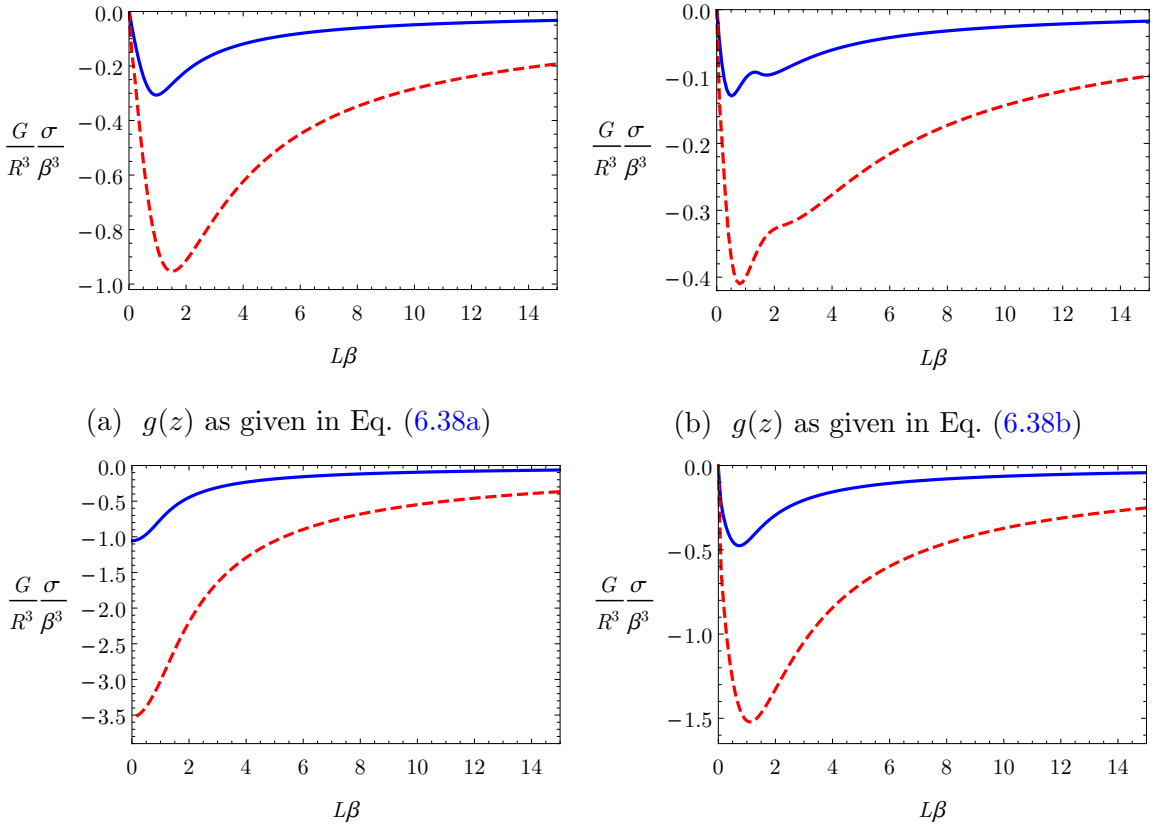

(a) $g(z)$ as given in Eq. (6.38a)

(b) $g(z)$ as given in Eq. (6.38b)

(c) $g(z)$ as given in Eq. (6.38c)

(d) $g(z)$ as given in Eq. (6.38d)

Figure 6.3: The ED, σ, in units of $\beta^3 R^3/G_N$, versus $L\beta$ for RG flows between holographic CFTs in $d = 4$. In each plot, the blue solid line is for the strip and the red dashed line is for the sphere. The label below each plot indicates the $g(z)$ we chose from Eq. (6.38). All curves are consistent with the area theorem since $\lim_{L\to\infty}\sigma \to s^- = 0^-$, as expected for Lorentz invariant RG lows.

second, local minimum, and corresponding local maximum, at intermediate L, for both the strip and sphere.

The $g(z)$ in Eq. (6.38c) yields $\Delta_- = 3/2$, hence Eq. (6.37) implies $\sigma \propto -L^0$ at small L, that is, σ starts at a negative constant value at $L = 0$, before monotonically rising as L increases, and then $\sigma \to 0^-$ as $L\beta \to \infty$, as shown in Fig. 6.3c. The $g(z)$ in Eq. (6.38d) yields $\Delta_- = 7/4$, hence Eq. (6.37) implies $\sigma \propto -L^{1/2}$ at small L. However, aside from the fractional power of L at small L, Fig. 6.3d shows that σ behaves similarly to that in Fig. 6.3a, with a single global minimum before $\sigma \to 0^-$ as $L\beta \to \infty$.

In summary, σ can clearly exhibit a variety of behaviors as a function of L, depend-

ing on details of the RG flow. However, σ often exhibits a unique *global* minimum, which by dimensional analysis must be at an $L \propto 1/\beta$. As discussed in Section 6.1, that L can be used to characterise and compare RG flows. For example, the L of σ's global minimum could provide a precise definition of the crossover scale from the UV to IR.

6.3.2 Finite temperature and AdS-Schwarzschild

In this section we consider a bulk action

$$S_{\text{bulk}} = \frac{1}{16\pi G_N} \int d^{d+1}x \sqrt{-\det g_{MN}} \left(\mathcal{R} + \frac{d(d-1)}{R^2} \right). \tag{6.39}$$

The corresponding Einstein equation admits the $(d+1)$-dimensional AdS-SCH black brane solution, of the form in Eq. (6.7) with

$$f(z) = g(z) = 1 - m\, z^d, \tag{6.40}$$

and hence a horizon at $z_H = m^{-1/d}$, with $\langle T_{tt} \rangle$, T, and s given by Eqs. (6.9) and (6.10).

As mentioned in Section 6.1, for AdS-SCH the FLEE requires $\sigma \propto \langle T_{tt} \rangle L$ at small L and we also expect $\lim_{L\to\infty} \sigma = s$. Our main result for AdS-SCH is the existence of a *critical dimension*, $d_{\text{crit}} \approx 6.7$, such that as $L \to \infty$, $\sigma \to s^-$ when $d < d_{\text{crit}}$, while $\sigma \to s^+$ when $d > d_{\text{crit}}$, indicating area theorem violation.

Fig. 6.4 shows σ/s versus LT for (a) the strip and (b) the sphere for $d = 3, 4, \ldots, 8$, illustrating the change of behavior at $d_{\text{crit}} \approx 6.7$. For both entangling surfaces, when $d = 3, 4, 5, 6 < d_{\text{crit}}$, we find σ/s increases monotonically and $\sigma/s \to 1^-$ as $LT \to \infty$. When $d = 7, 8 > d_{\text{crit}}$, we find σ/s rises to a global maximum before $\sigma/s \to 1^+$ as $LT \to \infty$.

The dotted lines in Fig. 6.5 show $s - \Delta\alpha \frac{A}{V}$ divided by s, with $\Delta\alpha$ from Eq. (6.29) agree with σ/s not only at large LT, as expected, but over a surprisingly large range of LT, down to $LT \approx 1$. Crucially, the dotted lines reveal that the transition between $\sigma \to s^\pm$ as $L \to \infty$ occurs when the coefficient $\Delta\alpha$ of the $1/L$ correction changes sign, from $\Delta\alpha > 0$ for $d = 4$ to $\Delta\alpha < 0$ for $d = 8$.

Indeed, Fig. 6.6 shows the dimensionless coefficient $C(z_H) \propto -\Delta\alpha$ from Eq. (6.29) as a function of d, which begins at $C(z_H) \approx -0.88$ when $d = 3$ and then monotonically

increases as d increases, eventually crossing through zero, which defines the critical dimension, $d_{\rm crit} \approx 6.7$. We can easily show that $C(z_H)$ is monotonically increasing for all d, and hence has only the single zero at $d_{\rm crit}$, by showing $\partial C(z_H)/\partial d \geq 0$, as follows. The $\frac{\partial}{\partial d}$ of Eq. (6.24) gives

$$\frac{\partial C(z_H)}{\partial d} = \frac{1}{(d-2)^2} + \int_0^1 du\, \frac{\log(u)}{u^{d-1}} \left(1 - \frac{1}{2}\frac{2 + u^{3d-2} - 3u^d}{(1-u^d)^{3/2}(1-u^{2d-2})^{1/2}}\right). \tag{6.41}$$

Since $\frac{\log(u)}{u^{d-1}} \leq 0$ for $u \in [0,1]$, we need to show that

$$\frac{1}{2}\frac{2 + u^{3d-2} - 3u^d}{(1-u^d)^{3/2}(1-u^{2d-2})^{1/2}} \geq 1, \tag{6.42}$$

for $u \in [0,1]$. The denominator in Eq. (6.42) is positive, so multiplying both sides of Eq. (6.42) by $(1-u^d)^{3/2}(1-u^{2d-2})^{1/2}$, squaring, and re-arranging, we find

$$\left(1 + \frac{1}{2}u^{3d-2} - \frac{3}{2}u^d\right)^2 - (1-u^d)^3(1-u^{2d-2}) \geq 0. \tag{6.43}$$

Since $u^{2d-2} \geq u^{2d}$ for $u \in [0,1]$, Eq. (6.43) implies

$$\begin{aligned}\left(1 + \frac{1}{2}u^{3d-2} - \frac{3}{2}u^d\right)^2 - (1-u^d)^3(1-u^{2d-2}) &\geq \left(1 + \frac{1}{2}u^{3d} - \frac{3}{2}u^d\right)^2 - (1-u^d)^3(1-u^{2d}) \\ &= \frac{1}{4}u^{2d}(1-u^d)^4 \geq 0,\end{aligned} \tag{6.44}$$

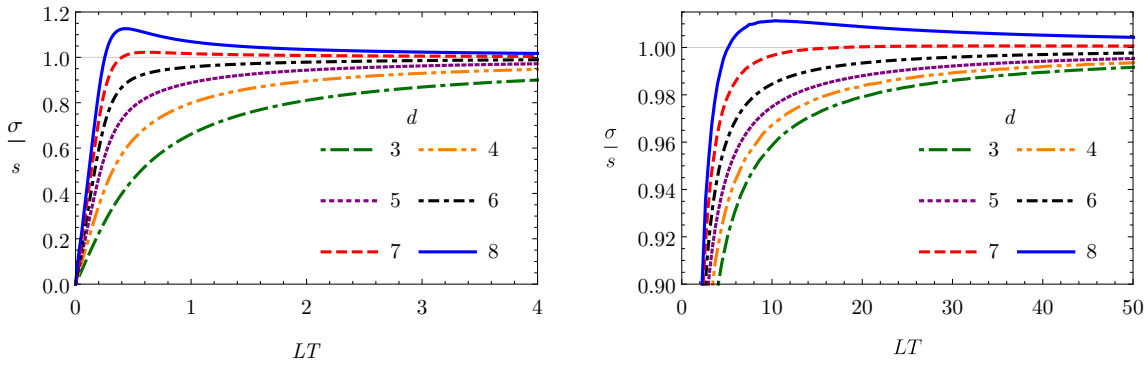

(a) (b)

Figure 6.4: The ED, σ, in units of entropy density s, versus LT for (a) the strip, and (b) the sphere, for AdS-SCH in $d = 3, 4, \ldots, 8$. For each entangling surface, when $d = 3, 4, 5, 6 < d_{\rm crit} \approx 6.7$, σ/s monotonically increases with LT and $\sigma/s \to 1^-$ as $L \to \infty$, whereas when $d = 7, 8 > d_{\rm crit}$, σ/s rises to a global maximum before $\sigma/s \to 1^+$ as $LT \to \infty$.

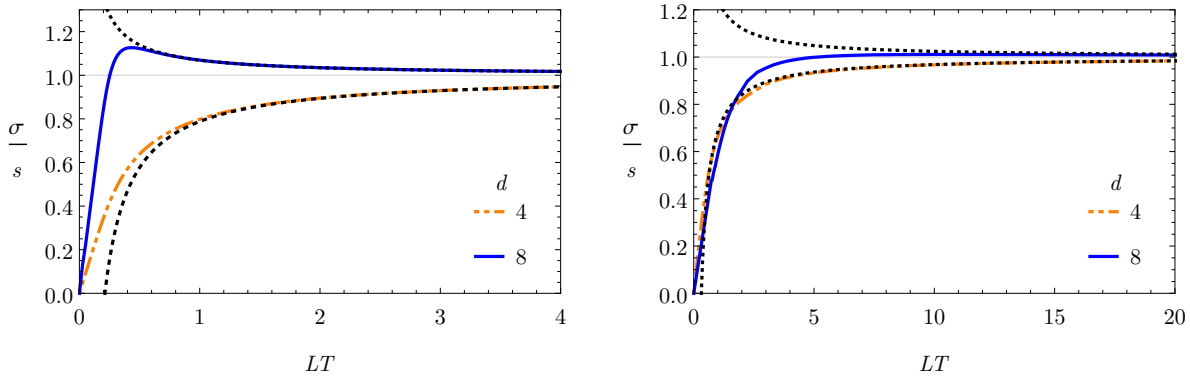

(a) (b)

Figure 6.5: The ED, σ, in units of entropy density, s, versus LT for (a) the strip and (b) the sphere, for AdS-SCH in $d = 4$ (orange dashed) and $d = 8$ (blue solid). The dotted lines are $1 - \frac{\Delta\alpha}{s}\frac{A}{V}$, with $\Delta\alpha$ in Eq. (6.29), representing the $LT \to \infty$ limit and first $1/L$ correction.

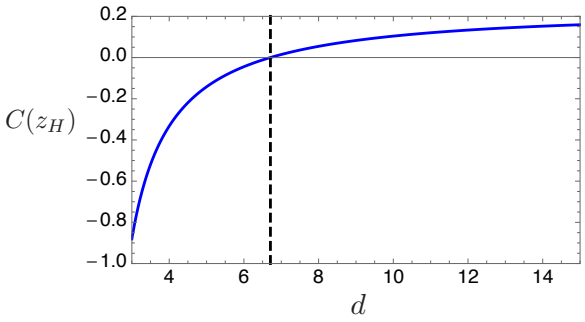

Figure 6.6: The dimensionless coefficient $C(z_H)$ from Eq. (6.29) for AdS-SCH, versus dimension d. At $d = 3$, $C(z_H) \approx -0.88$, and $C(z_H)$ then increases monotonically with d, reaching zero at $d_{\rm crit} \approx 6.7$, indicated by the dashed black vertical line.

and thus $\partial C(z_H)/\partial d \geq 0$, as advertised.

The above pattern extends also to CFTs at non-zero T in $d = 2$, where $S_{\rm ent}$ for an interval of length L is known exactly [80]. Given $d = 2 < d_{\rm crit}$, we expect $\sigma \to s^-$ as $LT \to \infty$. Indeed, the result of ref. [80] leads to

$$\sigma = \frac{c}{3}\frac{1}{L}\ln\left[\frac{\sinh(\pi LT)}{\pi LT}\right] = \frac{c}{3}\pi T - \frac{c}{3}\frac{\ln(2\pi LT)}{L} + \mathcal{O}\left(e^{-2\pi TL}/L\right),$$

where c is the CFT's central charge, and in the second equality we performed the $1/L$ expansion. In that expansion, the first term is Cardy's result for s [260], while the second term exhibits the area law violating factor $\ln(2\pi LT)$. Our key observation is: the leading correction has *negative* coefficient, so that indeed $\sigma \to s^-$ as $LT \to \infty$. All

the results at finite temperature derived in this subseciton, agree with the *exact* form for the EE of a strip in AdS-SCH derived in ref. [249].

Why does AdS-SCH violate the area theorem while relativistic RG flows do not? On the gravity side of the correspondence, the key difference is the behavior of $g(z)$. As mentioned below Eq. (6.35), for relativistic RG flows the NEC implies $g'(z) \geq 0$, that is, $g(z)$ is strictly non-decreasing as z increases. However, for AdS-SCH the NEC imposes no such constraint, and indeed $g(z) = 1 - mz^d$ *decreases* monotonically as z increases, from $g(z = 0) = 1$ to $g(z = z_H) = 0$. Apparently, as d increases, eventually $g(z)$ decreases quickly enough to render $C(z_H) > 0$.

How does AdS-SCH evades the field theory proofs in refs. [22, 23] of the area theorem for the sphere in relativistic RG flows? The proofs of refs. [22, 23] relied crucially on Lorentz invariance, which non-zero T clearly breaks. In fact, in the $d \to \infty$ limit AdS-SCH is dual to an RG flow from a $(d + 1)$-dimensional UV CFT to a $(0 + 1)$-dimensional IR CFT, which is clearly only possible when Lorentz symmetry is broken. More specifically, when $d \to \infty$ the AdS-SCH near-horizon geometry becomes $SL(2, \mathbb{R})/U(1) \times \mathbb{R}^{d-1}$, where the latter factor represents the spatial directions $\vec{x}$ [252, 253]. After a mode decomposition on $\mathbb{R}^{d-1}$, the action in Eq. (6.39) gives rise to a string theory with target space $SL(2, \mathbb{R})/U(1)$ [253]. Linearised fluctuations in the near-horizon region then exhibit scale invariance in t and z but not $\vec{x}$ [253, 261]. AdS-SCH thus provides our first hint that area theorem violation can occur as we dial a parameter towards a limiting value in which an IR fixed point emerges with scaling different from the UV fixed point. We will find further examples of such behavior in the following.

6.3.3 Chemical potential and AdS-Reissner-Nordström

In this section we consider the bulk action

$$S_{\text{bulk}} = \frac{1}{16\pi G_N} \int d^{d+1}x \sqrt{-\det g_{MN}} \left(\mathcal{R} + \frac{d(d-1)}{R^2} - R^2 F_{MN} F^{MN} \right), \tag{6.45}$$

where $F_{MN} = \partial_M A_N - \partial_N A_M$ is the field strength for a U(1) gauge field, A_M, dual to a conserved $U(1)$ current. The corresponding equations of motion admit the $(d+1)$-dimensional AdS-RN charged black brane solution [47], with metric of the form in

Eq. (6.7), with

$$f(z) = g(z) = 1 - mz^d + q^2 z^{2(d-1)}, \tag{6.46}$$

where q is proportional to the black brane's charge density. The solution has a horizon at the smallest positive root of $f(z_H) = 0$. The gauge field solution's only non-zero component is

$$A_t = \mu \left(1 - \frac{z^{d-2}}{z_H^{d-2}}\right), \qquad \mu = \sqrt{\frac{d-1}{2(d-2)}}\, z_H^{d-2}\, q. \tag{6.47}$$

AdS-RN is dual to a CFT with non-zero $\langle T_{tt} \rangle$, T, and s, given by Eqs. (6.9) and (6.10), and non-zero chemical potential μ and charge density, proportional to q. In particular,

$$T = \frac{d}{4\pi R^2} \frac{1}{z_H} \left(1 - \frac{d-2}{d}\, z_H^{2(d-2)}\, q^2\right), \tag{6.48}$$

so that $T \geq 0$ implies $q^2 \leq \frac{d}{d-2} z_H^{-2(d-1)}$. In the extremal limit, where q saturates the upper bound and $T = 0$, an extremal horizon is present, so that $s \neq 0$. Moreover, when $T = 0$ the near-horizon geometry becomes $AdS_2 \times \mathbb{R}^{d-1}$, with AdS_2 of radius $R/\sqrt{d(d-1)}$ in the t and z directions and the dual description is a semi-local quantum liquid state [201], describing an RG flow from a $(d+1)$-dimensional UV CFT to a $(0+1)$-dimensional IR CFT.

Our main result for AdS-RN is the existence of a dimension-dependent *critical temperature*, $(T/\mu)_{\text{crit}}$, such that as $L \to \infty$, $\sigma \to s^-$ when $T/\mu > (T/\mu)_{\text{crit}}$, while $\sigma \to s^+$ when $T/\mu < (T/\mu)_{\text{crit}}$. Specifically at $T/\mu = 0$, we find $C(z_H) > 0$ for all d, so that for both the strip and sphere the *area theorem is violated* as shown in Fig. 6.7.

When we start increasing $T/\mu \gg 1$, we expect to eventually recover the AdS-SCH results from Section 6.3.2, including the existence of the critical dimension $d_{\text{crit}} \approx 6.7$. Staring from the high temperature result in the $d < d_{\text{crit}}$ case we find that σ/s increases monotonically with LT, and eventually $\sigma/s \to 1^-$ as $LT \to \infty$, consistent with our results from Section 6.3.2. As T/μ decreases we find a transition in which eventually a global maximum appears and we recover the results from $T/\mu = 0$ and the area theorem violation.

For example, Fig. 6.8 shows σ/s versus LT for both the strip and the sphere in AdS-RN with $d = 4 < d_{\text{crit}}$ during their transition. As we decrease T/μ in the case of the strip, we find that the transition actually occurs in stages, as shown in Fig. 6.8a.

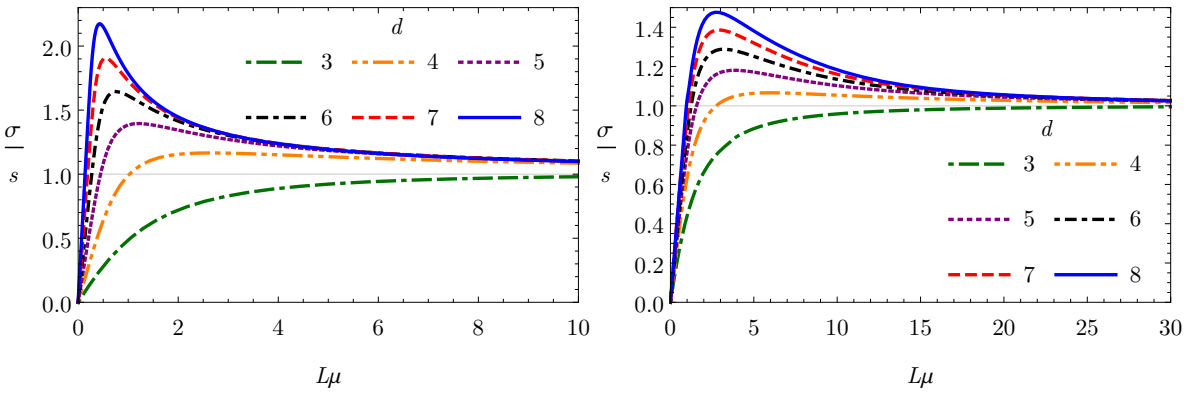

Figure 6.7: The ED, σ, in units of entropy density s, versus $L\mu$ for (a) the strip, and (b) the sphere, in AdS-RN with $d = 3, 4, 5, 6, 7, 8$ and $T/\mu = 0$. In all cases σ/s has a single global maximum and $\sigma/s \to 1^+$ as $L\mu \to \infty$. The maxima in the $d = 3$ case was correctly predicted using $C(z_H)$ and eventually it was found numerically around $L\mu \approx 50$ and $L\mu \approx 100$ for the strip and sphere respectively (not shown).

First, at $T/\mu \approx 0.107$, a local minimum and maximum appear, with $\sigma/s < 1$ for all LT. Second, at $T/\mu \approx 0.102$, the maximum rises above $\sigma/s = 1$, becoming a global maximum, but a local minimum persists at $\sigma/s < 1$, and then $\sigma/s \to 1^-$ as $LT \to \infty$. Third and finally, at $T/\mu \approx 0.097$, a transition occurs from $\sigma/s \to 1^-$ to $\sigma/s \to 1^+$ as $LT \to \infty$, and the local minimum disappears, indicating area theorem violation. In contrast,we find no evidence of such a multi-stage transition for the sphere in AdS-RN as shown in Fig. 6.8b.

We find qualitatively similar behavior for the strip in all $d < d_{\text{crit}}$: at some $(T/\mu)_1$ a local minimum and maximum appear, but σ/s remains below one for all LT, at some $(T/\mu)_2 < (T/\mu)_1$ a global maximum emerges, but still $\sigma/s \to 1^-$ for $LT \to \infty$, and finally at some $(T/\mu)_{\text{crit}} < (T/\mu)_2$ the transition occurs to $\sigma/s \to 1^+$ for $LT \to \infty$. Our numerical estimates for $(T/\mu)_1$, $(T/\mu)_2$, and $(T/\mu)_{\text{crit}}$ for $d = 3, 4, 5, 6 < d_{\text{crit}}$ appear in Table 6.3.

In all cases above, the transition between $\sigma/s \to 1^{\pm}$ as $LT \to \infty$ indicates area theorem violation. Indeed, Fig. 6.9 shows the dimensionless coefficient $C(z_H)$ as a function of T/μ for $d = 3, 4, 5, 6, 7$. For all $d < d_{\text{crit}}$, at high T/μ we find $C(z_H) < 0$, obeying the area theorem, but as T/μ decreases $C(z_H)$ eventually passes through zero

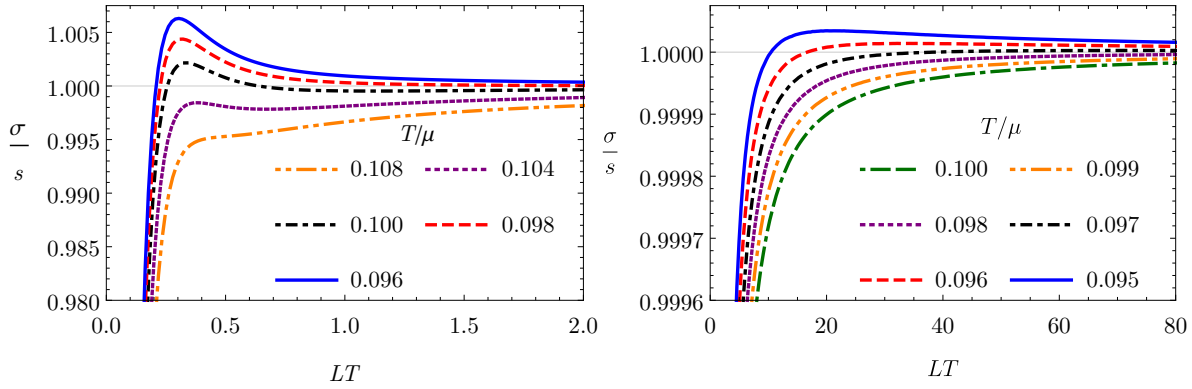

(a) (b)

Figure 6.8: The ED, σ, in units of entropy density s, versus LT for (a) the strip, and (b) the sphere, in AdS-RN with $d = 4$, showing the formation of a global maximum around $(T/\mu)_{\text{crit}} \approx 0.098$ in both cases. For the strip this happens in stages where first we observe the formation of a local minimum and maximum before the formation of the global maximum. In contrast, the transition in the sphere geometry is much simpler.

indicating area theorem violation. In each case, the critical T/μ where $C(z_H) = 0$ is precisely the $(T/\mu)_{\text{crit}}$ for the strip in Table 6.3, as expected. Of course, we still have that for all $d > d_{\text{crit}}$ $C(z_H) > 0$ and the area theorem is always violated.

In summary, in AdS-RN for either $d > d_{\text{crit}}$ at any T/μ, or for any d and sufficiently small T/μ, we find a global maximum in σ/s, and in particular $\sigma/s \to 1^+$ as $LT \to \infty$, indicating area theorem violation. In other words, as we dial a parameter towards a limiting value in which an IR fixed point appears with different scaling from the UV CFT ($d \to \infty$ or $T/\mu \to 0$), we find area theorem violation, as we saw in AdS-SCH.

d	$(T/\mu)_1$	$(T/\mu)_2$	$(T/\mu)_{\text{crit}}$
3	6.343×10^{-4}	4.858×10^{-4}	2.967×10^{-4}
4	0.107	0.102	0.098
5	0.407	0.403	0.399
6	1.219	1.215	1.213

Table 6.3: For the strip in AdS-RN with $d < d_{\text{crit}} \approx 6.7$, as (T/μ) decreases, at $(T/\mu)_1$ a local minimum and maximum appear in σ/s as a function of LT, at $(T/\mu)_2 < (T/\mu)_1$ the local maximum becomes a global maximum, but a local minimum remains, and $\sigma/s < 1$ for all LT, and then at $(T/\mu)_{\text{crit}} < (T/\mu)_2$ the global maximum rises above one, and the transition occurs to $\sigma/s \to 1^+$ as $LT \to \infty$.

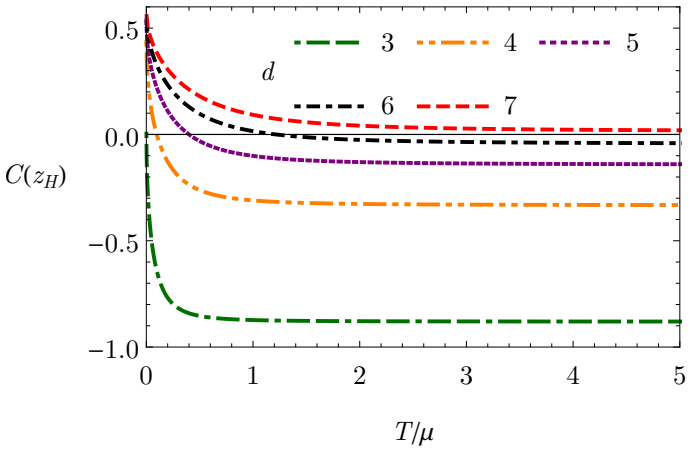

Figure 6.9: The dimensionless coefficient $C(z_H)$ from Eq. (6.29) versus T/μ for AdS-RN, for $d = 3, 4, 5, 6, 7, 8$. For $d > d_{\text{crit}} \approx 6.7$, $C(z_H) > 0$ for all T/μ, indicating area theorem violation. For $d < d_{\text{crit}}$, as T/μ decreases $C(z_H)$ changes sign from negative to positive at the $(T/\mu)_{\text{crit}}$ in Table 6.3, indicating area theorem violation for $T/\mu < (T/\mu)_{\text{crit}}$.

6.4 Outlook and discussions

Our results raise various questions for future research. For example, when does area theorem violation occur in holography? Is some version of non-relativistic scale invariance deep in the bulk necessary?

The near-horizon regions of extremal black branes generically have either AdS_2 or AdS_3 [262, 263]. Do they always exhibit area theorem violation? We considered examples of AdS_2, but not AdS_3, which is dual to a CFT in $d = 2$, which typically produces area law violation [264]. What about a more general holographic classification? Can the properties of the bulk metric that produce area theorem violation be fully characterised using $C(z_H)$?

Our findings also suggests that σ may indeed help characterise states of matter. For example, using σ's small- and large L behaviour, we can classify states of matter into those in which the FLEE or area theorem applies or not, respectively. More generally, we can divide states of matter into those where σ is monotonic, like the bottom curve in Fig. 6.1, and those where σ has one or more extrema, like the top curve in Fig. 6.1. In the latter case, the location of the global maximum provides a characteristic length

scale, namely the scale where the EE per unit volume is maximal or minimal. Such a characteristic length scale has various potential uses. One of them is to characterise near-horizon geometries. For example, in a solution such as extremal AdS-RN, the position of σ's global maximum could provide a precise division between near- and far-horizon regions in the bulk or a precise distinction between the UV and the IR of our theory, even when the near horizon geometry hasn't fully developed yet. Imagine for instance that we did not know the AdS-RN solution at $T/\mu = 0$ (as often occurs when numerically solving for a metric). Area theorem violation would occur at finite T/μ, not just at $T/\mu = 0$, already suggesting that the extremal near-horizon geometry may have scale invariance, but cannot be AdS_{d+1}.

Finally, according to our definition, σ is a well defined quantity for non-holographic systems as well. For example, what about SYK-type models [265, 266], which have $s \neq 0$ at $T = 0$ and AdS_2 IR scaling, similar to some of our examples? More generally, can the conditions for area theorem violation be fully characterised? Is some form of non-relativistic scale invariance in the IR necessary? If so, does area theorem violation imply that degrees of freedom with non-relativistic scale invariance somehow count as "more" degrees of freedom than in a CFT?

In sum, σ is clearly useful for "fingerprinting" states of QFTs, holographic or otherwise. We therefore believe σ deserves further exploration in future research.

Chapter 7

Conclusion

This thesis has explored holographic approaches to strongly-interacting systems. Chapters 2 and 3 motivated the holographic duality's origins within string theory and reviewed the holographic dictionary between the gauge theory and its gravity dual. In particular, we described how to compute real-time correlators and entanglement entropy of the dual gauge theory.

Our first application of the dictionary was in the context of the fluid/gravity correspondence, which was introduced in Chapter 4 in studying the convergence of the hydrodynamic gradient expansion of boost invariant Bjorken flow, holographically dual to Gauss-Bonnet gravity in 5D with a negative cosmological constant. As in all other known examples, we showed that the gradient expansion is an asymptotic series which we understood through applying the techniques of Borel-Padé summation, which linked the asymptotic nature of the series to the presence of non-perturbative quasi-normal modes in our theory. We found that the singularities in the Borel plane of this series showed qualitative features that smoothly interpolated between the infinitely strong coupling limit of $\mathcal{N} = 4$ SYM theory and the results from RTA kinetic theory. We further performed the Borel summation to construct the hydrodynamic attractor which provided an analytic continuation of hydrodynamics at early times. In particular, we found that at finite coupling, the convergence of different initial conditions to the attractor and their hydrodynamisation occurred at large values of the pressure anisotropy, before the plasma has had time to reach thermal equilibrium and thus outside of the formal regime of applicability of hydrodynamics.

Chapter 5 presented our results for sound modes of strongly-interacting CFT_3 with non-zero T and μ, dual to an Einstein-DBI charged black brane with two free parameters: the tension and the non-linearity parameter. For all values of the tension, non-linearity parameter, and T/μ, we found sound modes with speed given by the conformal value and attenuation constant of hydrodynamic form at arbitrarily low T/μ, even outside of the usual hydrodynamic regime. In fact, the sound attenuation constant as a function of T/μ qualitatively resembles that of a Fermi liquid, including a maximum, which in a LFL theory would correspond to crossover between the collisionless and the hydrodynamic regimes. We compared several definitions of this crossover based on the movement of the pole in the Green's functions and the change in residue in the charge density spectral function. However, we found that the temperature (5.37) provided by the maximum in the attenuation constant is the only definition for the crossover temperature valid for any finite backreaction.

Finally, in Chapter 6 we explored the entanglement entropy of CFT_d in the presence of various deformations: a relevant Lorentz scalar operator, T and μ. We defined the "entanglement density", σ, as the change in the entanglement entropy due to the deformations mentioned above, divided by the sub-region's volume. This quantity turns out to be useful for characterising the states of matter, according to the asymptotic behaviour of σ. In particular, we showed that when the Lorentz symmetry is broken and the IR fixed point has different scaling from the UV, σ does not increase monotonically with the size of the entangled region signalling the violation of the area law and the development of long-range entanglement, due to the effective IR theory. We showed that this was the case at low temperatures and/or large dimension, in the case of AdS-RN and AdS-SCH, respectively, and found an analytic expression for the asymptotic behaviour of σ in the presence of black branes Eq. (6.29), which we tested against the numerics with excellent agreement for both the strip and the sphere examples.

In future works, it would be interesting to understand to what extent the presence of long-range entanglement is fundamental for the existence of the holographic zero sound modes, by computing the entanglement density σ or computing the sign of the function $C(z_H)$ from Eq. (6.24), for the case of black brane geometries.

Appendix A

Calculation of Green's Functions

In this appendix we discuss technical details of our holographic calculations of the retarded Green's functions, their poles, and the spectral functions. We use standard techniques, and in particular the method of ref. [164].

We want to study the CFT's response to linearised perturbations about the equilibrium state described holographically by the solution in Eq. (5.6). Specifically, we want to compute the retarded Green's functions of $T^{\mu\nu}$ and J^{μ} as functions of complex frequency ω and real momentum k. In a retarded Green's function with fixed k, a pole in the complex ω plane at position ω_* with $\mathrm{Re}(\omega_*) \neq 0$ and $\mathrm{Im}(\omega_*) \neq 0$ represents a propagating excitation, with $|\mathrm{Im}(\omega_*)| \propto$ the excitation's decay rate. If $|\mathrm{Im}(\omega_*)| < |\mathrm{Re}(\omega_*)|$, then the excitation is a long-lived quasi-particle, like a sound wave. If $\mathrm{Re}(\omega_*) = 0$ then the excitation is dissipative rather than propagating, like a charge diffusion mode. Stability requires $\mathrm{Im}(\omega_*) \leq 0$, since $\mathrm{Im}(\omega_*) > 0$ means the mode grows without bound over time. The mode with smallest $|\mathrm{Im}(\omega_*)|$ dominates the late-time response, as all other modes will decay faster. We focus on the "highest" poles, *i.e.* those closest to the $\mathrm{Re}(\omega)$ axis, with relatively small $|\mathrm{Im}(\omega_*)|$.

For a set of operators $\mathcal{O}_i$ with $i = 1, 2, \ldots$, the matrix of spectral functions, $\rho_{ij}(\omega, k)$ is defined as the anti-Hermitian part of the matrix of retarded Green's functions, $G_{ij}(\omega, k)$:

$$\rho_{ij}(\omega, k) \equiv i \left(G_{ij}(\omega, k) - G_{ji}(\omega, k)^* \right) . \tag{A.1}$$

In general, a pole in $G_{ij}(\omega, k)$ at ω_* produces a peak in $\rho_{ij}(\omega, k)$ as a function of $\mathrm{Re}(\omega)$

with

$$\text{Peak width} \propto 2\,|\text{Im}(\omega_*)|, \qquad \text{Peak height} \propto \frac{\text{Res}[G_{ij}(\omega_*)]}{|\text{Im}(\omega_*)|} \tag{A.2}$$

In holography, the CFT's generating functional is proportional to the on-shell bulk action [2, 3]. To compute $G_{ij}(\omega, k)$ and hence $\rho_{ij}(\omega, k)$ holographically, we must thus solve for fluctuations of bulk fields with in-going boundary conditions at the horizon, plug the solutions into the bulk action, renormalise [57, 165, 213], and take two functional derivatives [9, 70, 72, 207–209]. However, we can obtain the location ω_* of a pole in $G_{ij}(\omega, k)$ simply by solving the bulk linearised equations of motion, without evaluating the on-shell action: ω_* corresponds to an ω value where a linearised, in-going, *normalisable* solution, namely a QNM, exists [70, 72].

To see this, remember that from linear response theory, you expect the response $\langle \mathcal{O}(\omega, k) \rangle$ generated by a small perturbation of the field $\phi_0(\omega, k)$, to be determined by the Green's function, which in momentum space can be written as

$$G_{\mathcal{O}\mathcal{O}}(\omega, k) \sim \frac{\langle \mathcal{O}(\omega, k) \rangle}{\phi_0(\omega, k)}. \tag{A.3}$$

As we saw in Section 3.1, in holography the source is related to the boundary expansion and in particular, we can interpret it as a modification of the original bulk field $\phi(z) \to \phi(z) + \delta\phi(\omega, k, z)$ where $\delta\phi(\omega, k, z) = \phi_0(\omega, k) z^{\Delta_-} + \ldots + \langle \mathcal{O}(\omega, k) \rangle\, z^{\Delta_+} + \ldots$ is determined by the equations of motion. Therefore we can find the poles of the retarded Green's function by computing the complex eigenvalues of the linearised equations of motion for the perturbation which satisfy the incoming-wave boundary condition at the horizon and Dirichlet boundary condition $\delta\phi_0(\omega_*, k) = 0$ at the asymptotic boundary. This approach generalizes to our case, where we have a coupled system of fluctuations.

We thus introduce fluctuations around the solutions $g_{MN}(z)$ and $A_M(z)$ in Eq. (5.6), with dependence on z, t, and without loss of generality due to rotational invariance, x but not y,

$$g_{MN}(z) \to g_{MN}(z) + \delta g_{MN}(z, t, x), \qquad A_M(z) \to A_M(z) + \delta A_M(z, t, x). \tag{A.4}$$

We next linearise the equations of motion in $\delta g_{MN}(z, t, x)$ and $\delta A_M(z, t, x)$, and then introduce Fourier transforms in t and x,

$$\delta g_{MN}(z, t, x) \equiv \int \frac{d\omega\, dk}{(2\pi)^2}\, e^{-i\omega t + ikx}\, \delta g_{MN}(z, \omega, k), \tag{A.5}$$

and similarly for $\delta A_M(z,\omega,k)$. We hence obtain fourteen equations for the ten components of $\delta g_{MN}(z,\omega,k)$ and four components of $\delta A_M(z,\omega,k)$. However, following refs. [165, 172, 189], for the sound channel we can reduce these to only two equations, in two steps, as follows.

At linearised order fluctuations in different representations of the parity transformation $y \to -y$ decouple, and the sound modes appear in the parity-even sector. The first step is thus to set to zero the parity-odd fluctuations, $(\delta g_{zy}, \delta g_{ty}, \delta g_{xy}, \delta A_y)$, leaving ten equations for $(\delta g_{zz}, \delta g_{tt}, \delta g_{xx}, \delta g_{yy}, \delta g_{zt}, \delta g_{zx}, \delta g_{tx}, \delta A_z, \delta A_t, \delta A_x)$, the parity-even fluctuations. These ten equations are cumbersome and unilluminating, so we will not write them here. They are special cases of the equations written explicitly in the appendix of ref. [189]. Six of these equations are second order (dynamical), four from Einstein's equation and two from Maxwell's equation, while the other four equation are first order (constraints), three from the radial components of Einstein's equation and one from the radial component of Maxwell's equation. The second-order equations are in fact linear combinations of derivatives of the first-order equations, hence the latter contain no independent information.

The second step is to form diffeomorphism- and $U(1)$-gauge invariant linear combinations of the fluctuations [72]. Any sum of diffeomorphism- and gauge-invariant fluctuations is again diffeomorphism- and gauge-invariant, so we must make a choice. For example, one choice is to use Ishibashi-Kodama "master fields" [267], involving z derivatives of fluctuations, which have the advantage of producing two *decoupled* equations [165]. However, we will instead use the linear combinations of refs. [172, 189, 212], involving fluctuations with no z index, which ultimately lead to two *coupled* equations. The fields of refs. [172, 189, 212] have several advantages over those of Ishibashi-Kodama, for example they make transparent not only the mapping from the fields' boundary values to the dual operator sources [165, 172] but also the fact that the CFT Ward identities for $T_{\mu\nu}$'s and J^μ's Green's functions are satisfied [172]. We thus choose the diffeomorphism- and gauge-invariant linear combinations of refs. [172, 189, 212],

$$Z_1 \equiv k\,\delta a_t + \omega\,\delta a_x + \frac{1}{2}\,k\,z\,F_{zt}\,\delta g^y{}_y, \tag{A.6a}$$

$$Z_2 \equiv -k^2\,f\,\delta g^t{}_t + \omega^2\,\delta g^x{}_x + 2\,\omega k\,\delta g^x{}_t + \left(-\omega^2 + k^2\,f - \frac{1}{2}\,k^2\,z\,f'\right)\delta g^y{}_y, \tag{A.6b}$$

where we raised an index on δg_{MN} using the background metric $g_{MN}(z)$ in Eq. (5.6). The equations of motion of Z_1 and Z_2 are of the form

$$Z_1'' + A_1 Z_1' + A_2 Z_2' + A_3 Z_1 + A_4 Z_2 = 0, \tag{A.7a}$$

$$Z_2'' + B_1 Z_1' + B_2 Z_2' + B_3 Z_1 + B_4 Z_2 = 0, \tag{A.7b}$$

The coefficients A_i and B_i are lengthy and uniluminating so we don't show them here.[1]

A key property is $B_1 \propto \tau$ and $B_3 \propto \tau$, so that the probe limit $\tau \to 0$ eliminates Z_1 from Z_2's equation of motion. In that case we can consistently set the metric fluctuations to zero, so that $Z_2 = 0$ and $Z_1 = k\,\delta a_t + \omega\,\delta a_x$, and then solve Z_1's equation of motion in the AdS-SCH background, thus reproducing the probe calculation of ref. [171].

The values of A_μ and $g^\mu{}_\nu$ at the boundary $z \to 0$ are sources for J^μ and $T_\mu{}^\nu$, respectively. Using $\lim_{z\to 0}(zF_{zt}) = 0$ and $\lim_{z\to 0}(zf') = 0$, the $z \to 0$ limit of Eq. (A.6) thus reveals that the linear combination of bulk fields Z_1 is dual to the linear combination of operators $k\,J^t + \omega\,J^x$, while Z_2 is dual to $-k^2\,T_t{}^t + \omega^2\,T_x{}^x + 2\omega k\,T_x{}^t + (-\omega^2 + k^2)T_y{}^y$. More precisely, the expansions of Z_1 and Z_2 about the boundary $z \to 0$ are

$$Z_1 = Z_1^{(0)} + Z_1^{(1)} z + \mathcal{O}(z^2), \tag{A.8a}$$

$$Z_2 = Z_2^{(0)} - \frac{1}{2} Z_2^{(0)} (k^2 - \omega^2) z^2 + Z_2^{(3)} z^3 + \mathcal{O}(z^4), \tag{A.8b}$$

where $Z_1^{(0)}$ and $Z_2^{(0)}$ are the sources for these dual operators.

The expansions of Z_1 and Z_2 about the horizon $z = z_H$ are

$$Z_1 = (z_H - z)^{-i\omega/4\pi T}\,\zeta_1^{\text{in}}(z) + (z_H - z)^{i\omega/4\pi T}\,\zeta_1^{\text{out}}(z), \tag{A.9a}$$

$$Z_2 = (z_H - z)^{-1-i\omega/4\pi T}\,\zeta_2^{\text{in}}(z) + (z_H - z)^{-1+i\omega/4\pi T}\,\zeta_2^{\text{out}}(z), \tag{A.9b}$$

where $\zeta_1^{\text{in}}(z)$, $\zeta_1^{\text{out}}(z)$, $\zeta_2^{\text{in}}(z)$, and $\zeta_2^{\text{out}}(z)$ are regular at $z = z_H$. We want to compute retarded Green's functions, which are dual to purely in-going solutions [70], so we will impose $\zeta_1^{\text{out}}(z_H) = 0$ and $\zeta_2^{\text{out}}(z_H) = 0$. QNMs are in-going solutions that are furthermore normalisable, meaning they also have $Z_1^{(0)} = 0$ and $Z_2^{(0)} = 0$. The values of ω at which such solutions exist are dual to the positions of poles in the retarded Green's

[1] The interested reader can find the coefficients in the appendix of [223].

functions. Crucially, Z_1 and Z_2 are coupled, hence the dual Green's functions will mix, and in particular will have poles at the same positions. However, the *residues* of these poles may differ, and hence the spectral functions may differ. Indeed, in our system, as in AdS-RN [172], the spectral functions differ in important ways, as we discuss in Section 5.3.2.

To compute the QNMs and Green's functions numerically, we use the method of ref. [164]. For given ω and k we form two linearly independent in-going solutions specified by

$$\begin{pmatrix} \zeta_1^{\text{in}}(z_H) \\ \zeta_2^{\text{in}}(z_H) \end{pmatrix} = \begin{pmatrix} 1 \\ \pm 1 \end{pmatrix}, \tag{A.10}$$

and then construct a matrix with columns given by these solutions,

$$H_{ia}(z) \equiv \begin{pmatrix} Z_1^+(z) & Z_1^-(z) \\ Z_2^+(z) & Z_2^-(z) \end{pmatrix}. \tag{A.11}$$

where the index $a = \pm$ (the superscripts) corresponds to the sign in Eq. (A.10). To find QNMs we compute

$$\lim_{z\to 0} H_{ia}(z) \equiv \begin{pmatrix} Z_1^{(0)+} & Z_1^{(0)-} \\ Z_2^{(0)+} & Z_2^{(0)-} \end{pmatrix}. \tag{A.12}$$

If the determinant of the matrix in Eq. (A.12) vanishes, then a normalisable linear combination of our two solutions, that is, a QNM, exists at the given ω and k. For the Green's functions we need the on-shell action, which may be written as

$$S = \int_\epsilon^{z_H} dz \int \frac{d\omega d^2k}{(2\pi)^3} C_{ij} \partial_z Z_i(z, -\omega, -k) \partial_z Z_j(z, \omega, k) + \ldots, \tag{A.13}$$

where ϵ is a near-boundary cutoff and $\ldots$ represent terms with at most a single ∂_z. These terms are both analytic, and so do not affect the poles of G_{ij}, and real-valued, and so do not contribute to ρ_{ij}. Following ref. [172], we only compute the diagonal components of the Green's functions, G_{11} and G_{22}, which we will denote G_J and G_{tt}, respectively, since Z_1 is dual to a linear combination of J^μ components and Z_2 is dual to an operator containing the energy density $T_t{}^t$. In the main text we somewhat sloppily refer to these as the "charge" and "energy" Green's functions. The coefficients C_{ij} that

we need for G_{11} and G_{22} are (with $\mathcal{F}(z) \equiv \sqrt{1-\tilde{\alpha}^2 z^4 F_{tz}^2}$)

$$C_{11} = \frac{1}{16\pi G_N} \frac{\tau\tilde{\alpha}^2 f}{\mathcal{F}\left(\omega^2 - f\mathcal{F}^2 k^2\right)}, \tag{A.14a}$$

$$C_{12} = -C_{21} = -\frac{1}{16\pi G_N} \frac{i\tau\tilde{\alpha}^2 L^2 z f^2 k F_{tz}}{\mathcal{F}\left(\omega^2 - f\mathcal{F}^2 k^2\right)\left(k^2\left(zf'(z) - 4f\right) + 4\omega^2\right)}, \tag{A.14b}$$

$$C_{22} = \frac{1}{16\pi G_N} \frac{f^3 L^2 \left[2\mathcal{F}(f\mathcal{F}^2 k^2 - \omega^2) - k^2 z^4 \tau\tilde{\alpha}^2 F_{tz}^2\right]}{z^2\left(fk^2\mathcal{F}^3 - \mathcal{F}\omega^2\right)\left(k^2\left(zf'(z) - 4f\right) + 4\omega^2\right)^2}. \tag{A.14c}$$

If we define the matrix

$$F_{ij}(z) \equiv H_{ia}(z) H_{aj}^{-1}(\epsilon), \tag{A.15}$$

then we can write the retarded Green's functions as [164]

$$G_{ij} = -\frac{1}{16\pi G_N} \lim_{\epsilon\to 0} \left[F_{ik}^{\dagger}\left(C_{kl} + C_{lk}^{*}\right) F_{lj}' + \ldots\right], \tag{A.16}$$

where $F' \equiv \partial_z F$ and all quantities in the brackets are evaluated at $z = \epsilon$. The $\ldots$ include terms descending from the $\ldots$ in Eq. (A.13), as well as the boundary terms, including the holographic renormalisation counterterms. We may safely ignore these terms, for the reasons mentioned above. Using the matrices $H_{ia}(z)$ and C_{ij} we can also compute the matrix of pole residues in Eq. (5.32) [164],

$$\mathcal{R}_{ij}^{(n)}(k) = -\left.\frac{\det\left[H_{ia}(\epsilon)\right]}{\partial_\omega \det\left[H_{ia}(\epsilon)\right]}\left(C_{ik} + C_{ki}^{*}\right) H_{ka}'(\epsilon) H_{aj}^{-1}(\epsilon)\right|_{\omega_*^{(n)}(k)}, \tag{A.17}$$

where $\omega_*^{(n)}(k)$ is the position of the n^{th} pole, computed numerically from the zeroes of the determinant of the matrix in Eq. (A.12), as described above.

Bibliography

[1] J. M. Maldacena, *The large N limit of superconformal field theories and supergravity*, *Adv. Theor. Math. Phys.* **2** (1998) 231–252, [hep-th/9711200].

[2] S. S. Gubser, I. R. Klebanov and A. M. Polyakov, *Gauge theory correlators from non-critical string theory*, *Phys. Lett.* **B428** (1998) 105–114, [hep-th/9802109].

[3] E. Witten, *Anti-de Sitter space and holography*, *Adv. Theor. Math. Phys.* **2** (1998) 253–291, [hep-th/9802150].

[4] O. Aharony, S. S. Gubser, J. M. Maldacena, H. Ooguri and Y. Oz, *Large N field theories, string theory and gravity*, *Phys. Rept.* **323** (2000) 183–386, [hep-th/9905111].

[5] H. B. Meyer, *Transport Properties of the Quark-Gluon Plasma: A Lattice QCD Perspective*, *Eur. Phys. J.* **A47** (2011) 86, [1104.3708].

[6] S. A. Hartnoll, A. Lucas and S. Sachdev, *Holographic quantum matter*, 1612.07324.

[7] G. 't Hooft, *A Planar Diagram Theory for Strong Interactions*, *Nucl. Phys.* **B72** (1974) 461.

[8] G. Policastro, D. T. Son and A. O. Starinets, *The Shear viscosity of strongly coupled N=4 supersymmetric Yang-Mills plasma*, *Phys. Rev. Lett.* **87** (2001) 081601, [hep-th/0104066].

[9] P. Kovtun, D. T. Son and A. O. Starinets, *Holography and hydrodynamics: Diffusion on stretched horizons*, *JHEP* **10** (2003) 064, [hep-th/0309213].

[10] A. Buchel and J. T. Liu, *Universality of the shear viscosity in supergravity*, *Phys. Rev. Lett.* **93** (2004) 090602, [hep-th/0311175].

[11] P. Kovtun, D. T. Son and A. O. Starinets, *Viscosity in strongly interacting quantum field theories from black hole physics*, *Phys. Rev. Lett.* **94** (2005) 111601, [hep-th/0405231].

[12] A. O. Starinets, *Quasinormal spectrum and the black hole membrane paradigm*, *Phys. Lett.* **B670** (2009) 442–445, [0806.3797].

[13] A. Adams, L. D. Carr, T. Schfer, P. Steinberg and J. E. Thomas, *Strongly Correlated Quantum Fluids: Ultracold Quantum Gases, Quantum Chromodynamic Plasmas, and Holographic Duality*, *New J. Phys.* **14** (2012) 115009, [1205.5180].

[14] M. Haack and A. Yarom, *Universality of second order transport coefficients from the gauge-string duality*, *Nucl. Phys.* **B813** (2009) 140–155, [0811.1794].

[15] E. Shaverin and A. Yarom, *Universality of second order transport in Gauss-Bonnet gravity*, *JHEP* **04** (2013) 013, [1211.1979].

[16] S. Grozdanov and A. O. Starinets, *On the universal identity in second order hydrodynamics*, *JHEP* **03** (2015) 007, [1412.5685].

[17] P. Kleinert and J. Probst, *Second-Order Hydrodynamics and Universality in Non-Conformal Holographic Fluids*, *JHEP* **12** (2016) 091, [1610.01081].

[18] S. Grozdanov and A. O. Starinets, *Second-order transport, quasinormal modes and zero-viscosity limit in the Gauss-Bonnet holographic fluid*, *JHEP* **03** (2017) 166, [1611.07053].

[19] J. Erdmenger, M. Haack, M. Kaminski and A. Yarom, *Fluid dynamics of R-charged black holes*, *JHEP* **01** (2009) 055, [0809.2488].

[20] N. Banerjee et al., *Hydrodynamics from charged black branes*, *JHEP* **01** (2011) 094, [0809.2596].

[21] D. T. Son and P. Surowka, *Hydrodynamics with Triangle Anomalies*, *Phys. Rev. Lett.* **103** (2009) 191601, [0906.5044].

[22] H. Casini and M. Huerta, *On the RG running of the entanglement entropy of a circle*, *Phys. Rev.* **D85** (2012) 125016, [1202.5650].

[23] H. Casini, E. Teste and G. Torroba, *Relative entropy and the RG flow*, *JHEP* **03** (2017) 089, [1611.00016].

[24] J. Casalderrey-Solana, H. Liu, D. Mateos, K. Rajagopal and U. A. Wiedemann, *Gauge/String Duality, Hot QCD and Heavy Ion Collisions*. Cambridge University Press, 2014, 10.1017/CBO9781139136747.

[25] A. M. Polyakov, *The Wall of the cave*, *Int. J. Mod. Phys.* **A14** (1999) 645–658, [hep-th/9809057].

[26] G. 't Hooft, *Dimensional reduction in quantum gravity*, in *Salamfest 1993:0284-296*, pp. 0284–296, 1993. gr-qc/9310026.

[27] L. Susskind, *The World as a hologram*, *J. Math. Phys.* **36** (1995) 6377–6396, [hep-th/9409089].

[28] A. Bzowski, *Dimensional renormalization in AdS/CFT*, 1612.03915.

[29] S. W. Hawking and G. F. R. Ellis, *The Large Scale Structure of Space-Time*. Cambridge Monographs on Mathematical Physics. Cambridge University Press, 2011, 10.1017/CBO9780511524646.

[30] J. L. Petersen, *Introduction to the Maldacena conjecture on AdS / CFT*, *Int. J. Mod. Phys.* **A14** (1999) 3597–3672, [hep-th/9902131].

[31] M. Jarvinen and E. Kiritsis, *Holographic Models for QCD in the Veneziano Limit*, *JHEP* **03** (2012) 002, [1112.1261].

[32] E. S. Fradkin and A. A. Tseytlin, *Effective Field Theory from Quantized Strings*, *Phys. Lett.* **B158** (1985) 316–322.

[33] E. S. Fradkin and A. A. Tseytlin, *Nonlinear Electrodynamics from Quantized Strings*, *Phys. Lett.* **B163** (1985) 123–130.

[34] J. Polchinski, *String Theory. Vol. 1: An Introduction to the Bosonic String*. Cambridge University Press, 2007.

[35] J. Polchinski, *String Theory. Vol. 2: Superstring Theory and Beyond*. Cambridge University Press, 2007.

[36] C. V. Johnson, *D-Branes*. Cambridge University Press, 2003.

[37] E. Witten, *Bound states of strings and p-branes*, *Nucl. Phys.* **B460** (1996) 335–350, [hep-th/9510135].

[38] M. F. Sohnius, *Introducing Supersymmetry*, *Phys. Rept.* **128** (1985) 39–204.

[39] J. Polchinski, *Introduction to Gauge/Gravity Duality*, in *Proceedings, Theoretical Advanced Study Institute in Elementary Particle Physics (TASI 2010). String Theory and Its Applications: From meV to the Planck Scale: Boulder, Colorado, USA, June 1-25, 2010*, pp. 3–46, 2010. 1010.6134. DOI.

[40] J. Polchinski, *Dirichlet Branes and Ramond-Ramond charges*, *Phys. Rev. Lett.* **75** (1995) 4724–4727, [hep-th/9510017].

[41] J. Maldacena, *The Gauge/gravity duality*, in *Black holes in higher dimensions* (G. T. Horowitz, ed.), pp. 325–347. 2012. 1106.6073.

[42] S. S. Gubser, I. R. Klebanov and A. A. Tseytlin, *Coupling constant dependence in the thermodynamics of N=4 supersymmetric Yang-Mills theory*, *Nucl. Phys.* **B534** (1998) 202–222, [hep-th/9805156].

[43] J. Pawelczyk and S. Theisen, *AdS(5) x S**5 black hole metric at O(alpha-prime**3)*, *JHEP* **09** (1998) 010, [hep-th/9808126].

[44] E. Witten, *Symmetry and Emergence*, *Nature Phys.* **14** (2018) 116–119, [1710.01791].

[45] M. Gunaydin and N. Marcus, *The spectrum of the S^5 compactification of the chiral N=2, D=10 supergravity and the unitary supermultiplets of U(2,2/4)*, *Classical and Quantum Gravity* **2** (1985) L11.

[46] H. J. Kim, L. J. Romans and P. van Nieuwenhuizen, *Mass spectrum of chiral ten-dimensional N=2 supergravity on S^5*, *Phys. Rev. D* **32** (Jul, 1985) 389–399.

[47] M. Ammon and J. Erdmenger, *Gauge/gravity duality*. Cambridge Univ. Pr., Cambridge, UK, 2015.

[48] J. Erlich, E. Katz, D. T. Son and M. A. Stephanov, *QCD and a Holographic Model of Hadrons*, *Phys. Rev. Lett.* **95** (2005) 261602, [hep-ph/0501128].

[49] A. Karch, E. Katz, D. T. Son and M. A. Stephanov, *Linear Confinement and AdS/QCD*, *Phys. Rev.* **D74** (2006) 015005, [hep-ph/0602229].

[50] H. Liu, J. McGreevy and D. Vegh, *Non-Fermi liquids from holography*, 0903.2477.

[51] T. Faulkner, H. Liu, J. McGreevy and D. Vegh, *Emergent quantum criticality, Fermi surfaces, and AdS2*, 0907.2694.

[52] C. Bender and S. Orszag, *Advanced Mathematical Methods for Scientists and Engineers I.* Springer-Verlag, New York, 1999.

[53] P. Breitenlohner and D. Z. Freedman, *Positive energy in anti-de Sitter backgrounds and gauged extended supergravity*, *Physics Letters B* **115** (1982) 197 – 201.

[54] P. Breitenlohner and D. Z. Freedman, *Stability in gauged extended supergravity*, *Annals of Physics* **144** (1982) 249 – 281.

[55] V. Balasubramanian, P. Kraus and A. E. Lawrence, *Bulk versus boundary dynamics in anti-de Sitter space-time*, *Phys. Rev.* **D59** (1999) 046003, [hep-th/9805171].

[56] S. de Haro, S. N. Solodukhin and K. Skenderis, *Holographic reconstruction of space-time and renormalization in the AdS / CFT correspondence*, *Commun. Math. Phys.* **217** (2001) 595–622, [hep-th/0002230].

[57] K. Skenderis, *Lecture notes on holographic renormalization*, *Class. Quant. Grav.* **19** (2002) 5849–5876, [hep-th/0209067].

[58] I. R. Klebanov and E. Witten, *AdS / CFT correspondence and symmetry breaking*, *Nucl.Phys.* **B556** (1999) 89–114, [hep-th/9905104].

[59] S.-J. Rey and J.-T. Yee, *Macroscopic strings as heavy quarks in large N gauge theory and anti-de Sitter supergravity*, *Eur. Phys. J.* **C22** (2001) 379–394, [hep-th/9803001].

[60] L. Susskind and E. Witten, *The Holographic bound in anti-de Sitter space*, hep-th/9805114.

[61] M. Henningson and K. Skenderis, *The Holographic Weyl anomaly*, *JHEP* **07** (1998) 023, [hep-th/9806087].

[62] M. Henningson and K. Skenderis, *Holography and the Weyl anomaly*, *Fortsch. Phys.* **48** (2000) 125–128, [hep-th/9812032].

[63] V. Balasubramanian and P. Kraus, *A Stress tensor for Anti-de Sitter gravity*, *Commun. Math. Phys.* **208** (1999) 413–428, [hep-th/9902121].

[64] W. Mueck and K. S. Viswanathan, *Counterterms for the Dirichlet prescription of the AdS / CFT correspondence*, hep-th/9905046.

[65] J. de Boer, E. P. Verlinde and H. L. Verlinde, *On the holographic renormalization group*, *JHEP* **08** (2000) 003, [hep-th/9912012].

[66] J. de Boer, *The Holographic Renormalization Group*, *Fortsch. Phys.* **49** (2001) 339–358, [hep-th/0101026].

[67] I. Papadimitriou and K. Skenderis, *AdS / CFT correspondence and geometry*, *IRMA Lect. Math. Theor. Phys.* **8** (2005) 73–101, [hep-th/0404176].

[68] N. Iqbal and H. Liu, *Universality of the hydrodynamic limit in AdS/CFT and the membrane paradigm*, *Phys. Rev.* **D79** (2009) 025023, [0809.3808].

[69] G. W. Gibbons and S. W. Hawking, *Action Integrals and Partition Functions in Quantum Gravity*, *Phys. Rev.* **D15** (1977) 2752–2756.

[70] D. T. Son and A. O. Starinets, *Minkowski-space correlators in AdS/CFT correspondence: Recipe and applications*, *JHEP* **09** (2002) 042, [hep-th/0205051].

[71] C. P. Herzog and D. T. Son, *Schwinger-Keldysh propagators from AdS/CFT correspondence*, *JHEP* **03** (2003) 046, [hep-th/0212072].

[72] P. K. Kovtun and A. O. Starinets, *Quasinormal modes and holography*, *Phys. Rev.* **D72** (2005) 086009, [hep-th/0506184].

[73] D. Z. Freedman, S. D. Mathur, A. Matusis and L. Rastelli, *Correlation functions in the CFT(d) / AdS(d+1) correspondence*, *Nucl. Phys.* **B546** (1999) 96–118, [hep-th/9804058].

[74] G. Chalmers, H. Nastase, K. Schalm and R. Siebelink, *R current correlators in N=4 superYang-Mills theory from anti-de Sitter supergravity*, *Nucl. Phys.* **B540** (1999) 247–270, [hep-th/9805105].

[75] E. Witten, *Anti-de Sitter space, thermal phase transition, and confinement in gauge theories*, *Adv. Theor. Math. Phys.* **2** (1998) 505–532, [hep-th/9803131].

[76] L. Bombelli, R. K. Koul, J. Lee and R. D. Sorkin, *A Quantum Source of Entropy for Black Holes*, *Phys. Rev.* **D34** (1986) 373–383.

[77] M. Srednicki, *Entropy and Area*, *Phys. Rev. Lett.* **71** (1993) 666–669, [hep-th/9303048].

[78] M. B. Hastings, *An area law for one-dimensional quantum systems*, *Journal of Statistical Mechanics: Theory and Experiment* **8** (Aug., 2007) 08024, [0705.2024].

[79] J. Eisert, M. Cramer and M. B. Plenio, *Area laws for the entanglement entropy - a review*, *Rev. Mod. Phys.* **82** (2010) 277–306, [0808.3773].

[80] P. Calabrese and J. L. Cardy, *Entanglement entropy and quantum field theory*, *J. Stat. Mech.* **0406** (2004) P06002, [hep-th/0405152].

[81] C. Holzhey, F. Larsen and F. Wilczek, *Geometric and renormalized entropy in conformal field theory*, *Nucl. Phys.* **B424** (1994) 443–467, [hep-th/9403108].

[82] S. Ryu and T. Takayanagi, *Holographic Derivation of Entanglement Entropy from AdS/CFT*, *Phys. Rev. Lett.* **96** (2006) 181602, [hep-th/0603001].

[83] S. Ryu and T. Takayanagi, *Aspects of Holographic Entanglement Entropy*, *JHEP* **08** (2006) 045, [hep-th/0605073].

[84] J. D. Brown and M. Henneaux, *Central Charges in the Canonical Realization of Asymptotic Symmetries: An Example from Three-Dimensional Gravity*, *Commun. Math. Phys.* **104** (1986) 207–226.

[85] T. Nishioka, S. Ryu and T. Takayanagi, *Holographic Entanglement Entropy: an Overview*, *J. Phys.* **A42** (2009) 504008, [0905.0932].

[86] STAR collaboration, K. H. Ackermann et al., *Elliptic flow in Au + Au collisions at $\sqrt{s_{NN}}$= 130 GeV*, *Phys. Rev. Lett.* **86** (2001) 402–407, [nucl-ex/0009011].

[87] PHENIX collaboration, S. S. Adler et al., *Elliptic flow of identified hadrons in Au+Au collisions at $\sqrt{s_{NN}}$ = 200-GeV*, *Phys. Rev. Lett.* **91** (2003) 182301, [nucl-ex/0305013].

[88] PHOBOS collaboration, B. B. Back et al., *Centrality and pseudorapidity dependence of elliptic flow for charged hadrons in Au+Au collisions at $\sqrt{s_{NN}}$ = 200-GeV*, *Phys. Rev.* **C72** (2005) 051901, [nucl-ex/0407012].

[89] ATLAS collaboration, G. Aad et al., *Measurement of the azimuthal anisotropy for charged particle production in $\sqrt{s_{NN}} = 2.76$ TeV lead-lead collisions with the ATLAS detector*, *Phys. Rev.* **C86** (2012) 014907, [1203.3087].

[90] CMS collaboration, S. Chatrchyan et al., *Measurement of the elliptic anisotropy of charged particles produced in PbPb collisions at $\sqrt{s}_{NN}$=2.76 TeV*, *Phys. Rev.* **C87** (2013) 014902, [1204.1409].

[91] ALICE collaboration, K. Aamodt et al., *Elliptic flow of charged particles in Pb-Pb collisions at 2.76 TeV*, *Phys. Rev. Lett.* **105** (2010) 252302, [1011.3914].

[92] P. Huovinen, P. F. Kolb, U. W. Heinz, P. V. Ruuskanen and S. A. Voloshin, *Radial and elliptic flow at RHIC: Further predictions*, *Phys. Lett.* **B503** (2001) 58–64, [hep-ph/0101136].

[93] D. Teaney, J. Lauret and E. V. Shuryak, *A Hydrodynamic description of heavy ion collisions at the SPS and RHIC*, nucl-th/0110037.

[94] T. Hirano, U. W. Heinz, D. Kharzeev, R. Lacey and Y. Nara, *Hadronic dissipative effects on elliptic flow in ultrarelativistic heavy-ion collisions*, *Phys. Lett.* **B636** (2006) 299–304, [nucl-th/0511046].

[95] B. Schenke, S. Jeon and C. Gale, *Elliptic and triangular flow in event-by-event (3+1)D viscous hydrodynamics*, *Phys. Rev. Lett.* **106** (2011) 042301, [1009.3244].

[96] T. Hirano, P. Huovinen and Y. Nara, *Elliptic flow in Pb+Pb collisions at $\sqrt{s_{NN}} = 2.76$ TeV: hybrid model assessment of the first data*, *Phys. Rev.* **C84** (2011) 011901, [1012.3955].

[97] C. Shen, Z. Qiu, H. Song, J. Bernhard, S. Bass and U. Heinz, *The iEBE-VISHNU code package for relativistic heavy-ion collisions*, *Comput. Phys. Commun.* **199** (2016) 61–85, [1409.8164].

[98] CMS collaboration, V. Khachatryan et al., *Observation of Long-Range Near-Side Angular Correlations in Proton-Proton Collisions at the LHC*, *JHEP* **09** (2010) 091, [1009.4122].

[99] ATLAS collaboration, G. Aad et al., *Observation of Long-Range Elliptic Azimuthal Anisotropies in $\sqrt{s}$ =13 and 2.76 TeV pp Collisions with the ATLAS Detector*, *Phys. Rev. Lett.* **116** (2016) 172301, [1509.04776].

[100] CMS collaboration, V. Khachatryan et al., *Evidence for collectivity in pp collisions at the LHC*, *Phys. Lett.* **B765** (2017) 193–220, [1606.06198].

[101] P. Bozek, *Collective flow in p-Pb and d-Pd collisions at TeV energies*, *Phys. Rev.* **C85** (2012) 014911, [1112.0915].

[102] I. Kozlov, M. Luzum, G. Denicol, S. Jeon and C. Gale, *Transverse momentum structure of pair correlations as a signature of collective behavior in small collision systems*, 1405.3976.

[103] R. D. Weller and P. Romatschke, *One fluid to rule them all: viscous hydrodynamic description of event-by-event central p+p, p+Pb and Pb+Pb collisions at* $\sqrt{s} = 5.02$ *TeV*, *Phys. Lett.* **B774** (2017) 351–356, [1701.07145].

[104] M. P. Heller, R. A. Janik and P. Witaszczyk, *The characteristics of thermalization of boost-invariant plasma from holography*, *Phys. Rev. Lett.* **108** (2012) 201602, [1103.3452].

[105] P. M. Chesler and L. G. Yaffe, *Boost invariant flow, black hole formation, and far-from-equilibrium dynamics in* $N = 4$ *supersymmetric Yang-Mills theory*, *Phys. Rev.* **D82** (2010) 026006, [0906.4426].

[106] P. M. Chesler and L. G. Yaffe, *Holography and colliding gravitational shock waves in asymptotically* AdS_5 *spacetime*, *Phys. Rev. Lett.* **106** (2011) 021601, [1011.3562].

[107] P. M. Chesler and L. G. Yaffe, *Holography and off-center collisions of localized shock waves*, *JHEP* **10** (2015) 070, [1501.04644].

[108] A. Kurkela and Y. Zhu, *Isotropization and hydrodynamization in weakly coupled heavy-ion collisions*, *Phys. Rev. Lett.* **115** (2015) 182301, [1506.06647].

[109] M. Attems, J. Casalderrey-Solana, D. Mateos, D. Santos-Olivn, C. F. Sopuerta, M. Triana et al., *Holographic Collisions in Non-conformal Theories*, *JHEP* **01** (2017) 026, [1604.06439].

[110] M. P. Heller, R. A. Janik and P. Witaszczyk, *Hydrodynamic Gradient Expansion in Gauge Theory Plasmas*, *Phys. Rev. Lett.* **110** (2013) 211602, [1302.0697].

[111] M. P. Heller and M. Spalinski, *Hydrodynamics Beyond the Gradient Expansion: Resurgence and Resummation*, *Phys. Rev. Lett.* **115** (2015) 072501, [1503.07514].

[112] G. Basar and G. V. Dunne, *Hydrodynamics, resurgence, and transasymptotics*, *Phys. Rev.* **D92** (2015) 125011, [1509.05046].

[113] I. Aniceto and M. Spaliński, *Resurgence in Extended Hydrodynamics*, *Phys. Rev.* **D93** (2016) 085008, [1511.06358].

[114] M. P. Heller, A. Kurkela and M. Spalinski, *Hydrodynamization and transient modes of expanding plasma in kinetic theory*, 1609.04803.

[115] G. S. Denicol and J. Noronha, *Divergence of the Chapman-Enskog expansion in relativistic kinetic theory*, 1608.07869.

[116] P. Romatschke, *Far From Equilibrium Fluid Dynamics*, 1704.08699.

[117] W. Israel and J. M. Stewart, *Transient relativistic thermodynamics and kinetic theory*, *Annals Phys.* **118** (1979) 341–372.

[118] R. Baier, P. Romatschke, D. T. Son, A. O. Starinets and M. A. Stephanov, *Relativistic viscous hydrodynamics, conformal invariance, and holography*, *JHEP* **04** (2008) 100, [0712.2451].

[119] G. S. Denicol and J. Noronha, *Analytical attractor and the divergence of the slow-roll expansion in relativistic hydrodynamics*, 1711.01657.

[120] M. Strickland, J. Noronha and G. Denicol, *The anisotropic non-equilibrium hydrodynamic attractor*, 1709.06644.

[121] M. Spaliński, *On the hydrodynamic attractor of Yang-Mills plasma*, 1708.01921.

[122] P. Romatschke, *Relativistic Hydrodynamic Attractors with Broken Symmetries: Non-Conformal and Non-Homogeneous*, 1710.03234.

[123] A. Behtash, C. N. Cruz-Camacho and M. Martinez, *Far-from-equilibrium attractors and nonlinear dynamical systems approach to the Gubser flow*, 1711.01745.

[124] S. Waeber, A. Schfer, A. Vuorinen and L. G. Yaffe, *Finite coupling corrections to holographic predictions for hot QCD*, *JHEP* **11** (2015) 087, [1509.02983].

[125] S. Grozdanov, N. Kaplis and A. O. Starinets, *From strong to weak coupling in holographic models of thermalization*, *JHEP* **07** (2016) 151, [1605.02173].

[126] S. A. Stricker, *Holographic thermalization in N=4 Super Yang-Mills theory at finite coupling*, *Eur. Phys. J.* **C74** (2014) 2727, [1307.2736].

[127] D. Steineder, S. A. Stricker and A. Vuorinen, *Probing the pattern of holographic thermalization with photons*, *JHEP* **07** (2013) 014, [1304.3404].

[128] S. Grozdanov and W. van der Schee, *Coupling Constant Corrections in a Holographic Model of Heavy Ion Collisions*, *Phys. Rev. Lett.* **119** (2017) 011601, [1610.08976].

[129] T. Andrade, J. Casalderrey-Solana and A. Ficnar, *Holographic Isotropisation in Gauss-Bonnet Gravity*, *JHEP* **02** (2017) 016, [1610.08987].

[130] B. S. DiNunno, S. Grozdanov, J. F. Pedraza and S. Young, *Holographic constraints on Bjorken hydrodynamics at finite coupling*, *JHEP* **10** (2017) 110, [1707.08812].

[131] A. Buchel, R. C. Myers and A. Sinha, *Beyond $\eta/s = 1/4\pi$*, *JHEP* **03** (2009) 084, [0812.2521].

[132] D. M. Hofman and J. Maldacena, *Conformal collider physics: Energy and charge correlations*, *JHEP* **05** (2008) 012, [0803.1467].

[133] D. M. Hofman, *Higher Derivative Gravity, Causality and Positivity of Energy in a UV complete QFT*, *Nucl. Phys.* **B823** (2009) 174–194, [0907.1625].

[134] A. Buchel and R. C. Myers, *Causality of Holographic Hydrodynamics*, *JHEP* **08** (2009) 016, [0906.2922].

[135] X. O. Camanho, J. D. Edelstein, J. Maldacena and A. Zhiboedov, *Causality Constraints on Corrections to the Graviton Three-Point Coupling*, *JHEP* **02** (2016) 020, [1407.5597].

[136] G. Papallo and H. S. Reall, *Graviton time delay and a speed limit for small black holes in Einstein-Gauss-Bonnet theory*, *JHEP* **11** (2015) 109, [1508.05303].

[137] T. Andrade, E. Caceres and C. Keeler, *Boundary causality versus hyperbolicity for spherical black holes in Gauss?Bonnet gravity*, *Class. Quant. Grav.* **34** (2017) 135003, [1610.06078].

[138] R. A. Konoplya and A. Zhidenko, *Quasinormal modes of Gauss-Bonnet-AdS black holes: towards holographic description of finite coupling*, *JHEP* **09** (2017) 139, [1705.07732].

[139] L. Keegan, A. Kurkela, P. Romatschke, W. van der Schee and Y. Zhu, *Weak and strong coupling equilibration in nonabelian gauge theories*, *JHEP* **04** (2016) 031, [1512.05347].

[140] P. Kovtun, *Lectures on hydrodynamic fluctuations in relativistic theories*, *J. Phys.* **A45** (2012) 473001, [1205.5040].

[141] S. Bhattacharyya, V. E. Hubeny, S. Minwalla and M. Rangamani, *Nonlinear Fluid Dynamics from Gravity*, *JHEP* **02** (2008) 045, [0712.2456].

[142] L. D. Landau and E. M. Lifshitz, *Fluid Mechanics*. Butterworth-Heinemann, Oxford, second ed., 1987.

[143] L. P. Kadanoff and P. C. Martin, *Hydrodynamic equations and correlation functions*, *Annals of Physics* **24** (Oct., 1963) 419–469.

[144] J. D. Bjorken, *Highly Relativistic Nucleus-Nucleus Collisions: The Central Rapidity Region*, *Phys. Rev.* **D27** (1983) 140–151.

[145] P. Romatschke, *Relativistic Viscous Fluid Dynamics and Non-Equilibrium Entropy*, *Class. Quant. Grav.* **27** (2010) 025006, [0906.4787].

[146] K. S. Thorne, R. H. Price and D. A. Macdonald, eds., *BLACK HOLES: THE MEMBRANE PARADIGM*. 1986.

[147] W. Florkowski, M. P. Heller and M. Spalinski, *New theories of relativistic hydrodynamics in the LHC era*, 1707.02282.

[148] M. Brigante, H. Liu, R. C. Myers, S. Shenker and S. Yaida, *Viscosity Bound Violation in Higher Derivative Gravity*, *Phys. Rev.* **D77** (2008) 126006, [0712.0805].

[149] A. Buchel, J. T. Liu and A. O. Starinets, *Coupling constant dependence of the shear viscosity in N=4 supersymmetric Yang-Mills theory*, *Nucl. Phys.* **B707** (2005) 56–68, [hep-th/0406264].

[150] Y. Brihaye and E. Radu, *Black objects in the Einstein-Gauss-Bonnet theory with negative cosmological constant and the boundary counterterm method*, *JHEP* **09** (2008) 006, [0806.1396].

[151] D. Astefanesei, N. Banerjee and S. Dutta, *(Un)attractor black holes in higher derivative AdS gravity*, *JHEP* **11** (2008) 070, [0806.1334].

[152] I. Aniceto, G. Basar and R. Schiappa, *A Primer on Resurgent Transseries and Their Asymptotics*, 1802.10441.

[153] D. Dorigoni, *An Introduction to Resurgence, Trans-Series and Alien Calculus*, 1411.3585.

[154] G. Dunne, "Resurgence and Trans-series in Quantum Theories.".

[155] A. Cherman, P. Koroteev and M. nsal, *Resurgence and Holomorphy: From Weak to Strong Coupling*, *J. Math. Phys.* **56** (2015) 053505, [1410.0388].

[156] H. S. Yamada and K. S. Ikeda, *A Numerical Test of Pade Approximation for Some Functions with singularity*, *ArXiv e-prints* (Aug., 2013) , [1308.4453].

[157] P. Romatschke, *Do nuclear collisions create a locally equilibrated quark?gluon plasma?*, *Eur. Phys. J.* **C77** (2017) 21, [1609.02820].

[158] M. P. Heller and V. Svensson, *How does relativistic kinetic theory remember about initial conditions?*, 1802.08225.

[159] A. Karch, D. T. Son and A. O. Starinets, *Zero Sound from Holography*, 0806.3796.

[160] M. Kulaxizi and A. Parnachev, *Comments on Fermi Liquid from Holography*, *Phys.Rev.* **D78** (2008) 086004, [0808.3953].

[161] M. Kulaxizi and A. Parnachev, *Holographic Responses of Fermion Matter*, *Nucl. Phys.* **B815** (2009) 125–141, [0811.2262].

[162] K.-Y. Kim and I. Zahed, *Baryonic Response of Dense Holographic QCD*, *JHEP* **0812** (2008) 075, [0811.0184].

[163] A. Karch, D. T. Son and A. O. Starinets, *Holographic Quantum Liquid*, *Phys. Rev. Lett.* **102** (2009) 051602.

[164] M. Kaminski, K. Landsteiner, J. Mas, J. P. Shock and J. Tarrio, *Holographic Operator Mixing and Quasinormal Modes on the Brane*, *JHEP* **1002** (2010) 021, [0911.3610].

[165] M. Edalati, J. I. Jottar and R. G. Leigh, *Holography and the sound of criticality*, *JHEP* **1010** (2010) 058, [1005.4075].

[166] C. Hoyos-Badajoz, A. O'Bannon and J. M. S. Wu, *Zero Sound in Strange Metallic Holography*, *JHEP* **09** (2010) 086, [1007.0590].

[167] D. Nickel and D. T. Son, *Deconstructing holographic liquids*, *New J.Phys.* **13** (2011) 075010, [1009.3094].

[168] B.-H. Lee, D.-W. Pang and C. Park, *Zero Sound in Effective Holographic Theories*, *JHEP* **11** (2010) 120, [1009.3966].

[169] O. Bergman, N. Jokela, G. Lifschytz and M. Lippert, *Striped instability of a holographic Fermi-like liquid*, 1106.3883.

[170] M. Ammon et al., *On Stability and Transport of Cold Holographic Matter*, *JHEP* **09** (2011) 030, [1108.1798].

[171] R. A. Davison and A. O. Starinets, *Holographic zero sound at finite temperature*, *Phys. Rev.* **D85** (2012) 026004, [1109.6343].

[172] R. A. Davison and N. K. Kaplis, *Bosonic excitations of the AdS_4 Reissner-Nordstrom black hole*, *JHEP* **12** (2011) 037, [1111.0660].

[173] N. Jokela, G. Lifschytz and M. Lippert, *Magnetic effects in a holographic Fermi-like liquid*, *JHEP* **05** (2012) 105, [1204.3914].

[174] M. Goykhman, A. Parnachev and J. Zaanen, *Fluctuations in finite density holographic quantum liquids*, *JHEP* **10** (2012) 045, [1204.6232].

[175] D. K. Brattan, R. A. Davison, S. A. Gentle and A. O'Bannon, *Collective Excitations of Holographic Quantum Liquids in a Magnetic Field*, *JHEP* **11** (2012) 084, [1209.0009].

[176] N. Jokela, M. Jarvinen and M. Lippert, *Fluctuations and instabilities of a holographic metal*, *JHEP* **02** (2013) 007, [1211.1381].

[177] D.-W. Pang, *Probing holographic semilocal quantum liquids with D-branes*, *Phys. Rev.* **D88** (2013) 046002, [1306.3816].

[178] P. Dey and S. Roy, *Zero sound in strange metals with hyperscaling violation from holography*, *Phys. Rev.* **D88** (2013) 046010, [1307.0195].

[179] M. Edalati and J. F. Pedraza, *Aspects of Current Correlators in Holographic Theories with Hyperscaling Violation*, *Phys. Rev.* **D88** (2013) 086004, [1307.0808].

[180] D. K. Brattan and G. Lifschytz, *Holographic plasma and anyonic fluids*, *JHEP* **02** (2014) 090, [1310.2610].

[181] R. A. Davison, M. Goykhman and A. Parnachev, *AdS/CFT and Landau Fermi liquids*, *JHEP* **07** (2014) 109, [1312.0463].

[182] B. S. DiNunno, M. Ihl, N. Jokela and J. F. Pedraza, *Holographic zero sound at finite temperature in the Sakai-Sugimoto model*, *JHEP* **04** (2014) 149, [1403.1827].

[183] N. Jokela and A. V. Ramallo, *Universal properties of cold holographic matter*, *Phys. Rev.* **D92** (2015) 026004, [1503.04327].

[184] G. Itsios, N. Jokela and A. V. Ramallo, *Collective excitations of massive flavor branes*, *Nucl. Phys.* **B909** (2016) 677–724, [1602.06106].

[185] N. Jokela, J. Jrvel and A. V. Ramallo, *Non-relativistic anyons from holography*, *Nucl. Phys.* **B916** (2017) 727–768, [1605.09156].

[186] D. Roychowdhury, *Probing η deformed backgrounds with Dp branes*, *Phys. Lett.* **B778** (2018) 167–173, [1706.02625].

[187] C.-F. Chen and A. Lucas, *Origin of the Drude peak and of zero sound in probe brane holography*, *Phys. Lett.* **B774** (2017) 569–574, [1709.01520].

[188] S. Sachdev, *What can gauge-gravity duality teach us about condensed matter physics?*, *Ann. Rev. Condensed Matter Phys.* **3** (2012) 9–33, [1108.1197].

[189] J. Tarrio, *Transport properties of spacetime-filling branes*, *JHEP* **04** (2014) 042, [1312.2902].

[190] A. Karch and E. Katz, *Adding Flavor to AdS/CFT*, *JHEP* **06** (2002) 043, [hep-th/0205236].

[191] L. Landau, *Oscillations in a Fermi Liquid*, *Zh. Eksp. Teor. Fiz.* **32** (1957) 59 [Sov. Phys. JETP 5 101 (1957)].

[192] W. R. Abel, A. C. Anderson and J. C. Wheatley, *Propagation of zero sound in liquid* he^3 *at low temperatures*, *Phys. Rev. Lett.* **17** (Jul, 1966) 74–78.

[193] D. Pines and P. Nozieres, *The Theory of Quantum Liquids*, vol. 1. W.A. Benjamin, Inc., New York City, 1 ed., 1966.

[194] E. M. Lifshitz and L. P. Pitaevskii, *Statistical Physics, Part 2: Theory of the Condensed State*, vol. 9 of *Course of Theoretical Physics*. Pergamon Press, Oxford, 1980.

[195] E. M. Lifshitz and L. P. Pitaevskii, *Physical Kinetics*, vol. 10 of *Course of Theoretical Physics*. Pergamon Press, Oxford, 1981.

[196] J. W. Negele and H. Orland, *Quantum Many-Particle Systems*, vol. 68 of *Frontiers In Physics*. Addison-Wesley, New York City, 1988.

[197] R. J. Anantua, S. A. Hartnoll, V. L. Martin and D. M. Ramirez, *The Pauli exclusion principle at strong coupling: Holographic matter and momentum space*, *JHEP* **03** (2013) 104, [1210.1590].

[198] R. A. Davison and B. Goutéraux, *Momentum dissipation and effective theories of coherent and incoherent transport*, *JHEP* **01** (2015) 039, [1411.1062].

[199] M. Cubrovic, J. Zaanen and K. Schalm, *String Theory, Quantum Phase Transitions and the Emergent Fermi-Liquid*, *Science* **325** (2009) 439–444, [0904.1993].

[200] M. Edalati, J. I. Jottar and R. G. Leigh, *Shear Modes, Criticality and Extremal Black Holes*, *JHEP* **1004** (2010) 075, [1001.0779].

[201] N. Iqbal, H. Liu and M. Mezei, *Semi-local quantum liquids*, *JHEP* **04** (2012) 086, [1105.4621].

[202] C. P. Herzog, *The Sound of M theory*, *Phys. Rev.* **D68** (2003) 024013, [hep-th/0302086].

[203] S. Fernando and D. Krug, *Charged black hole solutions in Einstein-Born-Infeld gravity with a cosmological constant*, *Gen. Rel. Grav.* **35** (2003) 129–137, [hep-th/0306120].

[204] T. K. Dey, *Born-Infeld black holes in the presence of a cosmological constant*, *Phys. Lett.* **B595** (2004) 484–490, [hep-th/0406169].

[205] R.-G. Cai, D.-W. Pang and A. Wang, *Born-Infeld black holes in (A)dS spaces*, *Phys. Rev.* **D70** (2004) 124034, [hep-th/0410158].

[206] S. S. Pal, *Fermi-like Liquid From Einstein-DBI-Dilaton System*, *JHEP* **04** (2013) 007, [1209.3559].

[207] G. Policastro, D. T. Son and A. O. Starinets, *From AdS / CFT correspondence to hydrodynamics*, *JHEP* **09** (2002) 043, [hep-th/0205052].

[208] A. O. Starinets, *Quasinormal modes of near extremal black branes*, *Phys. Rev.* **D66** (2002) 124013, [hep-th/0207133].

[209] G. Policastro, D. T. Son and A. O. Starinets, *From AdS / CFT correspondence to hydrodynamics. 2. Sound waves*, *JHEP* **0212** (2002) 054, [hep-th/0210220].

[210] N. I. Gushterov, *Quasinormal Modes and Correlators in the Shear Channel of Spacetime-Filling Branes*, 1807.11390.

[211] S. Bhattacharyya, S. Lahiri, R. Loganayagam and S. Minwalla, *Large rotating AdS black holes from fluid mechanics*, *JHEP* **09** (2008) 054, [0708.1770].

[212] R. A. Davison and A. Parnachev, *Hydrodynamics of cold holographic matter*, *JHEP* **06** (2013) 100, [1303.6334].

[213] S. de Haro, S. N. Solodukhin and K. Skenderis, *Holographic reconstruction of spacetime and renormalization in the AdS/CFT correspondence*, *Commun. Math. Phys.* **217** (2001) 595–622, [hep-th/0002230].

[214] J. I. Kapusta and C. Gale, *Finite-temperature field theory: Principles and applications*. Cambridge University Press, 2011.

[215] L. L.D. and E. M. Lifshitz, *Fluid Mechanics*, vol. 6 of *Course of Theoretical Physics*. Pergamon Press, Oxford, 1987.

[216] S. A. Hartnoll, J. Polchinski, E. Silverstein and D. Tong, *Towards strange metallic holography*, *JHEP* **1004** (2010) 120, [0912.1061].

[217] F. Bigazzi, A. L. Cotrone and J. Tarrio, *Charged D3-D7 plasmas: novel solutions, extremality and stability issues*, *JHEP* **07** (2013) 074, [1304.4802].

[218] D. Mateos, R. C. Myers and R. M. Thomson, *Holographic viscosity of fundamental matter*, *Phys. Rev. Lett.* **98** (2007) 101601, [hep-th/0610184].

[219] D. Mateos, R. C. Myers and R. M. Thomson, *Thermodynamics of the Brane*, *JHEP* **05** (2007) 067, [hep-th/0701132].

[220] F. Bigazzi, A. L. Cotrone, J. Mas, A. Paredes, A. V. Ramallo and J. Tarrio, *D3-D7 Quark-Gluon Plasmas*, *JHEP* **11** (2009) 117, [0909.2865].

[221] P. Di Francesco, P. Mathieu and D. Senechal, *Conformal Field Theory*. Graduate Texts in Contemporary Physics. Springer-Verlag, New York, 1997, 10.1007/978-1-4612-2256-9.

[222] J. Mas, J. P. Shock and J. Tarrio, *A Note on conductivity and charge diffusion in holographic flavour systems*, *JHEP* **0901** (2009) 025, [0811.1750].

[223] N. I. Gushterov, A. O'Bannon and R. Rodgers, *Holographic Zero Sound from Spacetime-Filling Branes*, 1807.11327.

[224] J. C. Solana, S. Grozdanov and A. O. Starinets, *Transport peak in thermal spectral function of $\mathcal{N} = 4$ supersymmetric Yang-Mills plasma at intermediate coupling*, 1806.10997.

[225] A. Lucas and K. C. Fong, *Hydrodynamics of electrons in graphene*, *J. Phys. Condens. Matter* **30** (2018) 053001, [1710.08425].

[226] A. Lucas and S. Das Sarma, *Electronic sound modes and plasmons in hydrodynamic two-dimensional metals*, *Phys. Rev. B* **97** (Mar, 2018) 115449.

[227] M. A. Metlitski and T. Grover, *Entanglement Entropy of Systems with Spontaneously Broken Continuous Symmetry*, 1112.5166.

[228] M. M. Wolf, *Violation of the entropic area law for Fermions*, *Phys. Rev. Lett.* **96** (2006) 010404, [quant-ph/0503219].

[229] D. Gioev and I. Klich, *Entanglement Entropy of Fermions in Any Dimension and the Widom Conjecture*, *Physical Review Letters* **96** (Mar., 2006) 100503, [quant-ph/0504151].

[230] B. Swingle, *Entanglement Entropy and the Fermi Surface*, *Phys. Rev. Lett.* **105** (2010) 050502, [0908.1724].

[231] B. Swingle, *Conformal Field Theory on the Fermi Surface*, *Phys. Rev.* **B86** (2012) 035116, [1002.4635].

[232] A. Kitaev and J. Preskill, *Topological Entanglement Entropy*, *Physical Review Letters* **96** (Mar., 2006) 110404, [hep-th/0510092].

[233] M. Levin and X.-G. Wen, *Detecting Topological Order in a Ground State Wave Function*, *Physical Review Letters* **96** (Mar., 2006) 110405, [cond-mat/0510613].

[234] C. Castelnovo and C. Chamon, *Topological order in a three-dimensional toric code at finite temperature*, *Phys. Rev. B* **78** (Oct., 2008) 155120, [0804.3591].

[235] T. Grover, A. M. Turner and A. Vishwanath, *Entanglement entropy of gapped phases and topological order in three dimensions*, *Phys. Rev. B* **84** (Nov., 2011) 195120, [1108.4038].

[236] M. Nozaki, T. Numasawa and T. Takayanagi, *Holographic Local Quenches and Entanglement Density*, *JHEP* **05** (2013) 080, [1302.5703].

[237] J. Bhattacharya, V. E. Hubeny, M. Rangamani and T. Takayanagi, *Entanglement density and gravitational thermodynamics*, *Phys. Rev.* **D91** (2015) 106009, [1412.5472].

[238] M. Taylor and W. Woodhead, *Renormalized entanglement entropy*, *JHEP* **08** (2016) 165, [1604.06808].

[239] M. Taylor and W. Woodhead, *The holographic F theorem*, 1604.06809.

[240] M. Taylor and W. Woodhead, *Non-conformal entanglement entropy*, 1704.08269.

[241] J. Bhattacharya, M. Nozaki, T. Takayanagi and T. Ugajin, *Thermodynamical Property of Entanglement Entropy for Excited States*, *Phys. Rev. Lett.* **110** (2013) 091602, [1212.1164].

[242] D. D. Blanco, H. Casini, L.-Y. Hung and R. C. Myers, *Relative Entropy and Holography*, *JHEP* **08** (2013) 060, [1305.3182].

[243] B. Swingle and T. Senthil, *Universal crossovers between entanglement entropy and thermal entropy*, *Phys. Rev.* **B87** (2013) 045123, [1112.1069].

[244] R. C. Myers and A. Singh, *Comments on Holographic Entanglement Entropy and RG Flows*, *JHEP* **04** (2012) 122, [1202.2068].

[245] M. Headrick and T. Takayanagi, *A Holographic proof of the strong subadditivity of entanglement entropy*, *Phys. Rev.* **D76** (2007) 106013, [0704.3719].

[246] A. C. Wall, *Maximin Surfaces, and the Strong Subadditivity of the Covariant Holographic Entanglement Entropy*, *Class. Quant. Grav.* **31** (2014) 225007, [1211.3494].

[247] B. Swingle, *Entanglement does not generally decrease under renormalization*, *J. Stat. Mech.* **1410** (2014) P10041, [1307.8117].

[248] D. Z. Freedman, S. S. Gubser, K. Pilch and N. P. Warner, *Renormalization group flows from holography supersymmetry and a c theorem*, *Adv. Theor. Math. Phys.* **3** (1999) 363–417, [hep-th/9904017].

[249] J. Erdmenger and N. Miekley, *Non-local observables at finite temperature in AdS/CFT*, 1709.07016.

[250] S. A. Hartnoll, *Lectures on holographic methods for condensed matter physics*, *Class. Quant. Grav.* **26** (2009) 224002, [0903.3246].

[251] N. Iqbal, H. Liu and M. Mezei, *Lectures on Holographic Non-Fermi Liquids and Quantum Phase Transitions*, in *Proceedings, Theoretical Advanced Study Institute in Elementary Particle Physics (TASI 2010). String Theory and Its Applications: From meV to the Planck Scale: Boulder, Colorado, USA, June 1-25, 2010*, pp. 707–816, 2011. 1110.3814.

[252] R. Emparan, R. Suzuki and K. Tanabe, *The large D limit of General Relativity*, *JHEP* **06** (2013) 009, [1302.6382].

[253] R. Emparan, D. Grumiller and K. Tanabe, *Large-D gravity and low-D strings*, *Phys. Rev. Lett.* **110** (2013) 251102, [1303.1995].

[254] R. C. Myers and A. Sinha, *Holographic c-theorems in arbitrary dimensions*, *JHEP* **01** (2011) 125, [1011.5819].

[255] H. Liu and M. Mezei, *A Refinement of entanglement entropy and the number of degrees of freedom*, *JHEP* **04** (2013) 162, [1202.2070].

[256] H. Liu and M. Mezei, *Probing renormalization group flows using entanglement entropy*, *JHEP* **01** (2014) 098, [1309.6935].

[257] S. Kundu and J. F. Pedraza, *Aspects of Holographic Entanglement at Finite Temperature and Chemical Potential*, *JHEP* **08** (2016) 177, [1602.07353].

[258] V. E. Hubeny, *Extremal surfaces as bulk probes in AdS/CFT*, *JHEP* **07** (2012) 093, [1203.1044].

[259] T. Albash and C. V. Johnson, *Holographic Entanglement Entropy and Renormalization Group Flow*, *JHEP* **02** (2012) 095, [1110.1074].

[260] J. L. Cardy, *Operator Content of Two-Dimensional Conformally Invariant Theories*, *Nucl. Phys.* **B270** (1986) 186–204.

[261] A. Castro, A. Maloney and A. Strominger, *Hidden Conformal Symmetry of the Kerr Black Hole*, *Phys. Rev.* **D82** (2010) 024008, [1004.0996].

[262] H. K. Kunduri, J. Lucietti and H. S. Reall, *Near-horizon symmetries of extremal black holes*, *Class. Quant. Grav.* **24** (2007) 4169–4190, [0705.4214].

[263] P. Figueras, H. K. Kunduri, J. Lucietti and M. Rangamani, *Extremal vacuum black holes in higher dimensions*, *Phys. Rev.* **D78** (2008) 044042, [0803.2998].

[264] B. Swingle, *Highly entangled quantum systems in 3+1 dimensions*, 1003.2434.

[265] S. Sachdev, *Bekenstein-Hawking Entropy and Strange Metals*, *Phys. Rev.* **X5** (2015) 041025, [1506.05111].

[266] A. Kitaev, *A simple model of quantum holography*, 2015.

[267] H. Kodama and A. Ishibashi, *Master equations for perturbations of generalized static black holes with charge in higher dimensions*, *Prog. Theor. Phys.* **111** (2004) 29–73, [hep-th/0308128].